Title
Improved Positive Electrode Materials for Li-ion Batteries

Author
Conry, Thomas Edward

Publication Date
2012

Peer reviewed|Thesis/dissertation

Improved Positive Electrode Materials for Li-ion Batteries

by

Thomas Edward Conry

A dissertation submitted in partial satisfaction of the

requirements for the degree of

Doctor of Philosophy

in

Engineering – Materials Science and Engineering

and the Designated Emphasis

in

Nanoscale Science and Engineering

in the

Graduate Division

of the

University of California, Berkeley

Committee in charge:

Professor Lutgard C. De Jonghe, Chair

Professor Ronald Gronsky

Professor Jeffrey A. Reimer

Spring 2012

Abstract

Improved Positive Electrode Materials for Li-ion Batteries

by

Thomas Edward Conry

Doctor of Philosophy in Engineering – Materials Science and Engineering

and the Designated Emphasis in Nanoscale Science and Engineering

University of California, Berkeley

Professor Lutgard C. De Jonghe, Chair

The introduction of the first commercially produced Li-ion battery by Sony in 1990 sparked a period of unprecedented growth in the consumer electronics industry. Now, with increasing efforts to move away from fossil-fuel-derived energy sources, a substantial amount of current research is focused on the development of an electrified transportation fleet. Unfortunately, existent battery technologies are unable to provide the necessary performance for electric vehicles (EV's) and plug-in hybrid electric vehicles (PHEV's) vehicles at a competitive cost. The cost and performance metrics of current Li-ion batteries are mainly determined by the positive electrode materials. The work here is concerned with understanding the structural and electrochemical consequences of cost-lowering mechanisms in two separate classes of Li-ion cathode materials; the LiMO$_2$ (M = Ni, Mn, Co) layered oxides and the LiMPO$_4$ olivine materials; with the goal of improving performance.

Al-substitution for Co in $LiNi_zMn_zCo_{1-2z}O_2$ ("NMC") materials not only decreases the costly Co-content, but also improves the safety aspects and, notably, enhances the cycling stability of the layered oxide electrodes. The structural and electrochemical effects of Al-substitution are investigated here in a model NMC compound, $LiNi_{0.45}Mn_{0.45}Co_{0.1-y}Al_yO_2$. In addition to electrochemical measurements, various synchrotron-based characterization methods are utilized, including high-resolution X-ray diffraction (XRD), *in situ* X-ray diffraction, and X-ray absorption spectroscopy (XAS). Al-substitution causes a slight distortion of the as-synthesized hexagonal layered oxide lattice, lowering the inherent octahedral strain within the transition metal layer. The presence of Al also is observed to limit the structural variation of the NMC materials upon Li-deintercalation, as well as extended cycling of the electrodes.

Various olivine materials, LiMPO$_4$ (M=Fe,Co) are produced using a custom-built spray pyrolysis system. Spray pyrolysis is a simple, inexpensive, and scalable method used to produce highly uniform and phase-pure particle materials. The materials are synthesized here as porous, carbon-coated spherical particles with micron-sized diameters and

nanoscale primary particles. The LiMPO$_4$ (M=Fe,Co) olivine electrodes display exceptional electrochemical properties, in terms of high discharge capacities, rate capability, and cycling stability. The excellent performance is due to the particle morphologies that include a hierarchical pore structure and conductive carbon network throughout the particles. This allows liquid electrolyte penetration into the particle interiors, thus limiting the necessary solid-state diffusion distances, as well as efficient charge transfer and collection.

This dissertation is dedicated to my incredible fiancé, Seema, and to my parents and brothers. I thank them for their unwavering support and patience throughout my studies, and for sharing both the exciting and difficult times of the past years.

Table of Contents

Acknowledgements

Acknowledgements are in order for my advisor, Prof. Lutgard De Jonghe for generously providing me the opportunity to continue my studies at Berkeley. I also have the highest regard for my other advisor, Dr. Marca Doeff, and sincerely acknowledge her support and guidance throughout the past three years. Her knowledge and patience have been instrumental in my growth as a scientist, and invaluably aided the pursuit of my passions.

I would also like to acknowledge the many people who have contributed to the work in this dissertation, through conversations, experiments, and by simply being available to provide expertise and ideas when needed. Jordi Cabana, Apurva Mehta, Kinson Kam, and Jun Liu have all had valuable influence on my progress. James Wu has been a constant source of knowledge and a wonderful colleague.

Finally, I'd also like to formally acknowledge my fiancé, Seema, who has stuck by me this entire time providing motivation and encouragement, and with whom I can't wait to write the next chapter of our lives. My parents, Eileen and Harry, and my brothers, Billy and Mikey, have been constantly supportive, giving me the confidence to reach my goals. I could not have done any of this without all of them.

The work in this dissertation was supported by the Assistant Secretary for Energy Efficiency and Renewable Energy, Office of Vehicle Technologies of the U.S. Department of Energy under Contract No. DE-AC02-05CH11231 through the BATT program. Portions of this research were carried out at the Stanford Synchrotron Radiation Lightsource, a Directorate of SLAC National Accelerator Laboratory and an Office of Science User Facility operated for the U.S. Department of Energy Office of Science by Stanford University. The SSRL Structural Molecular Biology Program is supported by the DOE Office of Biological and Environmental Research and by the National Institutes of Health, National Center for Research Resources, Biomedical Technology Program (P41RR001209). Use of the Advanced Photon Source at Argonne National Laboratory was supported by the U.S. Department of Energy, Office of Science, Office of Basic Energy Sciences, under Contract No. DE-AC02-06CH11357.

Chapter 1: Introduction

1.1 Motivation

Batteries are used to power everyday life. In a general sense, they are simply a medium in which energy is stored for use at a user-defined time. Whether primary (single use) or secondary (rechargeable), no other technology is able to provide reliable, compact, portable power on-demand like battery systems. Batteries are manufactured on a wide range of size and energy scales; the specifics are determined by the application needs and operation conditions. Primary batteries will continue to be used well into the future, as they are a mostly mature and inexpensive product. Rechargeable batteries, however, still represent an emerging and improving technology that has aided the development of common items such as cell phones and notebook computers that define today's interconnected world. Future applications abound for secondary batteries, such as grid-scale storage systems to partner with renewable energy generation sources (wind and solar farms, for example), and systems for load-leveling of today's power generation to improve efficiency. Perhaps most anticipated, however, is the development of an electrified transportation fleet.

The widespread deployment of electrified vehicles such as plug-in hybrids (PHEV's) and pure electric vehicles (EV's) would be a significant step towards a reduction of US dependence on foreign oil. The United States has more motor vehicles per person than any other country in the world, the amount of which is actually growing faster than the domestic population.[1] Figure 1-1 shows the number of motor vehicles in the US per 1000 people since the beginning of the 20th century through 2009. Also plotted for comparison along the US trend are the corresponding values for other countries and regions measured in both 1999 and 2009. Although most other regions are experiencing a large growth, none have reached values beyond those seen in the US in the early 1970's.[2]

The huge number of vehicles in use requires a substantial amount of energy to power them, and in fact, a staggering 28.1% of the total US energy consumption in 2010 was from the transportation sector, second only to the industrial sector that accounted for 31%. This value has shown an increasing trend since 1973 (+1.1% average annual change), while industry demands have been decreasing in the same time frame (-1.4% average annual change).[3]

In 2010, the transportation sector was 93.5% powered by petroleum-based energy sources, a value that does *not* include blended gasoline fuels with 10% or less ethanol content, which can account for up to an additional 4% of the energy sources.[3] The United States produced just 9.1% of the world's petroleum in 2010, while accounting for 22.5% of the total use, requiring almost half of the consumed petroleum to be imported.[4] About 70% of that total fuel was used for transportation applications.

The United States was able to meet all of its transportation petroleum needs until 1989, as can be seen in Figure 1-2. Today, however, transportation petroleum use is 172.5% of the domestic production. Thankfully, that value has decreased since peaking at 204.4% in 2007, but the substantial gap in production and use has left the country's energy dependence vulnerable to fluctuating oil prices and geopolitical issues.

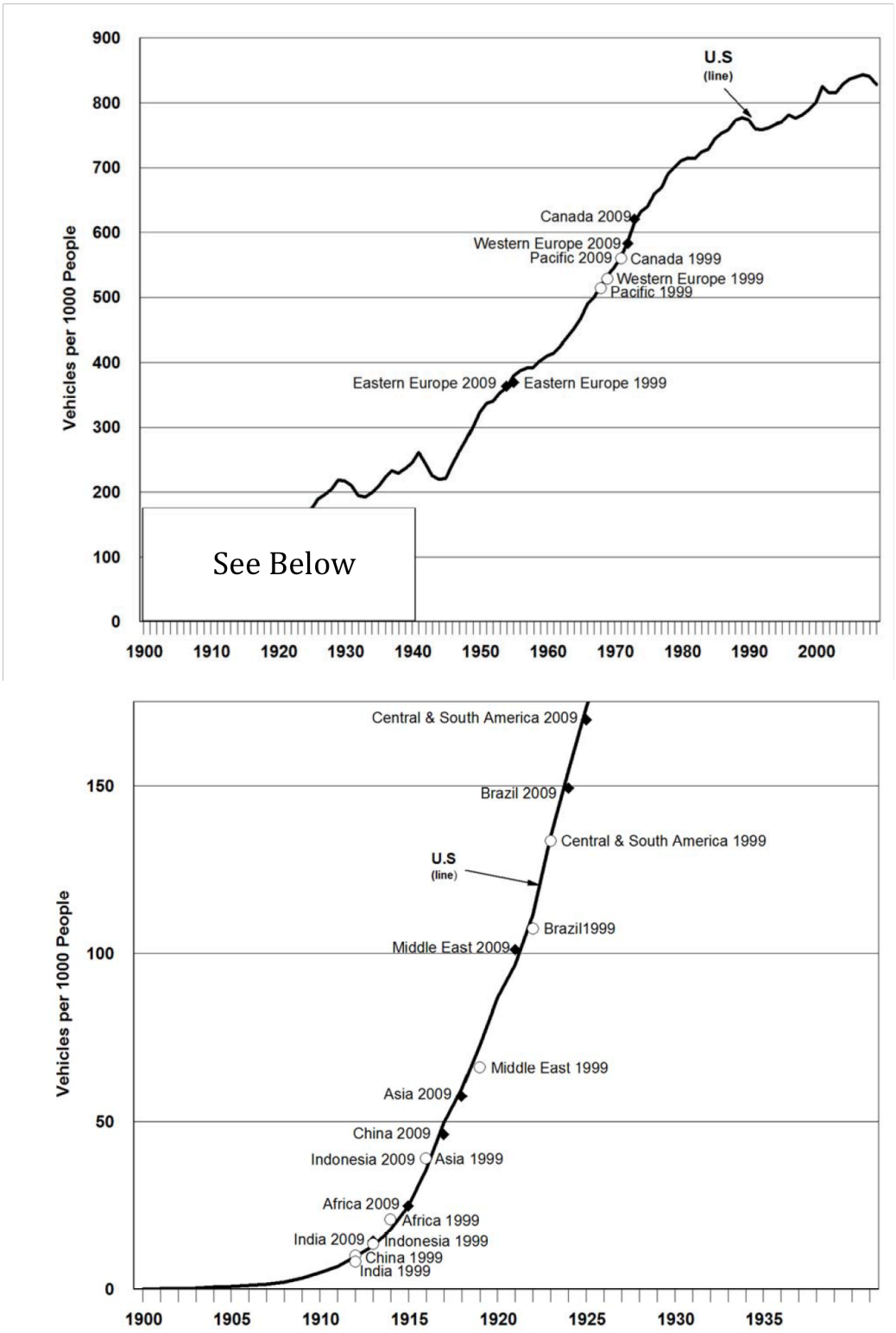

Figure 1-1: Number of vehicles in the United States per 1000 people since 1900 (line). Indicated are the number of vehicles per 1000 people in other regions of the world as measured in 1999 (open circles) and 2009 (filled diamonds).[2]

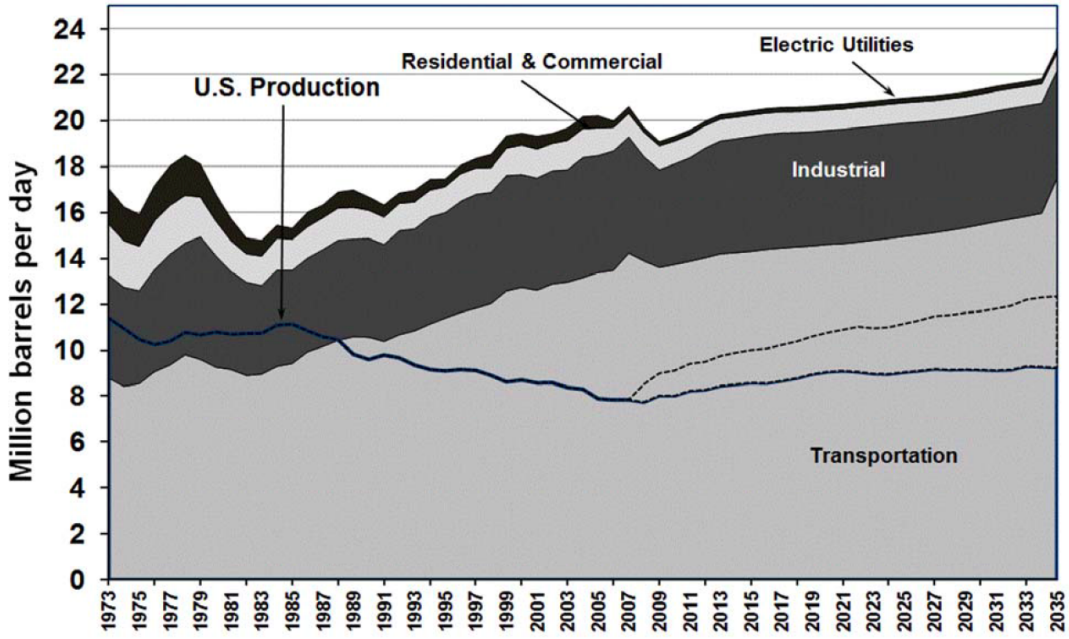

Figure 1-2: US petroleum production was sufficient for the transportation sector until 1989. The gap has been widening since. The solid line indicates production from conventional petroleum sources, while the dotted line includes non-petroleum sources like ethanol and other blending components.[4]

Additionally, the existence of human-exacerbated global warming is now widely accepted as scientific fact.[5] The burning of fossil fuels releases certain gases into the atmosphere that act to trap heat, warming the planet via a "greenhouse effect." CO_2 accounts for the majority of greenhouse gases, which additionally include methane, nitrous oxide, hydrofluorocarbons and perfluorocarbons.[6] Ice core and atmospheric measurements have correlated an increase of CO_2 and other greenhouse gas concentrations with the observed temperature increase since the industrial revolution. Pre-industrial CO_2 concentrations were about 280 ppm, increasing to about 380 ppm between 1906-2005.[7] Data from 2007 shows the United States accounted for one fifth (20.2%) of the worldwide CO_2 emissions. The largest contributor to these emissions is the transportation sector, which imparted 32.3% of the total in 2009.[6]

For these reasons, the development of electric vehicles is imperative. By transitioning to an electrified fleet, it has been estimated that US dependence on foreign oil can be decreased by up to 60%, while reducing greenhouse gas emissions by up to 40%.[8] Unfortunately a widely distributable rechargeable battery technology with adequate performance that is cost-competitive with internal combustion engines has yet to be demonstrated, though Li-ion batteries come the closest.

1.2 Li-ion Batteries

A battery, whether primary or secondary, is composed of one or more electrochemical cells that convert chemical energy into electrical energy through oxidation and reduction (redox) reactions. Each electrochemical cell consists of

electronically isolated positive and a negative electrodes with an ionically conductive electrolyte in between. When a load completes the external circuit and the battery is discharged, a chemical oxidation reaction occurs at the anode (negative electrode), producing an electron as part of the reaction. The electron travels through the circuit, performing work, where it is consumed at the cathode (positive electrode) in a complimentary reduction reaction. The physical separation of the oxidation and reduction reactions is key to the battery's ability to perform useful work. The redox reactions often produce or consume ions in the electrolyte. In a secondary battery, the chemical reactions at each electrode are reversible, and thus an external energy source can be applied to recharge the cell.

The spontaneous discharge of a battery couple is due to a chemical potential difference between the two electrodes in the cell. The energy stored in a cell is determined by the amount of reactants (stored charge) available and the potential energy difference. The specific chemistry of the reaction determines the theoretical capacity (Q, in Ah) of the system, described by Faraday's law, which simply states that the mass of a substance produced by electrolysis (redox products) is proportional to the charge passed:

$$Q = \frac{m_i n F}{s_i M_i} \qquad \text{(Eq. 1-1)}$$

where m_i is the mass of the produced species i, n is the number of electrons involved in the reaction, s_i is the stoichiometric coefficient of species i, M_i is the molar mass, and F is Faraday's constant (96,485 C/mol). Specific capacities are generally reported in mAh/g of the active materials, where 1 mAh = 3.6 C. The driving force for reaction is determined by the difference in Gibbs free energy, $\Delta G°$, between the electrodes:

$$\Delta G° = -nFE° \qquad \text{(Eqn. 1-2)}$$

where E° is the equilibrium potential difference between the electrodes under standard conditions. If the conditions are departed from standard state, the equilibrium potential, E, is modified according to the Nernst equation:

$$E = E° - \frac{RT}{nF} \ln \prod_i Q \qquad \text{(Eqn. 1-3)}$$

R is the ideal gas constant, T is temperature, and Q is the equilibrium reaction constant. When the cell is in operation, however, various kinetic resistances affect the observed potential further. These include ohmic losses from electronic and ionic transport through the electrode materials and the electrolyte, as well as kinetic limitations of interfacial charge transfer. This "overpotential," $\eta_s = E\text{-}E_{eq}$, is related to the current density drawn from the system, *i*, through the Butler-Volmer equation:

$$i = i_0 \left[\exp\left(\frac{\alpha_a F \eta_s}{RT} \right) - \exp\left(\frac{-\alpha_c F \eta_s}{RT} \right) \right] \qquad \text{(Eqn. 1-4)}$$

where α_a and α_c are transfer coefficients of the anode and cathode, respectively, that describe how the applied potential distributes between the two electrodes, and i_0 is the exchange current density, intrinsic to the cell. Finally, a note about battery nomenclature: C-rate describes the current density at which a battery is charged or discharged normalized to the included active material capacity; a battery is fully (dis)charged in X hours at a rate of X^{-1}C.

Compared to other electronic technologies, like semiconductor-based devices, battery technology has been slow to mature. Alessandro Volta demonstrated the first electrochemical cell in 1800; it consisted of stacked alternating plates of Cu and Zn metals separated by brine-soaked cardboard or cloths. The Pb-acid battery, the first rechargeable system, was invented in 1859 by Gaston Planté and is still widely used today – albeit with engineering improvements – in car and boat batteries, and home-storage systems (in conjunction with rooftop solar panels), for example.

As can be seen in Figure 1-3, secondary batteries have indeed improved over time both in terms of gravimetric and volumetric energy density.[9] The figure does not show important performance metrics such as cycle life, safety, or maintenance requirements, which have improved as well. The major advances, however, have been dependent on the development of new electrochemical couples. Li-ion batteries have the highest energy density of commercialized systems, but are not limited to one specific chemistry. There are several choices for both anodes and cathodes.

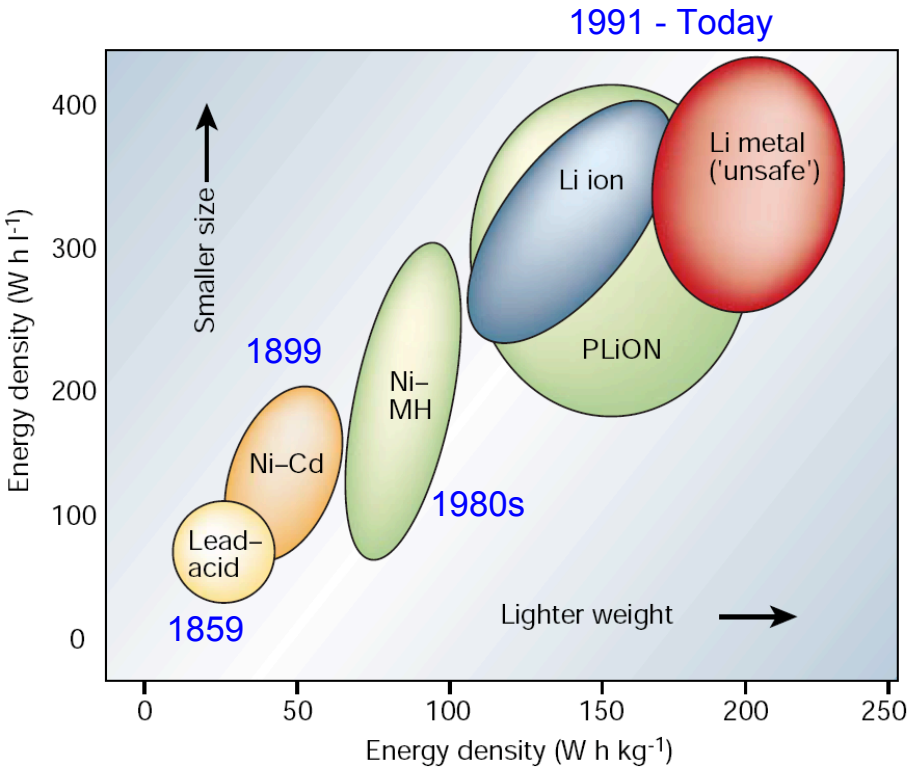

Figure 1-3: The volumetric and gravimetric energy densities of batteries have increased mostly with changes in chemistry.[9]

Most electrode materials under consideration for use in Li-ion batteries are intercalation materials, which undergo topotactic redox reactions. The host materials have a crystal structure (out of) into which Li ions are able to (de)intercalate during battery charge and discharge, shown schematically in Figure 1-4. Charge compensation within the material is achieved via the oxidation or reduction of a transition metal in almost all cathode materials. The general reactions on discharge at each electrode, where A and C are the active material components in the anode and cathode, respectively, are:

Anode (– electrode):	$LiA^n \rightarrow Li^+ + e^- + A^{n+1}$	(oxidation)
Cathode (+ electrode):	$Li^+ + e^- + C^{n+1} \rightarrow LiC^n$	(reduction)
Overall:	$LiA^n + C^{n+1} \rightarrow A^{n+1} + LiC^n$	

where *n* refers to the oxidation state of the redox-active component. The reactions are reversed on charge. An advantage of these types of materials is that the host structure undergoes a minimal structural change with varying Li concentration, and does not create any gaseous or soluble by-products from the charge compensating reaction (under normal operating conditions). The specific materials choices determine the performance and other characteristics of the assembled Li-ion battery, such as the operating voltage, energy densities, and power capability.

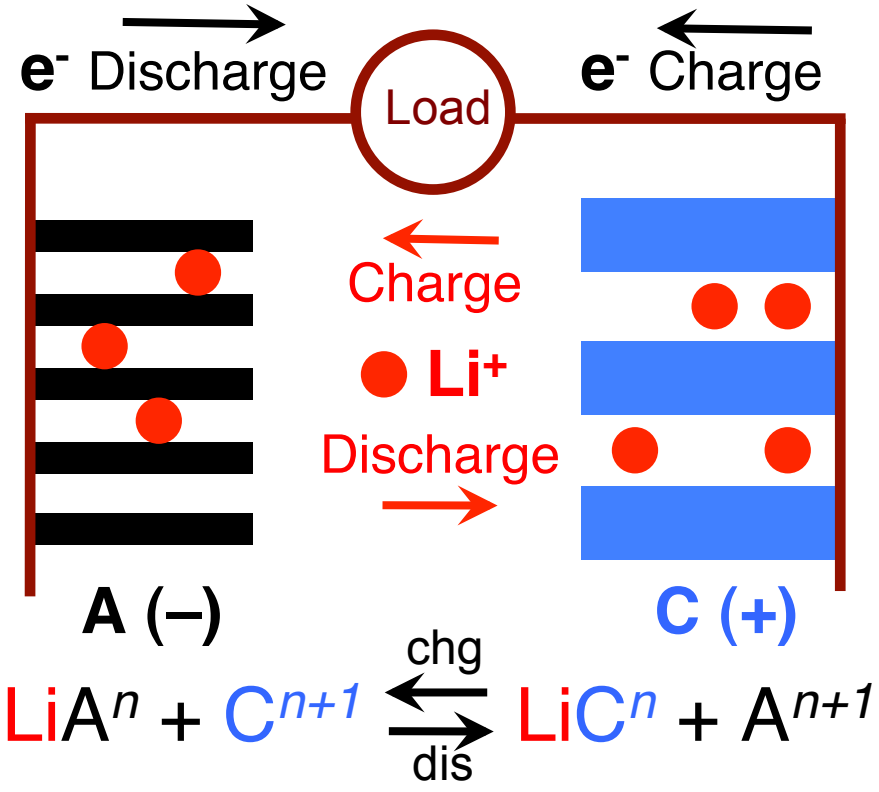

Figure 1-4: Schematic of a Li-ion battery. Li^+ ions are shuttled between two insertion materials during charge and discharge.

In addition to an anode and a cathode, a Li-ion cell generally contains a non-aqueous liquid electrolyte and a separator material between the electrodes to electronically isolate them but allow ionic conduction. The non-aqueous electrolyte is used both because Li reacts strongly with water and because water is not stable against oxidation at the high potentials inherent to Li-ion batteries. Today's electrolytes are commonly a mixture of organic carbonates such as ethylene carbonate (EC), diethyl carbonate (DEC), or dimethyl carbonate (DMC) in some volumetric ratio, with a dissolved Li-containing salt, like $LiPF_6$ or LiBOB (lithium bisoxalatoborate). The ionically conductive but electronically insulating separator allows the reversible transport, or "shuttling," of Li-ions between the electrodes during charge and discharge while forcing electron transport to progress through the external circuit.

Porous composite electrodes are made from the particulate active materials. This allows electrolyte penetration throughout the electrodes and maximizes surface area for Li-ion intercalation reactions. The construction of the porous electrodes requires a non-reactive polymer binder, often polyvinylidene fluoride (PVDF) or polytetrafluorethylene (PTFE), to help maintain structure. Additionally, carbon – graphite, carbon black, or a combination – is added to improve conductivity, and the composite electrodes are cast on metallic current collectors for efficient charge transfer through the circuit.

Despite the very large capacity of Li metal (3829 mAh/g), almost all commercial Li-ion batteries today use graphite or a mixture of carbons as the negative electrode. Graphite has a theoretical capacity of 380 mAh/g, representing a maximum intercalation of one Li per six carbon atoms to form LiC_6 (see ref. 10 to read about stages/phases of Li-intercalation into C).[10] Li metal anodes are not used because of the difficulties of plating Li during repeated charging of the cell.[11] Dendrites are formed that can result in shorting of the cell, leading to massive heat generation and burning of the organic electrolyte and other components. Thus, legitimate safety concerns have so far prevented the use of metallic Li in commercial secondary batteries (it is, however, used in certain primary batteries). Graphite has a potential of about 100 mV vs. Li/Li^+, consequently reducing the cell potential slightly compared to devices with Li anodes, though its use significantly improves the safety aspects.

Currently, Li-ion batteries are the only battery type able to meet the performance demands for PHEV's set by the United States Advanced Battery Consortium (USABC),[12] as can be seen in Figure 1-5. Here is shown a Ragone plot that compares the specific energy (kWh/kg) and the specific power (W/kg) capabilities for various electrochemical energy storage systems.[13] There is a compromise between energy and power, as shown in the plot, resulting from both cell design and material limitations. No current electrochemical technology can rival the internal combustion engine in regards to either energy or power density, and existing Li-ion battery system performance has yet to achieve the goals set for all-electric vehicles, though it does come close. Li-ion batteries, however, represent the state-of-the-art technology available today.

As described above, Li-ion cells are complex engineered systems, containing composite electrodes, non-aqueous electrolytes, separators, and current collectors. These are assembled into batteries and modules requiring non-active casing components. The resulting current cost of current Li-ion batteries can be between \$600-\$1,200/kWh, and analysis has suggested that this cost must be reduced at least by a factor of 3-4 before widespread deployment of EV's and PHEV's is viable.[14] USABC has a goal of

$150/kwh. Regardless of whether the Li-ion battery system is optimized for high energy or high power, the most expensive components are the electrolyte, separator, and cathode materials.[15] The cathode material in today's cells, regardless of choice, is the main determinant of energy density, as it has a smaller specific capacity than the graphite anode. The positive electrode material additionally establishes a host of other characteristics of a Li-ion battery system, including the safety attributes (both overcharge and thermal stabilities), cycle life, environmental toxicity and recyclability, and, as mentioned above, the active material costs. The identification of lower-cost solutions that do not compromise the other characteristics, equally important from a commercial standpoint, is critical. It is for these reasons that research on positive electrode materials has burgeoned since the first Li-ion battery was introduced twenty years ago.

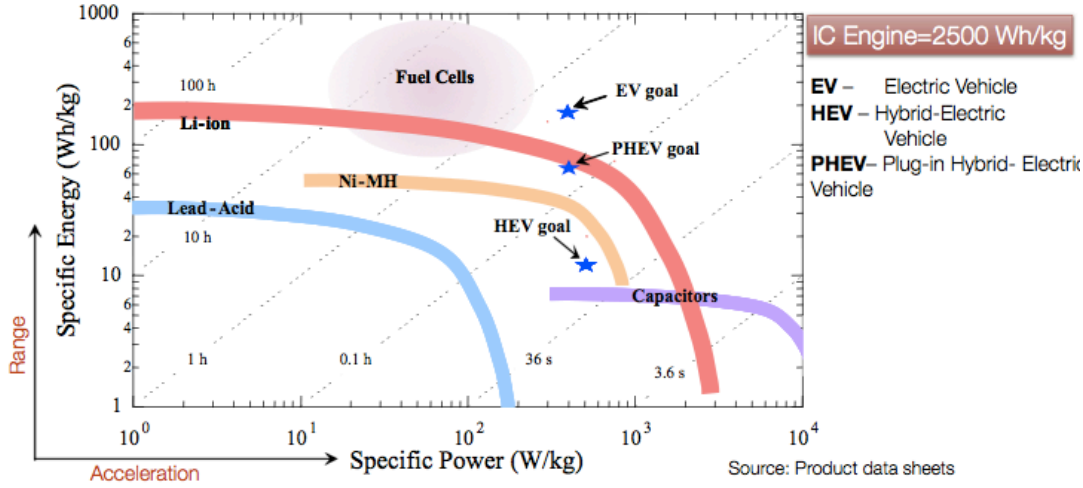

Figure 1-5: Ragone plot showing the specific energy vs. specific power of different electrochemical energy storage systems. Li-ion batteries are the only system that meets the USABC performance goals for PHEV's, and come close to the EV goals.[13]

1.3 Positive Electrode Materials

The first major breakthrough in the development of Li-ion batteries came in 1976 when Whittingham et. al. demonstrated the reversible intercalation of Li into TiS_2, after Steele et. al. suggested its use as a cathode material for Li batteries.[16,17] TiS_2 has a layered structure consisting of a hexagonal close packed sulfur anion lattice with titanium ions situated in octahedral sites between alternating sulfur sheets (Fig. 1-6). It was shown that a single phase existed for the entire composition range Li_xTiS_2 $0 \leq x \leq 1$, with Li-intercalation occurring at a potential of ~2.2 V vs. Li/Li^+.[18] This voltage was too low to mark a significant improvement over aqueous cells on a cost basis. Goodenough, however, noted that oxides could stabilize higher oxidation states, thereby increasing the cell potential.[19] As there were no MO_2 materials known to crystallize in a similar layered structure, focus turned to Li-containing compounds like $LiCoO_2$.[20] Li extraction was subsequently demonstrated at about 4 V vs. Li/Li^+, but there was minimal industrial interest in a cathode material originating in the discharged state. It was only Sony

Corporation that realized the potential, pairing the $LiCoO_2$ cathode with a carbon anode to introduce the first commercial Li-ion battery in 1990,[21] and subsequently enabling unprecedented growth in the portable electronics industry. Since then, a substantial amount of investigative effort has been directed towards discovering new materials and improving existent systems for Li-ion batteries, with performance, safety, and material and processing costs of equally paramount concern. The following sections will describe the most commonly used materials in the industry, and those under current development.

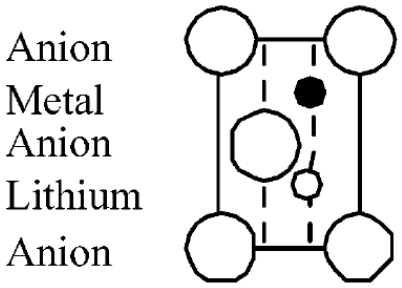

Figure 1-6: Schematic of the layered structure of $LiTiS_2$.[18]

Layered Transition Metal Oxides

The materials that crystallize in the hexagonal α-$NaFeO_2$ crystal structure (space group #166, *R-3m*) with the general stoichiometric formula Li*M*O_2 (*M* = transition metal) are some of the most important in today's Li-ion batteries. The structure, shown in Figure 1-7, consists of layers of edge-sharing *M*O_6 transition metal octahedra alternating with layers of Li^+ ions, also residing in octahedral sites. The structure is a derivative of the rock salt structure, which has a cubic close packed (ccp) arrangement of oxygen ions with ABCABC stacking, and a similar, offset cation lattice with cations in the octahedral interstitials. The α-$NaFeO_2$ structure has ABC stacking of the oxygen anions along the c-axis ([001], the layer stacking direction), similar to the [111] direction in the cubic rock salt structure. However, the Li and transition metal cations are segregated into separate, alternating layers in the *R-3m* structure. This structure is also sometimes referred to in layer notation as O3, indicating three layers of transition metals per unit cell. The cation ordering is driven in large part by a size difference between the Li and transition metal ions.[22] For consistency throughout the rest of this text, the lithium ions are assumed to occupy the 3a positions, transition metal ions the 3b, and oxygen anions the 6c Wyckoff positions.

The Li ions are often referenced as residing in the "Van der Waals" gaps in the structure. Li can be electrochemically extracted from the structure, with diffusion occurring in two dimensions. Li is believed to hop from one octahedral site to another via a tetrahedral site.[23] As the various transition metals relevant to today's batteries (Fe, Mn, Co, Ni) are similar in mass, all Li*M*O_2 compounds have a theoretical capacity of approximately 280 mAh/g, though the practical capacities can vary substantially depending on the identity of *M*. The following describes the important materials crystallizing in the *R-3m* layered structure.

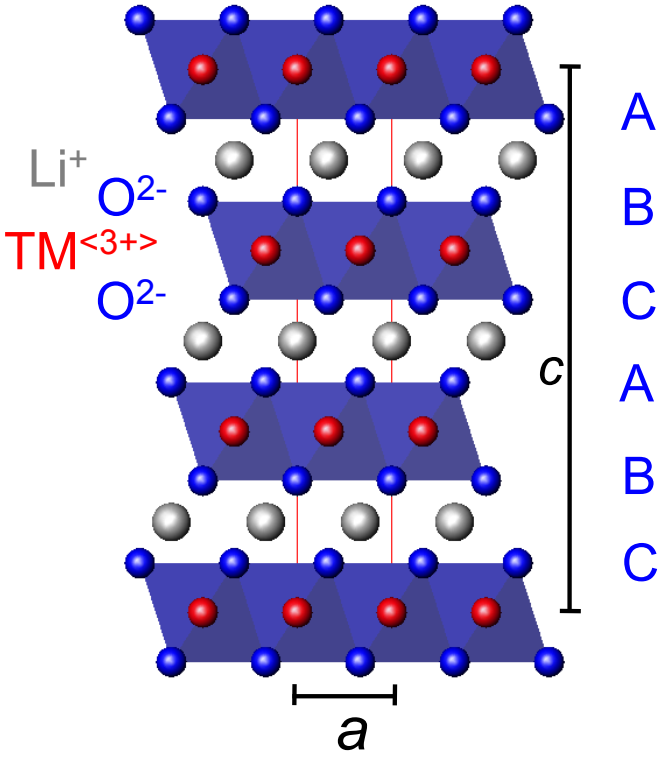

Figure 1-7: The α-$NaFeO_2$ structure (*R-3m* symmetry). The layered transition metal oxides Li*M*O_2 (*M* = transition metal) crystallize in this structure, which contains a close-packed oxygen stacking array and alternating layers of Li and transition metal ions. The unit cell parameters are indicated.

$LiCoO_2$

As mentioned above, Goodenough et. al. proposed the use of $LiCoO_2$ as an intercalation electrode after recognizing its structural similarities to the layered dichalcogenides. The first commercial Li-ion battery was then introduced by Sony in 1990, consisting of a $LiCoO_2$ positive electrode and a graphite negative electrode.[21] Since then, $LiCoO_2$ has remained the most common material used as battery cathodes for portable electronics (and is even the material used in batteries for the original Tesla Roadster EV). Li intercalation proceeds at a voltage of ~3.9 V vs. Li/Li^+ with a sloping voltage profile, indicating solid solution behavior. Despite a theoretical capacity of 280 mAh/g, $LiCoO_2$ is only reversibly able to provide about 140 mAh/g ($Li_{0.5}CoO_2$) due to phase transitions that occur when more than half of the Li is removed.[24,25,26] In this case, there is a cooperative sliding of the transition metal layers into an O1 stacking arrangement, shown in Figure 1-8, which has hexagonal close packed oxygen anions. This structure cannot accommodate re-intercalation of the removed Li, as the octahedral Li sites become face sharing with the CoO_6 octahedra, leading to a high-energy arrangement. Furthermore, the scarcity of Co results in a high price of the metal needed for these electrodes, and has motivated an expansive search for replacement materials. Still, $LiCoO_2$ continues to dominate the battery market for small, portable electronics such as cameras, cell phones, and computers.

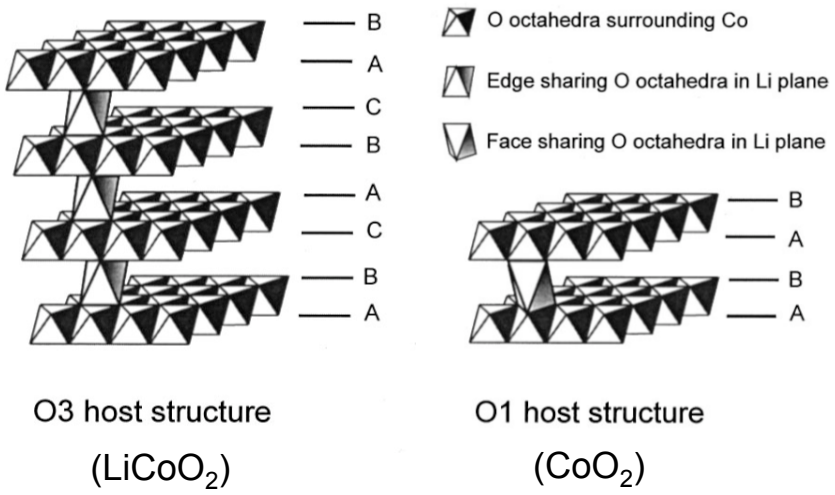

Figure 1-8: Schematic of the O3 structure of $LiCoO_2$ and the O1 structure that forms due to layer sliding when more than half of the Li is deintercalated.[26]

$LiNiO_2$

The isostructural $LiNiO_2$ was quickly pursued, in part because of its lower cost as compared to $LiCoO_2$. $LiNiO_2$ provides a higher reversible capacity (up to 200 mAh/g), as it does not undergo a similar undesirable layer-sliding phase change that prevents Li reintercalation, and can therefore be cycled to a lower value of Li content. Note, though, that various structural changes, such as a monoclinic solid solution for Li_xNiO_2 $0.5<x<0.75$, are observed in the material throughout the range of Li composition, though the deviation from the rhombohedral symmetry does not preclude Li diffusion for battery operation.[27] Additionally, the operation voltage (~3.8 V vs. Li/Li^+) is slightly lower than $LiCoO_2$, which limits the improvement in energy density from deeper cycling.

A stoichiometric $LiNiO_2$ compound cannot be easily produced, however, as it is not the thermodynamically stable structure. Rather, syntheses more accurately result in $(Li_{1-z}Ni^{2+}_z)(Ni^{2+}_zNi^{3+}_{1-z})O_2$ $(0<z<0.2)$ material.[28] The Ni^{3+} ion is less stable than the Ni^{2+}, and thus reduces in part with a concomitant loss of Li for charge balance. The Ni^{2+} ion (r=0.69 Å) is close in size to the Li^+ ion (r=0.76 Å),[29] and as the cation ordering in the α-$NaFeO_2$ crystal structure is in large part driven by size differences, some concentration of Ni^{2+} ions are found to reside on the *3a* Li sites (Figure 1-9).[30] These defects significantly affect the electrochemical properties of the material. The rate (power) performance is observed to suffer, as the interlayer Ni ions impede Li diffusion in the Li plane. Additionally, oxidation of the *3a* Ni to the smaller +3 or +4 states can cause local distortions and shrinking of the interlayer distances that decrease the reversible capacities of the materials.

Finally, $LiNiO_2$ in the fully charged state contains a significant amount of Ni^{4+}, which is inherently a strong oxidizer. The position of the Ni3+/4+ redox couple is such that oxidation of the O^{-2} anions or the organic electrolyte is a significant safety issue, as energy-releasing reactions with gaseous by-products can be produced. Additionally, the equilibrium oxygen partial pressure of NiO_2 (fully charged) is greater than 1 atm at room temperature, rendering the material unstable.[31] Thus, $LiNiO_2$ in the pure state is not used

in commercial battery electrodes, though solid solutions with other materials have been produced, as discussed in the following sections.

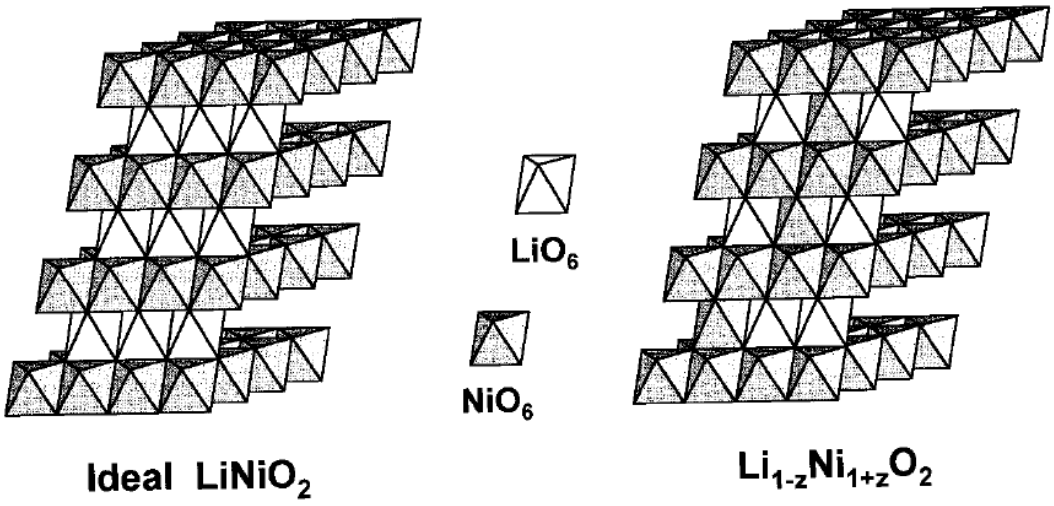

Figure 1-9: $LiNiO_2$ forms Ni-rich, with excess Ni ions residing in the Li-layer.[30]

$LiNi_{1-x-y}Co_xAl_yO_2$

The substitution of Ni^{3+} by Co^{3+} to form a solid solution of $LiNiO_2$ and $LiCoO_2$, was observed to improve the structure of the $LiNiO_2$-based material. Specifically, the incorporation of Co in $LiNi_{1-x}Co_xO_2$ reduced the formation of Ni^{2+}, thus decreasing the concentration of Ni 3a antisite defects. This in turn improved the power performance of the electrode materials, while maintaining the high capacity and reversibility.[30,32,33,34] Additionally, thermal stability at moderate temperatures was improved.

The stability and thermal properties, along with the material cost, are further advanced with the incorporation of an electrochemically inactive material such as Al.[35,36] Not only does this limit the amount of Li that can be removed from the system (thus limiting the oxidation of the transition metals, preventing overcharge), but also improves the thermal stability of charged materials.[37] For these reasons, NCA materials, especially $LiNi_{0.8}Co_{0.15}Al_{0.05}O_2$, have been successfully produced for commercial applications.

$LiNi_{0.5}Mn_{0.5}O_2$

Layered $LiMnO_2$ is very attractive for battery applications, as it contains relatively cheap and environmentally friendly Mn. Unfortunately, it does not form a thermodynamically stable *R-3m* layered phase like the Co- and Ni-containing analogues, but rather an orthorhombic structure with poor electrochemical properties.[38] The desired layered structure can be produced by ion-exchange methods with $NaMnO_2$, but this material (as well as the orthorhombic) converts to the spinel phase upon cycling ($Li_{0.5}MnO_2$ = $LiMn_2O_4$), which requires only cation rearrangement, as both structures have a ccp oxygen array.[39] The spinel material, which has very different electrochemical properties and is currently used in batteries, is discussed below.

Incorporation of Mn in $LiNiO_2$ to make $LiNi_{1-x}Mn_xO_2$ ($0 \leq x \leq 0.5$) was originally shown by Dahn et al. in 1992, though poor observed electrochemical performance caused

the material to be relatively ignored.[40] The $LiNi_{0.5}Mn_{0.5}O_2$ material was revisited, however, by Ohzuku in 2001, who reported very good capacity and cycling stability, up to 200 mAh/g between 2.5-4.5 V vs. Li/Li^+ at low current density (0.17 mA/cm^2).[41]

Interestingly, it was found that when Ni and Mn are included in the same proportion, the observed oxidations states are Ni^{2+} and Mn^{4+}. This distribution was confirmed experimentally by X-ray absorption spectroscopy (XAS) as well as first principles calculations.[42,43,44] Thus, charge compensation during Li deintercalation proceeds as $Ni^{2+} \rightarrow Ni^{4+}$, with the Mn ion remaining in the 4+ state throughout. The $LiNi_{0.5}Mn_{0.5}O_2$ material is observed to have better thermal stability as compared to $LiCoO_2$ and $LiNiO_2$, though the Mn^{4+} does not improve the structure of the material in a similar manner as Co-substitution, as 8-12% Ni 3a defects are observed. In this material, however, in contrast to $LiNiO_2$, a complimentary amount of Li resides within the transition metal layer, and the defects are termed "antisite" defects.

It has been both computationally predicted and experimentally confirmed (by NMR, EXAFS, and other studies) that the lowest energy structure includes the Li ions in the transition metal layer (~8.3% antisites) surrounded by 6 Mn^{4+} or 5 Mn^{4+} and 1 Ni^{2+}, with this first cation coordination shell surrounded by 12 Ni^{2+} ions.[45,46,47,48] This ordered arrangement, termed the flower pattern, is shown in Figure 1-10. The extent to which it is observed is affected by the details of the synthesis procedure and the exact Li stoichiometry, though the existence of antisite defects and therefore the flower pattern are intrinsic to the stabilization of the $LiNi_{0.5}Mn_{0.5}O_2$ material.

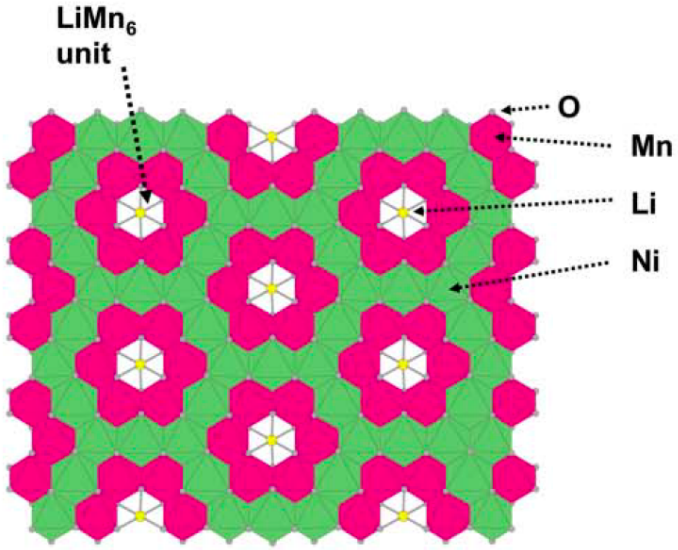

Figure 1-10: The ideal flower pattern for $LiNi_{0.5}Mn_{0.5}O_2$ with 8.3% Ni/Li antisite defects.[66]

As mentioned previously, the *3a* Ni defects significantly affect the rate (power) performance of the material. This is clearly illustrated in Figure 1-11, in which $LiNi_{0.5}Mn_{0.5}O_2$ materials synthesized by the common solid state (SS) method, containing ~10% antisite defects, are compared with materials generated by ion-exchange (IE) with $NaNi_{0.5}Mn_{0.5}O_2$ analogues, which contain very little (4%) antisite defects due better ordering as a result of the larger size mismatch between the Na^+ and Ni^{2+} ions.[49] The performance improvement is substantial in the better-ordered system.

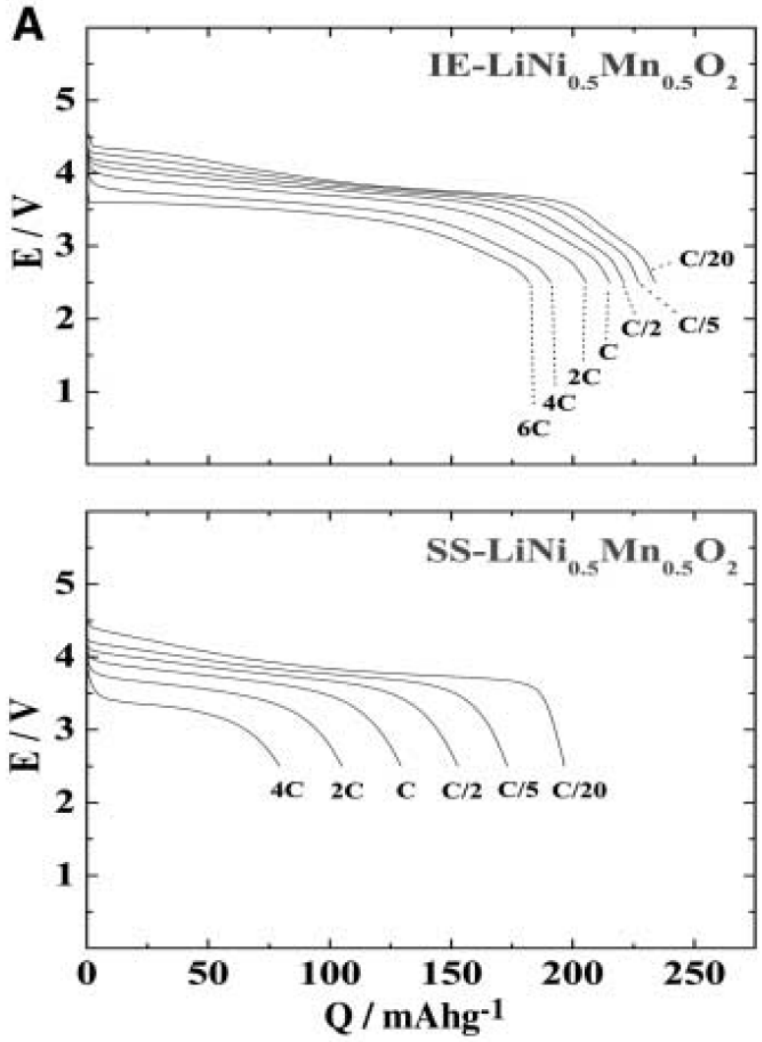

Figure 1-11: The presence of *3a*Ni/*3b*Li antisite defects significantly impacts the rate performance of layered oxide electrode materials. The $LiNi_{0.5}Mn_{0.5}O_2$ material made by ion-exchange (IE, top) has less defects and improved performance compared to the $LiNi_{0.5}Mn_{0.5}O_2$ material synthesized using solid state methods (SS, bottom).[49]

NMC Materials

The structure can be further improved by adding Co to the above system. With the addition of Co^{3+}, the oxidation states remain Ni^{2+} and Mn^{4+} if kept in the same proportion. Thus, $LiNi_xMn_xCo_{1-2x}O_2$, so-called "NMC" materials, can be considered a solid solution of $LiCoO_2$ and $LiNi_{0.5}Mn_{0.5}O_2$. These materials can also provide a higher reversible capacity than $LiCoO_2$, typically ~160 mAh/g below 4.3 V vs. Li/Li^+.[14] NMC materials maintain the advantages of a decreased Co-content and the structural stability imparted by Mn^{4+}. Though there is debate relating to the involvement of the O^{2-} anions, it is generally believed that oxidation is centered at the Ni-ions at the beginning of charge, only involving the Co-ions (or Co-O orbitals) at higher voltages.[50,51,52]

By far the most studied member is the formulation with x=1/3,[53,54,55] which is currently commercially produced,[56] though compositions with x=0.4[57,58] and x=0.45,[59,60] among others, have also been investigated in an effort to decrease the amount of costly Co. The Ni 3a antisite defect concentration, however, is significantly influenced by the amount of Co present in the materials.[61] This can be seen in Figure 1-12a, which compares $LiNi_xMn_xCo_{1-2x}O_2$ materials with $0 \leq x \leq 1$. As the Co-content is increased, the antisite concentration is lowered. This in turn has a drastic effect on the rate capability of the system, shown in Figure 1-12b. Despite the rate-performance-dependence on Co-content, the NMC materials display good reversible capacity and improved safety at high states of charge compared to the other layered oxides materials like $LiCoO_2$, $LiNiO_2$, and $LiNi_{1-x-y}Co_xAl_yO_2$.[62,63,64,65]

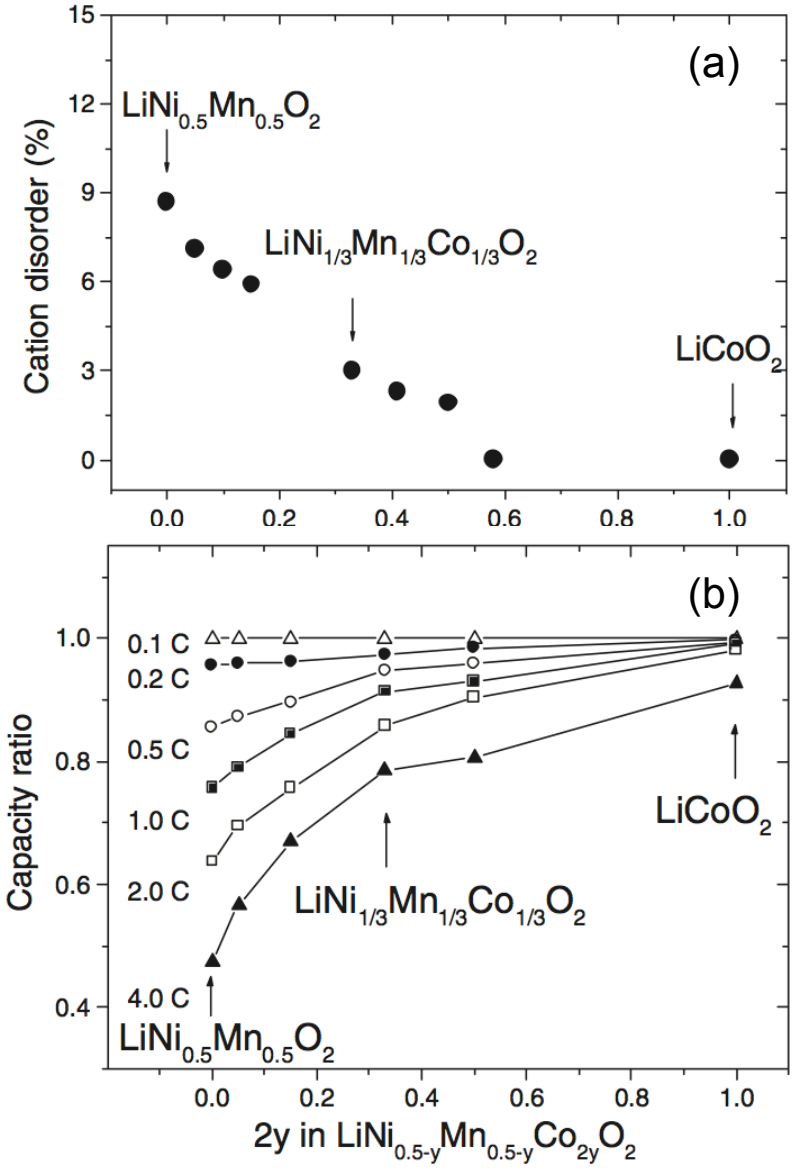

Figure 1-12: Solid solutions of $LiCoO_2$ and $LiNi_{0.5}Mn_{0.5}O_2$ contain fewer antisite defects as the Co-content increases. This, in turn, improves the rate performance of the electrode materials.[61]

Li_2MnO_3-Stabilized Materials

Recently, "layered-layered" composite materials with the general formula $xLi_2MnO_3 \bullet (1-x)LiMO_2$ have garnered much attention from the research community because of the possibility of attaining much higher capacities than with other layered compounds.[66] Li_2MnO_3 can be re-written in layered notation as $Li(Li_{1/3}Mn_{2/3})O_2$, and crystallizes in a layered monoclinic *C2/m* structure, similar to the *R-3m* hexagonal symmetry, with ordered Li occupancy in the Mn layer (Figure 1-13a,b). This close structural similarity allows layered materials such as $LiCoO_2$, $LiNi_{0.5}Mn_{0.5}O_2$, NMC's, or even spinel materials with excess Li and Mn to include coherent, integrated Li_2MnO_3 domains with nanoscale dimensions, as shown schematically in Figure 1-13c.[67,68]

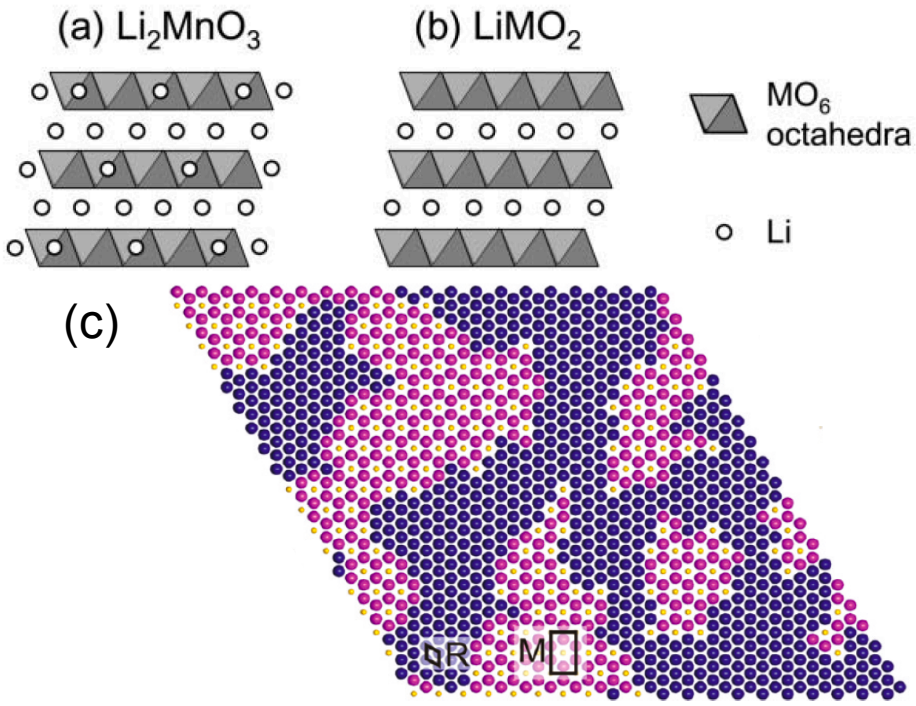

Figure 1-13: Schematics of a) Li_2MnO_3 ($Li[Li_{1/3}Mn_{2/3}]O_2$) and b) $LiMO_2$. c) The structural similarity allows integrated nanodomains of Li_2MnO_3 (magenta/yellow) to be contained within layered materials (blue), as illustrated. ("M" and "R" refer to monoclinic and rhombohedral unit cells for the materials in (a), and (b), respectively).[66,67]

In the pure state, Li_2MnO_3 contains only Mn^{4+}, which is electrochemically inactive, and remains such in the integrated composite materials when operated at voltages less than about 4.5 V vs. Li/Li^+. Upon charging to voltages higher than 4.5 V, a plateau is observed in the potential profile, indicating that the Li_2MnO_3 domains are "activated" (Figure 1-14). During this process, Li is deintercalated and oxygen is released from the structure (in stoichiometric equivalents of Li_2O), leaving MnO_2 units that are now electrochemically active upon re-intercalation of Li. Subsequent charge/discharge cycles show voltage profiles that are more characteristic of the layered oxides, except that very large capacities can be obtained (200-300 mAh/g depending on

the (1-x)LiMO$_2$-component stoichiometry and cycling conditions).[66] As of the time of this writing, Argonne National Laboratory, which has been developing these materials for use in traction applications, had signed a deal with GM for development and future deployment in their electric vehicle fleet.[69] However, the materials are not yet mature – there are problems with the structural evolution during repeated cycling that results in a drop of the average voltage, and the oxygen loss can damage particle surfaces, lowering performance, for example. These materials will require substantial cycle-life and safety characterization before becoming commercially acceptable.

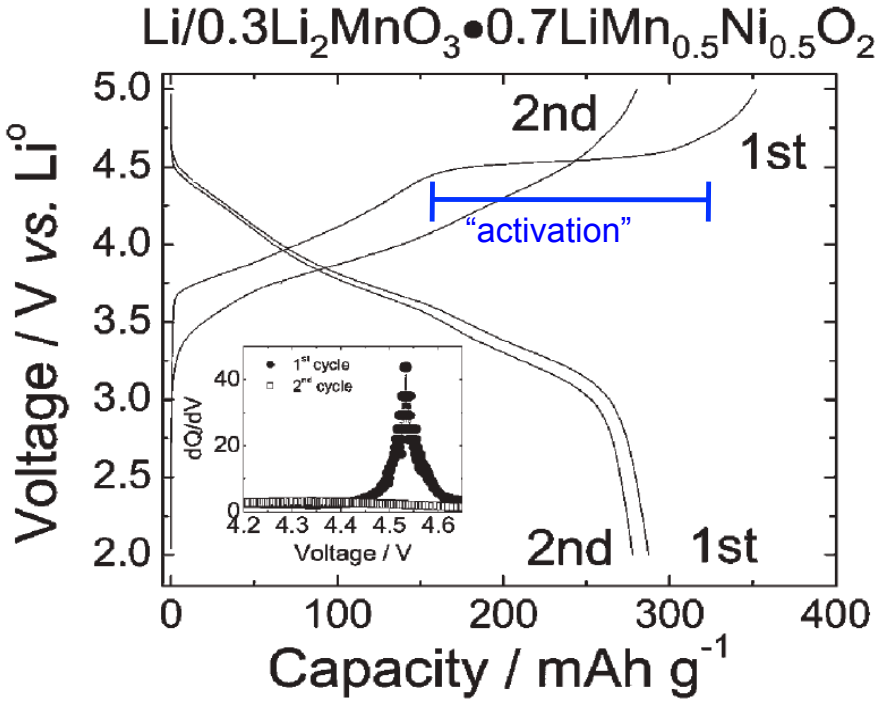

Figure 1-14: Voltage vs. capacity for the first and second cycles of an example Li_2MnO_3-stabilized electrode material. The "activation" plateau at ~4.5 V (vs. Li/Li$^+$) during the first cycle is indicated, attributed to irreversible loss of Li and O in "Li_2O" quantities. (inset) The plot of dQ/dV vs. V shows a peak at 4.5 V for the first cycle only.[66]

Spinels

Materials crystallizing in the spinel structure, which also has a ccp oxygen lattice, are another important class of battery cathodes (Figure 1-15). The most successful have been those based on $LiMn_2O_4$; spinel materials based on other transition metals such as Ni or Co have mediocre electrochemical properties compared to the corresponding layered structures. The $LiMn_2O_4$ material contains Li in 8a tetrahedral sites and Mn$^{<3.5+>}$ in 16d octahedral positions. Though the material has a smaller theoretical capacity than the layered structures (148 mAh/g), most of the Li can be extracted at 4.1 V vs. Li/Li$^+$. The material also exhibits good power capability and very good thermal safety properties. Additionally, a second Li per formula unit can be inserted into unfilled 16c octahedral sites at about 3 V vs. Li/Li$^+$. This causes the material to undergo a phase change,

however, causing particle fracture and disconnect, ruining the electrode. Thus, the material is not used in this regime.[14]

$LiMn_2O_4$ spinel materials suffer from capacity fade throughout the operation lifetime. One major cause is the disproportionation of 2 Mn^{3+} into Mn^{2+} and Mn^{4+}; Mn^{2+} can dissolve out of the material lattice in an acidic environment (such as when used with the common $LiPF_6$-based organic electrolytes, which can produce HF when trace water is present).[70,71] This is somewhat mitigated by substituting some excess Li onto the Mn site, producing $Li_{1+x}Mn_{2-x}O_4$, which lowers the amount of Mn^{3+} present in the system.[14] These "modified" spinels also improve the rate capability, but at the expense of delivered capacity (~110 mAh/g). They are commercially successful, used in some of the new electric vehicles like the Chevy Volt and Nissan Leaf.[72] However, the limited energy density and observed capacity fade of the materials has motivated the search for improvements.

In that respect, metal-substitutions have been explored in this system, with much interest now turned toward $LiNi_{0.5}Mn_{1.5}O_4$.[73,74,75] This material, similar to the $LiNi_{0.5}Mn_{0.5}O_2$ and NMC layered materials above, contains Ni^{2+} and Mn^{4+} in the as-made state. Charge compensation thus occurs by Ni oxidation, at an average potential of 4.7 V vs. Li/Li^+. This high-voltage spinel not only improves the energy density, but also (theoretically) eliminates Mn^{3+}, thus improving the cycling stability of the material. Despite only a modest improvement in the energy density due to the voltage increase, substantial cost savings can be realized with higher voltage materials because fewer cells are necessary for the 300 V modules used in EV's, leading to a substantial savings on packaging materials.

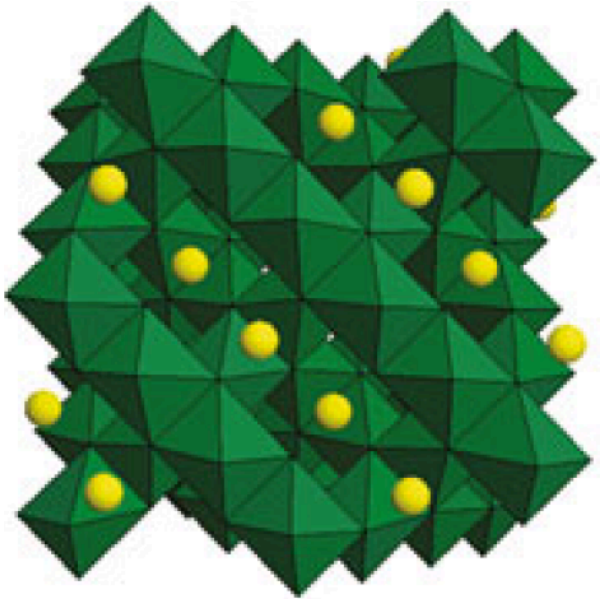

Figure 1-15: The spinel structure of $LiMn_2O_4$. Li (yellow circles) resides in tetrahedral (*8a*) sites amongst MnO_6 octahedra (green octahedra). The oxygen sublattice is cubic close packed.[14]

Olivines

Goodenough proposed $LiFePO_4$ as an electrode material in 1997.[76] $LiFePO_4$ has the olivine structure (space group Pnma), shown in Figure 1-16. It consists of corner-sharing FeO_6 octahedra and edge-sharing LiO_6 octahedra bridged by edge and corner sharing PO_4 tetrahedra. The oxygen anions are arranged in a distorted hexagonal close packed (hcp) lattice. $LiFePO_4$ is a naturally occurring mineral, triphylite, as is the Li-free $FePO_4$, heterosite. Due to the theoretical capacity of 170 mAh/g, and its composition of inexpensive, environmentally benign materials, $LiFePO_4$ has since drawn much interest as a low-cost replacement for $LiCoO_2$.

The original paper by Padhi, et. al. demonstrated reversible Li intercalation at about 3.4 V vs. Li/Li^+.[76] The electrochemistry displays a very flat voltage profile, indicative of a two-phase Li-extraction process.[77] The two relevant phases are $FePO_4$ and $LiFePO_4$, though further studies have suggested that there is a slight solubility in those phases of Li and Li-vacancies, respectively. The actual end members $Li_{1-\alpha}FePO_4$ and $Li_\beta FePO_4$ have been reported with a variety of values, α=0.038-0.17 and β=0.032-0.12, and seem to have a dependence on primary particle size, with larger values reported for smaller particles, indicating a narrower miscibility gap.[78]

Initial reports on the electrochemical behavior of $LiFePO_4$ suggested a "shrinking-core" model of Li-intercalation, in which Li (de)insertion proceeds from all surfaces of the particles. Discharge profiles were successfully modeled with this interpretation.[79] As seen in Figure 1-16, however, the olivine structure contains LiO_6 octahedra that are edge-sharing along the [010] direction, providing a pathway for Li diffusion. Although Li motion along the c-axis [001] seems feasible as well, calculations have suggested that the diffusion coefficient along the b-axis is orders of magnitude larger.[80,81] Experimental measurements have supported this preference, and $LiFePO_4$ is now known to be a one-dimensional conductor.[82,83]

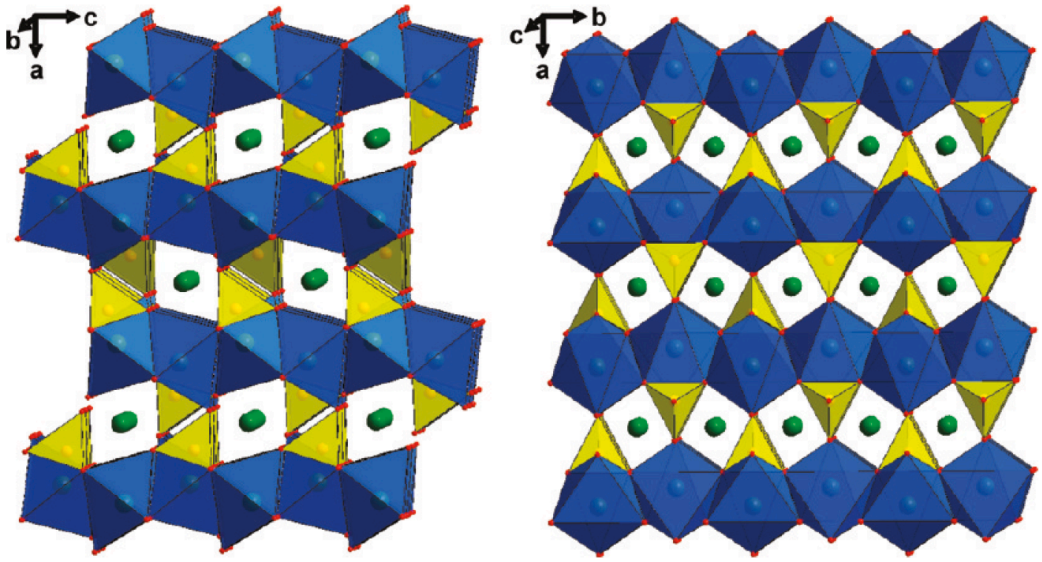

Figure 1-16: Two views of the olivine structure characteristic of Li*M*PO_4 (M=Fe, Mn, Co, Ni) materials. FeO_6 octahedra are shown in blue, PO_4 tetrahedra in yellow, and Li ions (octahedrally coordinated) in green.[78]

The progression of the phase boundary during Li (de)intercalation is less clear, however. Large, chemically delithiated particles observed by TEM showed striped domains of $LiFePO_4$ and $FePO_4$ in the *ac* plane with a disordered phase boundary in between, while an EELS study on smaller delithiated particles suggested a core of $FePO_4$.[84,85] Another study on partially delithiated electrodes observed particles that were either completely delithiated or not at all, leading to a "domino-cascade" interpretation.[86] The true mechanism(s) likely depends on the particle sizes and electrode structure.

Regardless of the exact Li (de)intercalation mechanism, $LiFePO_4$ shows very stable cycling performance. This is despite the very low electronic and ionic conductivities intrinsic to the olivine materials, with $LiFePO_4$ having values of about 10^{-10} S/cm and 10^{-13} S/cm, respectively, at room temperature. These issues are successfully mitigated for the materials' use in battery electrodes by two complimentary engineering approaches: nanosizing and carbon coating the active material particles.[87] Nanostructuring limits the Li-ion diffusion distances necessary during charge and discharge, while carbon coating provides an electronically conductive network to facilitate charge transfer. Carbon coating can be achieved after material production, for instance, by ball milling the active material with graphite or carbon black, or even produced *in situ* during material synthesis by decomposition of organic precursors. The quality of the carbon coatings can vary widely, and affect electrode performance.[88,89] Improving the conductivity of the materials by aliovalent doping to generate a mixed Fe2+/3+ valency is not likely to be feasible, as concluded by various studies.[81,90]

$LiFePO_4$ is additionally attractive as a battery material due to its excellent thermal safety properties. This is largely attributed to the polyatomic $(PO_4)^{3-}$ anion that consists of strong P-O covalent bonds.[78] The structure is very stable at low Li-contents (high states of charge) and upon heating transforms to a trigonal α-quartz structure with no concomitant oxygen evolution, unlike the oxide materials discussed above. This behavior seems to be unaffected by particle size.[76,91,92]

Combined with the high degree of thermal abuse tolerance and the inexpensive material components, the engineering approaches discussed above have resulted in high-performance $LiFePO_4$ cathodes. This, in turn, allows their use in devices for high-rate applications such as power tools and electric bikes. A123 Systems is now working to implement their $LiFePO_4$-based batteries in electric vehicles, as well as grid storage applications.[93]

Other transition metals, such as Mn, Co, and Ni also form stable olivine phases. In $LiMnPO_4$, Li is intercalated at ~4.1 V, significantly higher than in $LiFePO_4$ (~3.4 V). Mn is, additionally, a widely available and very inexpensive metal. Despite many investigations, however, high performance $LiMnPO_4$ cathodes displaying stable cycling and good reversible capacities of have not been broadly demonstrated, though there have been some promising reports.[94,95,96] The conductivity is orders of magnitude lower than $LiFePO_4$, resulting in inferior rate capability, but this can be somewhat mitigated with carbon coatings. Additionally, the thermal stability is worse than the Fe-containing analogue, as oxygen evolution is possible at lower temperatures (200°C), and the Jahn-Teller distortion in the delithiated structure (containing Mn^{3+}) exacerbates the thermal instability of charged samples.[97]

$LiCoPO_4$ and $LiNiPO_4$ have intercalation potentials of 4.8 V and 5.1 V vs. Li/Li^+, respectively.[98,99,100,101,102] This has made extensive testing difficult due to the lack of any

well-developed electrolytes that are stable at these high potentials. Additionally, the increased cost and environmental concerns associated with Co and Ni have tempered commercial appeal. However, mixed-metal phosphates have been demonstrated which show voltage plateaus for each redox couple, and appear to work better than pure $LiMnPO_4$ or $LiCoPO_4$.[103]

1.4 Scope

The work in this dissertation is concerned with understanding the structural and electrochemical consequences of cost-lowering mechanisms in two separate classes of Li-ion electrode materials; the NMC layered oxides and the Li*M*PO_4 olivine materials; with the goal of improving performance. The bulk of this work is focused on the layered oxides, in which Al-substitution in place of Co is used to limit the concentration of the expensive metal in the system. This actually results in enhanced cycling stability of the electrode material. The structural and electrochemical effects of Al-substitution are investigated in a model NMC compound, $LiNi_{0.45}Mn_{0.45}Co_{0.1-y}Al_yO_2$. Various synchrotron-based characterization methods are utilized, including high-resolution X-ray diffraction, *in situ* X-ray diffraction, and X-ray absorption spectroscopy. The later sections of this text discuss a spray pyrolysis production system that was designed to enable low-cost, continuous, and scalable processing of active Li-ion battery materials. Various olivine materials, Li*M*PO4 (*M*=Fe,Co) are synthesized as porous, carbon-coated spherical particles with micron-sized diameters. The materials display exceptional electrochemical properties, as discussed, due to the particle morphology.

1.5 References

[1] "Chapter 8: Household Vehicles and Characteristics" in S. Davis, S. Diegel, R. Boundy, *Transportation Energy Data Book: Edition 30.* Oak Ridge National Laboratory. Retrieved from cta.ornl.gov/data. **2011**

[2] "Chapter 3: All Highway Vehicles and Characteristics" in S. Davis, S. Diegel, R. Boundy, *Transportation Energy Data Book: Edition 30.* Oak Ridge National Laboratory. Retrieved from cta.ornl.gov/data. **2011**

[3] "Chapter 2: Energy" in S. Davis, S. Diegel, R. Boundy, *Transportation Energy Data Book: Edition 30.* Oak Ridge National Laboratory. Retrieved from cta.ornl.gov/data. **2011**

[4] "Chapter 1: Petroleum" in S. Davis, S. Diegel, R. Boundy, *Transportation Energy Data Book: Edition 30.* Oak Ridge National Laboratory. Retrieved from cta.ornl.gov/data. **2011**

[5] Muller, R. A. "The Case Against Global Warming Skepticism." *The Wall Street Journal*, October 21, 2011. Accessed online 10/22/11 http://online.wsj.com/article/SB10001424052970204422404576594872796327348.html#

[6] "Chapter 11: Greenhouse Gas Emissions" in S. Davis, S. Diegel, R. Boundy, *Transportation Energy Data Book: Edition 30.* Oak Ridge National Laboratory. Retrieved from cta.ornl.gov/data. **2011**

[7] IPCC, *Climate Change 2001: Synthesis Report.* **2007**.

[8] "Hybrid Electric Systems: Goals, Strategies, and Top Accomplishments." http://www1.eere.energy.gov/vehiclesandfuels/pdfs/hybrid_elec_sys_goals.pdf Acessed 12/14/11

[9] Tarascon, J., Armand, M. *Nature,* **2001***, 414***,** 359.

[10] Dahn, J. R. *Phys. Rev. B,* **1991***, 44*, 9170.

[11] F. Orsini, F., A. du Pasquier, B. Beaudouin, J. M. Tarascon, M. Trentin, N. Langenhuizen, E. de Beer, P. Notten. *J. Power Sources*, **1999**, *81-82,* 918.

[12] United States Council for Automotive Research, Energy Storage System Goals http://www.uscar.org/guest/article_view.php?articles_id=85 Accessed 12/14/11

[13] Srinivasan, V. *AIP Conference Proceedings Physics of Sustainable Energy,* **2008,** *1044*.

[14] "Batteries: Overview of Battery Cathodes." Doeff, M. M., in *Springer Encyclopedia of Sustainability Science and Technology,* Springer Science + Business Media, LLC, New York, in press **2011**.

[15] L. Gaines and R. Cuenca. "Costs of Lithium-Ion Batteries for Vechicles." Center for Transportation Research, Energy Systems Division, Argonne National Laboratory. **2000**

[16] M.S. Whittingham. *Science* **1976,** *192,* 1126.

[17] B.C.H. Steele in *Fast Ion Transport in Solids: Solid State Batteries and Devices*, Ed. by W. vn Gool North Holland/America Elsevier, Amsterdam/New York, (1973)

[18] Whittingham, M. S. *J. Electrochem. Soc*. **1976**, *123***,** 315.

[19] J. B. Goodenough. *J. Power Sources,* **2007,** *174***,** 996.

[20] K. Mitzushima, P. C. Jones, P. J. Wiseman, J. B. Goodenough, *Mater. Res. Bull.* **1980**, *15*, 783.

[21] Nagaura, T., Tozawa, K. Prog. Batteries Solar Cells **1990**, *9*, 209.

[22] E. J. Wu, P. D. Tepesch, and G. Ceder, *Phil. Mag. B*, **1998**, *77*, 1039.

[23] Van der Ven, A. and G. Ceder, *Electrochem. Solid State Lett.* **2000**, *3,* 304.

[24] G. Amatucci, J. M. Tarascon, L. Klein, L. *J. Electrochem. Soc.* **1996**, *143*, 1114.

[25] Chen, Lu, Dahn. *J. Electrochem Soc.* **2002,** *149***,** A1604.

[26] Van der Ven, Aydinol, Ceder. *Phys. Rev. B.* **1998,** *58***,** 2957.

[27] C. Delmas et al. *J. Power Sources*, **1997**, *68*, 120.

[28] A. Rougier, P. Gravereau, C. Delmas, *J. Electrochem. Soc.* **1996**, *143*, 1168.

[29] R. Shannon. *Acta Cryst. Section A: Crystal Physics, Diffraction, Theoretical and General Crystallography*, **1976**, *32,* 751.

[30] C. Delmas et al. *Electrochimica Acta*, **1999**, *45*, 243.

[31] M. S. Whittingham. *Chem. Rev.* **2004**, *104*, 4271.

[32] A. Rougier, I. Saadoune, P. Gravereau, P. Willmann, C. Demas. *Solid State Ionics*, **1996**, *90***,** 83.

[33] Saadoune, I. and C. Delmas. *J. Mater. Chem.* **1996**, *6,* 193.

[34] A. Ueda, T. Ohzuku, *J. Electrochem. Soc.* **1994**, *141*, 2010.

[35] S. Albrecht et al. *J. Power Sources,* **2003**, *119*, 178.

[36] Chen et al. *J. Power Sources*, **2004**, *128*, 278.

[37] T. Ohzuku et al. *J. Electrochem. Soc.* **1995**, *142*, 4033.

[38] S. K. Mishra, G. Ceder, G. *Phys. Rev. B* **1999,** *59,* 6120.

[39] G. Vitins, K. West. *J. Electrochem. Soc.* **1997**, *144* 2587.

[40] E. Rossen, C. D. W. Jones, J. R. Dahn. *Solid State Ionics* **1992**, *57***,** 311.

[41] T. Ohzuku, Y. Makimura, *Chem. Lett.* **2001,** 744.

[42] W. Yoon et al. *Electrochem. Solid State Lett.* **2002**, *5*, A263.

[43] J. Reed, G. Ceder. *Electrochem. Solid State Lett.* **2002**, *7*, A145.

[44] M. S. Islam et al. *Chem. Mater*. **2003**, *15*, 4280.

[45] A. Van der Ven, G. Ceder. *Electrochem Commun*. **2004**, *6*, 1045.

[46] J. Bréger et al. *Chem. Mater.* **2006**, *18*, 4768.

[47] W. S. Yoon, C. P. Grey, M. Balasubramanian, X. Yang, J. McBreen. *Chem. Mater.* **15** 3161 (2003).

[48] J. Bréger et al. *J. Amer. Chem. Soc.* **2005**, *127*, 7537.

[49] Kang et al. *Science* **2006**, *311*, 977.

[50] B. Hwang et al. *Chem.. Mater.* **2003**, *15*, 3676.

[51] Y. Tsai et al. *Chem. Mater.* **2005**, *17*, 3191

[52] S. Miao et al. *J. Phys. Chem. B,* **2005**, *109*, 23473.

[53] T. Ohzuku, Y. Makimura. Chem. Lett. **2001**, *7*, 642.

[54] N. Yabuuchi, T. Ohzuku. *J. Power Sources* **2003**, *119*, 171.

[55] I. Belharouak et al. *J. Power Sources,* **2003**, *123*, 247.

[56] Zhou et al. *J. Electrochem Soc.* **2009**, *156*, A343.

[57] J. Ngala et al. *J. Mater. Chem.* **2004**, *14*, 214

[58] M. Ma et al. *J. Power Sources,* **2007**, *165*, 517.

[59] Xiao et al. *Chem. Mater.* **2008**, *20*, 7454.

[60] Xiao et al. *Chem. Mater.* **2010**, *22*, 1180.

[61] A. Manthiram et al. *Solid State Ionics* **2006**, *177*, 2629.

[62] Y. Wang et al. *Electrochem. Commun.* **2007**, *9*, 2534.

[63] Lu et al. *Electrochem. Solid State Lett.* **2001**, *4,* A200.

[64] I. Belharouak et al. *Electrochem. Commun.* **2006**, *8*, 329.

[65] W. Choi, A. Manthiram. *J. Electrochem. Soc.* **2005**, *152*, A1714.

[66] M. Thackeray et al. *J. Mater. Chem.* **2007**, *17*, 3112.

[67] J. Bareño, et. al. *Chem. Mater.* **2011,** *23,* 2039.

[68] J. Bareño, et. al. *Adv. Mater.* **2010,** *22,* 1122.

[69] "Argonne battery technology helps power Chevy Volt." http://www.anl.gov/Media_Center/News/2011/news110110.html; "GM, Argonne sign licensing deal for advanced battery chemistry." http://news.uchicago.edu/article/2011/01/07/gm-argonne-sign-licensing-deal-advanced-battery-chemistry. Accessed 12/14/11.

[70] D. H. Jang, *et. al. J. Electrochem. Soc.* **1996**, *143*, 2204.

[71] Y. Xia, Y. Zhou, M. Yoshio, J. Electrochem. Soc. **1997**, *144*, 2593.

[72] "New materials could double Chevy Volt battery capacity." http://inhabitat.com/new-materials-could-double-chevy-volt-battery-capacity/chevy-volt3-4/; "Volt's Battery Capacity Could Double." http://www.technologyreview.com/energy/27049/page1/; "Details on Nissan Leaf battery pack, including how charging speed affects battery life." http://www.green.autoblog.com/2010/05/27/details-on-nissan-leaf-battery-pack-including-how-recharging-sp/. Accessed 12/14/11

[73] Q. Zhong et al. *J. Electrochem. Soc.* **1997**, *144*, 205.

[74] S.-H. Park, *et. al. Solid State Ionics* **2005**, *176*, 481.

[75] Y. Talyosef, *et. al. J. Power Sources* **2005**, *146*, 664.

[76] A. K. Padhi, *et. al. J. Electrochem. Soc.* **1997**, *144*, 1609.

[77] Tarascon, J., et. al. *Chem Mater* **2010**, *22*, 724.

[78] Ellis et al. *Chem. Mater.* **2010**, *22*, 691.

[79] V. Srinivasan, J. Newman. *J. Electrochem. Soc.* **2004**, *151*, A1517.

[80] Morgan et al. *Electrochem. Solid State Lett.* **2004**, *7*, A30.

[81] M. S. Islam, et. al. *Chem Mater.* **2005**, *17*, 5085.

[82] J. Li, et. al. *Solid State Ionics* **2008,** *179,* 2016.

[83] R. Amin, et al. *Solid State Ionics* **2008,** *179,* 1683.

[84] G. Chen, X. Song, T. J. Richardson *Electrochem. Solid State Lett.* **2006,** *9,* A295.

[85] L. Laffont, et. al. *Chem. Mater.* **2008,** *7,* 665.

[86] C. Delmas et al. *Nature Mater.* **2008,** *7,* 665.

[87] J. Liu, T. E. Conry, et al. *Energy Environ. Sci.* **2011,** *4,* 885.

[88] M. M. Doeff et al. *Electrochem. Solid State Lett.* **2003,** *6,* A207.

[89] M. M. Doeff, et. al. *J. Power Sources* **2006**, *163,* 180.

[90] C. A. Fisher, et. al. *Chem Mater* **2008,** *20*, 5907.

[91] J. Jiang, J.R. Dahn, *Electrochem Commun.* **2004**, *6,* 724.

[92] C. Delacourt, P. Poizot, J.-M. Tarascon, C. Masquelier, *Nat. Mater*. **2005**, *4*, 254.

[93] A123 Systems company website: http://www.a123systems.com/ Accessed 12/14/11

[94] M. M. Doeff, J. Chen, T. E. Conry et al. *J. Mater. Res.* **2010,** *25,* 1460.

[95] Yonemura et al. *J. Electrochem Soc.* **2004,** *151,* A1352.

[96] Martha et al. *J. Electrochem Soc.* **2009,** *156,* A541.

[97] G. Chen, T. J. Richardson, *J. Power Sources* **2010,** *195,* 1221.

[98] Bramnik et al. *Chem. Mater.* **2007,** *19,* 908.

[99] J. Liu, T. E. Conry, et al. *J. Mater. Chem.* **2011,** *21,* 9984

[100] K. Amine, H. Yasuda, M. Yamachi, *Electrochem. Solid State Lett.* **2000,** *3,* 178.

[101] J. Wolfenstine, J. Allen *J. Power Sources* **2004,** *136,* 150.

[102] S. Okada, et al. *J. Power Sources* **2001,** *97-98,* 430.

[103] T. Muraliganth, A. Manthiram. *J. Phys. Chem. C,* **2010,** *114*, 15530.

Chapter 2: Synthesis and Electrochemistry of $LiNi_{0.45}Mn_{0.45}Co_{0.1-y}Al_yO_2$ ($0 \leq y \leq 0.1$) Materials

2.1 Al-substitution in Layered Oxides

Metal substitution in layered oxide materials ($LiCoO_2$, $LiNiO_2$, NMC, etc.) has been explored since the early development of Li-ion batteries. Studies have been carried out using a variety of substituent species, including electrochemically inactive substituents (B, Mg, Zr, and Al, for example).[1,2,3,4,5,6,7,8,9] Redox active transition metals (such as Ti, Fe),[7,8,9,10,11] in addition to varying the compositions of Ni, Mn, and Co in $LiMO_2$, have also been investigated.[12,13] Not all substitutions are beneficial, however; Fe substitution in $LiNi_{1/3}Mn_{1/3}Co_{1/3}O_2$ materials, for instance, lowers the delivered capacity, while Zr substitution provides no improvement in the safety or capacity retention.[3,7] On the other hand, Ti-substitution in the same system appears to improve the discharge capacity,[8,10] and Al substitution has many benefits that are discussed below.

Aluminum is an inexpensive and lightweight metal, and thus partial substitution does not adversely impact the cost or density of the materials. Importantly, Al forms a stable layered structure with the R-3m hexagonal symmetry, α-$LiAlO_2$.[14] Although Al is not electrochemically active, because only a +3 oxidation state is stable, Li extraction from α-$LiAlO_2$ has been predicted to be feasible from first principles calculations (though it occurs at potentials >5 V).[14,15] The charge compensation is thought to occur within the oxygen 2p bands. This is not, however, reversible, and has not been experimentally demonstrated. Thus Al can be considered inactive from an electrochemical standpoint. Regardless, small concentrations of Al substituted in another layered-oxide material do not significantly lower the discharge capacities of the parent materials, as full Li extraction does not occur during regular use.

In fact, a number of improvements are observed with the substitution of Al in place of transition metals in layered oxide materials (like $LiCoO_2$, $LiNiO_2$, and $LiNi_{1-z}Co_zO_2$). The most marked is the enhancement of the thermal stability in Al-substituted systems.[2,16,17] Additionally, Al incorporation has been shown to prevent phase changes during Li deintercalation, thus improving the cycling performance of the materials.[18,19,20] Also, because the Al^{3+} ion is electrochemically inactive, substitution helps to prevent overcharge.[21] These beneficial effects, as mentioned in Chapter 1, were the driving force towards the introduction of $LiNi_{0.8}Co_{0.15}Al_{0.05}O_2$ materials for commercial applications.

$LiNi_zMn_zCo_{1-2z}O_2$ (NMC) materials provide similar improvements over $LiCoO_2$, $LiNiO_2$, and $LiNi_{1-x-y}Co_xAl_yO_2$ cathodes, such as improved stability and safety.[22,23,24,25] Additionally, higher reversible cycling capacities are achieved, as mentioned in the previous chapter. Al-substitution for Co in NMC materials can additionally decrease the cost and further improve the properties of the cathode materials. Al-substitution in NMC layered-oxide systems, for example, substantially improves the thermal stability of the materials. The Dahn group[26,27] and others[28] have investigated this effect using a variety of methods including differential scanning calorimetry (DSC), thermogravimetric analysis (TGA), and accelerating rate calorimetry (ARC). Experiments have been performed at various states-of-charge (SOC), in the presence or absence of common electrolytes, and in comparison to Al-free NMC compounds, spinel materials, and other commercially

available layered oxides. The results consistently suggest a beneficial thermal consequence of Al-substitution. Zhou et. al., for instance, have shown that the self-heating-rate (dT/dt) in charged samples, a measure of reaction rate, is significantly limited in Al-containing $Li_xNi_{0.33}Mn_{0.33}Co_{0.33-y}Al_yO_2$ materials as compared to the parent oxide, regardless of charge state. Additionally, Croguennec et al. have observed a delay in the onset temperature of an exothermic decomposition reaction of approximately 50°C for $Li_xNi_{0.4}Mn_{0.4}Co_{0.15}Al_{0.05}O_2$ compared to the Al-free sample, and a 100°C gap compared to an industrial NCA material.

Notably, the presence of Al in $LiNi_zMn_zCo_{1-2z}O_2$ layered-oxide systems has also been shown to improve the cycling stability of the electrode materials.[7,8,9,27] This has been observed in a number of different stoichiometries including z=0.33 and z=0.4. Capacity fade over the operation lifetime is a significant issue in layered-oxide battery materials. The explicit mechanism, however, is not fully understood.[29] Reports on various layered-oxide stoichiometries have referenced phase transformations or local structural disorder in the active particle bulk or surface,[30,31,32,33] loss of contact or microcracking from cyclic volume changes,[34,35,36] and reactivity with the electrolyte to produce surface films[32,34,35,37] as cathode-based capacity-fade schemes. The extent of each can vary based on the specific chemistry of the cathode and the electrode environment, such as the operation temperature, voltage limits and composition of the electrolyte.

However, as the exact mechanisms of cathode capacity fade are not well understood, the means by which Al-substitution improves the material performance cannot be definitively stated. To help design improved battery materials capable of powering an electrified fleet, the role that Al plays in improving the cycling stability of substituted NMC materials must be explicitly understood. For the present study, the electrochemical and structural consequences of Al-substitution for Co in $LiNi_zMn_zCo_{1-2z-y}Al_yO_2$ (z=0.45) have been investigated. This stoichiometry is chosen because the Co-content is simultaneously decreased by both Al-substitution and the concurrent increase in Ni and Mn content, compared to the more common z=0.33 and z=0.4 compositions. This allows for materials along the entire substitution range to be characterized, as will be discussed in the following chapters.

2.2 Synthesis and Methods

Glycine-Nitrate Combustion

$LiNi_{0.45}Mn_{0.45}Co_{0.1-y}Al_yO_2$ ($0 \leq y \leq 0.1$) layered oxide materials over the entire Co-substitution range were prepared using the glycine-nitrate combustion method.[38] Stoichiometric amounts of $LiNO_3$ (Mallinckrodt), $Ni(NO_3)_2 \cdot 6H_2O$ (Sigma Aldrich), $Co(NO_3)_2 \cdot 6H_2O$ (Sigma Aldrich), $Al(NO_3)_3 \cdot 9H_2O$ (Sigma Aldrich), and $Mn(NO_3)_2$ (45-50 wt% solution in dilute nitric acid, Sigma Aldrich) were mixed with glycine ($C_2H_5NO_2$, 98.5%, Sigma Alrich) in an aqueous solution using distilled water. Glycine was added such that the glycine:transition metal ratio was 1:2. A 5% excess of $LiNO_3$ was used in all samples to account for Li loss during the synthesis procedure. The precursor solution was transferred to a heated stainless steel beaker in 20 mL increments, where it was concentrated by the evaporation of water and a subsequent rapid, exothermic self-

propagating combustion reaction ensued, in which the glycine was oxidized by the nitrate ions. A flame temperature of about 1350°C can be reached, and depending on the glycine:nitrate ratio. A nanosized oxide powder with the desired metal stoichiometry was generated. The combustion product was subsequently planetary ball-milled in acetone and dried under flowing N_2 gas, then calcined at 800°C for 4 hours in air to crystallize the material in the desired layered structure.

The glycine-nitrate combustion method is a simple and fast method for the synthesis of Al-substituted NMC materials. Glycine is a "zwitterionic" molecule, containing two functional groups – one carboxylic acid, one amine – at either end of the molecule (Fig. 2-1). Both sites have the ability to complex with metal ion species, and due to the different end groups, the molecule can accommodate ions of various sizes, such as the Li and transition metal ions in this study. The complexation of the dissolved metal nitrates results in an intimately mixed precursor solution, and additionally, prevents the selective precipitation of any species as the solution is concentrated. The high temperatures reached during the combustion allow for complete and tunable reactions, and result in homogeneous nanoparticulate products.[39]

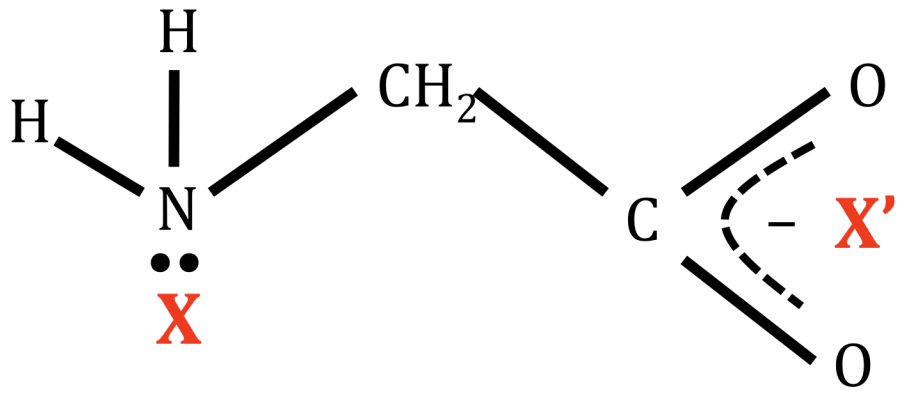

Figure 2-1: The glycine molecule, showing the Zwitterionic character.

The GNC method is advantageous over others for Al-incorporation. This synthesis procedure avoids the issues described by Dahn in using more common co-precipitation techniques such as the mixed hydroxide method to incorporate Al into the NMC lattice.[40] The mixed hydroxide method is a two-step synthesis procedure that includes the formation of an intermediate, well-ordered layered metal hydroxide crystal via co-precipitation from a basic solution of metal salts (often nitrates or sulfates) and LiOH or NH_4OH. In the case of NMC synthesis, the precipitated $M(OH)_2$ material contains M^{2+} (M=Ni, Mn, Co) ions homogeneously distributed throughout the crystal. This intermediate solid is then mixed with Li_2CO_3 or LiOH and calcined in air to form the desired layered $LiMO_2$ product.

The incorporation of the Al^{3+} ion in the intermediate hydroxide structure requires an additional charge-compensating ion, such as NO_3^- or SO_4^{2-}, to also exist in the crystal. The extra ions and H_2O reside between the $M'(OH)_2$ (M'=Ni, Mn, Co, Al) layers, frustrating the well ordered structure, and leading to the formation of a two-phase "layered double hydroxide" precursor, composed of both Al-free and Al-containing

$M'(OH)_2$ phases. In this case, there is significant turbostatic disorder amongst the $M_{1-z}Al_z(OH)_2$ layers, leading to ion-segregation and stacking faults in the resultant layered oxide crystal (Fig. 2-2).[40]

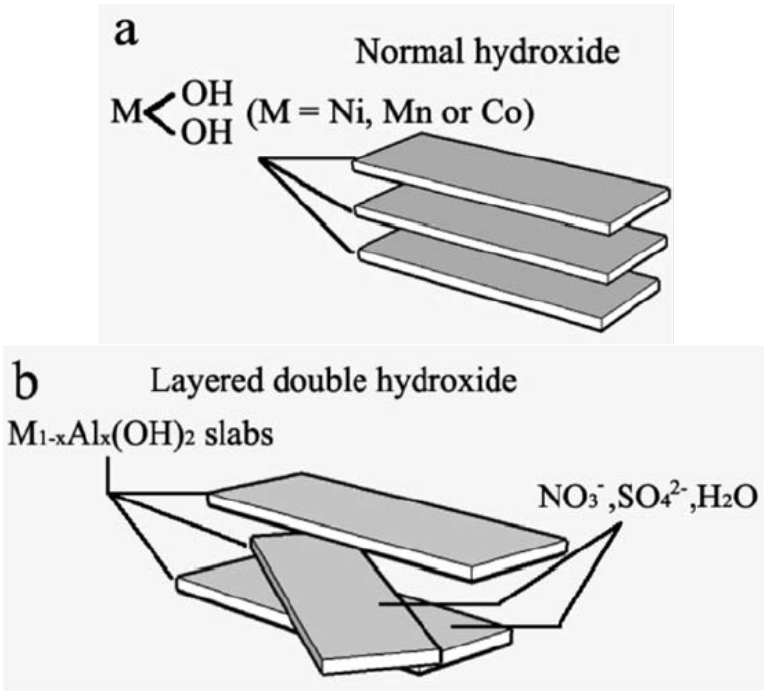

Figure 2-2: a) Normal layered hydroxide formed during co-precipitation, b) layered double hydroxide formed due to the Al^{3+} and counterions.[40]

Another common method is to incorporate the Al during the solid-state heating step. Though often referred to as solid-state synthesis, most procedures involve the initial coprecipitation of a $M^{2+}(OH)_2$ layered hydroxide or another metal-containing precursor, which is subsequently mixed and heated with one of the above Li-compounds and an Al-containing salt.[41] These methods rely on solid-state diffusion at high temperatures to distribute the Al amongst the metal ions, and almost always involve repeating the mixing and heating steps 1-2 times.

The GNC method is superior to these more common synthesis techniques in terms of synthesis time, energy, and the ability to form high-quality, homogeneous, crystalline structures. The other methods require multistep heat treatments at temperatures as high as 1000°C (intermediate treatments at 450-500°C) for periods up to 24 hr. The lengthy heat treatments, in addition to being energy intensive, can limit the production of as-synthesized particles with truly nanoscale dimensions. Additionally, solid-state synthesis may not ensure a homogeneous Al distribution.[41] This is exemplified in Figure 2-3, which compares mixed-hydroxide and solid-state-produced samples subjected to the same heat treatments. The Al signal measured by EDX for each shows clear evidence of segregation in the solid-state sample. A non-uniform cation distribution counteracts the benefits of Al-substitution, and thus has a negative impact on thermal stability.

The GNC synthesis method, however, does not rely on solid-state diffusion to generate a uniform metal distribution throughout the particles. Rather, the metal homogeneity in GNC-based materials is mainly determined by the mixing and complexation in solution prior to combustion. Thus, it is an appropriate synthesis technique to employ for the systematic evaluation of the structural and electrochemical effects of Al-substitution in $LiNi_{0.45}Mn_{0.45}Co_{0.1-y}Al_yO_2$ ($0 \leq y \leq 0.1$) layered oxide materials.

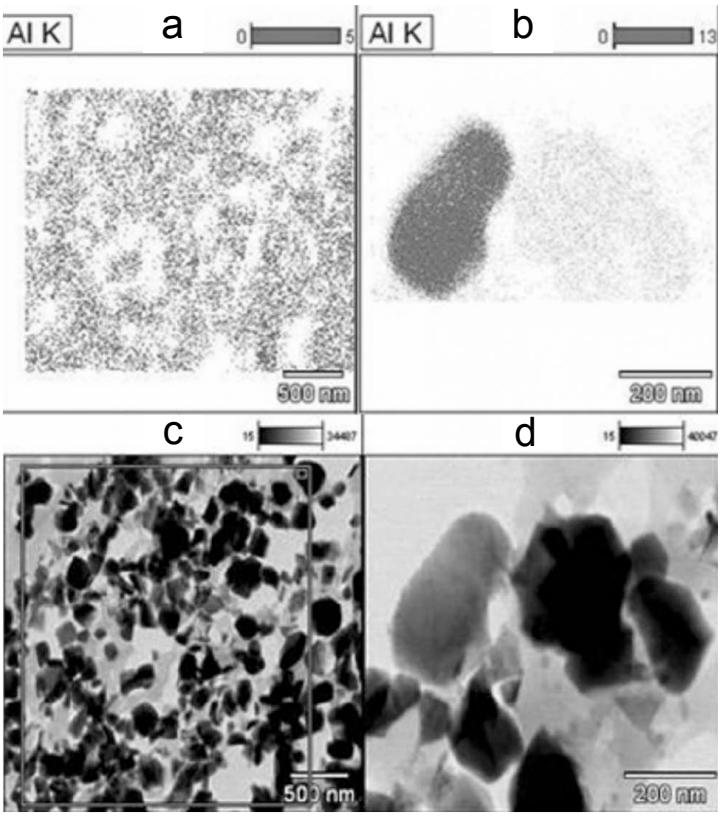

Figure 2-3: a, b) EDX images showing Al distribution (dark) in $LiNi_{1/3}Mn_{1/3}Co_{1/3-z}Al_zO_2$ (z=0.06) prepared by two methods. c, d) STEM images of the sample areas analyzed by EDX. (a) and (c) correspond to a coprecipitation sample, while (b) and (d) correspond to a solid state synthesis sample. Both were calcined at 500°C then 900°C for three hours at each temperature.[41]

Electrode formulation

Porous composite electrodes for electrochemical cells used in these studies were composed of 84 wt% active oxide, 8 wt% polyvinylidine fluoride (PVdF) binder (Kureha Chemical Ind. Co. Limited), 4 wt% synthetic flake graphite (SFG-6, Timcal Ltd.), and 4 wt% acetylene black (Denka). The carbons are added to improve electronic conduction. Slurries were stirred in 1-methyl-2-pyrrolidinone (NMP, Sigma Aldrich) for 48 hrs then mixed with a shear mixer for 30 min, then cast onto carbon-coated aluminum foil current collectors (Intelicoat Technologies) using an automated doctor blade. Typical active material loadings were 5-8 mg/cm^2. The electrodes were dried for at least 24 hours in air, then overnight in a vacuum oven at 120°C.

Circular electrodes were punched (either 1.26 or 1.97 cm^2) for size 2032 coin cells (Fig. 2-4). They were assembled in a helium-filled glovebox with Li-metal counter electrodes, two layers of porous polypropylene separators (Celgard 3401), and electrolyte composed of 1 M $LiPF_6$ in 1:2 (v/v) ethylene carbonate (EC):dimethyl carbonate (DMC) solution (Ferro) (Fig. 2-4). Electrochemical testing of the coin cells was performed using a VMP3 potentiostat/galvanostat (BioLogic). Cells were cycled galvanostatically at various current densities between voltage limits (2.0-4.0, 4.3, or 4.7 V). Experiments were performed at constant current densities (mA/g) across samples for valid comparisons of the effect of Al substitution. The cited C-rates are calculated based on the total Li content and densities of the $LiNi_{0.45}Mn_{0.45}Co_{0.1-y}Al_yO_2$ ($0 \leq y \leq 0.1$) materials.

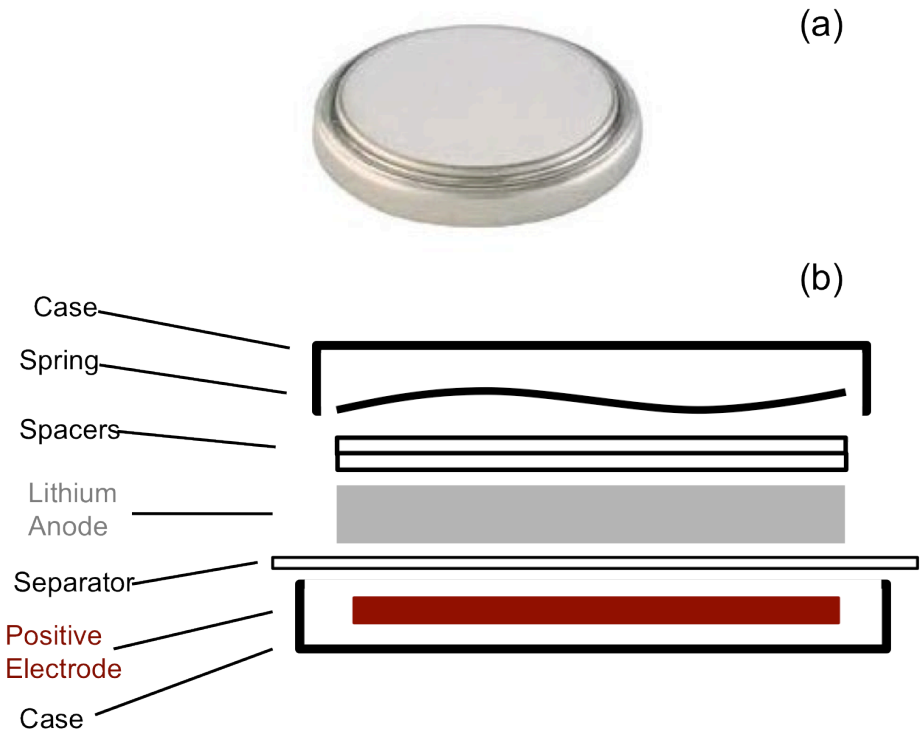

Figure 2-4: a) Coin cell picture. b) Schematic of coin cell assembly.

2.3 Material Characterization

As-Synthesized Powders

Standard laboratory (Panalytical X'Pert Pro) powder XRD patterns for the materials in the series $LiNi_{0.45}Mn_{0.45}Co_{0.1-y}Al_yO_2$ ($0 \geq y \geq 0.1$) are shown in Figure 2-5. All diffraction peaks can initially be indexed in the *R-3m* space group (α-$NaFeO_2$ structure), and no impurity phases are observed. Rietveld refinement of the patterns indicates Al-substitution in place of Co causes an increase in the c_{hex} and a corresponding decrease in a_{hex} lattice parameters (Table 2-1). The behavior has been observed in other Al-substituted NMC materials and is attributed in part to the slightly smaller size of the Al^{3+}

ion in an octahedral environment (0.535 Å) compared to the low spin Co^{3+} ion (0.545 Å) it replaces, though electronic effects relating to the differences in Al-O and Co-O bonding character may also contribute.[7,9,42,43] The reader should note, however, that high-resolution synchrotron XRD reveals a slight structural distortion in the structure with the highest Al-content (y=0.1), which is further discussed in Chapter 3. This distortion is not observed here due to both instrument resolution and the limited measurement range.

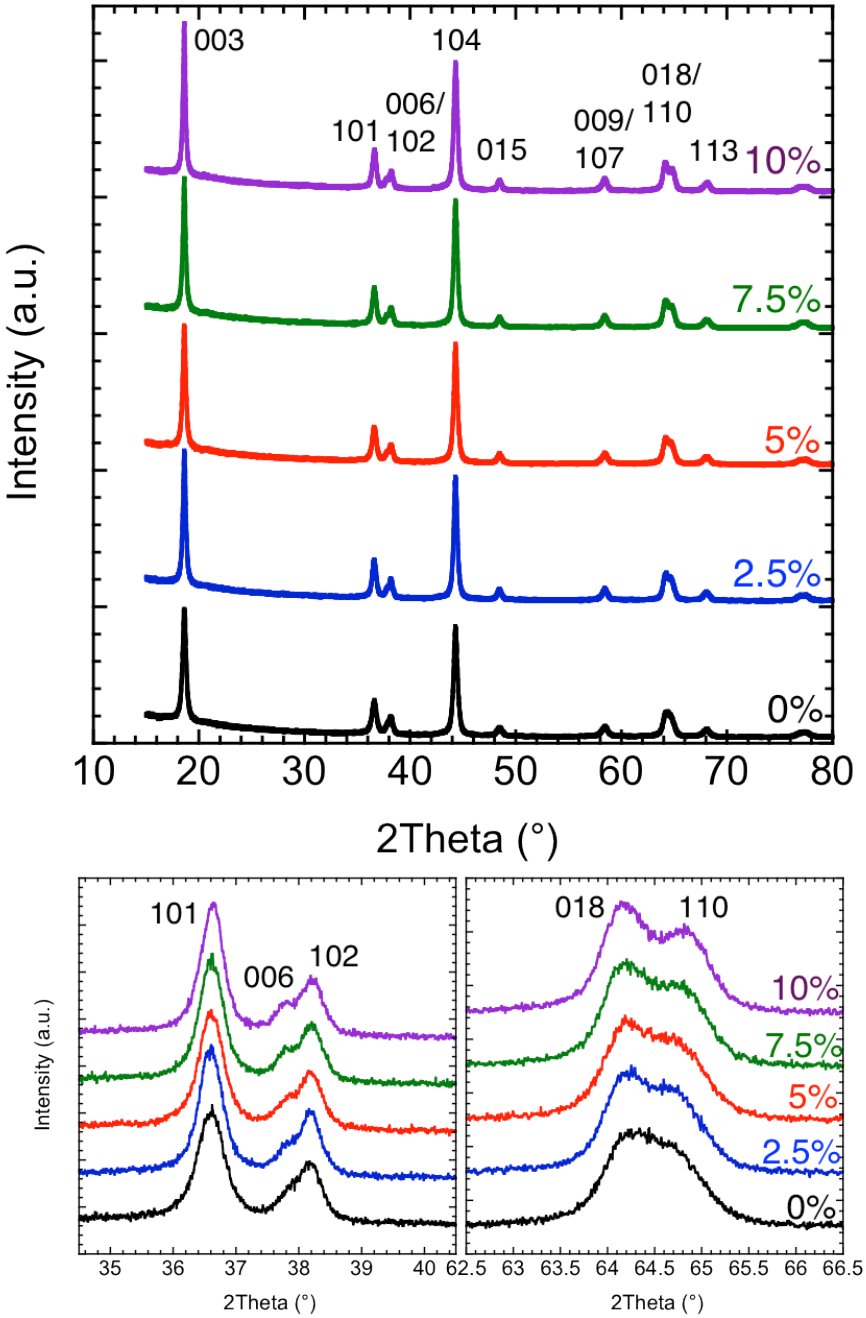

Figure 2-5: X-ray diffraction patterns of the $LiNi_{0.45}Mn_{0.45}Co_{0.1-y}Al_yO_2$ ($0 \leq y \leq 0.1$) materials.

All materials are observed to have approximately 9-10% Ni-Li antisite mixing: ~10% Ni resides on the 3a Li sites and an equivalent amount of Li resides on the transition metal 3b sites. A very slight increase in antisite concentration (<1%) is observed as the Al-substitution is increased, though the change is not large enough to significantly affect the electrochemical properties. This is consistent with previous reports,[7] though the results here differ somewhat from other groups' work.[28] Different synthesis methods, such as that used in the latter reference, can result in significant variations of the observed defect concentrations, however. The effect of antisite defects is further discussed below in the following sections. The parameters obtained from the refinements are presented in Table 2-1. Improved peak splitting of the 006/012 and 018/110 reflections with Al-content observed in Figures 1c and d is the result of the changes in lattice parameters with Al-substitution, and not a difference in Ni_{Li} antisite mixing, as is commonly assumed.

Table 2-1: Results of Rietveld refinement of the $LiNi_{0.45}Mn_{0.45}Co_{0.1-y}Al_yO_2$ ($0 \leq y \leq 0.1$) XRD patterns

Al Content (%)	a (Å)	c (Å)	V (Å^3)	R_{wp}	Particle size (Å)
0	2.87883 ± 0.00004	14.2699 ± 0.0007	102.42 ± 0.005	6.05	40.6
2.5	2.87867 ± 0.00003	14.2745 ± 0.0006	102.441 ± 0.004	6.06	46.1
5	2.87777 ± 0.00004	14.2742 ± 0.0006	102.375 ± 0.005	6.03	43.7
7.5	2.87747 ± 0.00003	14.2796 ± 0.0006	102.393 ± 0.005	6.15	44.8
10	2.87692 ± 0.00003	14.2878 ± 0.0006	102.412 ± 0.004	6.43	46.1

The powder morphologies are similar for all synthesized materials. Average primary particle sizes are ~40-45nm for all materials, calculated from peak broadening during the Rietveld refinements. Particle sizes observed using scanning electron microscopy agree well with those calculated by XRD (Fig. 2-6), and show that the primary particles are organized into larger agglomerates. Thus, performance comparisons between the materials sets are complicated neither by size effects nor significant differences in antisite mixing among the compositions.

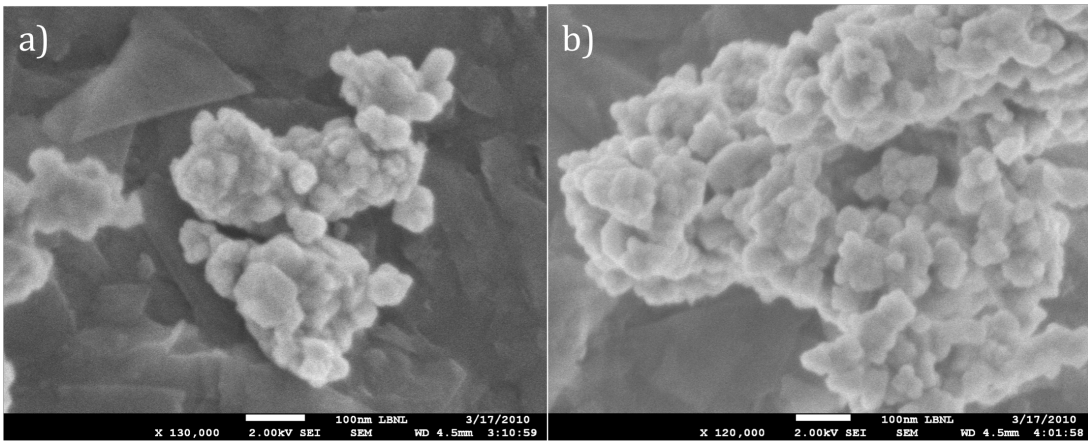

Figure 2-6: SEM images of as-synthesized $LiNi_{0.45}Mn_{0.45}Co_{0.1-y}Al_yO_2$ powders with a) y=0.25 and b) y=0.75. All powders had similar primary particle sizes and agglomeration. Scale bars are 100 nm.

2.4 Electrochemical Performance

First Cycle

The first charge and discharge of half cells containing $LiNi_{0.45}Mn_{0.45}Co_{0.1-y}Al_yO_2$ ($0 \leq y \leq 0.1$) materials are shown in Figure 2-7. The coin cells were operated galvanostatically at 12 mA/g (~C/23) between 2-4.3 V vs. Li/Li^+ using Li-metal anodes. All of the cells display a sloping voltage profile, indicating single-phase solid-solution behavior for the samples during Li de(intercalation). Al-substitution increases the reaction potential at which Li^+ is both removed and replaced in the $LiNi_{0.45}Mn_{0.45}Co_{0.1-y}Al_yO_2$ material during charge and discharge (Fig. 2-7 top, inset). This is more clearly perceived in the derivatives of the specific capacity curves (normalized dQ/dV), shown in Figure 2-7. The peaks in the derivative curves of the Al-substituted samples occur at potentials 50-75 mV higher than those of the unsubstituted material during both oxidation and reduction, consistent with results obtained for other NMC compositions.[7,8]

The increase in both the charge and discharge operating potentials is additional evidence of the full incorporation of Al in the NMC lattice. The presence of a secondary phase (such as insulating γ-$LiAlO_2$), in contrast, would most likely increase the impedance of the system, if anything, resulting in higher charge potentials but lower discharge potentials. The incorporation of Al potentially causes an increase in the ionicity of some or all of the *M*-O bonds (where *M*=Ni, Mn, or Co), which in turn lowers the relative redox energy and increases the operating voltage.

The increase in operating potential with Al-content, coupled with the characteristic sloping voltage profile due to the solid-solution intercalation mechanism, consequently results in a modest decrease in the specific charge and discharge capacities on the first cycle when operated galvanostatically between voltage limits. This effect can also be clearly observed in Figure 2-7 (top), where the parent material delivers approximately 150 mAh/g discharge capacity, compared to 137 mAh/g for the fully substituted sample. The impact is minimal, however, for $y \leq 0.05$ materials. The first cycles of cells charged to 4.7 V are shown in Figure 2-8. A larger capacity is delivered compared to the 4.3 V-cycled cells, as more Li is extracted during the charging process.

All samples display an apparent first cycle irreversibility, in that only 90-95% of the initial charge capacity is recovered on discharge, while 98-99% efficiency is achieved on subsequent cycles. This is in part due to irreversible oxidation of the non-aqueous electrolyte at the high potentials reached during charge, which contributes to the measured charge capacity. Other side reactions, such as anion intercalation from the electrolyte into the carbon, or corrosion of the current collector, may also contribute. The inefficiency is observed upon charge to 4.3 V, though, which is within the oxidative stability limit of the electrolyte and cell components, strongly suggesting a phenomena based on the active layered oxide material is at least partially responsible. Some have suggested the irreversibility is possibly due to the oxidation of Ni^{2+} in the 3a sites (antisite Ni) in the material at high potentials. The oxidation of the antisite Ni can cause a local structural collapse within the Li-layer, thus preventing the re-intercalation of Li except at very slow rates.[44,45] Other studies, however, have concluded that most of the 3a Ni migrates into the transition metal layer at high potentials after removal of the 3b Li.[46,47] Other structural changes, such as oxygen evolution, are possible explanations,

though this should not occur at low states-of-charge. Sluggish Li-diffusion kinetics at the end of discharge has also been cited.[48] The specific causes remain a mystery.

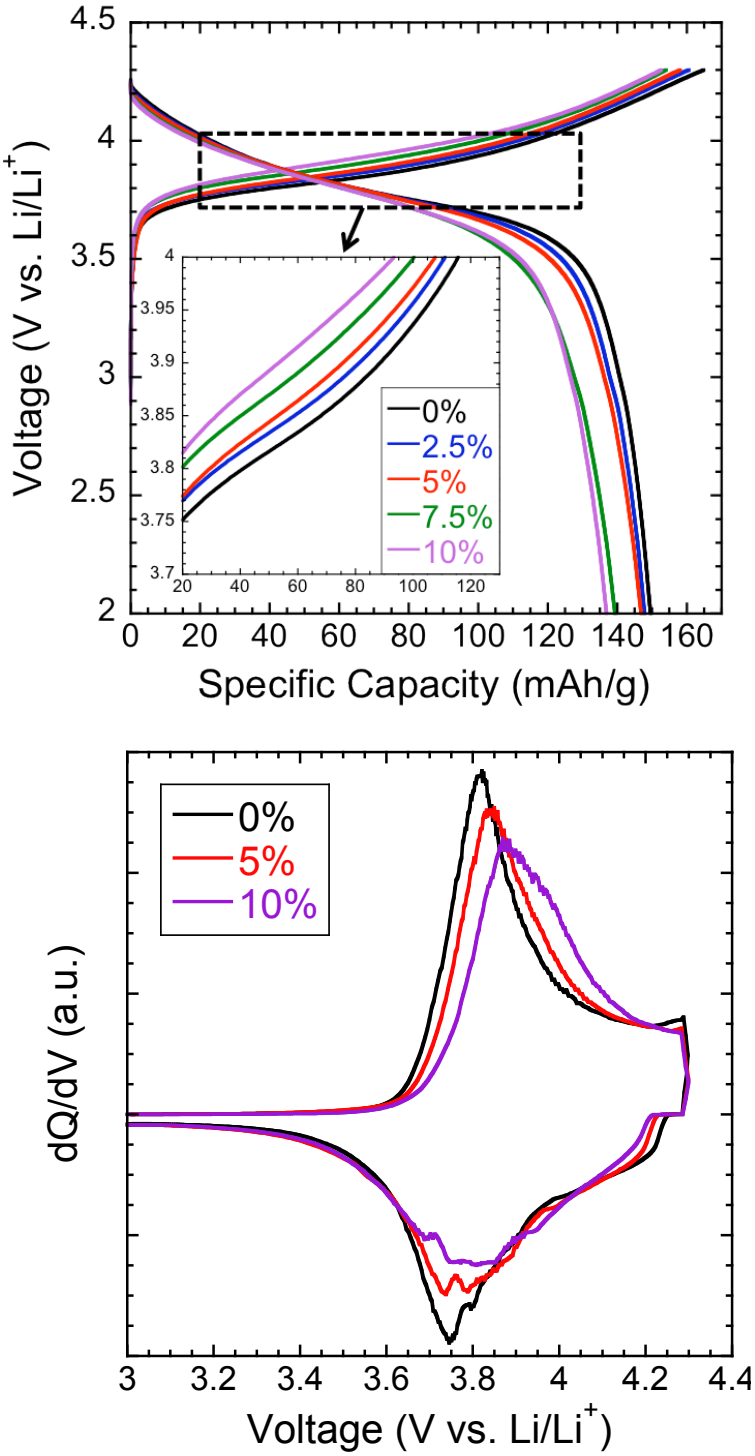

Figure 2-7: Top) First cycle of $LiNi_{0.45}Mn_{0.45}Co_{0.1-y}Al_yO_2$ materials cycled 2.0-4.3 V vs. Li/Li^+. The inset shows the increased operating potential of the electrodes due to Al-substitution. Bottom) Plot of dQ/dV again showing the increased operating potential. The Al content is indicated as a percentage.

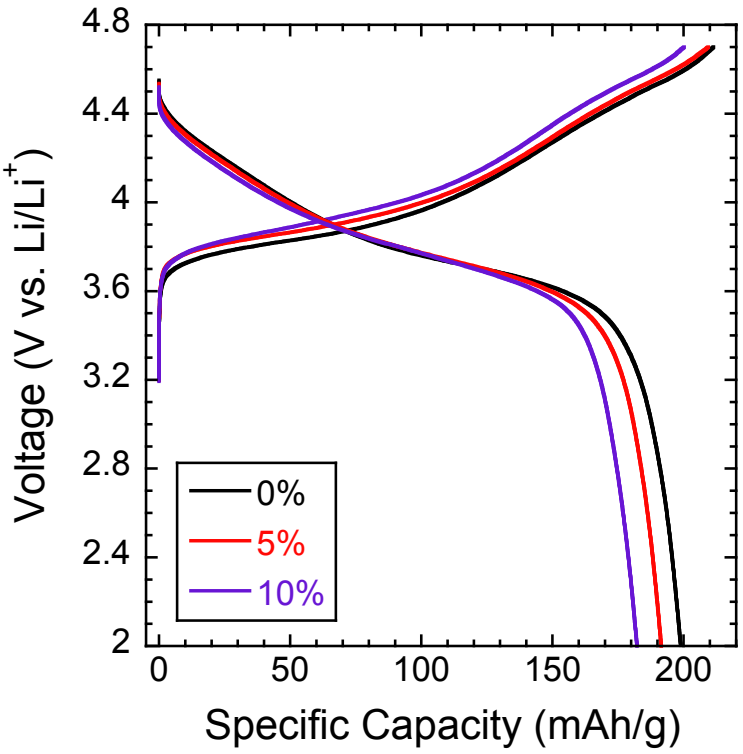

Figure 2-8: The first cycle of $LiNi_{0.45}Mn_{0.45}Co_{0.1-y}Al_yO_2$ materials cycled 2.0-4.7 V vs. Li/Li^+.

Rate Capability

As mentioned above, practical charge and discharge capacities between the set voltage limits decrease somewhat in proportion to the Al content, due to the increase in operating potential and sloping voltage profile. Al substitution has no significant effect, however, on the rate capability of the materials. In Figure 2-9a, the discharge profiles at various rates are shown for the parent material with 0% Al-substitution. As the current density is increased from about C/50 to 2C, ohmic and charge transfer resistances cause a decrease in the discharge potential, lowering the delivered capacity. The decrease in specific capacity with an increase in discharge current density, however, remains essentially constant as a function of Al content in the materials. This can be seen in the modified Peukert plot of Figure 2-9b.

The rate capabilities of Ni-containing layered oxides – such as NMC materials – is strongly dependent on the Ni 3a antisite concentration, as shown in Figures 1-11 and 1-12b (Ch. 1). Greater Ni/Li antisite mixing, which acts to block Li diffusion during battery operation, decreases the rate capability of the electrode materials. The limitation is exaggerated at higher rates and leads to greater declines with current density in the modified Peukert plots. The lack of any such major differences amongst the $LiNi_{0.45}Mn_{0.45}Co_{0.1-y}Al_yO_2$ ($0 \leq y \leq 0.1$) materials over the full substitution range, therefore, indicates that the very slight increase in antisite defect concentration with Al-substitution (<1%) has a minimal effect on the electrochemical performance.

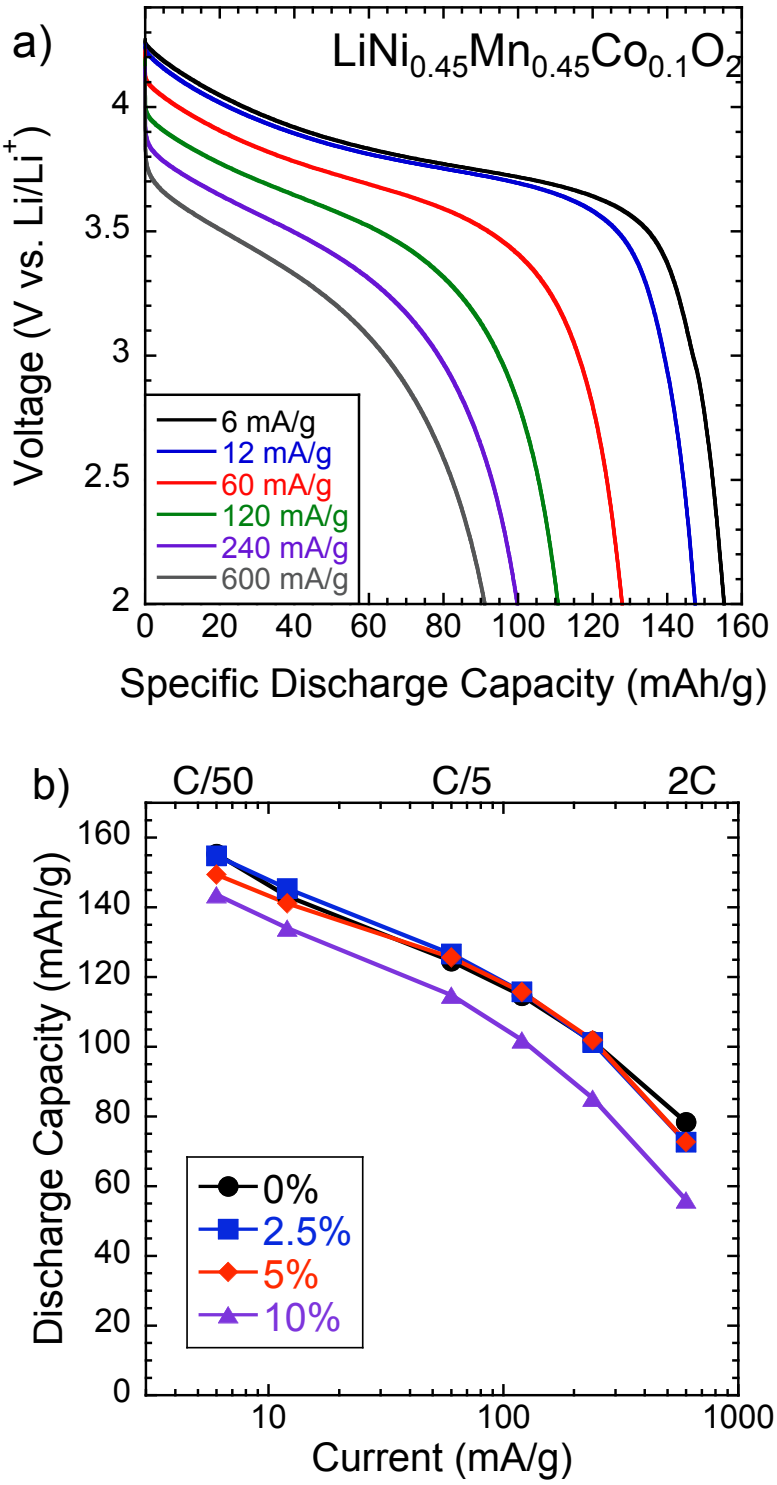

Figure 2-9: a) Discharge profiles of the $LiNi_{0.45}Mn_{0.45}Co_{0.1}O_2$ material at various current densities. b) Modified Peukert plot showing the similar rate capabilities of materials with different Al-contents.

Cycling Performance

Figure 2-10 shows that there is, importantly, a clear enhancement in the cycling stability with the presence of Al. After approximately 30 cycles at 12 mA/g (~C/23) between 2-4.3 V, the material with 5% Al-substitution provides a higher discharge capacity than the Al-free material, while the fully substituted sample (10% Al) outperforms the parent material after about 100 cycles. Both materials have first cycle discharge capacities lower than that of the unsubstituted material due to the effect of the increased operating voltage, as discussed above – but the presence of Al limits the rate of capacity fade in the substituted materials. Discharge profiles at various cycles during cell operation are shown in Figure 2-11. The operating voltage is seen to decrease as a function of cycle number for all materials. There is a larger voltage decrease in the discharge potential profiles of the unsubstituted samples compared to those containing Al, consistent with the improved cycleability due to Al-substitution.

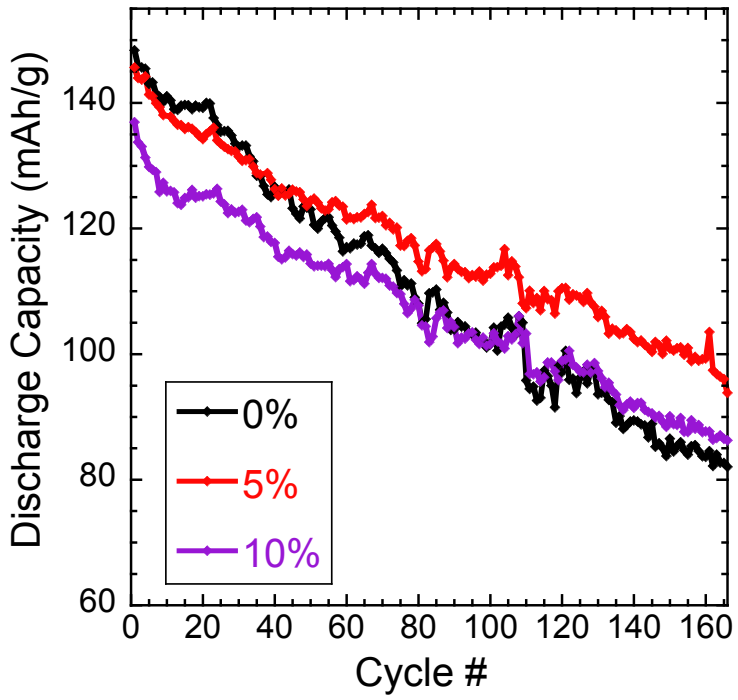

Figure 2-10: Discharge capacity vs. cycle number for $LiNi_{0.45}Mn_{0.45}Co_{0.1-y}Al_yO_2$ materials cycled between 2.0-4.3 V vs. Li/Li^+ at 12 mAh/g. Al-substitution leads to enhanced cycling stability.

A faster rate of capacity fade is seen upon cycling between 2-4.7 V at 18 mA/g (Figure 2-12). The stabilizing effect of Al is still observed, with the Al-substituted samples out-performing the parent material after about 25 cycles. The discharge profiles at various stages of cycling are shown in Figure 2-13. All materials show a drastic decrease in operating potential. Again, the changes are somewhat limited in the samples containing Al. Cycling between 2-4.0 V at 18 mA/g also results in some capacity fade of the $LiNi_{0.45}Mn_{0.45}Co_{0.1-y}Al_yO_2$ materials, though at a slower rate than the higher voltage cycling (Fig. 2-14). A stabilizing effect of Al, however, is not readily apparent within 30 cycles when operated in this relatively low voltage range.

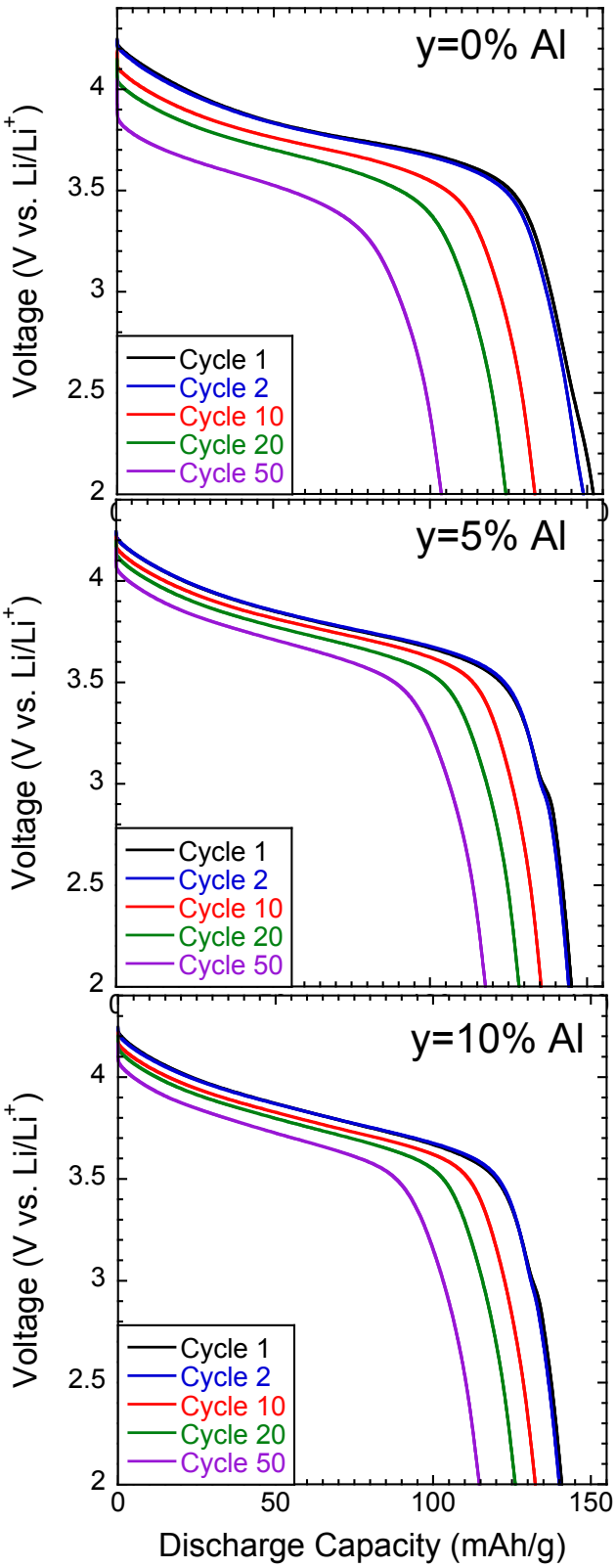

Figure 2-11: Discharge profiles at select cycles for $LiNi_{0.45}Mn_{0.45}Co_{0.1-y}Al_yO_2$ materials (y=0, 0.05, 0.1) cycled 2.0-4.3 V vs. Li/Li^+. All axes have the same scale.

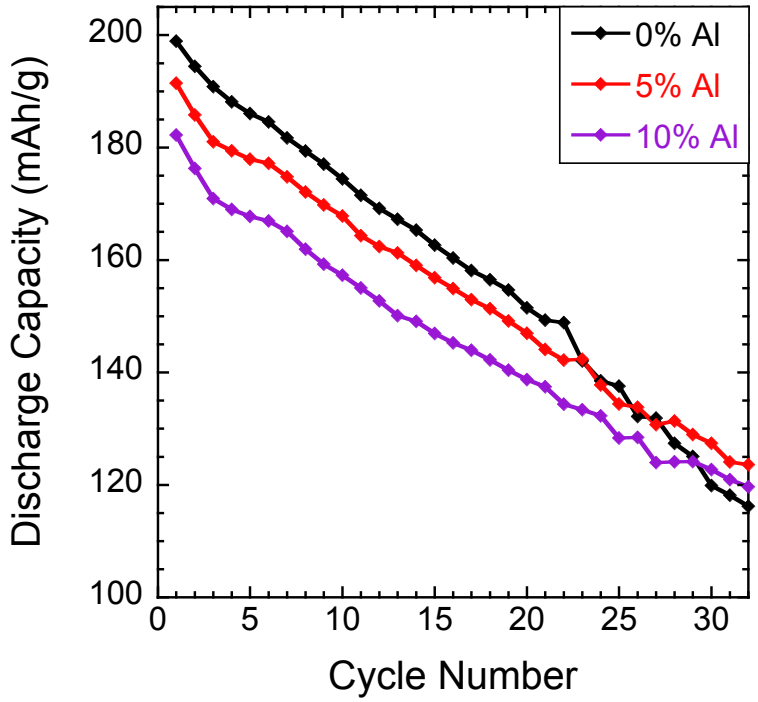

Figure 2-12: Discharge capacity vs. cycle number for $LiNi_{0.45}Mn_{0.45}Co_{0.1-y}Al_yO_2$ materials cycled between 2.0-4.7 V vs. Li/Li^+ at 18 mAh/g. The stabilizing effect of Al can be seen.

Al-substitution in $LiNi_{0.45}Mn_{0.45}Co_{0.1-y}Al_yO_2$ ($0 \leq y \leq 0.1$) clearly improves the electrochemical properties of the layered oxide material. When homogeneously incorporated in the lattice, as results from the glycine-nitrate combustion method, Al raises the operating voltage of the cathode on both charge and discharge. Low concentrations ($y \leq 0.05$) do not substantially decrease the initial discharge capacities, nor does substitution significantly affect the defect structure (antisite concentration), as evidenced by the similar rate behavior of the various materials. Al-substitution does, however, provide a clear enhancement of the cycling stability for charging voltages greater than 4V. The next chapters will investigate the structural consequences of Al substitution in $LiNi_{0.45}Mn_{0.45}Co_{0.1-y}Al_yO_2$ ($0 \leq y \leq 0.1$) materials on both long-range and short-range scales.

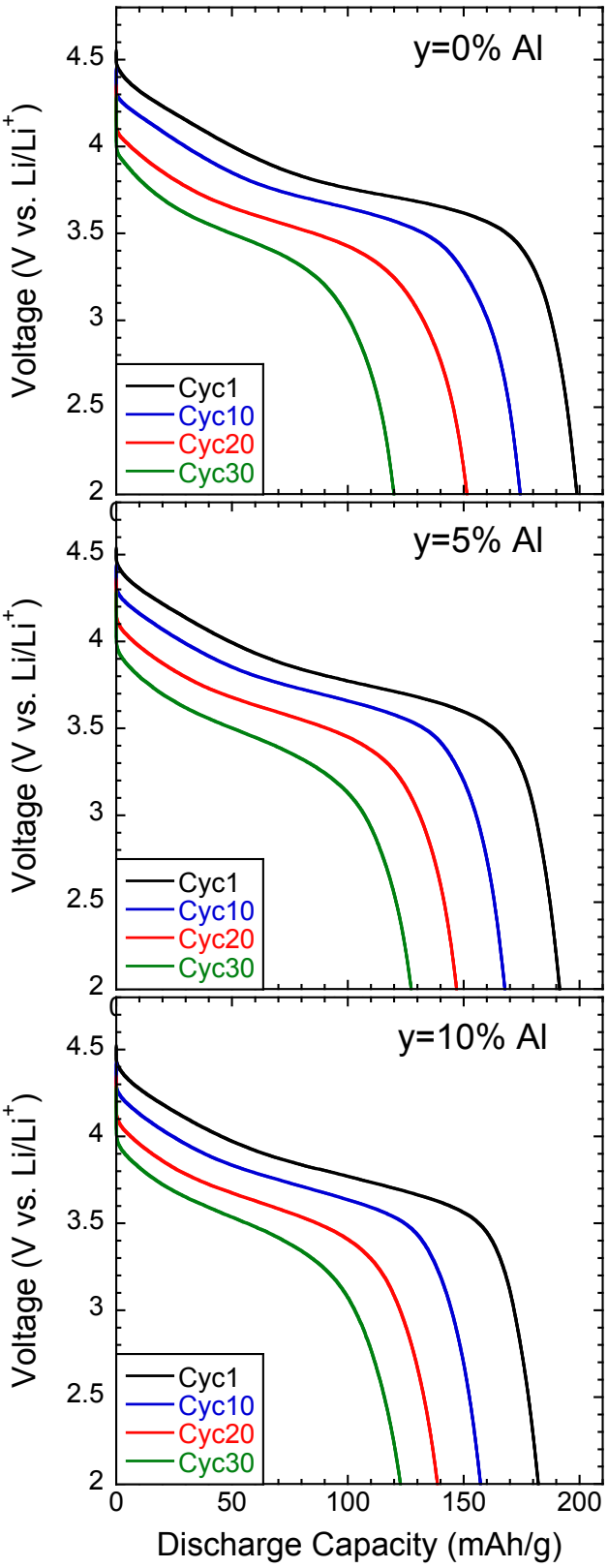

Figure 2-13: Discharge profiles at select cycles for $LiNi_{0.45}Mn_{0.45}Co_{0.1-y}Al_yO_2$ materials (y=0, 0.05, 0.1) cycled 2.0-4.3 V vs. Li/Li^+. All axes have the same scale.

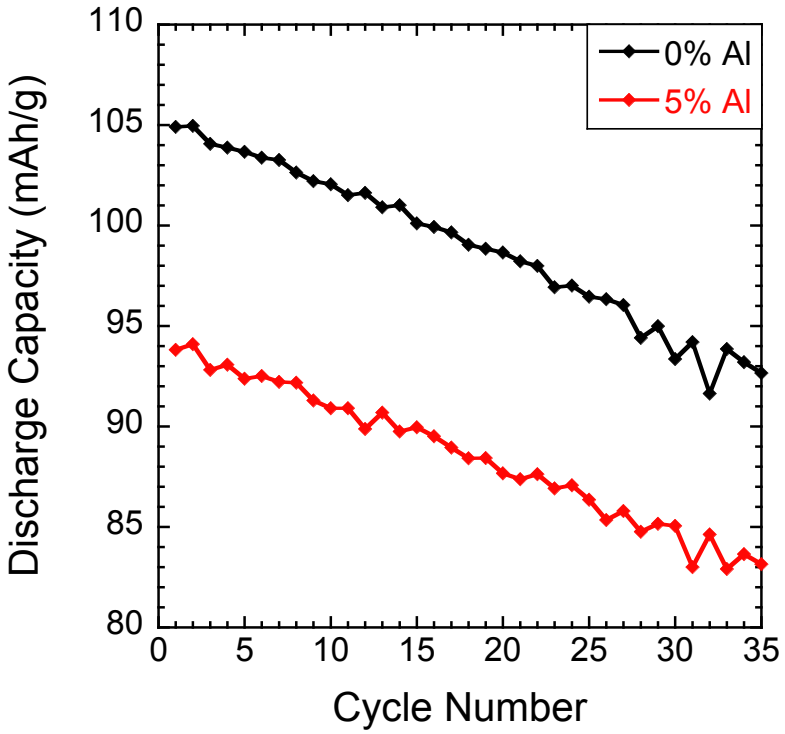

Figure 2-14: Discharge capacity vs. cycle number for $LiNi_{0.45}Mn_{0.45}Co_{0.1-y}Al_yO_2$ materials cycled between 2.0-4.0 V vs. Li/Li^+ at 18 mAh/g. Al does not seem to affect the cycling stability for electrodes cycled within the low-voltage window. The lower discharge capacity is due to the higher operating potential of Al-containing materials, as explained in the text.

2.5 References

[1] Alcantara et al. *J. Solid State Chem.* **1997,** *134,* 265.

[2] Albrecht et al. *J. Power Sources*, **2003,** *119,* 178.

[3] W. Luo, J. R. Dahn. *J. Electrochem. Soc.* **2011,** *158,* A428.

[4] Kim et al. *Electrochimica Acta,* **2006,** *51,* 2447.

[5] Pouillerie et al. *J. Electrochem Soc.* **2000,** *147,* 2061.

[6] Nazri et al. *Mater. Res. Soc. Symp. Proc.* **1996,** *453,* 635.

[7] J. Wilcox, E. E. Rodriguez, M. M. Doeff. *J. Electrochem. Soc.* **2009,** *156,* A1011.

[8] J. Wilcox, S. Patoux, M. M. Doeff. *J. Electrochem. Soc.* **2009,** *156,* A192.

[9] Liu et al. *Electrochimica Acta,* **2006,** *51,* 4199.

[10] K. Kam, M. M. Doeff. *J. Mater. Chem.* **2011,** *21,* 9991.

[11] Delmas et al. *Electrochimica Acta,* **1999,** *45,* 243.

[12] Li et al. J. *Electrochem. Soc.* **2011,** *158,* A516.

[13] Ngala et al. *Mat. Res. Soc. Symp. Proc.* **2003,** *756,* 1.

[14] Buta et al. *J. Electrochem. Soc.* **1999,** *146,* 4335.

[15] Ceder et al. *Nature*, **1998,** *392,* 694.

[16] Guilmard et al. *Chem. Mater.* **2003,** *15,* 4476.

[17] Ohzuku et al. *J. Power Sources,* **1997,** *68,* 131.

[18] Amdouni et al. *Materials Chemistry and Physics*, **2003,** *80,* 205.

[19] Guilmard et al. *J. Power Sources,* **2003,** *115,* 305.

[20] Chen et al. *J. Power Sources,* **2004,** *128,* 278.

[21] Ohzuku et al. *J. Electrochem. Soc.* **1995,** *142,* 4033.

[22] Y. Wang et al. *Electrochem. Commun.* **2007**, *9*, 2534.

[23] Lu et al. *Electrochem. Solid State Lett.* **2001**, *4,* A200.

[24] I. Belharouak et al. *Electrochem. Commun.* **2006**, *8*, 329.

[25] W. Choi, A. Manthiram. *J. Electrochem. Soc.* **2005**, *152*, A1714.

[26] F. Zhou, X. Zhao, Z. Lu, J. Jiang, J. R. Dahn. *Electrochem. Commun.* **2008,** *10,* 1168.

[27] F. Zhou, X. Zhao, J. R. Dahn. *J. Electrochem. Soc.* **2009,** *156,* A343.

[28] L. Croguennec, J. Bains, J. Bréger, C. Tessier, P. Biensan, S. Levasseur, C. Delmas. *J. Electrochem. Soc.* **2011,** *158,* A664.

[29] J. Vetter, P. Novák,, M. Wagner, C. Veit, K. Möller, J. Besenhard, M. Winter, M. Wohlfahrt-Mehrens, C. Wogler, A. Hammouche. *J. Power Sources,* **2005,** *147,* 269.

[30] H. Gabrisch, T. Yi, R. Yazami. *Electrochem. Solid State Lett.* **2008,** *11,* A119.

[31] D. Abraham et al. *Electrochem. Commun.* **2002,** *4,* 620.

[32] H. Kobayashi, M. Shikano, S. Koike, H. Sakaebe, K. Tatsumi. *J. Power Sources,* **2007,** *174,* 380.

[33] S. Muto, et al. *J. Electrochem. Soc.* **2009,** *156,* A371.

[34] D. Aurbach, B. Markovsky, A. Rodkin, M. Cojocaru, E. Levi, H. Kim H. *Electrochimica Acta,* **2002,** *47,* 1899.

[35] R. Kostecki, J. Lei, F. McLarnon, J. Shim, K. Striebel. *J. Electrochem. Soc.* **2006,** *153,* A669.

[36] H. Wang, et al. *J. Electrochem. Soc.* **1999,** *146,* 473.

[37] M. Kerlau, J. Reimer, E. Cairns. *J. Electrochem. Soc.* **2005,** *152,* A1629.

[38] Chick et al. *Mater. Lett.* **1990,** *10,* 6.

[39] K.C. Patil, M. S. Hegde, T. Rattan, S. T. Aruna, *Chemistry of Nanocrystalline Oxide Materials: Combustion Synthesis, Properties and Applications.* World Scientific, **2008**.

[40] Zhao et al. *J. Electrochem. Soc.* **2008,** *155,* A642.

[41] Zhou et al. *J. Electrochem. Soc.* **2009,** *156,* A796.

[42] R. D. Shannon. *Acta Cryst.* **1976,** *32,* 751.

[43] A. Manthiram, J. B. Goodenough. *J. Power Sources,* **1989,** *26,* 403.

[44] J. P. Peres, et al. *J. Phys. Chem. of Solids,* **1996,** *57,* 1057.

[45] C. Delmas, et al. *J. Power Sources,* **1997,** *68,* 120.

[46] J. Bréger et al. *Chem. Mater.* **2006,** *18,* 4768.

[47] Yabuuchi et al. *J. Electrochem. Soc.* **2007,** *154,* A566.

[48] S. Kang et al. *Electrochimica Acta,* **2008,** *54,* 684.

Chapter 3: Synchrotron X-ray Diffraction Studies

3.1 Introduction

X-ray diffraction is a powerful, non-destructive characterization method that allows the determination of the long-range structure of (mostly) crystalline materials. Since the initial quantitative development of the technique by W. H. and W. L. Bragg in 1913, X-ray diffraction techniques have advanced and matured much like the materials characterized. The introduction of synchrotron radiation sources caused a sharp increase in the development of advanced and versatile methods. The high brilliance and short wavelengths available at these beamlines has improved resolution and lowered the necessary data collection times. Focusing optics have been introduced to allow illumination spot sizes on the order of microns or smaller.[1] Today, versatile measurement configurations and diverse beamline endstations have enabled novel experiments such as the characterization of nanostructures and *in situ* observation of material evolution.[2,3,4] The structural evolution of various Li-ion battery electrodes, for example, have been observed during electrochemical cycling and thermal exposure.[5,6,7]

Two different synchrotron X-ray diffraction techniques were used to study the structural effect of Al-substitution in the $LiNi_{0.45}Mn_{0.45}Co_{0.1-y}Al_yO_2$ cathode materials for this work. Powder samples were characterized by high-resolution XRD; both as-synthesized powders and *ex situ* recovered electrode materials. *In situ* XRD was performed to observe the electrode materials during electrochemical extraction and insertion of Li^+ ions during battery operations. Both methods provide complimentary information about the structural consequences of Al-incorporation.

3.2 Methods

High resolution XRD was performed on *ex situ* samples at beamline 11-BM of the Advanced Photon Source (APS) at Argonne National Laboratory (ANL). Fresh powder, fresh electrode materials (including carbon and PVDF), and electrode materials recovered from coin cells after 20 and 50 cycles (2-4.3V, 15 mA/g) were hermetically sealed in Kapton capillaries for measurements.

The high-resolution beamline utilizes 30 keV xrays (~0.413 Å) and a double crystal Si(111) monochromater. An ion gauge just before the sample specimen monitors any intensity fluctuations in the source radiation. A spinning sample mount (90 Hz) reduces preferred orientation in the samples. Twelve discrete perfect Si(111) single crystal analyzers are used, at a spacing of 2° 2θ over the angular range -6 to 16° 2θ. Each detector is mounted on a separate goniometer and independently adjustable. The perfect crystals provide excellent energy discrimination, limiting background contributions from sample fluorescence and Comption scattering. Oxford-Danfysik $LaCl_3$ Cyberstar scintillators are used to detect photons diffracted from the analyzer crystals (Lee et al., 2008). The entire detector construction is scanned over a 34° 2θ range at a rate of 0.01°/s, with data collected every 0.001° 2θ. The resolution, $\Delta Q/Q$ ($Q=2\pi/d$), is better than $2x10^{-4}$.[8,9,10]

For the data from each of the twelve discrete detectors, calibration corrections were applied to account for, among other issues, detector sensitivities, 2θ offsets, and intensity variations. Calibration was performed using a mixture of NIST standard reference materials, Si (SRM 640c) and Al_2O_3 (SRM 676), with the Si lattice parameter determining the exact x-ray wavelength. The corrected data from each detector was then merged on a common 2θ grid, resulting in a single intensity vs. 2θ data set. Rietveld refinements of the final collected spectra were performed using the GSAS/EXPGUI software package, with the accompanying calibration file for each individual scan.[11,12]

In situ synchrotron x-ray diffraction studies were performed at beamline 11-3 at the Stanford Synchrotron Radiation Laboratory (SSRL) at the SLAC National Accelerator Laboratory. *In situ* XRD requires a battery cell construction that allows the transmission of X-rays. Thus, pouch cells are utilized, in which the battery components (electrodes, separator, electrolyte, etc.) are contained within a hermetically sealed, x-ray transparent polymer pouch (polyester in these studies). Pouch cells were assembled in an argon-filled glovebox with composite cathodes, Li-metal counter electrodes, Celgard 2400 porous polypropylene separators, and 1 M $LiPF_6$ in 1:1 ethylene carbonate (EC):diethyl carbonate (DEC) electrolyte solution (Ferro). The polyester pouches were hermetically sealed with a thermal vacuum sealer to limit trapped gas bubbles. Aluminum and nickel tabs with a sealable polymer attachment were used for accessible electronic connection to the positive and negative electrodes, respectively. The Al tabs were ultrasonically welded to the cathode current collectors, while the soft Li metal used as the anode was simply pressed around the Ni tab for electronic contact.

The cells were cycled galvanostatically using an FAS2 Femptostat (Gamry Instruments, Inc.) at ~C/13 or ~C/21 depending on time constraints. To maintain pressure, the pouch cells were constrained within a custom frame of two aluminum plates, both containing a small 2 mm diameter hole that allows for transmission of the x-ray beam through the electrode. The back plate has a conical section of material removed around the transmission hole so as not to interfere with the diffracted radiation exiting the sample.

Transmission XRD ring patterns were detected using a 345 mm MAR imaging plate, requiring an exposure time of approximately 10 s with a data readout time of less than 2 min. Figure 3-1 shows a photograph of the experimental setup. Linescans (intensity vs. Q) were generated by integrating the calibrated image patterns. The beamline uses a single Si(311) monochrometer, generating an incident wavelength of approximately 0.97 Å (12,735 eV), though energy fluctuations (mostly diurnal shifts due to temperature changes of the synchrotron ring) are observed over the course of the lengthy charge and discharge measurements. Thus, image calibration for each scan is essential to de-convolute diffraction pattern changes due separately to energy fluctuations and material changes.

Calibrations were performed for every diffraction profile considered, using The Area Diffraction Machine software developed in conjunction with the 11-3 beamline.[13] A two-step process was established for accurate analysis of the electrode materials, given the number of constraints inherent to this specific experimental set-up. Although the Li metal anode does not contribute a diffraction signal, the polyester pouch and separator materials provide significant background signal as well as both intense and minor diffraction peaks throughout the angular range observed. Reflections from the Al metal

current collector are additionally present in the diffraction spectra. The Al peaks are well resolved in the fresh (uncharged) electrode samples, but specific layered-oxide material reflections shift towards the Al peaks during Li de-intercalation, resulting in overlap.

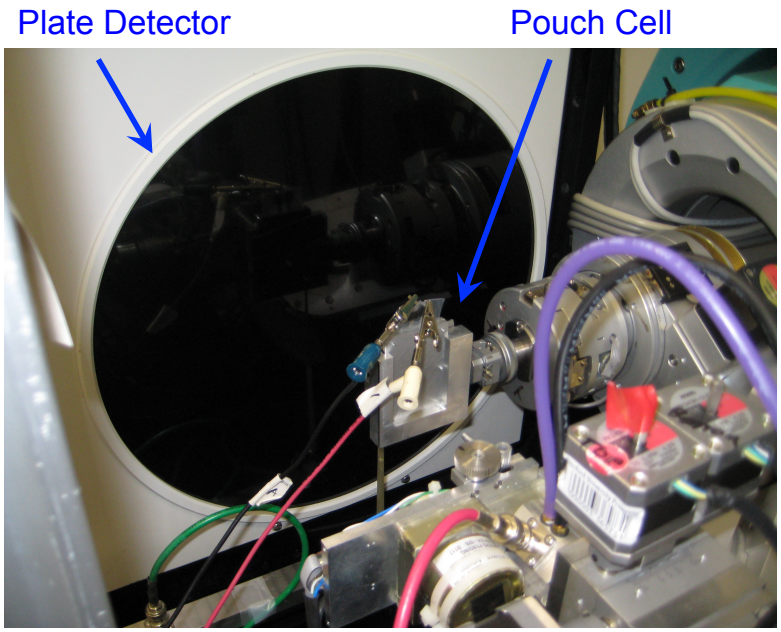

Figure 3-1: Photograph of the experimental set-up for *in situ* X-ray diffraction studies at beamline 11-3, SSRL.

During calibration, the incident x-ray energy and sample position values were varied as free parameters. The initial scan of the fresh material after setting up the pouch cell in the experimental hutch is calibrated using the observed Al reflections; calibration of the ring patterns is achieved by a non-linear least-squares fit of registered diffraction signals to user-supplied theoretical Q values of the refinement standard(s). The initial calibration of the fresh material is used to set the sample position, which is subsequently fixed for the remainder of the experiment. Calibration of all further patterns is based on a subset of Al reflections that are not obscured by the evolving layered-oxide material peaks throughout the full range of Li-concentrations observed, in addition to two strong peaks from the polyester pouch material that remain isolated during battery operation. The exact positions (Q) of these polyester reflections were determined based on one initial dataset and used for all samples studied to ensure valid comparisons of the relative changes observed.

The significant background signal contributed by the polyester pouch and separator materials, along with the periodic overlap of the active material and Al current collector peaks during cell operation, make both perfect background subtraction and Rietveld refinement of the entire diffraction patterns an extremely difficult undertaking. To circumvent this problem, backgrounds are manually subtracted and a specific set of peaks (7 total) that are not obscured by the current collector during cell operation are fit with pseudo-Voigt lineshapes to determine the peak positions. The unit cell lattice parameters at various states-of-charge (SOC) are subsequently calculated by a least-squares refinement using the available peak positions and the program CelRef, with constraints imposed by the assumed *R-3m* symmetry.

3.3 High Resolution XRD of Fresh $LiNi_{0.45}Mn_{0.45}Co_{0.1-y}Al_yO_2$ Materials

High-resolution synchrotron XRD spectra for as-synthesized $LiNi_{0.45}Mn_{0.45}Co_{0.1-y}Al_yO_2$ powders with y=0, 0.05, and 0.1 are shown in Figure 3-2, indexed here in the hexagonal *R-3m* symmetry. High-resolution X-ray diffraction allows subtle structural variations to be observed due to the small wavelength and large angular range used in the measurements. No secondary or impurity phases are observed in any of the materials. Partial substitution of Al for Co causes an expansion of the crystal along the layered direction, as observed by a shift of the *R-3m* 003 peak (Fig. 3-2b), and a slight corresponding contraction within the transition metal plane (Table 3-1). This is attributed in part to the slightly smaller size of the Al^{3+} ion in an octahedral environment (0.535 Å) compared to the low spin Co^{3+} ion (0.545 Å) it replaces, though electronic effects relating to the differences in Al-O and Co-O bonding character may also contribute.[14,15]

All materials are observed to contain approximately 9-10% Ni-Li antisite mixing, corresponding to 9-10% Ni ions residing on the Li sites (*3a* in *R-3m*) between the transition metal layers and an equivalent amount of Li residing on the transition metal sites (*3b* in *R-3m*). This is calculated during the Rietveld refinement, detailed below. The 003/104 peak ratios in particular are quite sensitive to the *3a* Ni/*3b* Li concentration.[16] A slight increase in antisite concentration (~1%) is observed as the Al-substitution is increased, consistent with previous reports, though the change is not large enough to significantly affect the electrochemical properties between samples with different Al-concentrations, as seen in Chapter 2.[17] It was shown in Chapter 1 (Figure 1-11) that the relative concentration of *3a* Ni antisite defects can have a profound effect on the rate capability of layered oxide materials; because no significant effect is observed throughout the range of Al-substitution studied here, the defect structures are considered similar.

The existence of a small shoulder peak on the high-angle side of the 003 (*R-3m*) reflection of all samples (Fig. 3-2a, inset) provides evidence of at least some extent of metal ordering within the transition metal layers. Intensity in this shoulder region is commonly attributed to Li_2MnO_3-like domains within the structure.[18,19] Li_2MnO_3 (or "$Li[Li_{1/3}Mn_{2/3}]O_2$"), as mentioned in Chapter 1, crystallizes in a monoclinic C2/m layered structure that closely resembles the *R-3m* structure of the NMC layered oxides (Figure 1-13). The ordered distribution of Li^+ and Mn^{4+} ions in the transition metal layer forms a superstructure, lowering the symmetry. As these $LiNi_{0.45}Mn_{0.45}Co_{0.1-y}Al_yO_2$ materials include up to 10% antisite defects, metal ordering around the Li 3b defects is anticipated. NMR investigations have concluded that Li^+ ions in the transition metal layers of $LiNi_zMn_zCo_{1-2z}O_2$ materials are preferentially surrounded by 6 Mn^{4+} or 5 Mn^{4+} and 1 Ni^{2+}, forming a nearest-neighbor environment of the Li^+ ions similar to that found in Li_2MnO_3.[20,21,22] A perfectly ordered flower pattern (Figure 1-10) is generated in $LiNi_{0.5}Mn_{0.5}O_2$ with an 8.3% antisite defect concentration; the ideal stoichiometric formula is thus $[Li_{11/12}Ni_{1/12}]_{3a}[Li_{1/12}Ni_{5/12}Mn_{1/2}]_{3b}O_2$. X-ray absorption studies have provided some confirmation of this structure experimentally.[23] The $LiNi_{0.45}Mn_{0.45}Co_{0.1-y}Al_yO_2$ system is expected to behave similarly, based on the large defect concentration and high Ni/Mn content in the materials.

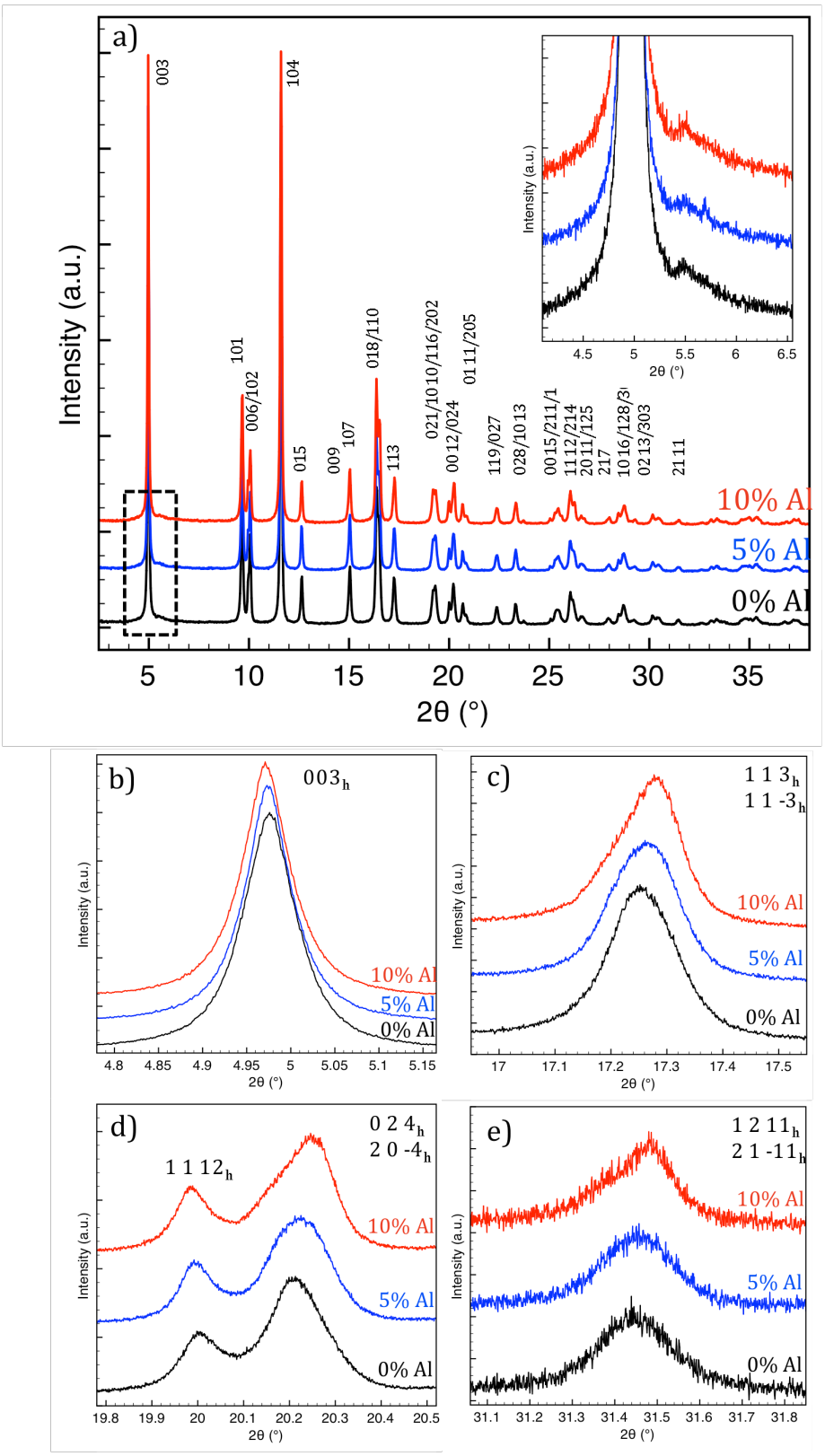

Figure 3-2: a) High-resolution XRD patterns of as-synthesized $LiNi_{0.45}Mn_{0.45}Co_{0.1-y}Al_yO_2$ (y=0, 0.05, 0.1) powders. A magnification of the indicated region is shown in the inset. b-e) Magnified regions of the patterns shown in (a). Al-substitution causes a slight structural distortion in the materials.

All samples show inhomogeneous broadening of some peaks, such as for the 018/110 reflections. The particles are equiaxial (see SEM images in Figure 2-6, Chapter 2) eliminating the possibility of anisotropic sample size broadening. The features are taken into account by using a semi-empirical microstrain correction developed by Stephens during the Rietveld refinements.[24] The model improves the peak profile fits in cases where broadening is not a smoothly varying function of d-spacing (2θ), such as here. It assumes a distribution of lattice metric parameters amongst crystallites, constrained on average by the crystal symmetry.

Closer observation of the XRD spectra reveals further anisotropic broadening of some reflections in the fully substituted y=0.1 sample (Figs. 3-2 c-e). These further distortions cannot be accounted for simply with the microstrain correction described above. Neither is the existence of a second phase plausible: the splitting occurs at only specific *hkl* reflections, the electrochemical behavior of the materials suggests full incorporation of Al, and X-ray absorption measurements (Chapter 4) indicate a local-order distribution of Al within the materials.

Rather, the specific occurrences indicate a removal of the degeneracy of hexagonal *hkl* and *kh-l* reflections, signifying a symmetry-lowering distortion within the transition metal plane. Indeed, while the y=0 and y=0.05 XRD patterns can be well fit using the *R-3m* hexagonal space group, the y=0.1 fully substituted material is best fit using the monoclinic *C2/m* symmetry (space group #12). *C2/m* symmetry is a maximal non-isomorphic subgroup of *R-3m*, generated by the removal of the 3-fold axis of the hexagonal structure. In the current system, this is accomplished by a slight change of one in-plane metal-metal distance relative to the other in a non-random manner. Figure 3-3 provides a schematic comparison of the *R-3m* and *C2/m* unit cells in the transition metal plane.

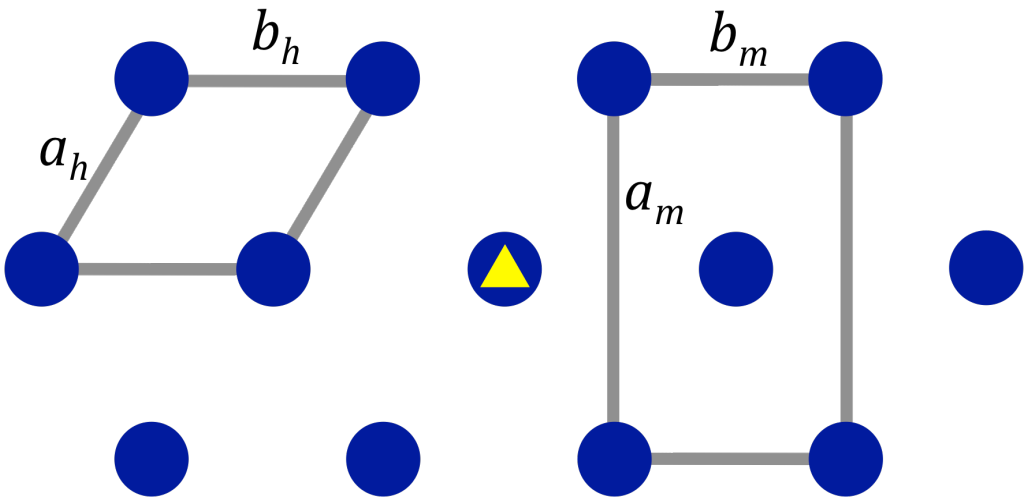

Figure 3-3: Schematic of the transition metal plane, indicating the difference between *R-3m* (h=hexagonal) and *C2/m* (m=monoclinic) symmetries by showing the relative orientation of the *a* and *b* lattice parameters. The yellow triangle indicates the 3-fold axis of the hexagonal structure.

The nanoscale dimensions of the primary particles in all samples (~40 nm diameter) cause significant peak broadening, which can mask smaller distortions in the peak profiles. Despite achieving good fits with the *R-3m* symmetry for the y=0 and y=0.05 samples, one can only truthfully refer to (at least) the Al-containing materials (y<0.1) as having a pseudo-hexagonal crystal structure. The changes in voltage profile and XAS spectra (discussed in Chapter 4) vary in a monotonic fashion with Al content. Thus, whether the observed structural distortion occurs at a specific Al-concentration or is a linearly varying change would require more sample data points and higher resolution diffraction profiles. The baseline material, which is well-fit using the *R-3m* structure, may also contain local-scale distortions that are not resolved on average here.

The results of Rietveld refinements of the as-synthesized $LiNi_{0.45}Mn_{0.45}Co_{0.1-y}Al_yO_2$ (y=0, 0.05, 0.1) powder samples are presented in Table 1. Figure 3-4 shows the collected data, calculated profile, and difference spectra for each material. The refinement of the y=0.1 sample was performed using *C2/m* symmetry, and the results are additionally presented after conversion to *R-3m* using geometric relations and averaging the converted *a* and *b* lattice parameters to generate a single a_{hex}.

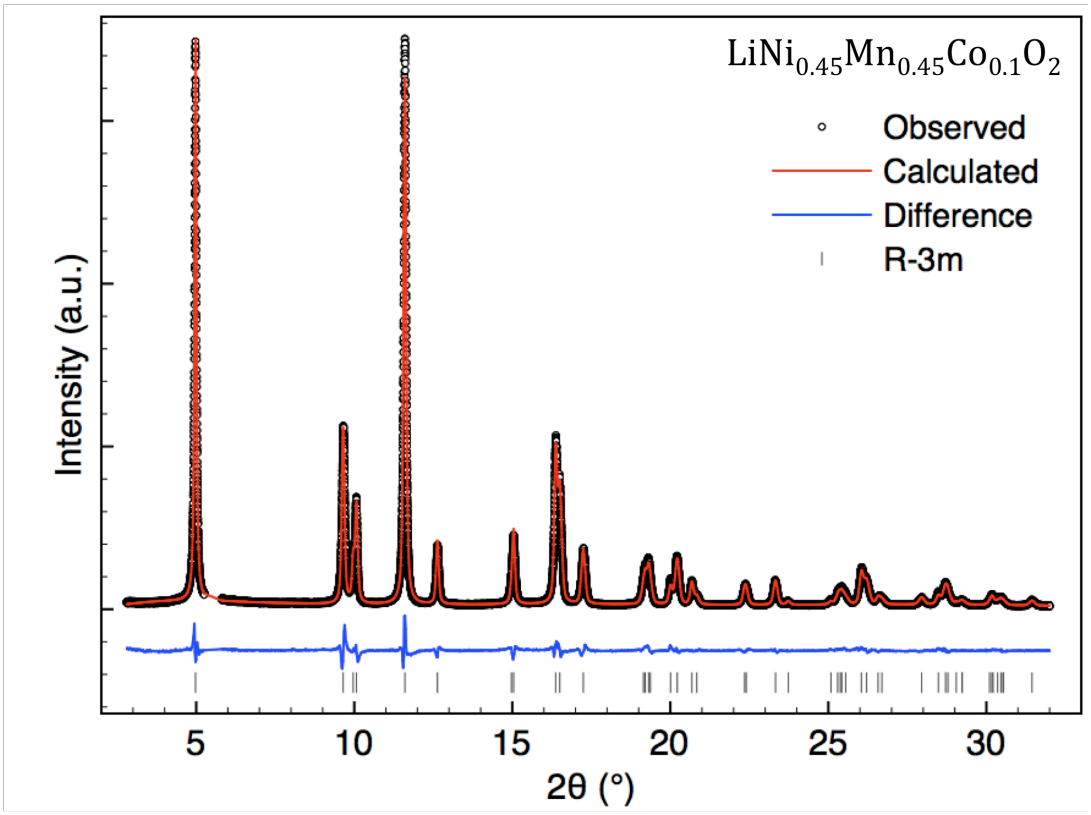

Figure 3-4: High-resolution XRD patterns and Rietveld refinements of the $LiNi_{0.45}Mn_{0.45}Co_{0.1-y}Al_yO_2$ ($0 \leq y \leq 0.1$) materials. The materials are indicated in the figures.

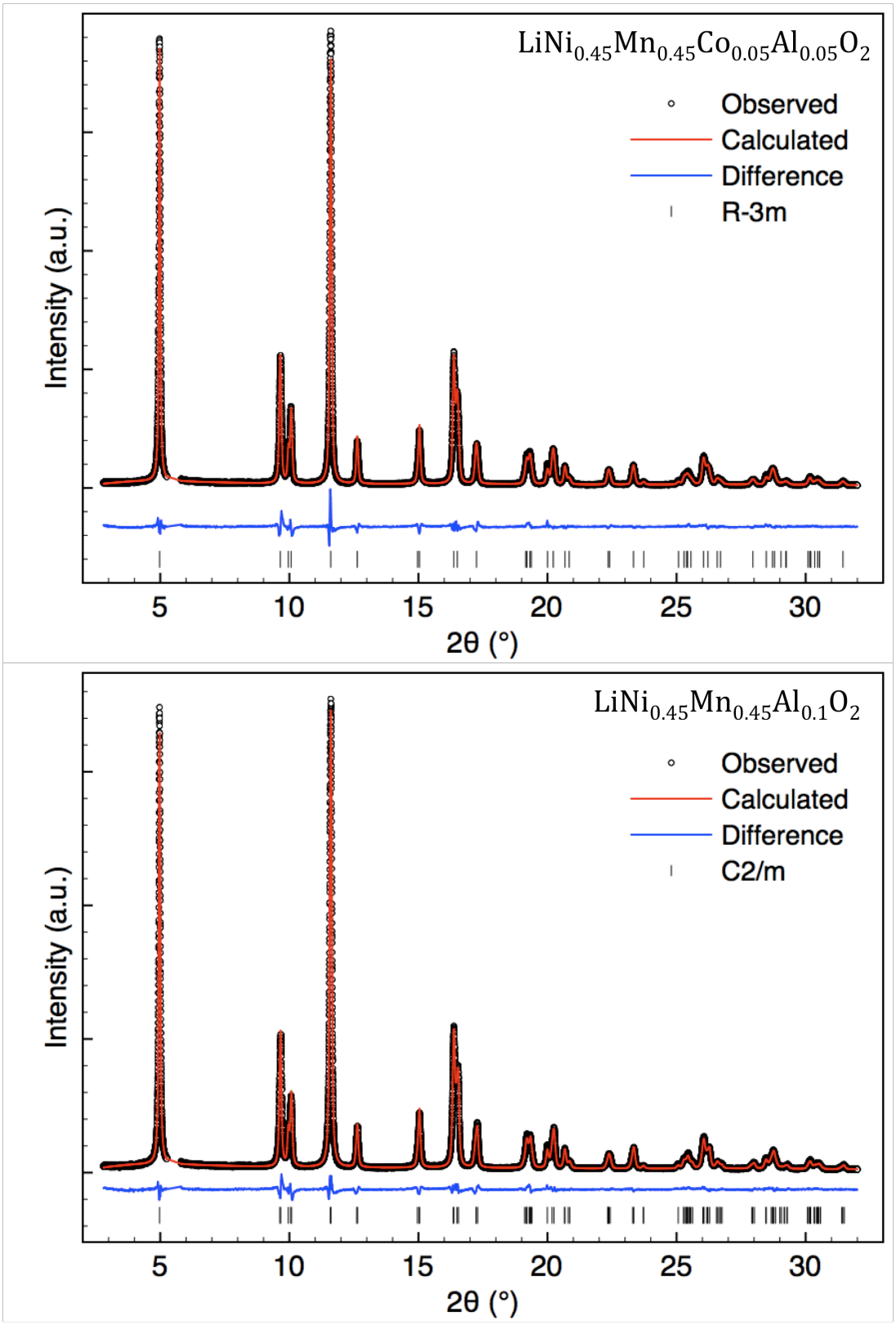

Figure 3-4 (cont'd): High-resolution XRD patterns and Rietveld refinements of the $LiNi_{0.45}Mn_{0.45}Co_{0.1-y}Al_yO_2$ ($0 \leq y \leq 0.1$) materials. The materials are indicated in the figures.

Table 3-1: Results of Rietveld refinement of high-resolution XRD patterns of as-synthesized $LiNi_{0.45}Mn_{0.45}Co_{0.1-y}Al_yO_2$ (y=0, 0.05, 0.1) powders

Al content (%)	Symmetry	a (Å)	b (Å)	c (Å)	β (°)	V (Å^3)	Ni_{Li} (%)	Rwp
0	*R-3m*	2.88045(3)	–	14.2772(2)	–	102.588(2)	9.06	8.19
5	*R-3m*	2.87964(2)	–	14.2812(2)	–	102.558(2)	9.49	7.96
10	*C2/m*	4.9984(1)	2.87200(5)	5.0447(1)	109.258(4)	68.368(2)	10.08	7.34
10	*R-3m*	2.8789	–	14.2873	–	102.552	10.08	–

The transition metal planes are composed of edge-sharing MO_6 octahedra, with M = Ni, Mn, Co, Al, or Li (antisite) ions at the octahedral centers. Depending on the central ion species and oxidation state, each octahedron has different equilibrium M-O bond distances. Their edge-sharing configuration therefore leads to an inherent octahedral strain within the transition metal layer. As mentioned above, layered-oxide systems such as $LiNi_{0.5}Mn_{0.5}O_2$ boast an ordered transition metal layer in the lowest-energy configuration, which arises due to size, magnetic, and electrostatic effects.[25] It is hypothesized that the incorporation of Al into the $LiNi_{0.45}Mn_{0.45}Co_{0.1-y}Al_yO_2$ lattice induces a further local-scale ordering of the metals within the transition metal layers. This ordering acts to relieve some of the inherent strain within the edge-sharing octahedral layer, and ultimately results in the observed symmetry-lowering distortion. This strain-relaxation hypothesis is supported by X-ray absorption spectroscopy results, discussed in detail in Chapter 4.

3.4 *In situ* X-ray Diffraction

The question remains how Al-substitution affects the materials during electrochemical operation. In this light, *in situ* x-ray diffraction is a powerful technique that is used to probe the structural evolution of the materials during battery cycling. Performing XRD *in situ* allows observation of the changes occurring during the charge and discharge processes of single cells, eliminating the uncertainties that could arise from the use of numerous *ex situ* samples to observe different SOC's. When carried out in transmission, as mentioned above, the material need only be exposed for <10 seconds to generate a diffraction ring pattern on a plate detector, which can subsequently be integrated to produce a linescan for analysis. Additionally, the short exposure time necessary for an adequate signal allows for the continuity of the electrochemical processes, as in real battery operation, without having to stop the cycling procedure and allow the cells to relax during a lengthy θ-2θ scan. Thus, essentially instantaneous snapshots of the material structure at any and all discreet stages of cycling can be generated to investigate the changes occurring over wide ranges of Li^+ content.

Figure 3-5 shows plots of potential vs. composition (x) for $Li/Li_xNi_{0.45}Mn_{0.45}Co_{0.1}O_2$ pouch cells electrochemically charged and discharged during the *in situ* XRD experiments. A similar regime was used for cells containing $Li_xNi_{0.45}Mn_{0.45}Co_{0.05}Al_{0.05}O_2$ cathodes. The points at which integrated linescans are analyzed for this work are specified on each plot; these correspond to 5% changes in composition for all cells, an interval considered small enough to capture the details of the structural changes occurring in the cathodes. The cells are not charged or cycled between voltage limits during *in situ* experiments because of the increased (and varying) amount of overpotential existent in the pouch cell construction compared to coin cells. Rather, charge limits are used. Unlike a coin cell, there is no internal spring to maintain pressure between the electrodes – the pouch cells are not optimized for electrochemical measurements, but instead to allow for X-ray transmission.

Figure 3-6 presents the full diffraction patterns showing the structural evolution of the $Li_xNi_{0.45}Mn_{0.45}Co_{0.05}Al_{0.05}O_2$ material during charge and discharge. The peaks are indexed in the *R-3m* symmetry, and the reflections due to the polyester pouch and

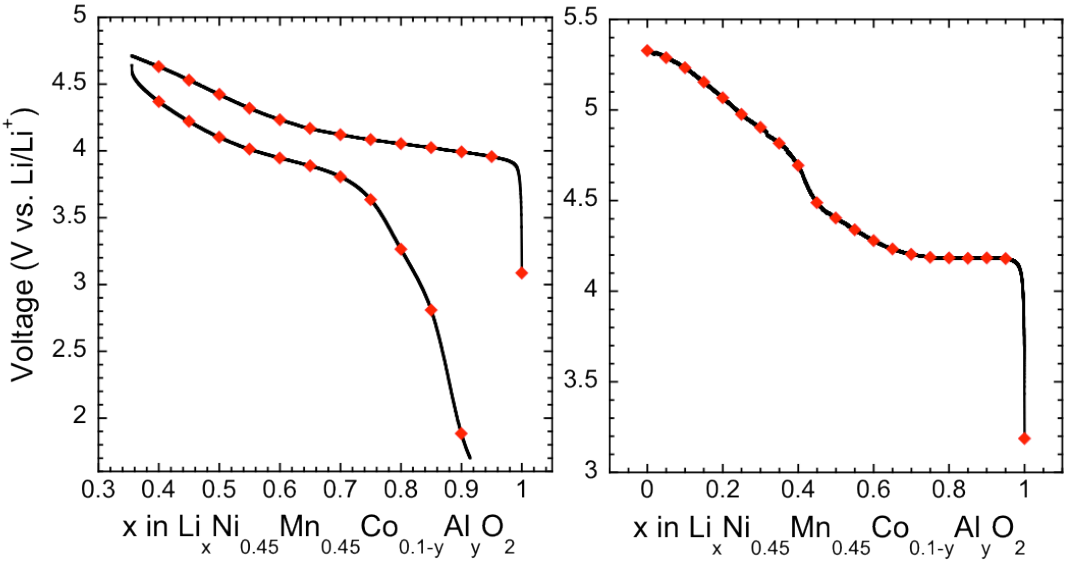

Figure 3-5: Voltage vs. Li-content for $LiNi_{0.45}Mn_{0.45}Co_{0.1-y}Al_yO_2$ (y=0) electrodes operated during *in situ* XRD measurements. The y=0.05 sample is similar. Indicated points correspond to the presented XRD patterns.

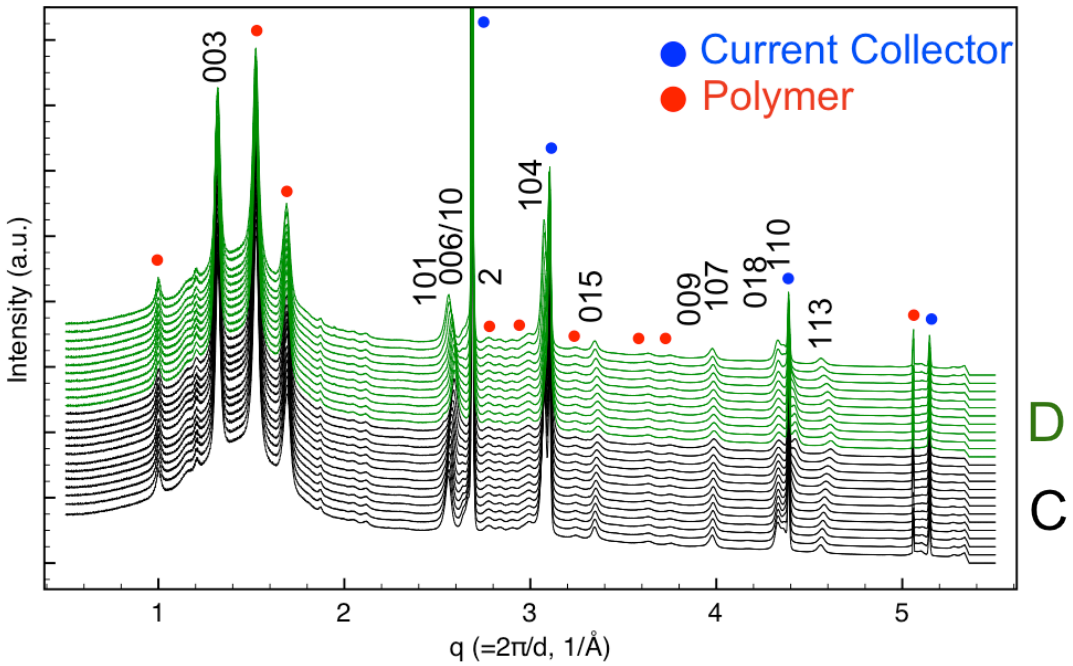

Figure 3-6: *In situ* XRD patterns for a $LiNi_{0.45}Mn_{0.45}Co_{0.1-y}Al_yO_2$ (y=0.05) electrode. Each pattern corresponds to a 5% change in Li-content during charge ("C," black) and discharge ("D," green). The numerous peaks from the additional cell components are indicated.

polypropylene separator, as well as the Al current collector are indicated. More detail is shown for three separate regions for each material during oxidation (black) and reduction (green) in Figure 3-7. Neither the y=0 (Fig. 3-7a) nor y=0.05 (Fig. 3-7b) materials undergo an observable phase change or generate any secondary phases, as evidenced by

the absence of new peaks at any point in the redox processes. The peak shifting due to changing lattice parameters as Li-ions are removed and reinserted can clearly be observed for both materials, as expected for layered oxide systems in which Li-ions reside within Van der Waal's gaps between MO_6 planes.

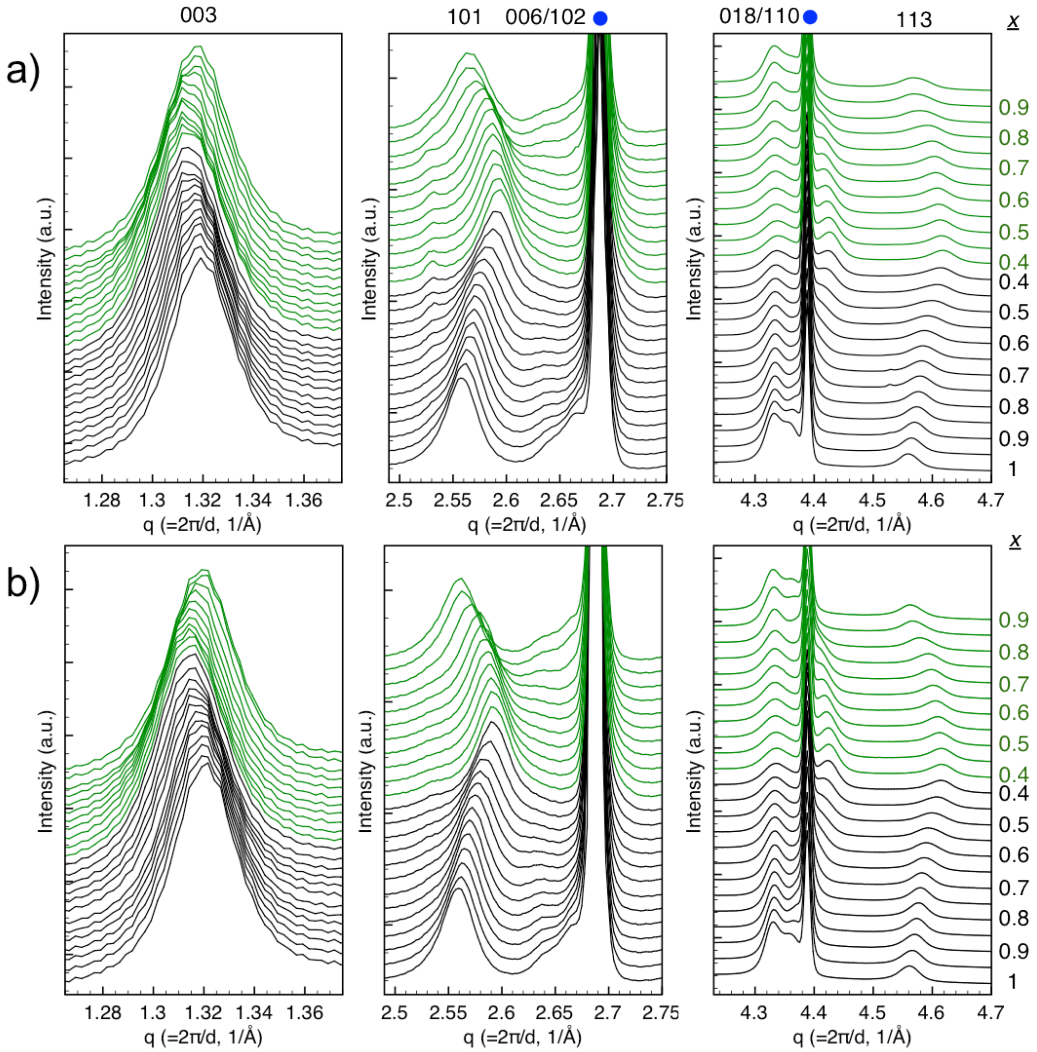

Figure 3-7: Selected regions of *in situ* XRD patterns for $Li_xNi_{0.45}Mn_{0.45}Co_{0.1-y}Al_yO_2$ electrode materials during cycling. a) y=0, b) y=0.05. Each pattern corresponds to a 5% change in Li-content during charge (black) and discharge (green). Values of *x* correspond to the Li-content in the materials.

Although they behave very similarly, the y=0.05 material can be seen to return closer to the fresh state at the end of discharge than the unsubstituted material, in terms of both peak position and shape (Fig. 3-8). There is significantly increased peak broadening in the fully discharged y=0 material, seen especially in the 101, 110, and 113 reflections, indicating either a larger degree of disorder or a decrease in particle size after the first charge/discharge cycle. The Li-content after discharge is similar for both materials, validating the comparison.

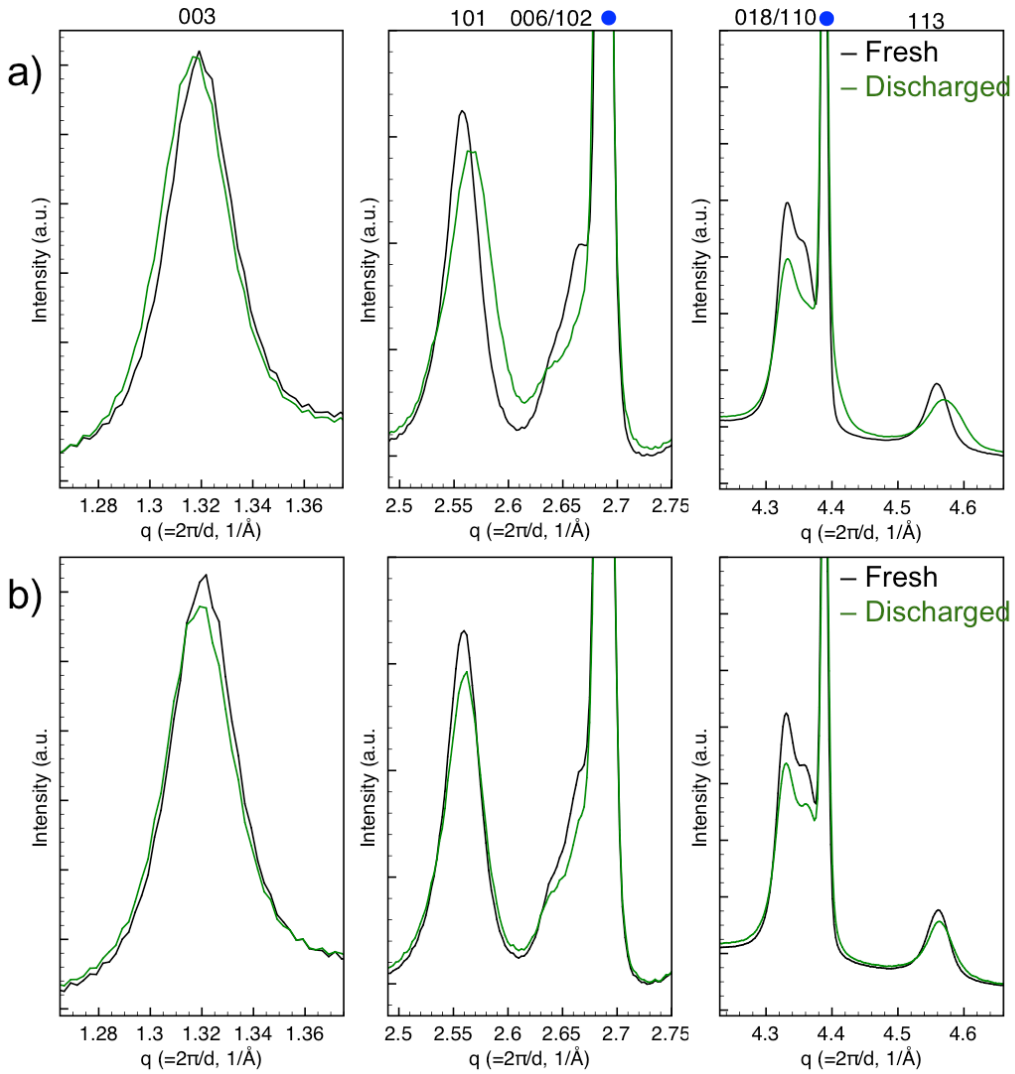

Figure 3-8: Selected regions of *in situ* XRD patterns for fresh (black) and fully discharged (green) $LiNi_{0.45}Mn_{0.45}Co_{0.1-y}Al_yO_2$ electrode materials for one cycle. a) y=0, b) y=0.05. The Al-substituted sample shown in (b) is more reversible.

Figure 3-9 presents integrated linescans (in increments of 5% Li^+ removal) for both cathode materials during complete Li-ion removal. Neither the y=0 nor y=0.05 materials undergo an observable phase change upon the full extraction of Li (nominally 100% SOC). This is consistent with previous observations on related NMC materials such as $Li_xNi_{0.4}Mn_{0.4}Co_{0.2}O_2$, which maintains the rhombohedral structure to about x=0.05.[26] However, significant structural evolution differences between $Li_xNi_{0.45}Mn_{0.45}Co_{0.1}O_2$ and $Li_xNi_{0.45}Mn_{0.45}Co_{0.05}Al_{0.05}O_2$ are apparent. The 003, 006/102, and 108 peaks move to higher q (smaller d-spacing) at the end of charge in the unsubstituted material compared to that containing Al. The shift of these peaks suggests a greater change of the structure in the basal direction (c_{hex}, indicated by the 003 position) within the parent compound at high states-of-charge. In contrast, there is much less change in c_{hex} for $Li_xNi_{0.45}Mn_{0.45}Co_{0.1-y}Al_yO_2$.

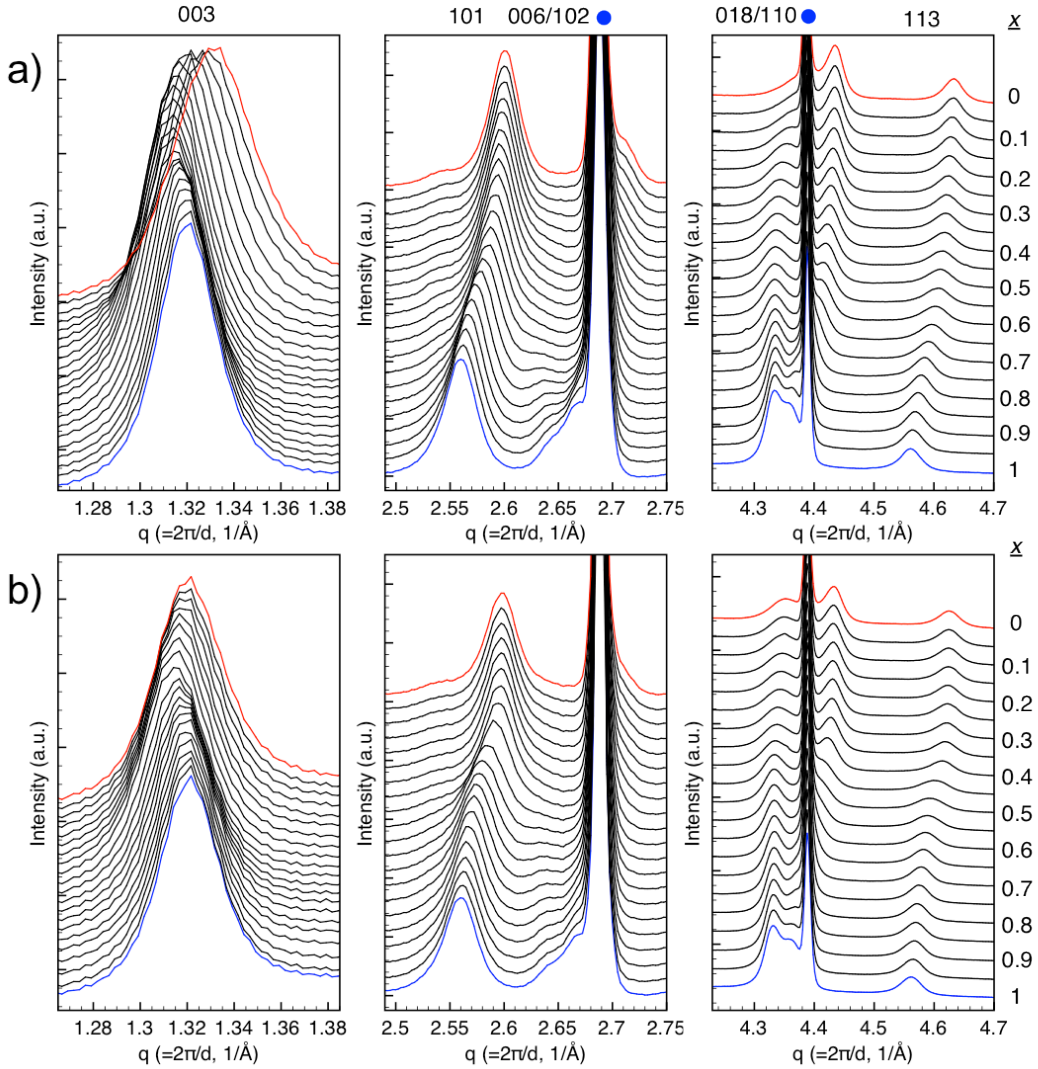

Figure 3-9: Selected regions of *in situ* XRD patterns for $Li_xNi_{0.45}Mn_{0.45}Co_{0.1-y}Al_yO_2$ electrode materials during full Li extraction. a) y=0, b) y=0.05. Each pattern corresponds to a 5% change in Li-content during charge from the fresh state (blue) to complete Li-deintercalation (red). Values of *x* correspond to the Li-content in the materials.

In the case of the Al-substituted sample, a current was passed for an amount of time corresponding to 100% Li^+ extraction, despite the fact that the Al^{3+} ion is redox inactive in this voltage range. Theoretical calculations, however, have suggested that Li^+ can be extracted from layered $LiAlO_2$, with oxidation occurring in the oxygen 2*p* band.[27] Most likely at high potentials, irreversible side reactions such as oxidation of the electrolyte, contribute to the charge capacity, so that not all of the lithium is actually removed from the $Li_xNi_{0.45}Mn_{0.45}Co_{0.05}Al_{0.05}O_2$ structure. Similarly, coulombic inefficiencies at high voltage may cause some uncertainty regarding the exact state-of-charge of the baseline $Li_{1-x}Ni_{0.45}Mn_{0.45}Co_{0.1}O_2$ electrode material.

The normalized changes in lattice parameters, calculated from the integrated linescans, are shown in Figures 3-10 and 3-11 as a function of Li-content in the materials. The results indicate that the presence of Al limits the changes in the *c*-parameter, and

somewhat in a_{hex}, during cycling of the material (Fig. 3-10). Moreover, Al-substitution is seen to significantly impede the contraction of the lattice along the basal direction (c-axis) at high states-of-charge, quantified in Figure 3-11b. For both samples the *c*-parameter initially increases up to x≈0.5, indicating an expansion along the layer-stacking direction of the oxide. At higher SOC (lower values of *x*), the *c*-parameter decreases. The "turnover" point – the charge state at which the lattice begins to contract along the axial direction – is shifted to a higher SOC for the Al-substituted material.

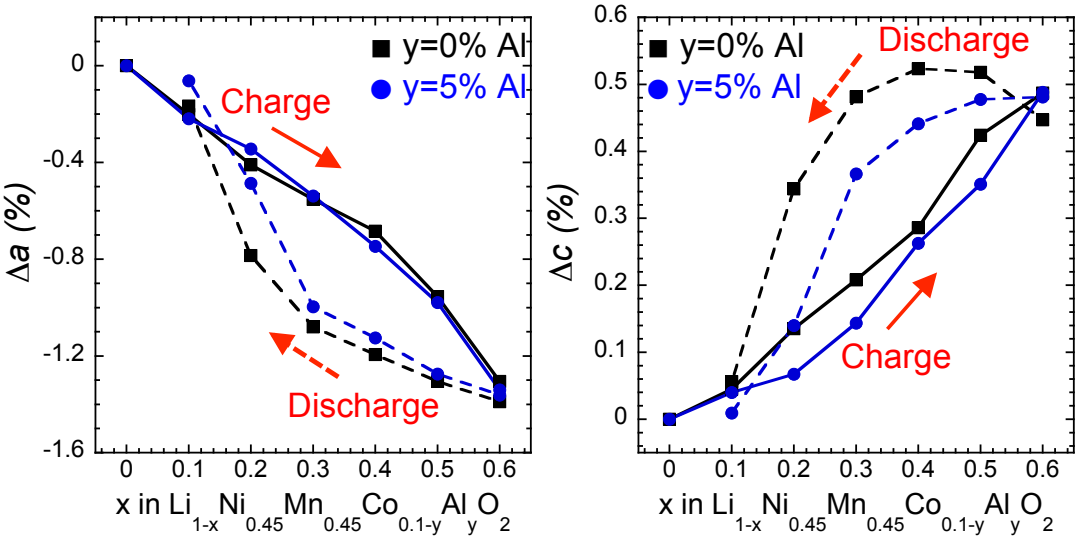

Figure 3-10: Relative chances in the calculated lattice parameters for the $Li_{1-x}Ni_{0.45}Mn_{0.45}Co_{0.1-y}Al_yO_2$ (y=0, 0.05) materials during cycling. More variation is observed in the Al-free (y=0) material.

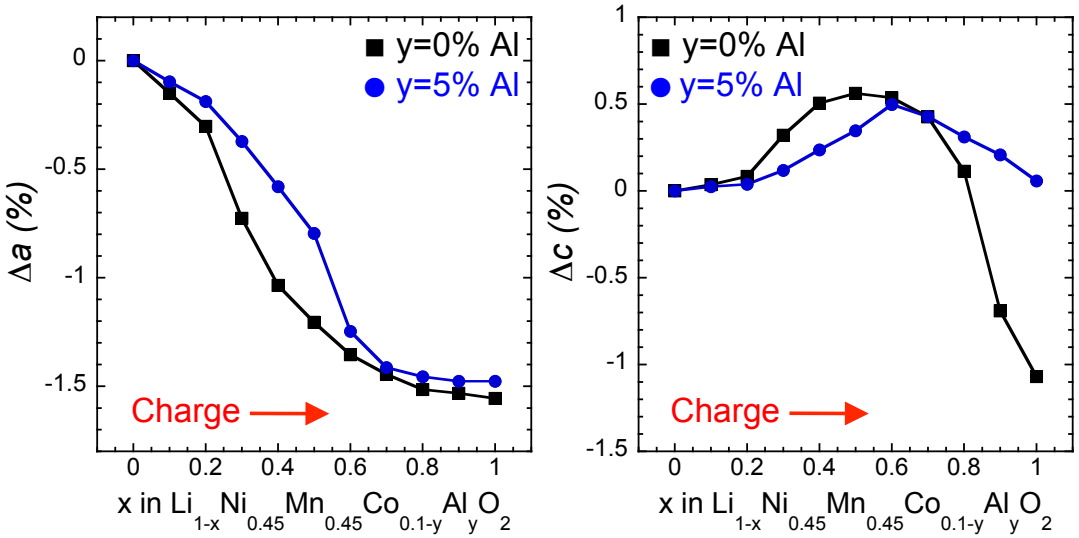

Figure 3-11: Relative chances in the calculated lattice parameters for the $Li_{1-x}Ni_{0.45}Mn_{0.45}Co_{0.1-y}Al_yO_2$ (y=0, 0.05) materials during full Li deintercalation. Al-substitution limits the structural changes observed at high states-of-charge.

The enhancement of the cycling stability of Al-containing materials was discussed in Chapter 2. Samples charged to 4.3 or 4.7 V during the cycling experiments displayed improved discharge capacities compared to the Al-free electrodes. A similar effect was not observed for a maximum voltage of 4.0 V. The 4.3 and 4.7 V bounds correspond to about 60 and 75% SOC, respectively, with the 4.0 V limit only cycles to a SOC of 40%. Comparing with the measured lattice parameters, it seems plausible that the delay in lattice contraction, owing to the structural stability conveyed by the Al, correlates with the improved electrochemical properties.

Note also that the changes in lattice parameters appear to have a slight dependence on cycling rate. The cells that were charged and discharged (to approximately x=0.35 in $Li_xNi_{0.45}Mn_{0.45}Co_{0.1-y}Al_yO_2$) show a smaller divergence between the two materials (y=0 and y=0.05) during the first charge region compared to the behavior of the materials during the full charge experiment over the same composition range. In these latter samples, the electrochemical Li-extraction was performed at a higher rate (~C/13) than those in the cycling experiment (~C/21). Though no significant difference in the delivered discharge capacities as a function of rate was observed between the materials with and without Al (Fig. 2-9b), a more rapid structural change upon charge is observed for the unsubstituted material as the rate is slightly increased in this study.

3.5 High Resolution XRD of Cycled Electrodes

High-resolution XRD spectra for fresh and cycled $LiNi_{0.45}Mn_{0.45}Co_{0.1-y}Al_yO_2$ (y=0, 0.05, 0.1) materials are shown in Figure 3-12. The samples were charged and discharged in coin cells between 2-4.3V at 15 mA g^{-1} for 20 and 50 cycles; the electrodes were harvested in the fully discharged state and measured *ex situ*. For comparison, the fresh samples measured were also produced from fresh composite electrodes, as opposed to the powder samples discussed at the beginning of this chapter.

Results from Rietveld refinements are presented in Table 2. No new peaks indicating any secondary phase growth are observed with cycling. All samples do, however, show a relative expansion of all lattice parameters with cycle number. This enlargement is clearly observed by peak shifts to lower 2θ angles, as seen in Figure 3-13 for the $LiNi_{0.45}Mn_{0.45}Co_{0.1}O_2$ baseline material. The behavior is similar for the y=0.05 and y=0.1 Al-substituted samples. Although some of the shifts can possibly be explained by an incomplete re-lithiation of the materials upon discharge (such as 003), the lower-angle shift of many others (for example, the 101, 104, and 113 reflections) cannot. In these cases, the peak shift from cycling is in the 2θ-direction opposite to that seen above during the *in situ* measurement of the electrode materials, indicating a structural change that is not simply due to differing Li-content. Additionally, the refinements suggest a decrease in the Ni_{Li} antisite concentration of all samples due to cycling. The relative changes in lattice parameters are minimized, and the decrease in antisite concentration is highest, in the y=0.05 sample, which displays the best cycling performance.

It can clearly be observed that Al substitution imparts a beneficial structural effect on the $LiNi_{0.45}Mn_{0.45}Co_{0.1-y}Al_yO_2$ materials. High resolution XRD of fresh powder materials indicates a lowering of the crystal symmetry with higher Al-content. Most

likely this results from metal ordering within the transition metal layers. *In situ* XRD shows Al-substitution limits the changes in lattice parameters, especially along the layered direction, during electrochemical charging and discharging. The point at which the expanding *c*-axis begins to contract – the "turnover" point – is pushed to lower Li-content (higher SOC) in the Al-substituted samples. Upon extended cycling, there is a slight structural change in all materials that manifests in an expansion of all the lattice parameters. Additionally, the Ni/Li antisite concentration decreases upon extended cycling. Chapter 4 will explore the local structure of the $LiNi_{0.45}Mn_{0.45}Co_{0.1-y}Al_yO_2$ materials using X-ray absorption spectroscopy (XAS).

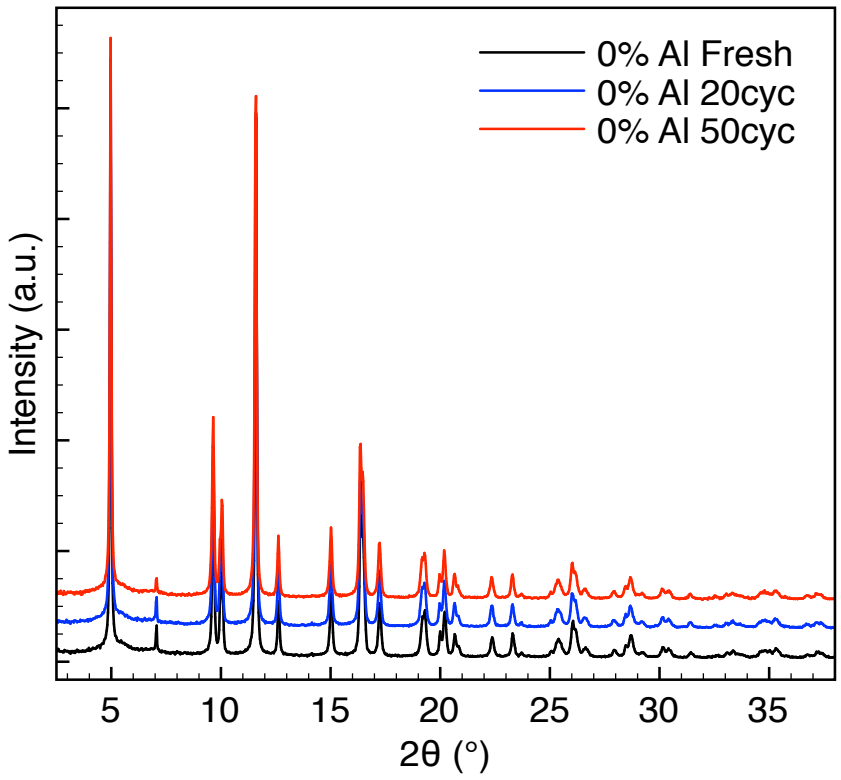

Figure 3-12: High-resolution XRD patterns of fresh and cycled $LiNi_{0.45}Mn_{0.45}Co_{0.1-y}Al_yO_2$ (y=0, 0.05, 0.1) electrodes. The Al-concentrations are indicated in the figures. Cycled electrodes were recovered from coin cells and measured *ex situ*. The small peak at ~7° 2θ is due to graphite.

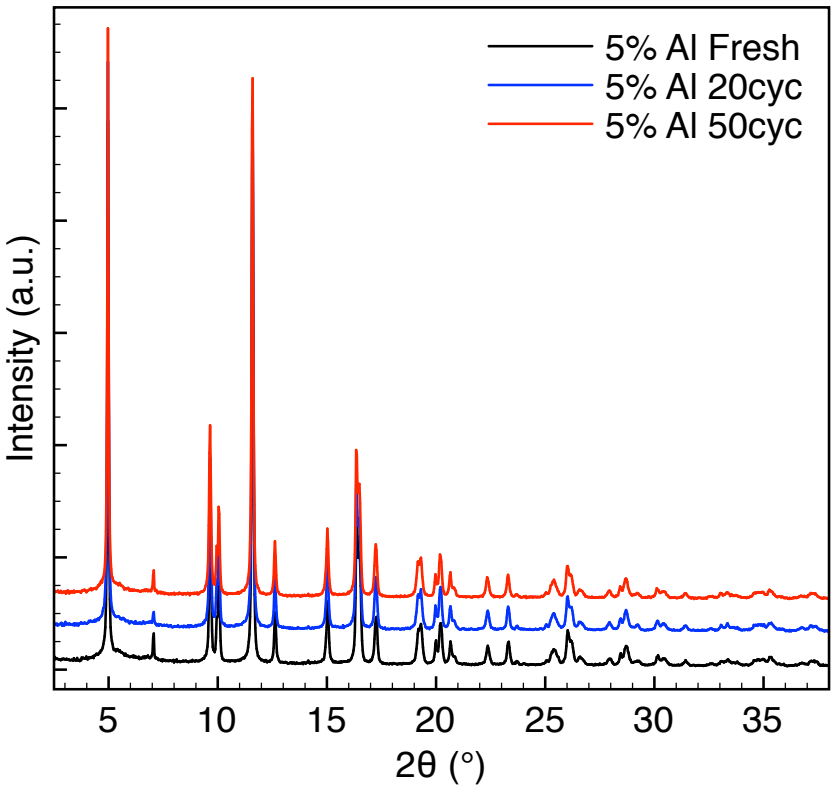

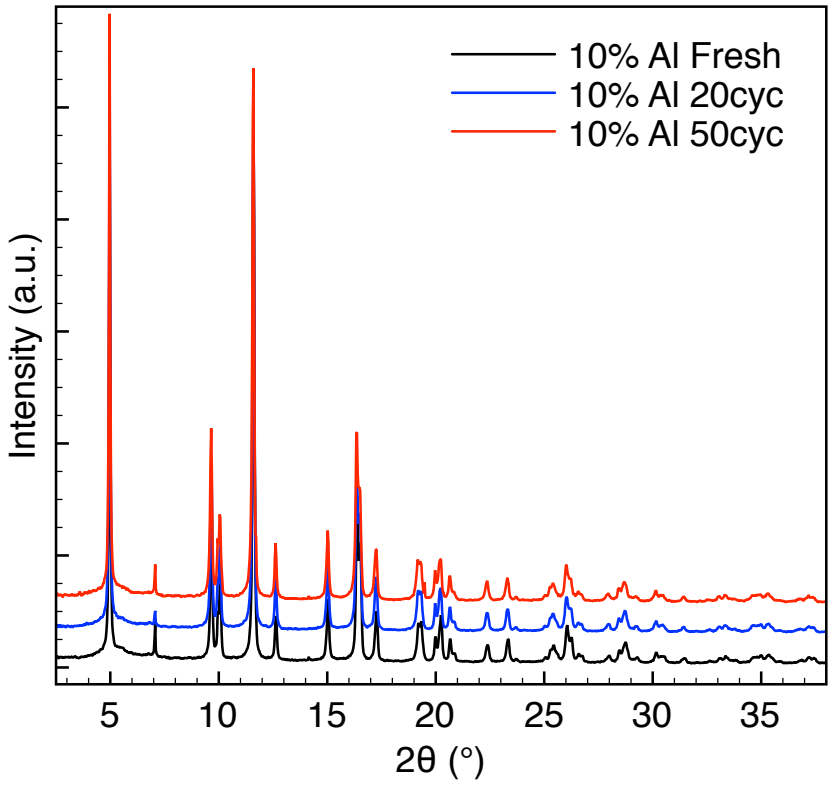

Figure 3-12 (cont'd): High-resolution XRD patterns of fresh and cycled $LiNi_{0.45}Mn_{0.45}Co_{0.1-y}Al_yO_2$ (y=0, 0.05, 0.1) electrodes. The Al-concentrations are indicated in the figures. Cycled electrodes were recovered from coin cells and measured *ex situ*. The small peak at ~7° 2θ is due to graphite.

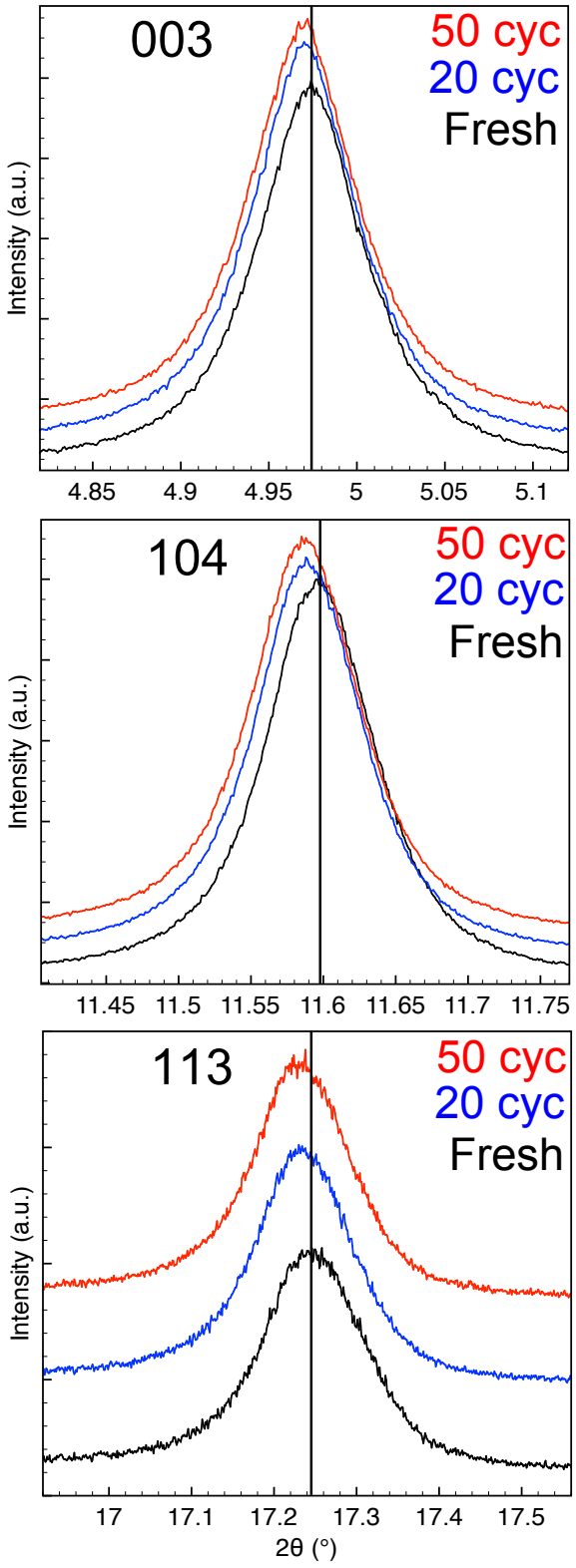

Figure 3-13: Magnified regions of the $LiNi_{0.45}Mn_{0.45}Co_{0.1-y}Al_yO_2$ (y=0) XRD patterns showing the shift of all peaks to lower 2θ with cycling. All materials showed a similar trend.

Table 3-2: Results of Rietveld refinement of high-resolution XRD patterns of the fresh and cycled $LiNi_{0.45}Mn_{0.45}Co_{0.1-y}Al_yO_2$ (y=0, 0.05, 0.1) electrodes

Al content (%)	# Cycles	Symmetry	a (Å)	b (Å)	c (Å)	β (°)	Ni_{Li} (%)	Rwp	Rp	Δa (%)	Δb (%)	Δc (%)
0	0	R-3m	2.88080(3)	-	14.2771(2)	-	9.17	7.98	6.17	0	-	0
0	20	R-3m	2.88274(3)	-	14.2884(2)	-	8.3	7.92	6.1	0.067	-	0.079
0	50	R-3m	2.88331(3)	-	14.2923(2)	-	8.36	7.73	5.95	0.087	-	0.106
5	0	R-3m	2.87994(3)	-	14.2810(2)	-	9.62	7.98	6.26	0	-	0
5	20	R-3m	2.88126(3)	-	14.2894(2)	-	8.48	7.73	6.03	0.046	-	0.058
5	50	R-3m	2.88190(3)	-	14.2917(2)	-	8.37	7.92	6.15	0.068	-	0.075
10	0	C2/m	4.9991(1)	2.87234(5)	5.0449(1)	109.259(4)	10.2	7.38	5.66	0	0	0
10	20	C2/m	5.0043(1)	2.87503(6)	5.0490(1)	109.267(3)	9.23	7.55	5.66	0.102	0.094	0.082
10	50	C2/m	5.0084(1)	2.87689(7)	5.0511(1)	109.282(3)	9.3	7.78	5.77	0.185	0.159	0.123

3.6 References

[1] J. Liu, M. Kunz, K. Chen, N. Tamura, T. J. Richardson. *J. Phys. Chem. Lett.* **2010,** *1,* 2120.

[2] M. L. Calzada et. al. *Nanotechnology,* **2007,** *18,* 375603.

[3] J. Guzman, C. Boswell-Koller, J. Beeman, K. Bustillo, T. Conry, O. Dubon, W. Hansen, A. Levander, C. Liao, R. Lieten, C. Sawyer, M. Sherburne, S. Shin, P. Stone, M. Watanabe, K. Yu, J Ager, D. Chrzan, E. Haller. *Appl. Phys. Lett.* **2011,** *98,* 193101.

[4] M. Balasubramanian et al. *J. Power Sources,* **2001,** *92,* 1.

[5] C. Johnson et al. *Chem. Mater.* **2003,** *15,* 2313.

[6] N. Bramnik et al. *Electrochem. Solid State Lett.* **2008,** *11,* A89.

[7] S. Kang et al. *Electrochimica Acta*, **2008,** *54,* 684.

[8] D. E. Cox, B. H. Toby, M. M. Eddy. *Australian Journal of Physics*, **1988,** *41,* 117.

[9] P. Lee, et al. *J. Synch. Rad.* **2008,** *15,* 427.

[10] 11-BM website. http://11bm.xor.aps.anl.gov. Accessed 12/1/11.

[11] A.C. Larson, R.B. Von Dreele, "General Structure Analysis System (GSAS)," *Los Alamos National Laboratory Report LAUR 86-748*, **1994**.

[12] B.H. Toby. *J. Appl. Cryst.* **2001,** *34,* 210.

[13] J. Lande, D. Bronfenbrenner, A. Mehta, S. Webb. "The Area Diffraction Machine." http://code.google.com/p/areadiffractionmachine/

[14] R. D. Shannon. *Acta Cryst.* **1976,** *32,* 751.

[15] A. Manthiram, J. B. Goodenough. *J. Power Sources,* **1989,** *26,* 403.

[16] M. S. Whittingham. *Chem. Rev.* **2004,** *104,* 4271.

[17] J. Wilcox, E. E. Rodriguez, M. M. Doeff. *J. Electrochem. Soc.* **2009,** *156,* A1011.

[18] M. Thackeray et al. *J. Mater. Chem.* **2007,** *17,* 3112.

[19] N. Yabuuchi et al. *J. Electrochem. Soc.* **2007,** *154,* A566.

[20] W. Yoon et al. *Electrochem. Solid State Lett.* **2004,** *7,* A53.

[21] J. Bréger et al. *J. Amer. Chem. Soc.* **2005,** *127,* 7529.

[22] J. Bréger et al. *Chem. Mater.* **2006**, *18*, 4768.

[23] W. Yoon et al. *Chem. Mater.* **2003**, *15*, 3161.

[24] P. Stephens. *J. Appl. Cryst.* **1999,** *32,* 281.

[25] A. Van der Ven, G. Ceder. *Electrochem Commun*. **2004**, *6*, 1045.

[26] M. Ma, N. Chernova, B. Toby, P. Zavalij, M. S. Whittingham. *J. Power Sources,* **2007**, *165*, 517.

[27] Ceder et al. *Nature*, **1998,** *392,* 694.

Chapter 4: X-ray Absorption Spectroscopy Studies

4.1 Introduction

Overview

X-ray absorption spectroscopy (XAS) is a powerful local structure characterization technique that is independent of a material's long-range order. Thus, it is equally appropriate for the characterization of crystalline materials, gaseous substances, adsorbed monolayer films, and almost all samples in between. XAS involves the analysis of the x-ray absorption coefficient (μ(E), eqn. 4-1) as a function of energy:

$$\mu(E) = \frac{-d\ln I(E)}{dx} \qquad \text{(Eqn. 4-1)}$$

The absorption coefficient is a measure of the attenuation of an incident x-ray beam per unit distance through a material, or equivalently, the probability that an x-ray is absorbed. In XAS, the absorption coefficient is measured through energy ranges about characteristic absorption edges – the step-like jumps at specific energies – of the elements in the sample under investigation. The energy positions of the absorption edges depend on atomic number, as seen in Figure 4-1, making XAS an element-specific technique.

The x-ray absorption event is the excitation of a core electron into a higher energy unoccupied bound state above the Fermi level or into the continuum, which leaves behind a core hole. The incident X-ray must therefore have an energy greater than or equal to the binding energy of the core electron in order for absorption to occur. The initial ground state of the excited photoelectron indicates the absorption edge being probed: XAS studies commonly measure the K (n=1), or L (n=2) edges, where n is the principle quantum number. Lower-energy electrons closer to the nucleus (like those in the 1s orbital) have a larger binding energy, and thus require a higher energy photon to generate a photoelectron. The K and/or L edges of almost all materials lie at energies that are most easily accessible using today's synchrotron sources.

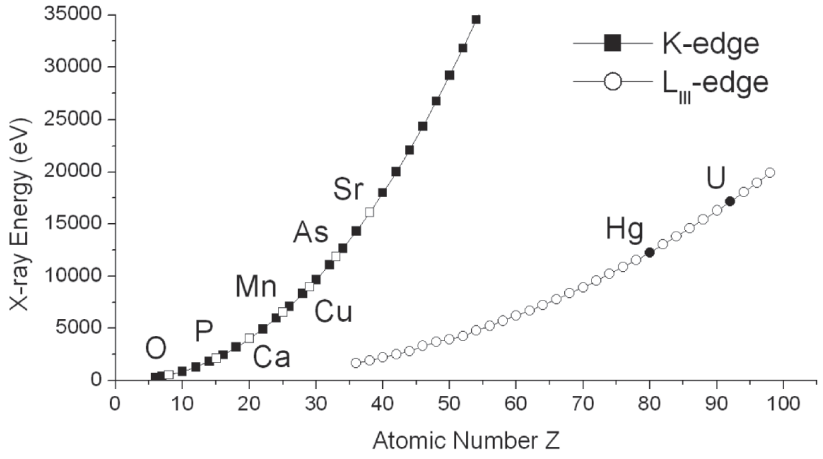

Figure 4-1: X-ray absorption edge energies scale with atomic number, *Z*.[5]

An example absorption spectrum μ(E) vs. E (Fe K-edge in FeO sample) is shown in Figure 4-2. The spectrum can be divided into two separate regions, each with abundant information about the material under study. Though the mechanistic origin is the same, the distinction makes interpretation more straightforward. As indicated in the figure, the region containing the actual absorption edge, and extending out ~30-50 eV beyond, is termed the X-ray Absorption Near Edge Structure (XANES). The edge position indicates the ionization threshold to continuum states. From the XANES portion, information about the oxidation state and coordination chemistry of the absorber can be inferred.

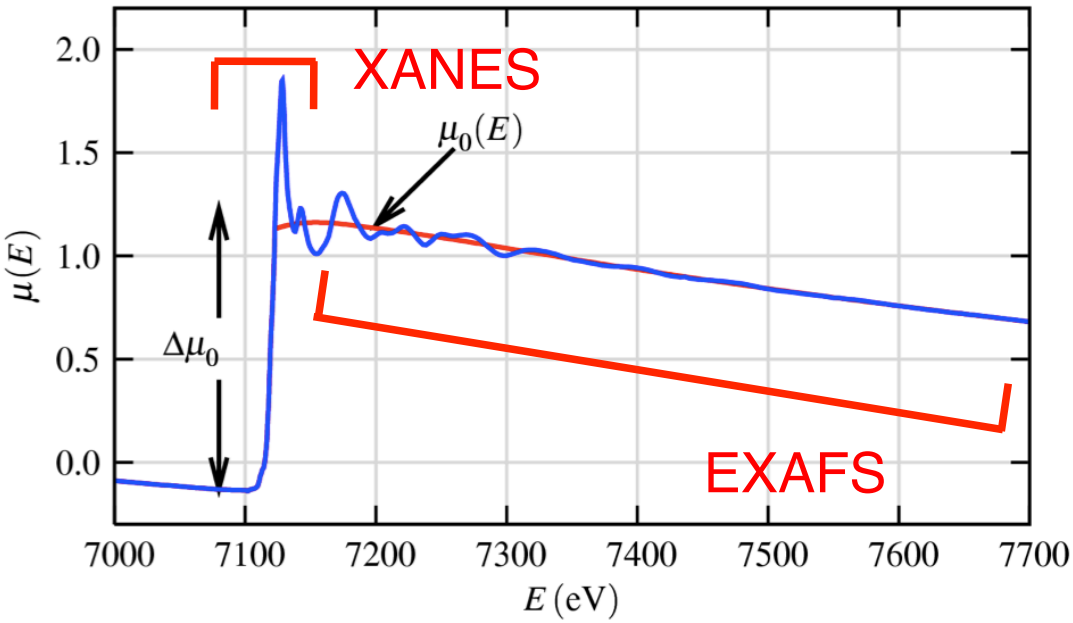

Figure 4-2: Example XAS spectra (FeO) showing the XANES and EXAFS regions.[2] The peak in the absorption edge around 7112 eV is termed the "white line."

The most intense features in the XANES are due to electric dipole allowed transitions, those in which angular momentum is conserved ($\Delta\ell = \pm 1$). For the Fe K-edge shown, the excitation describes a 1s→4p electronic transition. The energy position of the absorption edge provides a measure of the binding energy of the core electron. A higher oxidation state of the element being probed will result in a shift of the edge to higher energies, on the order of a few eV, due to a decreased screening effect. Some interpretations consider the shift a second order effect of a change in bond distance due to an oxidation change.[1] In oxides and other ionic solids, a "white line" is often observed, which refers to a peak at the absorption edge (as in Figure 4-2). This represents a photoelectron excitation into a bound state above the Fermi level, such as exists in many oxides and insulating crystals. Metals, on the other hand, with delocalized conduction band states above the Fermi level, do not show this feature.

Many materials, such as metal oxides, display features at energies below the characteristic absorption edges, termed "pre-edge" peaks or features. These peaks often arise from "dipole-forbidden" electronic transitions to empty bound states, such as 1s-3d transitions ($\Delta\ell = 0$). They can arise from 3d-4p orbital mixing due to a non-

centrosymmetric environment around the absorbing ion, such as in a tetrahedral or distorted octahedral coordination. Pure quadrupole 1s→3d transitions ($\Delta\ell = 0, \pm 2$) are also possible, but the transition probability is about 2 orders of magnitude smaller.[2,3] The pre-edge features can therefore be strongly indicative of the surrounding environment of the absorbing atom. Figure 4-3, for instance, shows Ti K-edges for two compounds containing Ti^{4+}, illustrating the difference in pre-edge between octahedral and tetrahedral coordination.

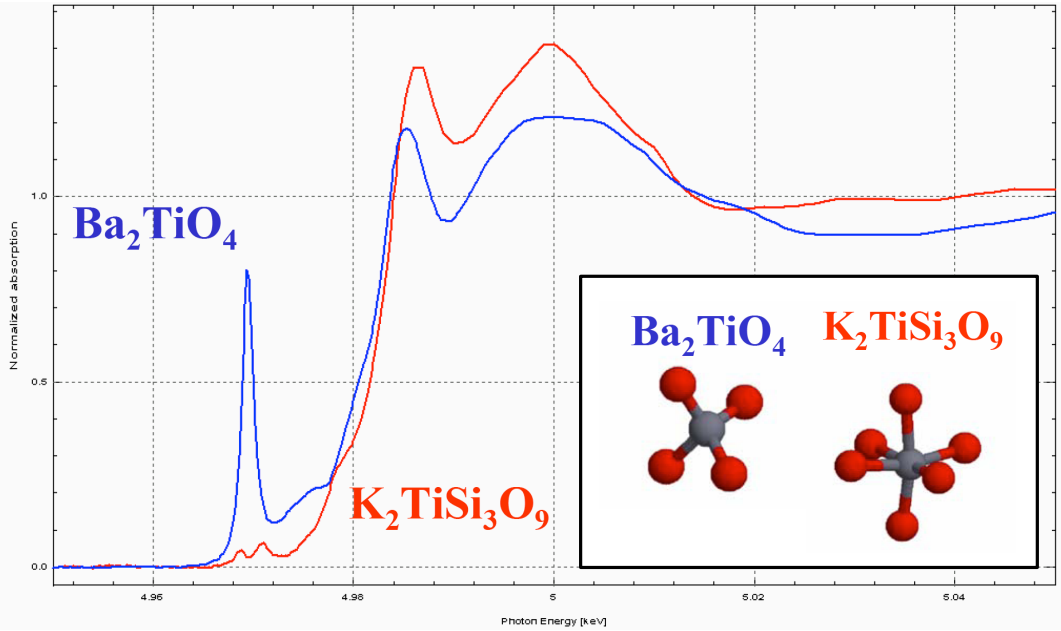

Figure 4-3: The surrounding environment of an absorbing element has a significant effect on the XANES edge character. The difference between tetrahedral Ti^{4+} (in Ba_2TiO_4) and octahedral Ti^{4+} (in $K_2TiSi_3O_9$) is shown here for the Ti K-edge.[3]

Beyond the XANES, the higher energy portion of a material's absorption spectra is the Extended X-ray Absorption Fine Structure (EXAFS) region. At these energies, x-ray absorption produces a photoelectron that can propagate through the material. The fine structure describes the oscillatory features of the absorption coefficient, appearing as "wiggles" in the absorption spectra as a function of energy. These wiggles, as explained in detail in the following paragraphs, result from the scattering of the generated photoelectron waves from the surrounding atoms. The EXAFS, $\chi(E)$, are the modulations added on top of the smoothly varying behavior of the absorption coefficient of an isolated atom. As a function of energy, the EXAFS can be described as:

$$\chi(E) = \frac{\mu(E) - \mu_0(E)}{\Delta\mu_0(E)} \qquad \text{(Eqn. 4-2)}$$

where $\mu_0(E)$ is the smooth background describing an isolated atom and $\Delta\mu_0(E)$ is the jump in absorption due to the characteristic transition, measured at the edge step. These are depicted in Figure 4-2.[4] Proper analysis of the EXAFS allows quantitative local structural information to be determined, including bond distances, coordination numbers and identities, as well as local mean-square disorder of the absorbing atom environment.

Taken together, the fine structure throughout the entire absorption spectrum, including both the XANES and EXAFS regions, is referred to as XAFS.

The oscillating structure of the X-ray absorption behavior results from scattering of the photoelectron from neighboring atoms. The effect depends on the wave-nature of the photoelectron, and thus it is convenient to describe it in terms of the wave number, k:

$$k = \sqrt{\frac{2m_e(E - E_0)}{\hbar^2}} \qquad \text{(Eqn. 4-3)}$$

where E is the incident photon energy, E_0 is the absorption edge (binding) energy, and m_e is the mass of the electron. The generated photoelectron propagates as a spherical wave from the absorbing atom. Treating the neighboring atoms as point scatterers, the interaction of the photoelectron wave with the surrounding neighbors will produce scattered waves that also propagate in all directions, including back towards the absorbing atom. The backscattered photoelectron waves constructively or destructively interfere with the outgoing photoelectron wavefunction *at the absorbing atom*, schematically shown in Figure 4-4 for various measurement points.[5] The interference due to scattering from neighboring atoms modifies the transition probability, and thus the absorption coefficient, leading to the observed EXAFS.

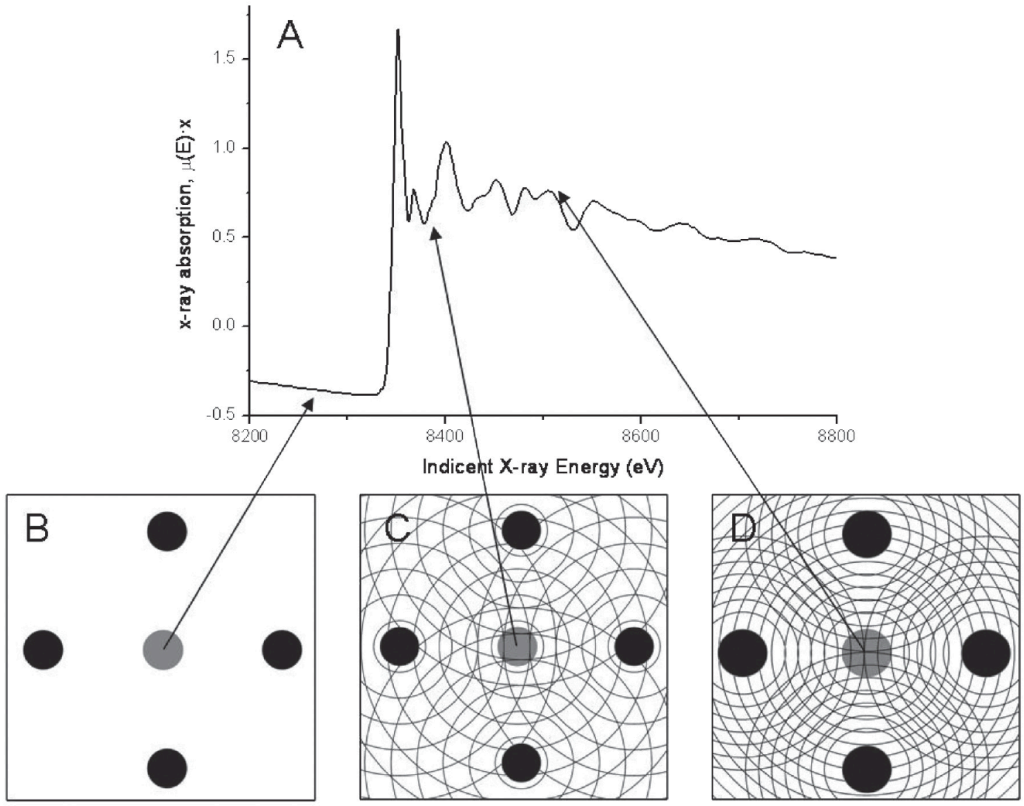

Figure 4-4: Schematic of the scattered photoelectron interfering at the absorbing atom for different energies: B) below, C) just above, and D) far above the absorption edge. The absorbing site is shown in grey, surrounding atoms in black. The energy dependence of the photoelectron wavelength is illustrated. The spectrum in (A) is the Ni K-edge from a NiO sample.[5]

Specifically, the transition probability can be described with Fermi's Golden Rule:

$$\mu \propto \left|\langle f|H|i\rangle\right|^2 \qquad \text{(Eqn. 4-4)}$$

where $|i\rangle$ and $|f\rangle$ are the initial and final states, respectively, and H is an interaction term. Compared to the isolated atom process, the initial state – the core electron – is unaltered by the surrounding atoms. The dipole approximation is valid for deep-core excitations, such that the interaction term becomes $H = e^{ikr} \approx 1$.[6] The final state, however, consists not only of the outgoing photoelectron, but the incoming backscattered waves at the absorbing atom. This adds a perturbation term ($|\Delta f\rangle$) to the isolated atom case ($|f_0\rangle$), such that it becomes $|f_0 + \Delta f\rangle$.[4,6]

Considering separately this modulation in the transition probability on top of the behavior of the bare atom, Sayers, Stern, and Lytle derived an expression for the oscillatory EXAFS structure, $\chi(k)$, based on a model treating the surrounding atoms as point scatters of the propagating photoelectron:[6,7,8,9]

$$\chi(k) = \sum_j \frac{S_0^2 N_j f_j(k) e^{\frac{-2R_j}{\lambda(k)}} e^{-2k^2\sigma_j^2}}{kR_j^2} \sin\left(2kR_j + \varphi_j(k)\right) \qquad \text{(Eqn. 4-5)}$$

where the summation is taken over each coordination shell, j, composed of similar atoms at approximately the same distance from the central absorbing atom. Here, N is the number of coordinating atoms within the shell, j, S_0^2 is the passive electron reduction factor, $f_j(k)$ is the effective scattering amplitude, $\lambda(k)$ is the photoelectron mean-free-path, σ_j^2 is the mean-square displacement between the absorbing atom and those in a coordination shell, and $\varphi(k)$ is a phase shift of the scattered photoelectron. Both $f_j(k)$ and $\varphi(k)$ depend on atomic number Z of the scattering atom. S_0^2, also known as the amplitude reduction factor, accounts for the relaxation of the remaining electrons in the absorbing atom due to the core hole, and is usually taken as a constant $0.7<S_0^2<1$.[10]

As seen above, the fine structure is a sum of sine waves with a dependence on scatterer distance (R) from the absorbing site. A Fourier transform of the $\chi(k)$ data isolates the contribution of signals from different scattering shells. This in turn generates an effective radial distribution function (RDF) showing different coordination shells. [Note, however, that the EXAFS Fourier transform is *not* an RDF. Unlike a true RDF, the peak positions (R) are not at the exact bond distances due to phase shifts depending on both the absorber and the scatterer identities, the peak amplitudes have a dependence on the mean-free-path and other variables, not just coordination number, and multiple scattering effects can produce features not observed in an RDF.] The well-developed mathematical description of the scattering that generates EXAFS allows the bond distances, neighbor identities, and coordination numbers to be quantitatively determined by modeling the $\chi(k)$ or more often (selected regions of) the Fourier transformed data. These capabilities, and the element-selectivity of the technique, make XAS a prodigious probe of the local structural environment, and permit the determination of unknown

structures. The technique has been made more widely available due to the development of computer programs and interfaces to aid analysis.[11] Many utilize FEFF code to calculate the complex scattering function $f_j(k)$ and mean-free-paths $\lambda(k)$ necessary to produce theoretical spectra *ab initio*.[12,13,14,15]

A similar understanding of the XANES spectra is not as mature. In regions just past (and at) the absorption edge, the excited photoelectron does not have sufficient kinetic energy such that interactions with the core-hole can be considered negligible. The EXAFS equation breaks down at low k due to the $1/k$ term and the increase in the mean-free-path of the photoelectron at very low k.[4,15] Additionally, the XANES spectra features arise mainly due to multiple scattering from the nearest neighbors, making them more difficult to calculate. Contributions from additional electronic transitions also exist, such as shakedown or shakeup effects. In these cases, absorption occurs at slightly lower energy than the continuum threshold, with concurrent charge transfer to the absorbing atom from the ligand ("ligand-to-metal charge transfer," LMCT).[16,17] A well-developed mathematical model notwithstanding, the XANES region provides substantial information about the surrounding environment and electronic structure of the absorbing atom. The information gives significant insight into the coordination chemistry of the materials under study, and a more descriptive theory continues to be developed today.

Brief History

Although the fine structure in absorption spectra had been observed as far back as the 1920s, the modern physical interpretation of the phenomenon and its use as a structure-determination tool took many decades to develop. Ralph Kronig published the first theoretical description of the X-ray absorption fine structure for crystalline materials in 1931 and 1932.[18,19] It was based on a three-dimensional expression of the then-recent Kronig-Penny model, which described allowed and forbidden energy states in a 1-dimensional atomic lattice. The observed oscillations were attributed to gaps in the allowed photoelectron final states due to the long-range order (LRO) of the lattice, with a dependence on wavelength. The explanation was accordingly called the LRO theory and the fine structure termed the "Kronig structure." Experimentalists at the time were almost always able to *generally* correlate features of their results with the fairly simple theory presented, allowing the explanation to persist.[20]

The fine structure oscillations were also observed in the absorption spectra of gaseous samples, however, which obviously had no long-range crystalline order.[21] Kronig developed a separate short-range order (SRO) theory to explain this molecular effect. The basic physics described in the second model were actually correct, in that the final state described a free photoelectron with a modified wavefunction due to scattering from the neighboring atoms. However, the two separate interpretations – LRO for solids, SRO for molecules – widely persevered for decades, despite a number of studies correctly suggesting the SRO mechanism is solely responsible in all materials. Hanawalt, for instance, made this connection in 1931 based on his experimental data.[20,21] Kosterov published a short-range order theory in Russia in 1941 that included coordination shells and a phase shift due to the scattering atom, but it was some time before western scientists were able to access a translation.[22] Work in Japan also concluded the near neighbor atomic scattering produced the fine structure, and included a photoelectron lifetime term in the description to limit the interaction to short range.[23]

Nevertheless, it was not until the early 1970's that the correct mathematical description of the EXAFS was produced. Farrel Lytle, then at the Boeing Scientific Research Laboratories, became convinced of the validity of the SRO explanation alone based on his own measurements and those on crystalline/amorphous samples previously published.[20,21,23] Teaming with Ed Stern at the University of Washington and his graduate student Dale Sayers, they developed the modern theoretical understanding and the EXAFS equation above (Eqn. 4-5), successfully using it to describe the EXAFS of materials with known structures.[8] The major breakthrough, however, was the inverse: describing an unknown structure from the EXAFS.[24] This was soon after achieved by applying a Fourier transform integral to the isolated $\chi(k)$ spectra, resulting in peaks similar to a radial distribution function (but not a true RDF, as discussed above). The procedure simplified the fitting problem to specific coordination shells by breaking down the full $\chi(k)$ spectra into Fourier components. Figure 4-5 shows picture of the trio accepting the 1979 Warren Award from the American Crystallographic Society. X-ray absorption studies are now widely used by researchers spanning many diverse interests, and measurements are almost exclusively performed at synchrotron facilities.

Figure 4-5: From left, Ed Stern, Dale Sayers, and Farrel Lytle accepting the 1979 Warren Award for their work developing the modern theory of EXAFS.[20]

Previous Work

A number of XAS studies on layered oxide positive electrode materials have been performed in the last decade. Measurements are common at the transition metal K- and L-edges, as well as the O K-edge, providing complimentary information about the materials systems. XANES analyses of $LiNi_{0.5}Mn_{0.5}O_2$, $LiNi_{0.33}Co_{0.33}Mn_{0.33}O_2$, and $LiNi_{0.4}Co_{0.2}Mn_{0.4}O_2$ materials have confirmed the that the redox states of Ni, Mn and Co are +2, +4, and +3, respectively, in the as-synthesized fresh materials when the Ni:Mn

ratio is 1:1, in agreement with theoretical calculations.[25,2627,28] This has been most directly observed by comparison of the absorption edges of the layered oxide components with measured reference compounds containing transition metals with specified oxidation states.

XAFS measurements on Li-ion battery cathodes have been increasingly recorded *in situ* to characterize the electrodes during operation. Studies have shown that the main charge compensation mechanism in NMC layered oxides proceeds via the oxidation of Ni^{2+} first to Ni^{3+} then to Ni^{4+}, rather than a direct oxidation from the +2 to the +4 state as occurs in other materials such as $LiNi_{0.5}Mn_{1.5}O_4$.[29,30,31] This is indicated not only by the positions and shapes of the absorption edges during charging, but through quantitative EXAFS analysis of the Ni-O bond distances and coordination. Ni^{3+} is a Jahn-Teller active ion, and the NiO_6 octahedron distorts such that there are two longer and four shorter Ni-O bonds, which can be resolved in the EXAFS, exposing the presence of Ni^{3+} ions at intermediate states of charge. The Mn^{4+} ion, on the other hand, does not undergo any significant changes, and is considered to be electrochemically inactive.[25,26,30]

The behavior of Co in NMC materials, however, is less clear, as alluded to in Chapter 1. It is well established that the Co ion is in a +3 oxidation state in the fresh materials.[32,33] There is no significant edge shift, however, observed in the XANES during Li deintercalation, suggesting it remains Co^{3+}, though some reports have made claims to the contrary.[29,33,34,35,36] Oxidation of all the Ni ions alone, though, cannot account for all of the necessary charge compensation in these materials during Li removal to high states-of-charge (SOC). In this light, the role of the oxygen ions has been probed via O K-edge XAS.[26,37] Comparison of the pre-edge peaks of the oxygen absorption spectra in $LiNi_{0.33}Co_{0.33}Mn_{0.33}O_2$ and $LiNi_{0.5}Mn_{0.5}O_2$ electrodes during Li removal indicates a larger increase of the intensity of the pre-peak in the Co-containing material, owing to the covalency of the Co-O bond. The results suggest that the oxygen ions do indeed donate charge during the oxidation of Co-containing layered oxide materials, with the hole remaining at the oxygen site. This mechanism remains an issue of strong debate in the community, however, and will require a more rigorous assessment across various stoichiometries before being settled.

4.2 Experimental

Fresh, charged, and cycled $LiNi_{0.45}Mn_{0.45}Co_{0.1-y}Al_yO_2$ ($0 \leq y \leq 0.1$) electrode materials were studied. Electrochemical charging and cycling of coin cells containing composite cathodes and Li-metal anodes was performed using a VMP3 potentiostat/galvanostat (BioLogic). Cells were delithiated galvanostatically to various states-of-charge (SOC). A rate of 12 mA/g (~C/23) was used to charge all electrodes up to SOC = 50%, and subsequently 18 mA/g (~C/16) was used to complete any charging beyond that (i.e. to SOC = 70, 90%). The faster rate was used to limit organic electrolyte decomposition at the positive electrode due to the high potentials. Coin cells were cycled galvanostatically at 15 mA/g (c/d) between 2.0-4.3 V for 20 or 50 cycles. The coin cells were disassembled in a He-filled glovebox to recover the charged and cycled electrodes, which were subsequently rinsed in DMC and encased in Kapton tape for the XAS measurements.

The X-ray absorption measurements were performed at beamline 4-1 at the Stanford Synchrotron Radiation Lightsource (SSRL) in transmission mode using a Si(220) double crystal monochromator. Measurements were taken on fresh, charged, and cycled electrodes *ex situ*, with the monochromator detuned by 30-50% to eliminate higher order harmonics. Two scans each of the Ni, Mn, and Co K-edge μ(E) spectra were measured and merged after alignment for each electrode specimen. For each edge measurement, a similar metal foil (Ni, Mn, or Co) spectrum was recorded simultaneously in series for energy reference.

The collected data was analyzed in a standard manner using Athena and Artemis software packages.[11] The data was calibrated using the first peak in the derivative of the absorption spectra of the reference metals. Energy values of 6539 eV, 7709 eV, and 8333 eV were used for the Mn, Co, and Ni metal edges, respectively. After merging like scans, the background contribution was subtracted by fitting a linear function to the pre-edge region and a cubic polynomial to the post-edge region, and the data were normalized. A piece-wise spline was fit using the AUTOBK function to isolate the $\chi(k)$ EXAFS, which were subsequently weighted by k^3 to magnify the higher-k signal during further processing.[38]

The $k^3*\chi(k)$ weighted data was Fourier transformed between 3.8-13.8 $Å^{-1}$ in k-space for Ni (3.8-13.6 $Å^{-1}$ for the fresh sample series), 3.9-11.3 $Å^{-1}$ for Mn, and 3.9-11.1 $Å^{-1}$ for Co, using a hanning window with dk=1 $Å^{-1}$. Structural information was obtained by a least squares fitting of the Fourier transformed spectra in R-space from R=1.0-3.0 for Mn and Co data, and R=1.0-3.1 for Ni data using scattering paths calculated with FEFF6.[13,39] The amplitude reduction factors S_0^2 were fixed at 0.95 and 0.9 for the Ni and Mn/Co fits, respectively, after initial refinements. In all fits, the contribution of photoelectron scattering by Li was ignored due to the very weak scattering amplitude.

4.3 Fresh $LiNi_{0.45}Mn_{0.45}Co_{0.1-y}Al_yO_2$ Samples

XANES spectra measured at the Ni and Mn K-edges for fresh $LiNi_{0.45}Mn_{0.45}Co_{0.1-y}Al_yO_2$ ($0 \leq y \leq 0.1$) electrode materials are presented in Figures 4-6 and 4-7, respectively. For each edge, the pre-edge features and derivative spectrum are additionally shown. A number of trends are observed over the Al-substitution range in the Ni edge. First, there is no observed shift in energy of the edge position with increased Al-content. There is, however, a slight increase in the white line intensity. This is more clearly seen in the derivative spectrum (Fig. 4-6b). The sharpening of the white line peak is apparent in the growing positive and negative derivative peak features centered about 8350.5 eV. Furthermore, the intensity of the pre-edge peak at about 8333.5 eV decreases with larger Al concentrations (Fig. 4-6c).

Similar trends are observed in the Mn K-edge data for the same samples, though only the y=0 and y=0.05 data are available (Figs. 7a-c). Regardless, the observed trends are similar to those seen in the Ni-edge data for the whole Al-substitution set and thus considered characteristic of the materials; there is no observed shift in the absorption edge position, but there is an increase in the white line intensity (seen again more clearly in the derivative spectrum) and a decrease in the pre-edge peak intensities.

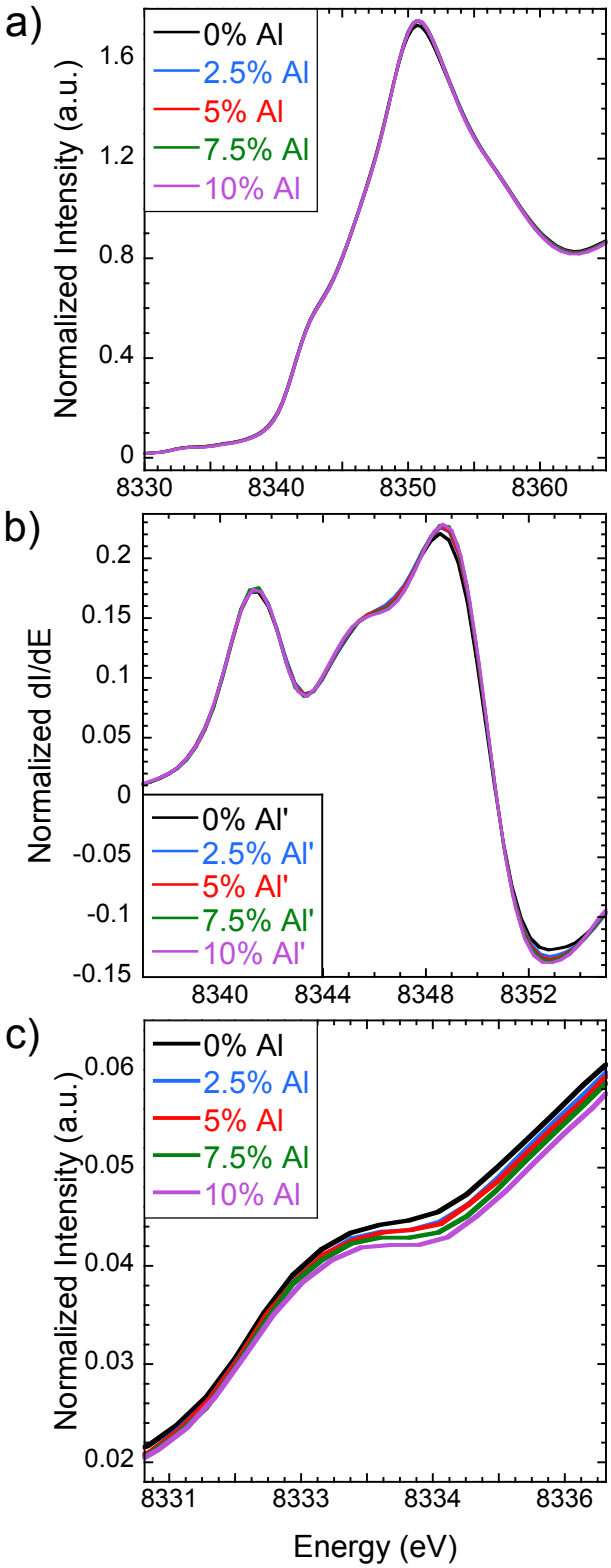

Figure 4-6: a) The normalized edge, b) derivative, and c) pre-edge of the Ni K-edge XANES of the $LiNi_{0.45}Mn_{0.45}Co_{0.1-y}Al_yO_2$ ($0 \leq y \leq 0.1$) fresh electrode materials.

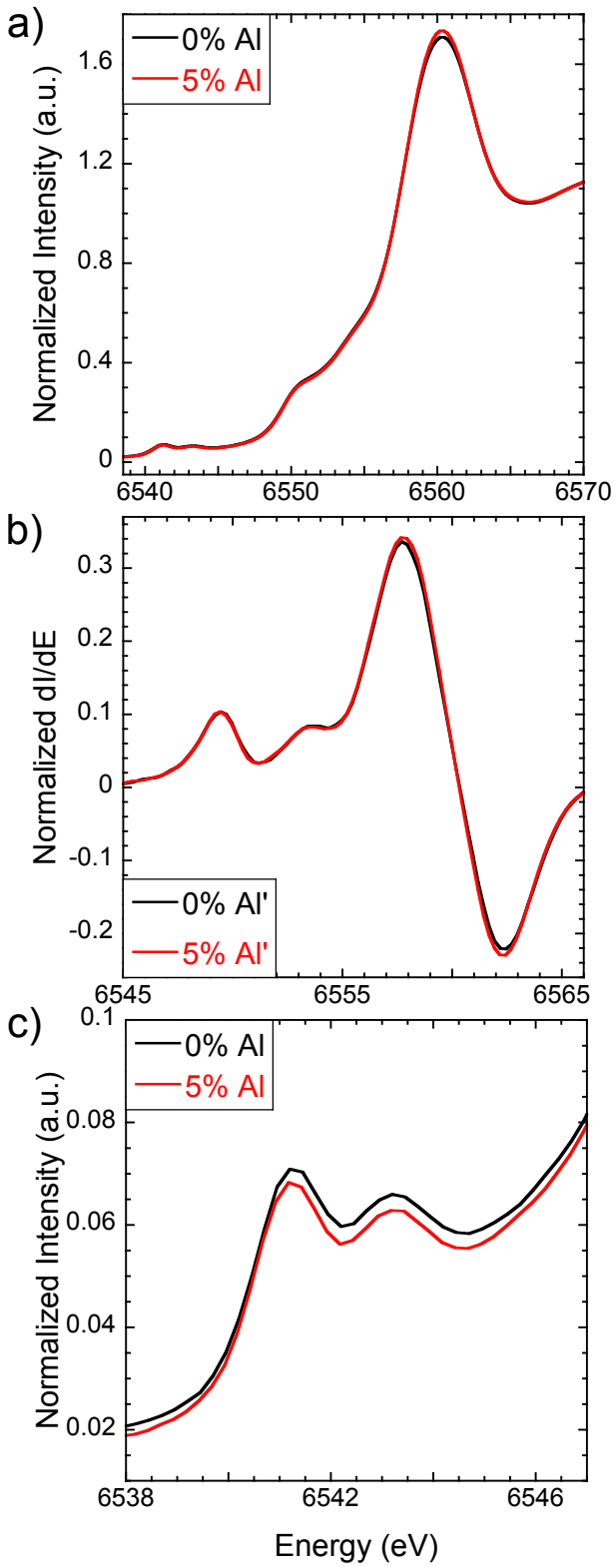

Figure 4-7: a) The normalized edge, b) derivative, and c) pre-edge of the Mn K-edge XANES of the $LiNi_{0.45}Mn_{0.45}Co_{0.1-y}Al_yO_2$ ($0 \leq y \leq 0.1$) fresh electrode materials.

In the previous chapter, high-resolution X-ray diffraction results were presented indicating a symmetry-lowering structural distortion in $LiNi_{0.45}Mn_{0.45}Co_{0.1-y}Al_yO_2$ materials at high Al-contents. It was speculated that this structural effect resulted from a strain-relaxing ordering of the transition metal octahedra as the degree of Al-substitution increased. The layered oxide materials are composed of edge-sharing transition metal octahedra alternating with planes of octahedrally coordinated Li^+ ions. As each MO_6 has a different equilibrium *M*-O bond length, a highly strained system emerges from the edge-sharing octahedral arrangement. Metal ordering within the transition metal plane occurs for Ni-rich NMC-type systems, manifested, in some cases, by the "flower" pattern (Figure 1-10).[26,40,41] The substitution of Al for Co, a smaller ion, relieves some of the inherent strain, perhaps by inducing further ordering.

The features highlighted above; the white line intensity and the pre-edge peak intensity; are strongly dependent on the disorder within the MO_6 octahedra, where *M* is the absorbing metal. An increase in the octahedral distortion enhances the *M*3d-4p orbital overlap due to a decrease in the inversion symmetry of the environment surrounding the absorbing atom. Al-substitution leads to a decrease in the observed pre-edge peak intensities and a sharpening of the white line, suggesting less strained (disordered) MO_6 octahedra.

The peak feature present within the rising edges (resulting in the first peak shown in the derivative spectra) is attributed to a 1s→4p electronic transition with a ligand-to-metal charge transfer (LMCT) shakedown process.[30,35] In this case, the final electronic configuration can be described as $1s^1c3d^{n+1}L4p^1$, where *c* is the 1s core hole and *L* is an O-2p hole (n_{Ni2+}=8, n_{Mn4+}=3). It occurs at lower energy than the main 1s→4p transition without shakedown due to increased screening of the core hole. The intensity of this feature can be used to infer the degree of covalency of the *M*-ligand bonds, as the charge transfer requires orbital overlap. As there is no observed change in the peak shape or amplitude due to the presence of Al, the covalency of the M-O bonds are assumed invariant with Al-substitution.

The magnitudes of the Fourier transform of the EXAFS spectra, weighted by k^3, are shown in Figures 4-8a and 4-9a for the Ni and Mn K-edges as a function of Al-content in $LiNi_{0.45}Mn_{0.45}Co_{0.1-y}Al_yO_2$. The real parts of the Fourier transforms are also shown for comparison (Figs. 4-8b and 4-9b). Focusing on the magnitude plots because the trends are more apparent, the behavior is similar for both data sets: a systematic decrease in intensity is clearly seen for the second large peak (R≈2.5 Å for both edges) and some higher-R features, while a slight increase occurs in the first peak with increased Al-substitution.

The peaks in the Fourier transform magnitude plots describe different scattering paths of the photoelectron, which are schematically shown for the layered oxides in Figure 4-10. At the top, the real part of the Fourier transform depicting an example Ni spectrum from the $LiNi_{0.45}Mn_{0.45}Co_{0.1-y}Al_yO_2$ materials is shown along with the corresponding magnitude (envelope). Individual scattering paths contributing to the full signal are shown below, and indicated in the transition metal layer schematic in (Fig. 4-10b).

The first main peak is almost entirely due to scattering from the nearest neighbor oxygen ions. The slight increase observed in the *M*-O peak intensity can be explained by a decrease in σ^2 of the first coordination shell. This agrees with the XANES results,

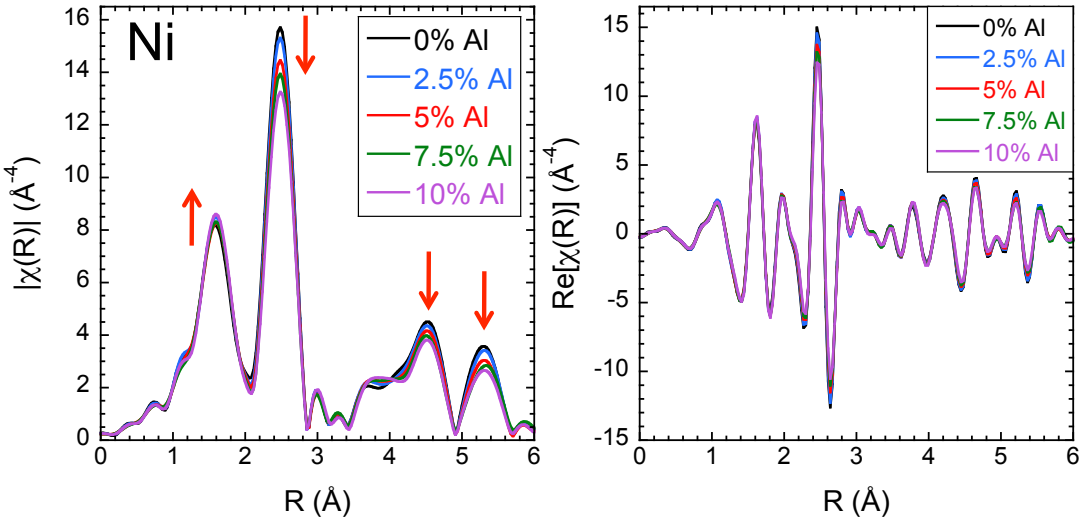

Figure 4-8: The a) magnitude (left) and b) real part (right) of the Fourier transforms of the Ni χ(k) data weighted by k^3 for $LiNi_{0.45}Mn_{0.45}Co_{0.1-y}Al_yO_2$ ($0 \leq y \leq 0.1$) materials.

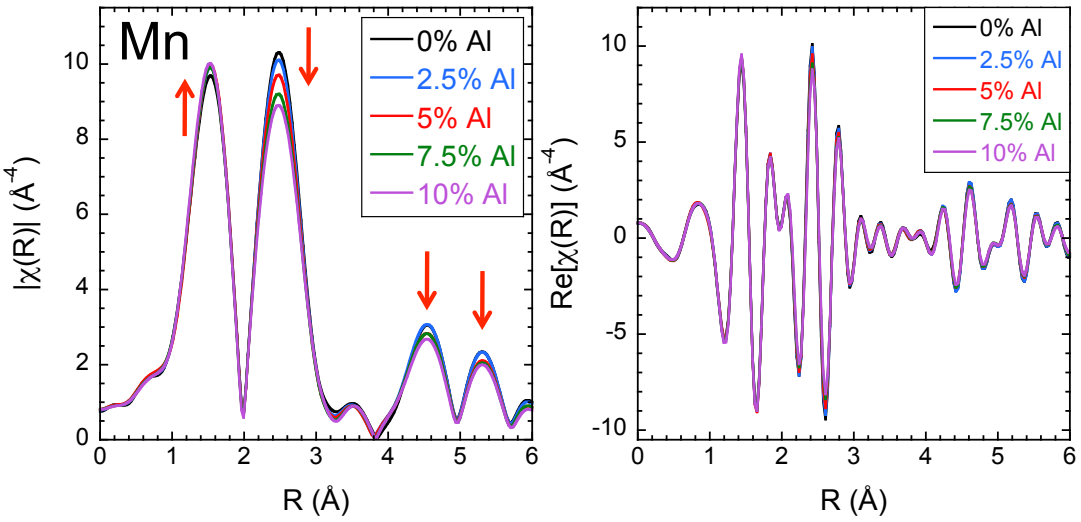

Figure 4-9: The a) magnitude (left) and b) real part (right) of the Fourier transforms of the Mn χ(k) data weighted by k^3 for $LiNi_{0.45}Mn_{0.45}Co_{0.1-y}Al_yO_2$ ($0 \leq y \leq 0.1$) materials.

suggesting a decrease in octahedral disorder (strain) with Al-substitution. The second main peaks in the Ni and Mn Fourier transformed EXAFS mostly describe photoelectron scattering from the nearest in-plane metal ions surrounding the absorber. The higher order peaks are due to scattering from metal ions at larger radial distances, as well as multiple scattering of the photoelectron from more than one neighbor. The specific peaks displaying a decreased amplitude with higher Al-content suggest Al is well distributed throughout the NMC lattice, as all of the metal-metal scattering peaks are affected. Al is a lighter metal than Ni, Mn, or Co, residing one row above the transition metals in the periodic table, and thus displays weaker photoelectron scattering properties. The

magnitude of the intensity variations observed here are much larger than those caused solely by the slight decrease in lattice *a*-parameter (<0.002 Å) and increase in *3b* Li content (<1%) that are consequences of the Al-substitution.

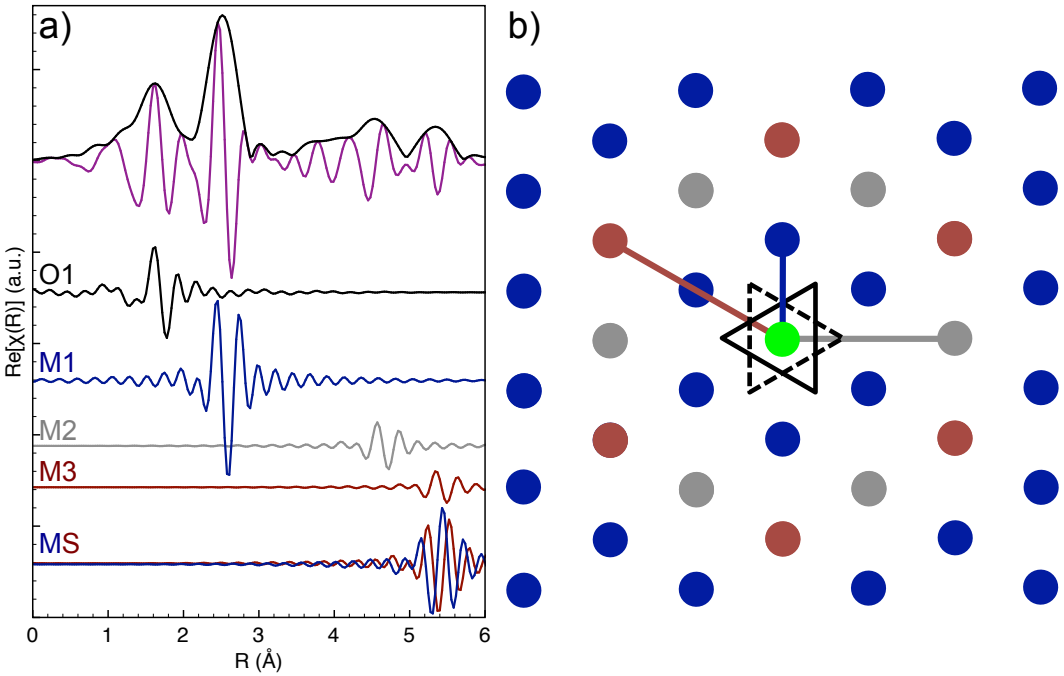

Figure 4-10: a) The real part of the Fourier transform (top, purple) and magnitude (black) with individual signals from different scattering shells shown below. b) A schematic of the transition metal plane showing the orientation of the scattering shells depicted in (a), with matching colors for each scatterer. The example spectrum is Ni K-edge data from $LiNi_{0.45}Mn_{0.45}Co_{0.1-y}Al_yO_2$ (y=0).

The results of fitting the first and second shell of the Fourier transformed EXAFS data for the Ni and Mn K-edges as a function of Al-content are shown in Figure 4-11a. The calculated Ni-O bond lengths of about 2.05 Å agree well with reported values of octahedrally coordinated Ni^{2+}, as do the Mn-O bond lengths of approximately 1.91 Å with accepted values for Mn^{4+} ions.[42] There is a very slight increase in the observed Ni-O distance with Al-substitution, and no significant change in the Mn-O bond length. As mentioned, there is a decrease in the calculated σ^2 values of the first coordination shell with Al-incorporation (Fig. 4-11b).

The first nearest neighbor metal distances resulting from the EXAFS fits are shown in Figure 4-11c. The Ni-M bond distances show no significant trend, while the Mn-M bond distances appear to increase slightly with Al content. The uncertainties of the calculations, however, are quite large in comparison to the observed changes. Curiously, the Mn-M distances resulting from the fits increase with Al-substitution, while XRD results suggest a decrease in the average a_{hex} lattice parameter. If the trend accurately describes the system, the discrepancy could suggest selective ordering around the Mn ions upon Al-incorporation.

However, the data is modeled here with a single M-M bond distance, as is the case in a perfect hexagonal crystal. This is not likely to be the case, as at least the y=0.1

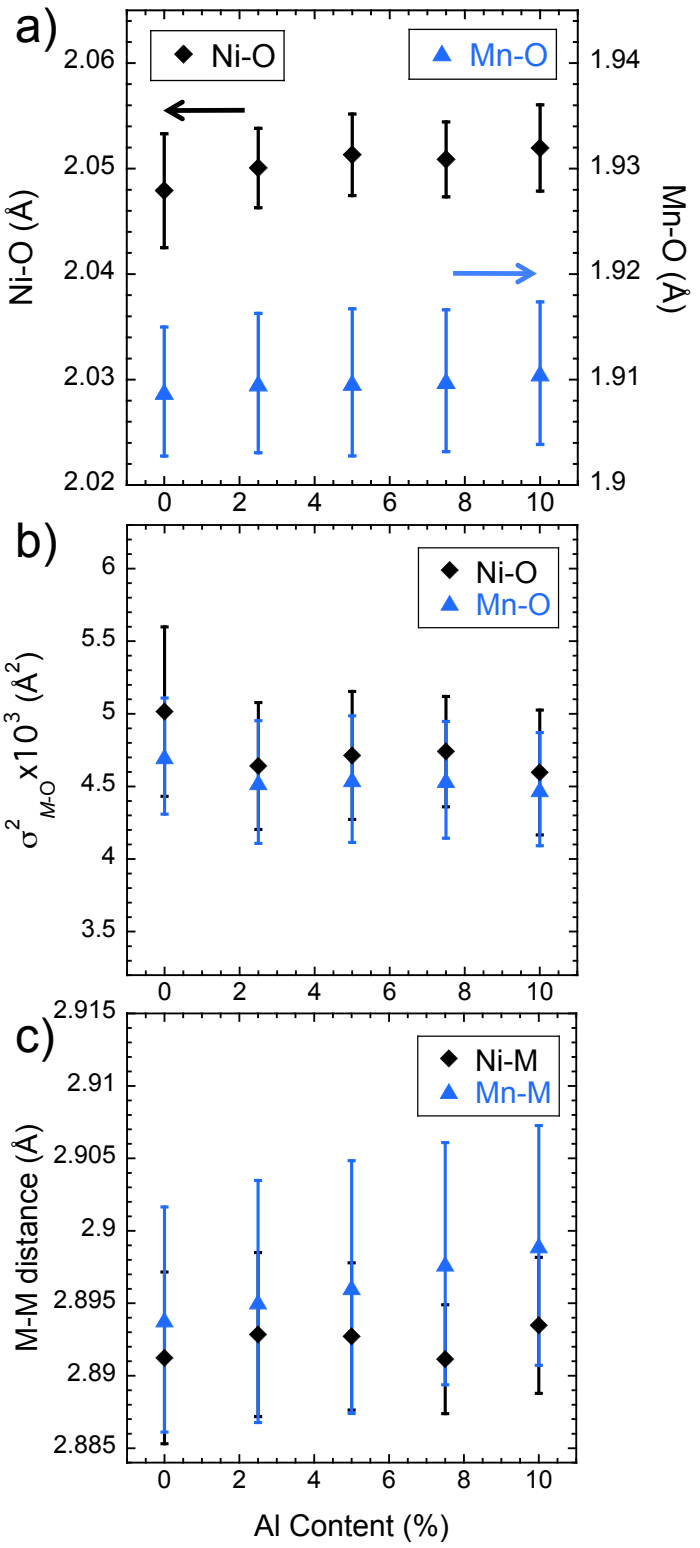

Figure 4-11: Fitted values for the first coordination shell: a) Ni-O and Mn-O bond distances and b) σ^2 values for the Ni and Mn absorbers as a function of Al-content in $LiNi_{0.45}Mn_{0.45}Co_{0.1-y}Al_yO_2$ ($0 \leq y \leq 0.1$). c) Fitted values of the Ni-*M* and Mn-*M* in-plane first-nearest metal distances.

material displays peak splitting in the high-resolution XRD patterns that suggests a structural distortion within the transition metal planes. The distortion, unfortunately, cannot be definitively resolved in this EXAFS study. Two distances can only be reliably differentiated in EXAFS modeling if they differ by more than $\Delta R = \frac{\pi}{2\Delta k}$. For the Ni EXAFS fits, which included the largest data ranges, this results in a distance resolution of ~0.15 Å. By contrast, the two nearest neighbor metal distances in the high Al-content oxides differ by only about 0.01 Å, as calculated by Rietveld refinement. [This is, of course, an average measure due to the long-range structure.] Note, though, that the above describes the resolution of two different coordination shells, not the precision with which single bond lengths can be calculated (typically ~0.01 Å). Additionally, Al is assumed randomly distributed in the fitting model, which may not be the case in an ordered system. Higher resolution data and modeling would allow for further, more accurate detail to be revealed.

Unfortunately the $LiNi_{0.45}Mn_{0.45}Co_{0.1-y}Al_yO_2$ samples appear to contain a very small Fe impurity, which limits the usable *k*-range for the Mn data. The amount is not detectable by inductive-current plasma elemental analysis (ICP), but XAS measurements are sensitive to ppm levels.[43] The Fe impurity may originate from the precursor materials – the ACS-grade metal nitrate reagents can contain trace amounts of Fe – or arise from either the combustion reaction in the stainless steel beaker or during the collection step.[44] The Fe K-edge lies at 7112 eV, putting it at about k=12 $Å^{-1}$ in the Mn EXAFS. The small Fe absorption edge step in the μ(E) data adds a different signal than the modulations resulting from the photoelectron scattering originating at the Mn absorption sites, as seen in Figure 4-12. This spurious signal cannot simply be subtracted, and thus limits the EXAFS analysis to a smaller range exclusive of the Fe edge.

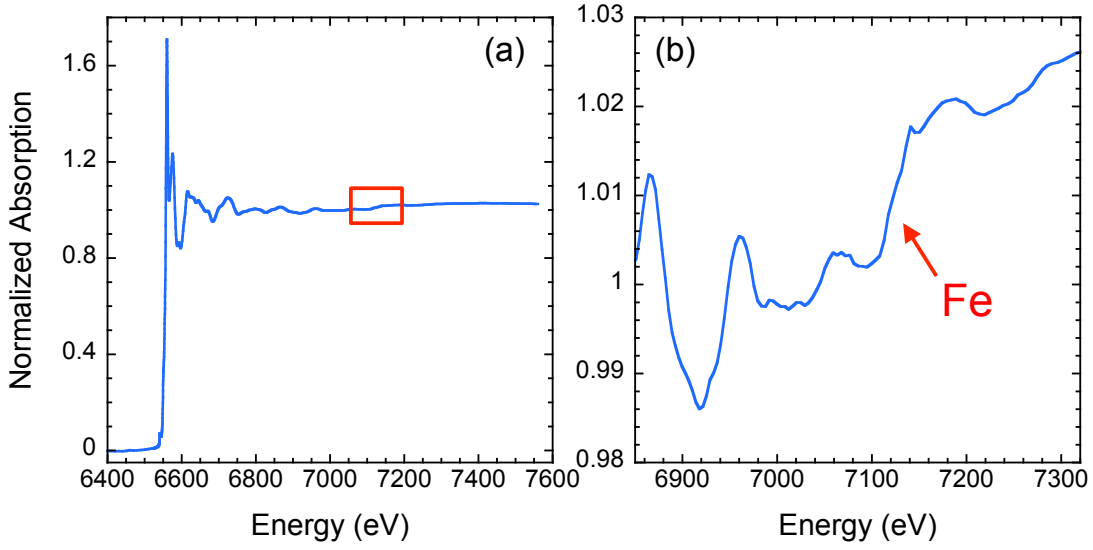

Figure 4-12: a) A small Fe impurity is detected in the Mn EXAFS of the $LiNi_{0.45}Mn_{0.45}Co_{0.1-y}Al_yO_2$ materials. b) A magnified view of the region indicated in (a), showing the small Fe-edge.

4.4 Charging Series

To elucidate the effect of Al-substitution on the $LiNi_{0.45}Mn_{0.45}Co_{0.1-y}Al_yO_2$ materials during battery operation, XAS spectra of electrodes at various states-of-charge (SOC) were measured *ex situ* for y=0 and y=0.05 materials. Voltage vs. Li-content curves are shown in Figure 4-13 with the measurement points indicated, spanning from fresh samples to SOC=90%. The higher operating potential of the 5% Al-substituted sample can be seen; electrodes were charged here to specified Li-contents rather than maximum voltage limits to ensure a direct comparison of states-of-charge between the samples.

The normalized Ni K-edge XANES spectra throughout the charging region are shown in Figure 4-14 for the y=0 and y=0.05 materials. For both samples, there is a shift of the entire edge to about 2 eV higher energy as the materials are electrochemically charged. This shift indicates oxidation of the Ni ions for charge compensation as Li ions are deintercalated. Beyond SOC=50%, however, the Ni-edge shift is less pronounced in both materials (y=0, y=0.05). There is significantly less progression in the XANES as the material is charged from 50% to 90% SOC than during the first half of the charging process. In contrast, the Mn and Co K-edges of both the y=0 and y=0.05 materials do not show a similar energy shift as the Ni-edge at any point during Li-removal. There is, however, a clear evolution of the edge-shape for both elements, presented in Figures 4-15 and 4-16. Compared to the Ni spectra, the observed edge variations suggest the Mn and Co ions remain in the +4 and +3 states, respectively, throughout charge. The behavior of Co in the materials, though, is discussed further below.

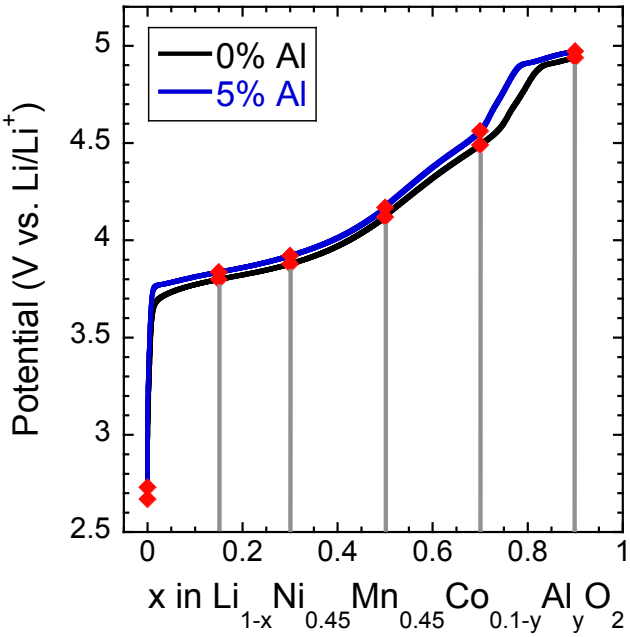

Figure 4-13: Voltage profiles for the electrochemically charged $LiNi_{0.45}Mn_{0.45}Co_{0.1-y}Al_yO_2$ (y=0, 0.05) electrode materials. XAS measurements were made *ex situ* for samples charged to the indicated points.

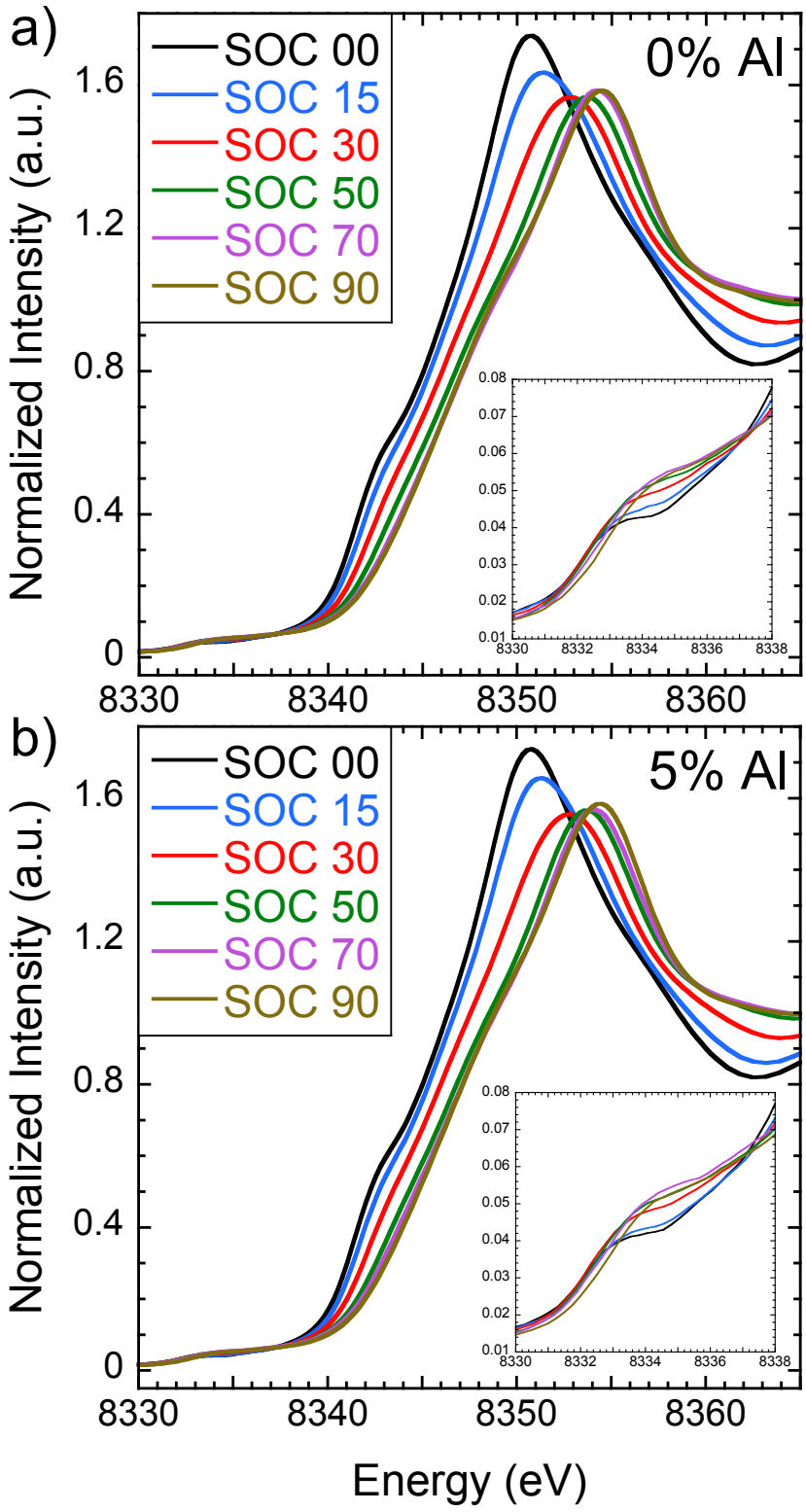

Figure 4-14: Normalized Ni K-edge XANES of $Li_{1-x}Ni_{0.45}Mn_{0.45}Co_{0.1-y}Al_yO_2$ materials with a) y=0 and b) y=0.05 shown for various states-of-charge. The pre-edge peaks are shown in the insets.

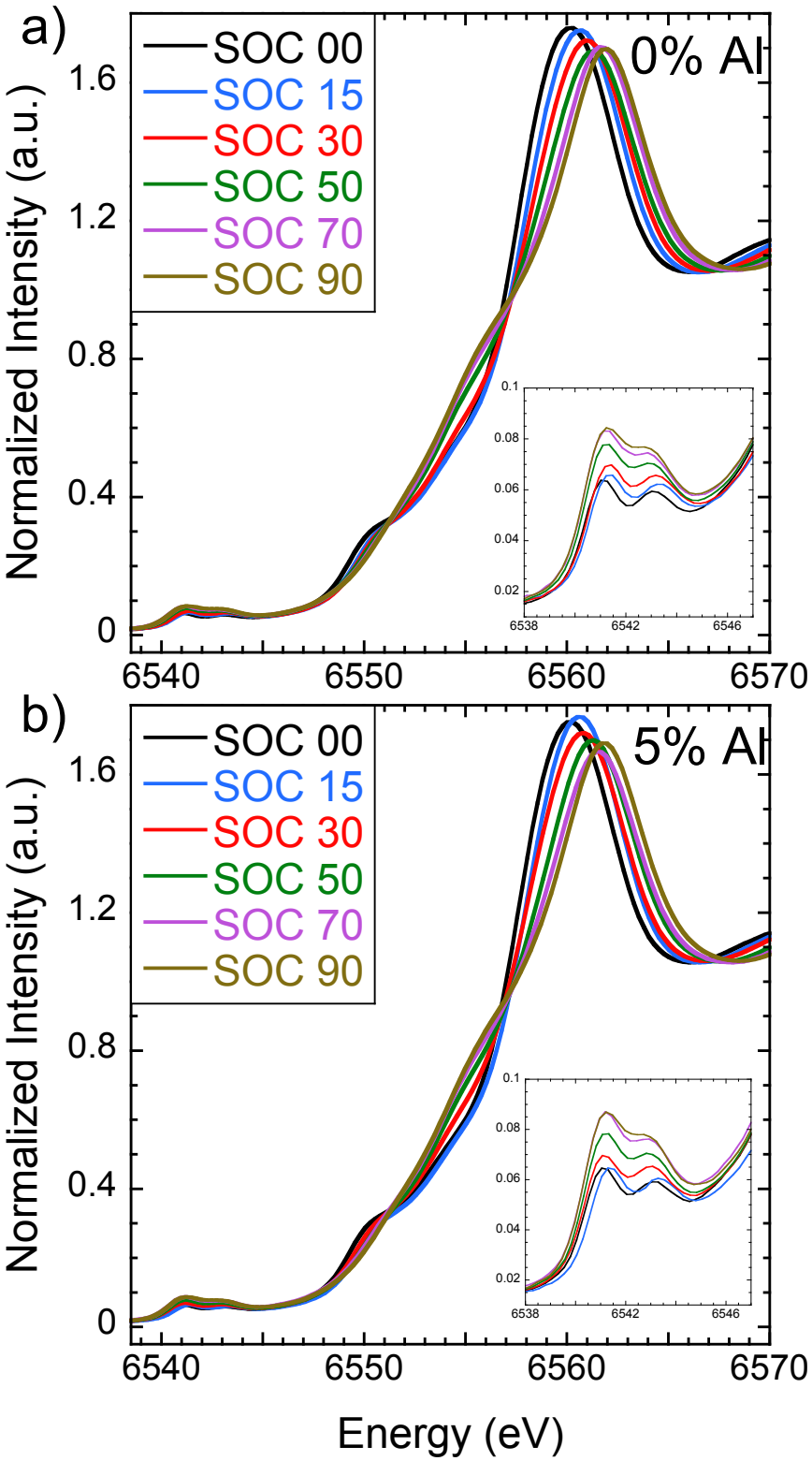

Figure 4-15: Normalized Mn K-edge XANES of $Li_{1-x}Ni_{0.45}Mn_{0.45}Co_{0.1-y}Al_yO_2$ materials with a) y=0 and b) y=0.05 shown for various states-of-charge. The pre-edge peaks are shown in the insets.

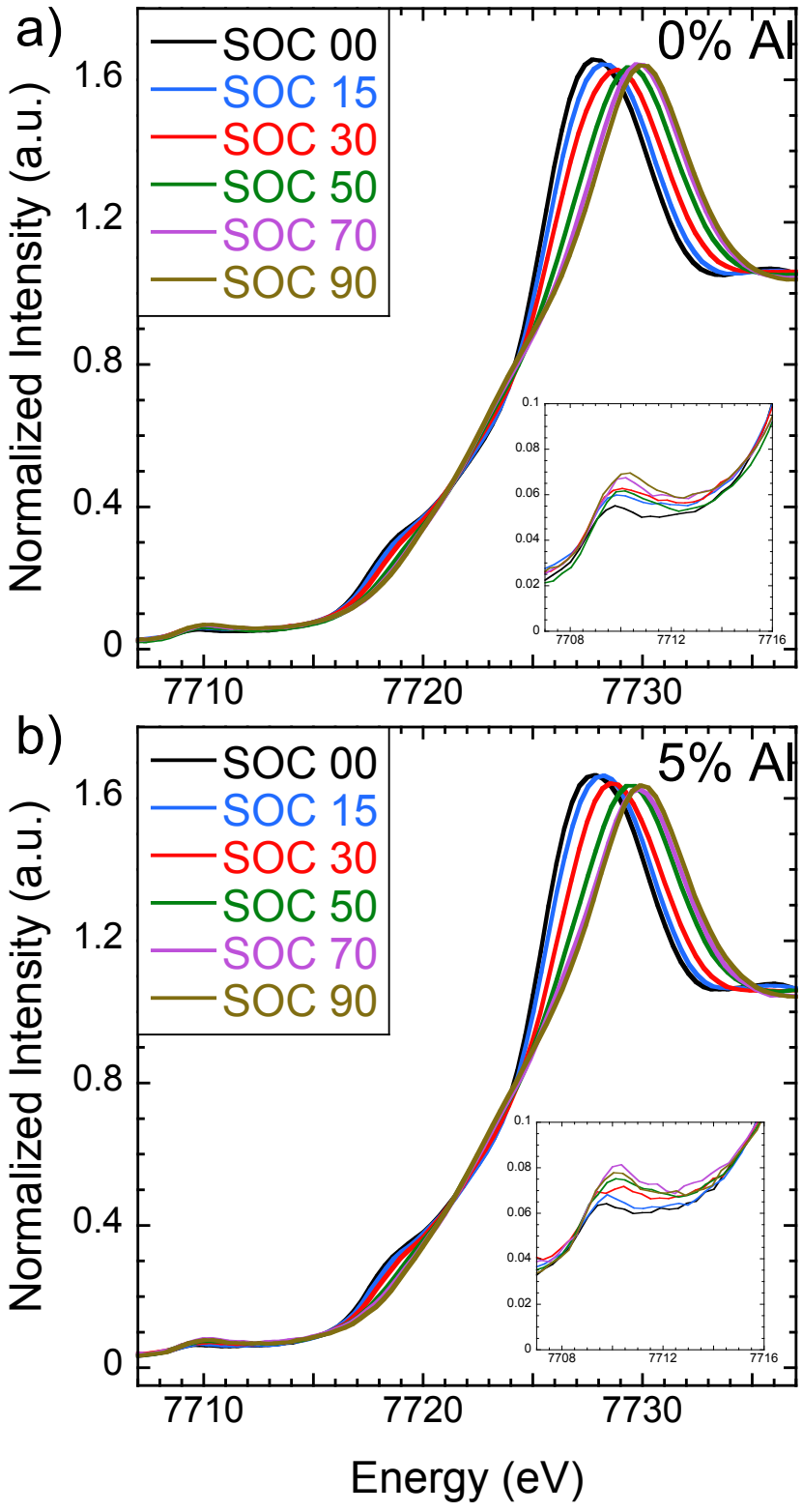

Figure 4-16: Normalized Co K-edge XANES of $Li_{1-x}Ni_{0.45}Mn_{0.45}Co_{0.1-y}Al_yO_2$ materials with a) y=0 and b) y=0.05 shown for various states-of-charge. The pre-edge peaks are shown in the insets.

As previously mentioned, XANES measurements are quite sensitive to the local geometric and electronic structure of the absorbing atoms. When Li ions are removed during charge, there is a substantial structural evolution of the electrode material: a decrease in the in-plane metal distances (*a* lattice parameter) and a corresponding increase along the layered direction occurs during the initial oxidation stages, before a contraction at higher SOC (*c* lattice parameter). This behavior was observed using *in situ* synchrotron XRD (Chapter 3). The geometric evolution can also be observed by the changes in the shapes of the XANES edges. The bond lengths and distortion of the MO_6 octahedra are modified as a function of SOC, in turn varying the orbital overlap (both *M*3d-*M*4p and *M*3d-O2p) that gives rise to various features observed in the XANES, such as the pre-edge peaks and those ascribed to LMCT shakedown processes.[30]

The pre-edge features of each edge are shown in the insets of the figures. The relatively low intensity pre-edge peaks are indicative of the distorted octahedral coordination of the transition metals, as mentioned above. In octahedral symmetry, crystal field splitting removes the electronic degeneracy of the transition metal d-orbitals. The Ni^{2+} electronic configuration is $t_{2g}^6 e_g^2$, and the single pre-edge electronic transition observed corresponds to excitation into an unfilled e_g orbital. The shift of the Ni pre-edge to higher energy is due to the oxidation of the Ni ions during charge, which increases the binding energy. The Mn^{4+} configuration ($t_{2g}^3 e_g^0$) leads to the existence of two pre-edge peaks, indicating electronic transitions to open t_{2g} and e_g states. The slight initial shift in energy from the fresh state to SOC=15% is suggestive of a small amount of Mn^{3+} in the as-synthesized materials that is immediately oxidized.

The Co pre-edges are more difficult to interpret here; there is a smaller signal-to-noise ratio of the measured spectra due to the lower Co-concentration compared to the other metals. Low-spin Co^{3+} ($t_{2g}^6 e_g^0$) should display a single pre-edge peak, while higher spin-states will result in the observation of a second peak. There appears to be a single pre-edge peak for both the $LiNi_{0.45}Mn_{0.45}Co_{0.1-y}Al_yO_2$ (y=0 and y=0.05) samples in this study, though other investigations of NMC materials have resolved a second peak indicating a mixture of low and high spin states, and that possibility cannot be definitively excluded by the data presented here.[34] Despite no significant shift of the main Co absorption edge, there is a slight shift of the Co pre-edge peaks to higher energy during charge. It is less pronounced than that of the Ni pre-peak, but suggests some contribution to the oxidation scheme centered at the Co ions. As mentioned previously, there is currently substantial debate within the community regarding the role of Co and O-anions in charge compensation. Despite theoretical calculations for NMC systems suggesting the electrochemical oxidation of Co (or oxygen) occurs only at high voltages after the full oxidation of the Ni-content, the reality is less well defined.[29,37,45] Rather, the results here suggest activity of the Co (or oxygen) at lower voltages, simultaneous with the oxidation of Ni.

The intensities of the pre-edge features increase with SOC for all metals in both the Al-substituted and the unsubstituted parent materials. This suggests an increase in the octahedral distortion throughout the charging process, leading to enhanced *M*3d-4p orbital overlap. This can be at least partly due to the Jahn-Teller active Ni^{3+} ions produced as an intermediate state during the charging process.[34] The distortion due to the

Ni^{3+} will transmit in part to the surrounding edge-sharing metal octahedra. Al-substitution does not appear to affect this.

As mentioned above, a more quantitative analysis of the XANES spectra features is difficult, as a sufficient mathematical description has not yet been widely disseminated. However, the relative evolution of the absorbing environments can be further evaluated with linear combination fitting of the XANES edges. To this end, the fitting was performed for each element using the collected spectra at SOC=0% and SOC=90% as end members. Fitting the entire edge provides a more robust analysis than tracking the position of a single edge feature, such as the peak of the white line or the energy position at half of the edge step. This is especially true in cases where the edge shape changes throughout the measured series, such as here.

The results of the linear combination fitting of the Ni edges are shown in Figure 4-17a for both $LiNi_{0.45}Mn_{0.45}Co_{0.1-y}Al_yO_2$ (y=0, 0.05) materials. The changes in the Ni K-edges are mostly confined to the first part of the charging process (SOC<70%), and there is minimal change between SOC=70% and SOC=90%. Although only the end members describing the fresh (Ni^{2+}) and fully charged (Ni^{4+}) states are considered, satisfactory fits are achieved to describe the relative spectra shape of intermediate charge states containing Ni^{3+}. Again, there does not appear to be a significant effect due to Al on the charging mechanism.

Interestingly, the linear combination fitting of the Co spectra (Fig. 4-17b) also shows a tapering of the spectral changes at higher states of charge. If Co-oxidation were responsible for charge compensation following the Ni-contribution, a larger change between SOC=70% and SOC=90% would be expected. Rather, the Co environment seems to undergo most of the observed evolution below 70% SOC. It is the Mn edge that actually shows the largest variation at high states-of-charge relative to the beginning of the charging process (Fig. 4-17c). Thus, it is clear that the entire layered oxide structure evolves during the Li deintercalation process, with the immediate environments of the Ni, Mn, and Co ions transforming. From the XANES analysis, however, a specific effect of Al-substitution cannot be definitely determined.

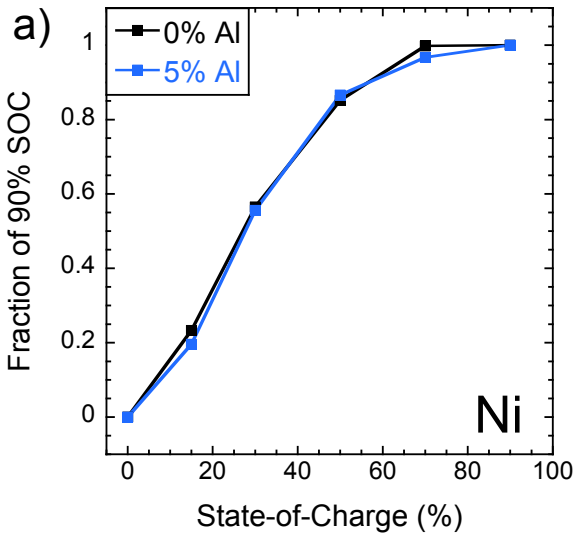

Figure 4-17: Results of linear combination fittings of the a) Ni, b) Co, and c) Mn XANES edges. "Fraction of 90% SOC" indicates the relative proximity of each charge state to the final observed.

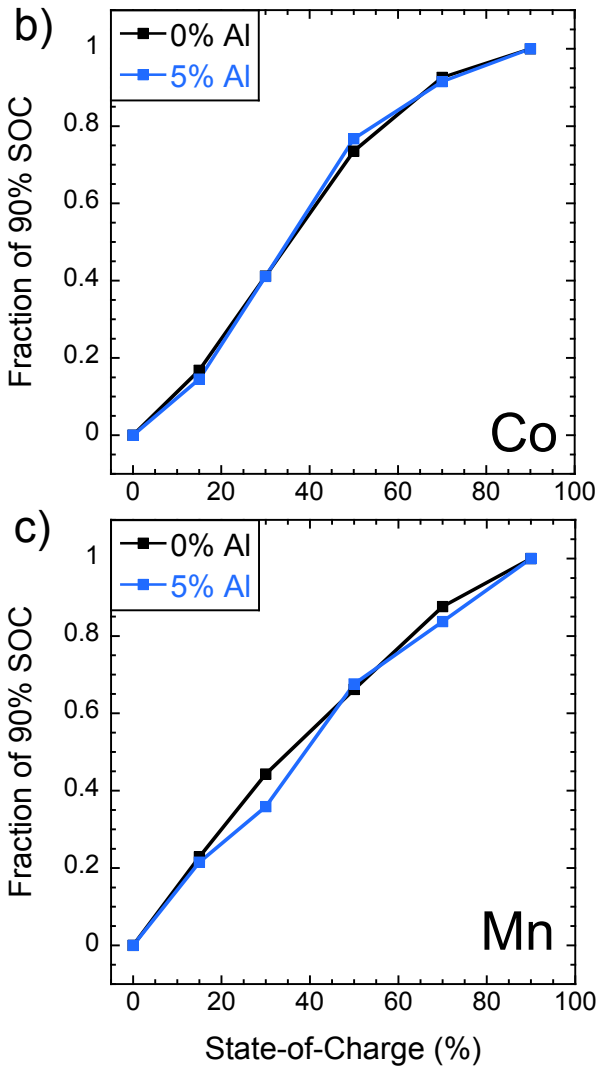

Figure 4-17 (cont'd): Results of linear combination fittings of the a) Ni, b) Co, and c) Mn XANES edges. "Fraction of 90% SOC" indicates the relative proximity of each charge state to the final observed.

The magnitudes of the Fourier transformed k^3-weighted EXAFS data are shown in Figures 4-18 through 4-20. The Ni data (Fig. 4-18) shows substantial development throughout the charging process, as expected. The first peak in the Fourier transform data (R≈1.5) mainly results from scattering of the photoelectrons by the nearest neighbor oxygen anions. At the beginning of charge, this Ni-O peak decreases in amplitude. The peak shifts to lower R, and the intensity then increases from 30-90% SOC. The trend is indicative of the Jahn-Teller distortion associated with a Ni^{3+} intermediate ion initially formed during the charging process, which is subsequently oxidized to the non-distorted Ni^{4+}.

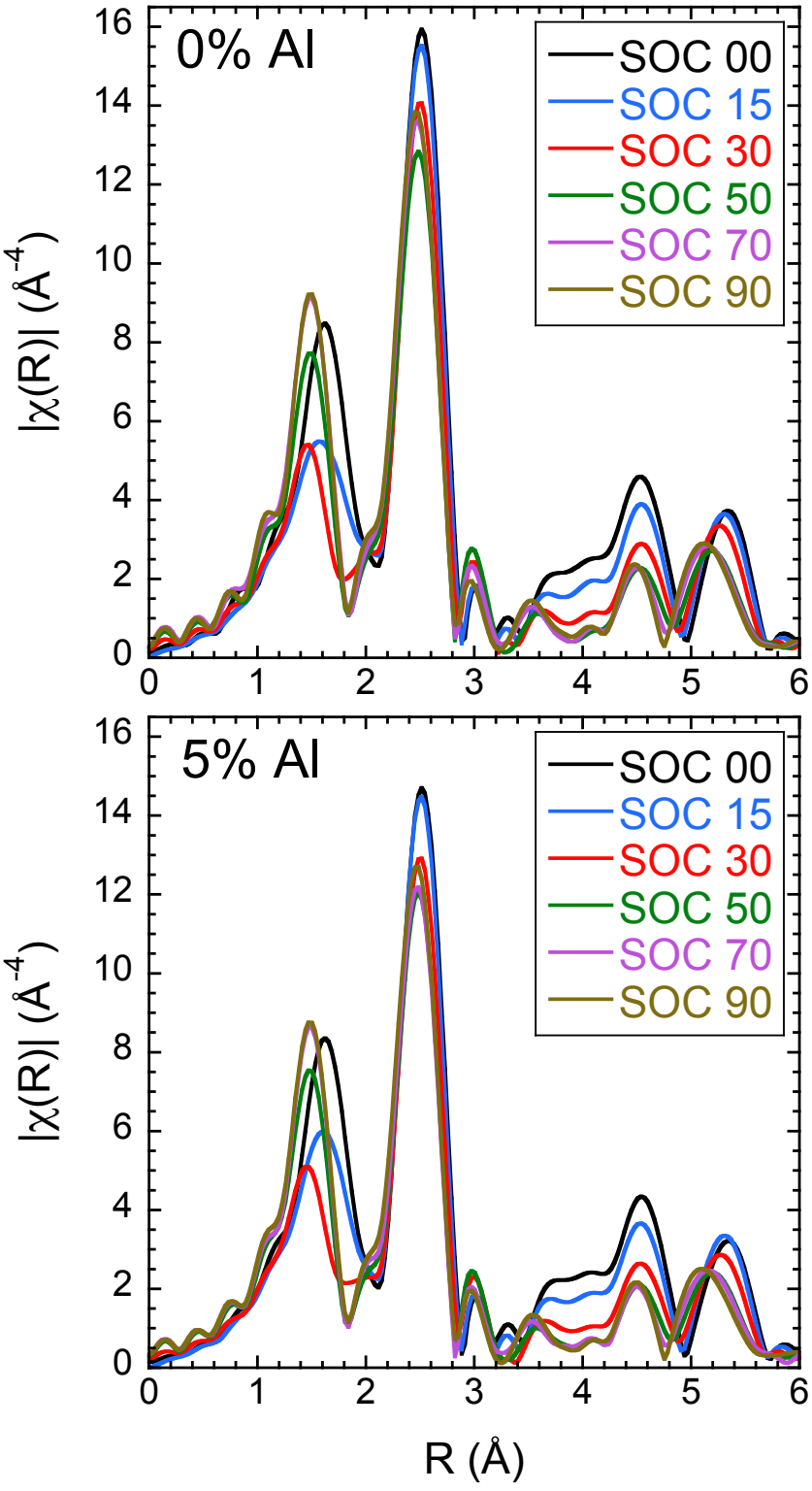

Figure 4-18: Magnitudes of the Fourier transformed k^3-weighted Ni K-edge EXAFS for $Li_{1-x}Ni_{0.45}Mn_{0.45}Co_{0.1-y}Al_yO_2$ materials with a) y=0 (top) and b) y=0.05 (bottom), shown for various states-of-charge.

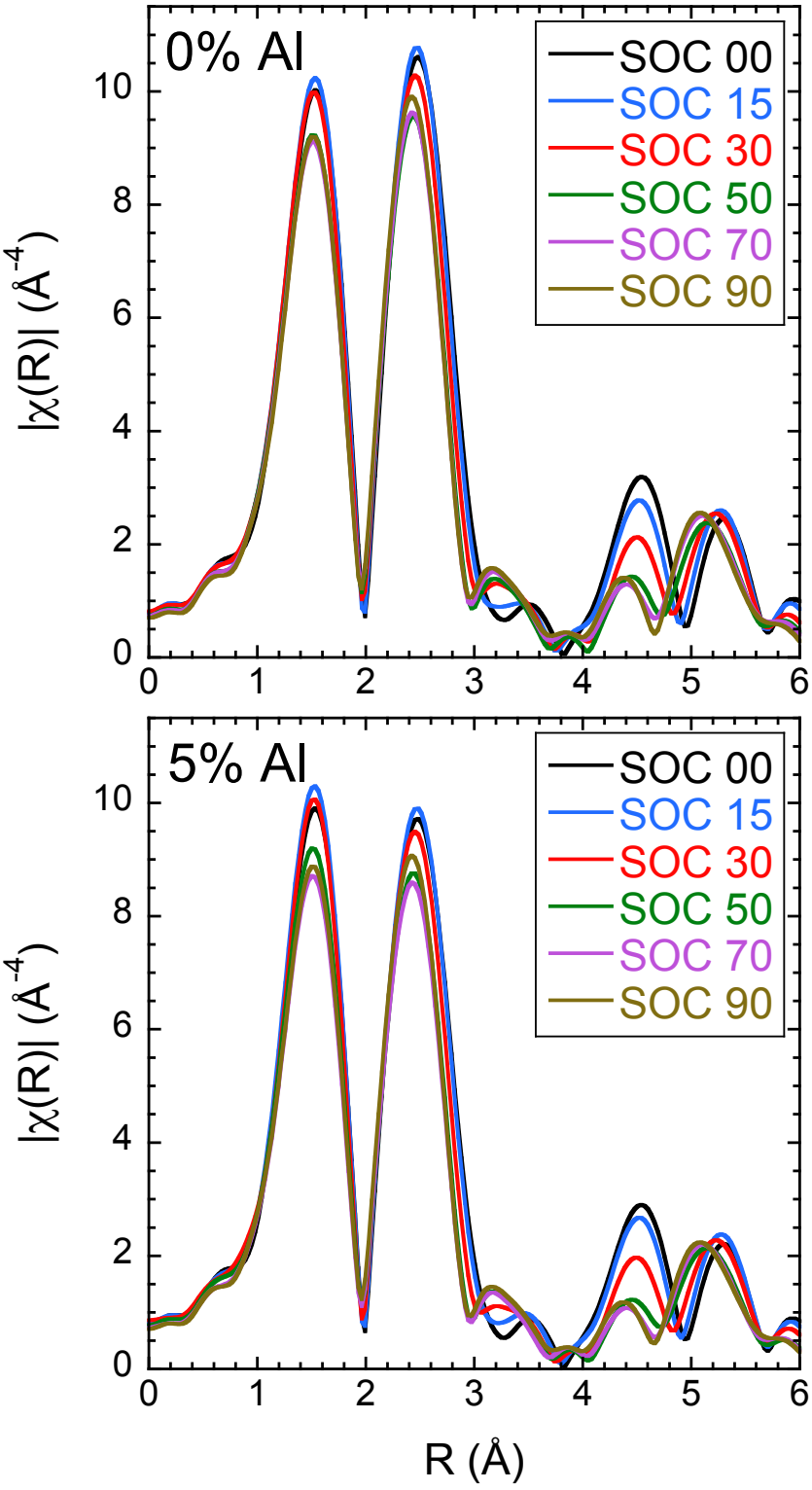

Figure 4-19: Magnitudes of the Fourier transformed k^3-weighted Mn K-edge EXAFS for $Li_{1-x}Ni_{0.45}Mn_{0.45}Co_{0.1-y}Al_yO_2$ materials with a) y=0 (top) and b) y=0.05 (bottom), shown for various states-of-charge.

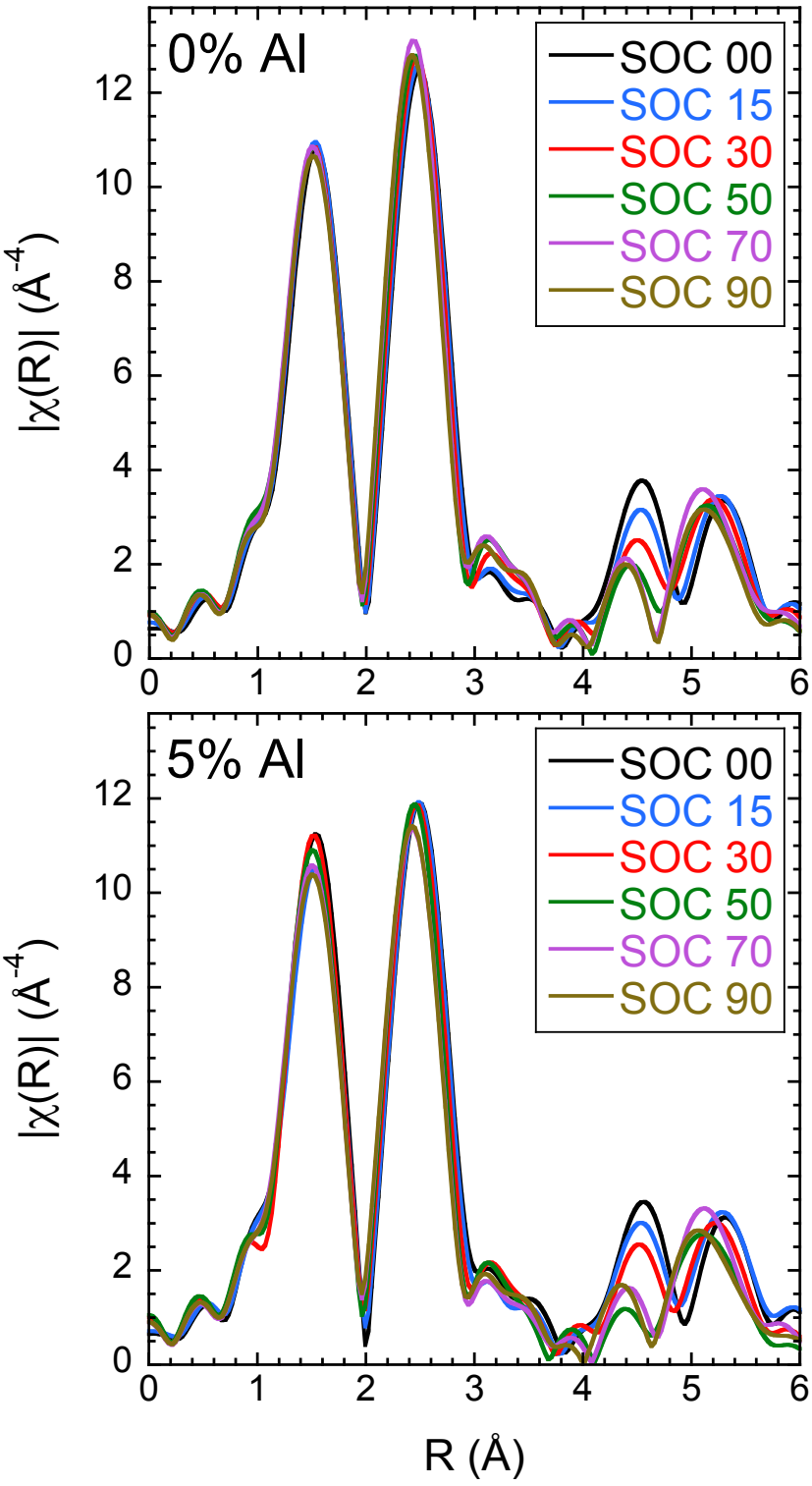

Figure 4-20: Magnitudes of the Fourier transformed k^3-weighted Co K-edge EXAFS for $Li_{1-x}Ni_{0.45}Mn_{0.45}Co_{0.1-y}Al_yO_2$ materials with a) y=0 (top) and b) y=0.05 (bottom), shown for various states-of-charge.

The Fourier transformed EXAFS data was fitted using a two-shell model for quantitative analysis. The bond distances of the first nearest neighbor oxygen ions and second nearest neighbor metal ions were fitted as free parameters along with the Debye-Waller factors (σ^2). Figure 4-21 shows the results of the y=0 material Ni data and illustrates the quality of the structural model. The Ni data presented a more difficult task than the Mn or Co spectra; the Jahn-Teller distortion and the *3a* Ni content (representing a different absorbing environment) both had to be incorporated to adequately fit the spectra. The Jahn-Teller distortion that exists at intermediate charge states was accommodated by assuming four "short" and two "long" Ni-O bonds, with the values determined by initial refinements of the fresh (Ni^{2+}=long) and fully-charged (Ni^{4+}=short) end members. The relative concentration of each was allowed to float. The *3a* Ni was treated as a second absorber linearly contributing to the measured EXAFS spectra, with an initial concentration determined by the high-resolution XRD Rietveld refinements.

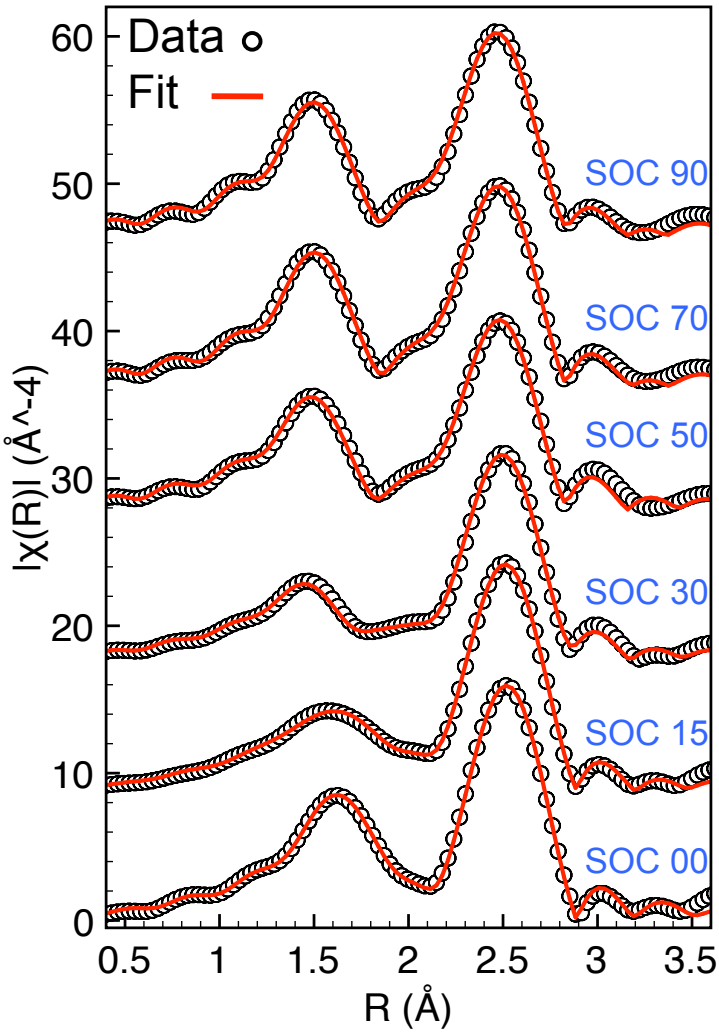

Figure 4-21: Fits of the magnitudes of the Fourier transformed k^3-weighted Ni K-edge EXAFS for the $Li_{1-x}Ni_{0.45}Mn_{0.45}Co_{0.1-y}Al_yO_2$ (y=0) material at various states-of-charge.

The *M*-O bond distances throughout the charging process, determined by fitting the Fourier transformed EXAFS spectra, are presented in Figure 4-22. The largest change in bond length is observed for the Ni-O bond in both the y=0 and y=0.05 materials. This is expected, as the Ni ion is oxidized during Li-extraction from the materials, as was seen clearly in the XANES analysis. The single values given for the intermediate charge states (15≤SOC≤70) correspond to an average value of the total short and long bonds calculated during the fit. The change is minimal at >70% SOC, also in good agreement with the data above.

The Mn-O bond lengths vary much less, suggesting again that the Mn^{4+} ions do not substantially oxidize throughout the charging region (except for the very slight Mn^{3+} content), as discussed above. The small observed changes (<0.02 Å) are likely a secondary effect from the surrounding MO_6 octahedra. The Co-O distances vary slightly more throughout the charging process, with most of the changes occurring at SOC<70%. This is also in agreement with the linear combination fitting of the XANES spectra. A contribution to the charge compensation centered at the Co ions, likely including the surrounding O-anions, cannot be ruled out. In fact, the decrease in ionic radius upon oxidizing from Co^{3+} to Co^{4+} in octahedral coordination is only 0.015 Å according to Shannon, less than the 0.04 Å change calculated here.[42] In disagreement with theoretical suggestions, however, the majority of the bond length reduction occurs during the first half of charge. Measurement of the oxygen K-edge spectra will help to determine the exact mechanism of charge compensation throughout the oxidation regime. The variation of each *M*-O (*M*=Ni, Mn, Co) bond length is the same within the windows of uncertainty of the fits for both of the $LiNi_{0.45}Mn_{0.45}Co_{0.1-y}Al_yO_2$ (y=0, 0.05) materials.

The variation of the *M-M'* bond distances are shown in Figure 4-23, where *M'* indicates the nearest neighbor metals to the absorbing ion. The *M-M'* distance is a determinant of the *a*-parameter in the α-$NaFeO_2$ structure. A Co-scatterer was used in all fits to account for scattering from Ni, Mn, or Co ions; all three transition metals are close on the periodic table and have similar scattering properties, with Co (Z=27) between Mn (Z=25) and Ni (Z=28). Al was assumed randomly distributed for the y=0.05 material in the best fits. The behavior of the Ni-*M'*, Mn-*M'*, and Co-*M'* bond lengths are all similar: there is a continuous decrease in the nearest metal-neighbor distance as Li is deintercalated. Slightly less change is observed at the end of charge (70≤SOC≤90%), in agreement with the *in situ* XRD results (Fig. 3-11a).

The calculated bond lengths differ slightly for the Ni, Mn, and Co absorbers. This could be a result of using Co as the lone transition metal scatterer, when in actuality the generated photoelectrons are interacting with mostly Ni or Mn neighbors, based on the $LiNi_{0.45}Mn_{0.45}Co_{0.1-y}Al_yO_2$ stoichiometry. Each metal will scatter the photoelectron with a slightly different phase and amplitude, affecting the fits: previous EXAFS analyses have suggested differences of ±0.01 Å result when assuming all Ni or Mn surroundings instead of Co in a $LiNi_{0.4}Mn_{0.4}Co_{0.15}Al_{0.05}O_2$ material.[34] *M-M'* distances that vary with the absorbing element identity would be expected in an ordered structure; in this case each absorbing ion has a distinct surrounding environment. No substantial local structural effect of Al-substitution in the layered structure can be resolved within the quantitative resolution of this EXAFS probe.

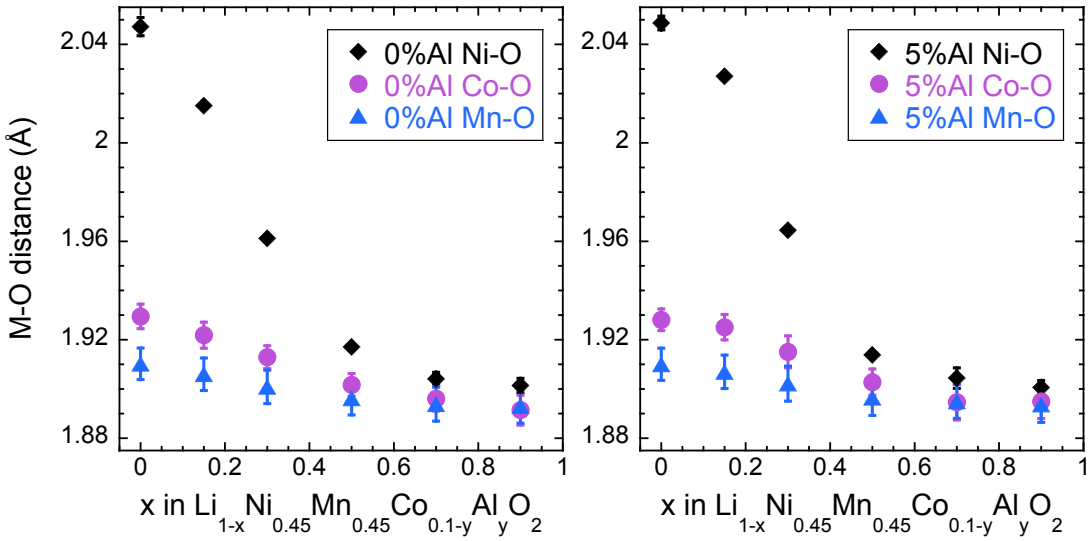

Figure 4-22: Fitted values for the first coordination shell *M*-O bond distances (*M*=Ni, Mn, Co) as a function of Li-content in $Li_{1-x}Ni_{0.45}Mn_{0.45}Co_{0.1-y}Al_yO_2$ for the y=0 (left) and y=0.05 (right) materials.

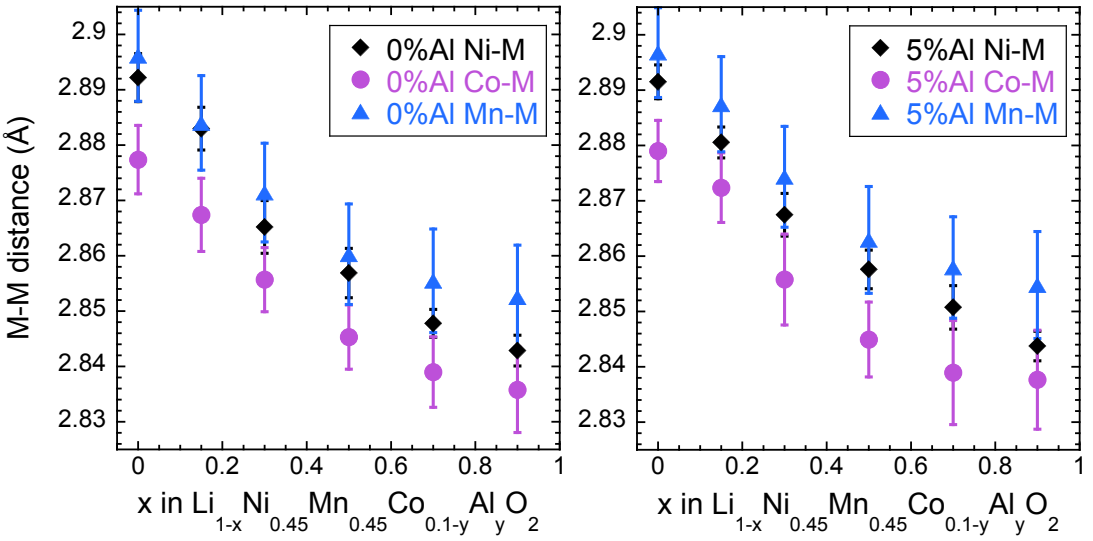

Figure 4-23: Fitted values for the second coordination shell *M*-*M'* bond distances (*M*=Ni, Mn, Co) as a function of Li-content in $Li_{1-x}Ni_{0.45}Mn_{0.45}Co_{0.1-y}Al_yO_2$ for the y=0 (left) and y=0.05 (right) materials. A *M'*=Co scatterer was used in all fits to account for Ni, Mn, or Co neighbors.

4.5 Cycled Electrodes

XAS measurements were also taken for $LiNi_{0.45}Mn_{0.45}Co_{0.1-y}Al_yO_2$ (y=0, 0.05) electrodes cycled between 2.0-4.3 V at 15 mA/g for 20 and 50 cycles. Coin cells were disassembled in the fully discharged state, and the composite electrodes were measured *ex situ*.

The Mn XANES data for fresh and cycled samples is shown in Figure 4-24. Cycling causes a decrease in the white line intensity, which is plainly seen both in the normalized edge and derivative spectra (Figs. 4-24a-d). The changes are accompanied by an increase in the pre-edge peak intensities, shown in Figures 4-24e, f. The evolution of the spectra suggests cycling-induced disorder in the immediate environment surrounding the Mn ions, similar to that observed due to Li deintercalation during the charging process. The changes can be at least partially attributed to less-than-complete re-intercalation of Li on subsequent discharges; unsurprising, as the measured discharge capacities decrease with cycling (Chapter 2). Although the intensity increase of the pre-edges appears similar for both the y=0 and y=0.05 materials, the magnitude of the white line intensity-reduction is lower for the Al-substituted compound, suggesting improved reversibility.

The Ni XANES data is shown in Figure 4-25. There is a decrease in the white line intensity in the cycled samples compared to the fresh electrodes. This is clearly observed in the derivative plots of the absorption edge, where a slight shift to higher energy can also be resolved (Figs. 4-25c, d). The changes are somewhat less in the Al-substituted samples. Additionally, there is an intensity increase and simultaneous narrowing of both the edge feature attributed to LMCT and the pre-edge peaks for both materials (Figs. 4-25c-f). These trends suggest further octahedral disorder that leads to more orbital overlap.

The slimmer peak characteristics of the highly cycled material cannot be explained at this time, but possibly result from increased homogeneity of the Ni-absorber environments. This can entail either a decrease in the *3a* Ni concentration (via migration to the transition metal layer) or removal of the *3a* Ni into a NiO-like layer on the particle surfaces, for instance.[46,47] A similar narrowing of the pre-edge peak feature is not observed during charge to high potentials, as seen above (Fig. 4-14). Many studies have suggested that a majority (~75%) of the *3a* Ni moves into the transition metal layer in this voltage region (and much returns to the Li-layer upon discharge).[41,48] Additionally, high-resolution XRD refinements indicate a relative decrease of the antisite Ni concentration on the order of 10% in the cycled samples compared to the fresh materials (Chapter 3). A decrease in *3a* Ni content alone is therefore is not likely the only explanation, but rather additional structural changes must contribute. A high-resolution TEM study will help determine the cause of the pre-edge peak narrowing observed in the Ni spectra.

The magnitudes of the Fourier transformed k^3-weighted Ni EXAFS data are shown in Figure 4-26 for the fresh and cycled materials. There is a slight decrease with cycling in the amplitudes of both the main peaks at R≈1.6 Å and R≈2.5 Å, corresponding mostly to Ni-O and Ni-*M'* scattering, respectively, in the unsubstituted material. These changes are clearly limited with Al-substitution (Fig. 4-26b). The corresponding Mn EXAFS data is shown in Figure 4-27. A similar decrease in the amplitude of the Mn-O scattering peak is observed in the y=0 material, while the changes are negligible in the corresponding y=0.05 material. In contrast to the evolution of the Ni environments, the Mn-*M'* scattering peak amplitudes increase upon cycling. This is in agreement with the decreased *3a* Ni concentration after cycling (observed by high-resolution XRD), suggesting the antisite Ni that migrates to the transition metal layer preferentially occupies lattice sites next to Mn ions, as would be expected with the existence of flower-type ordering.

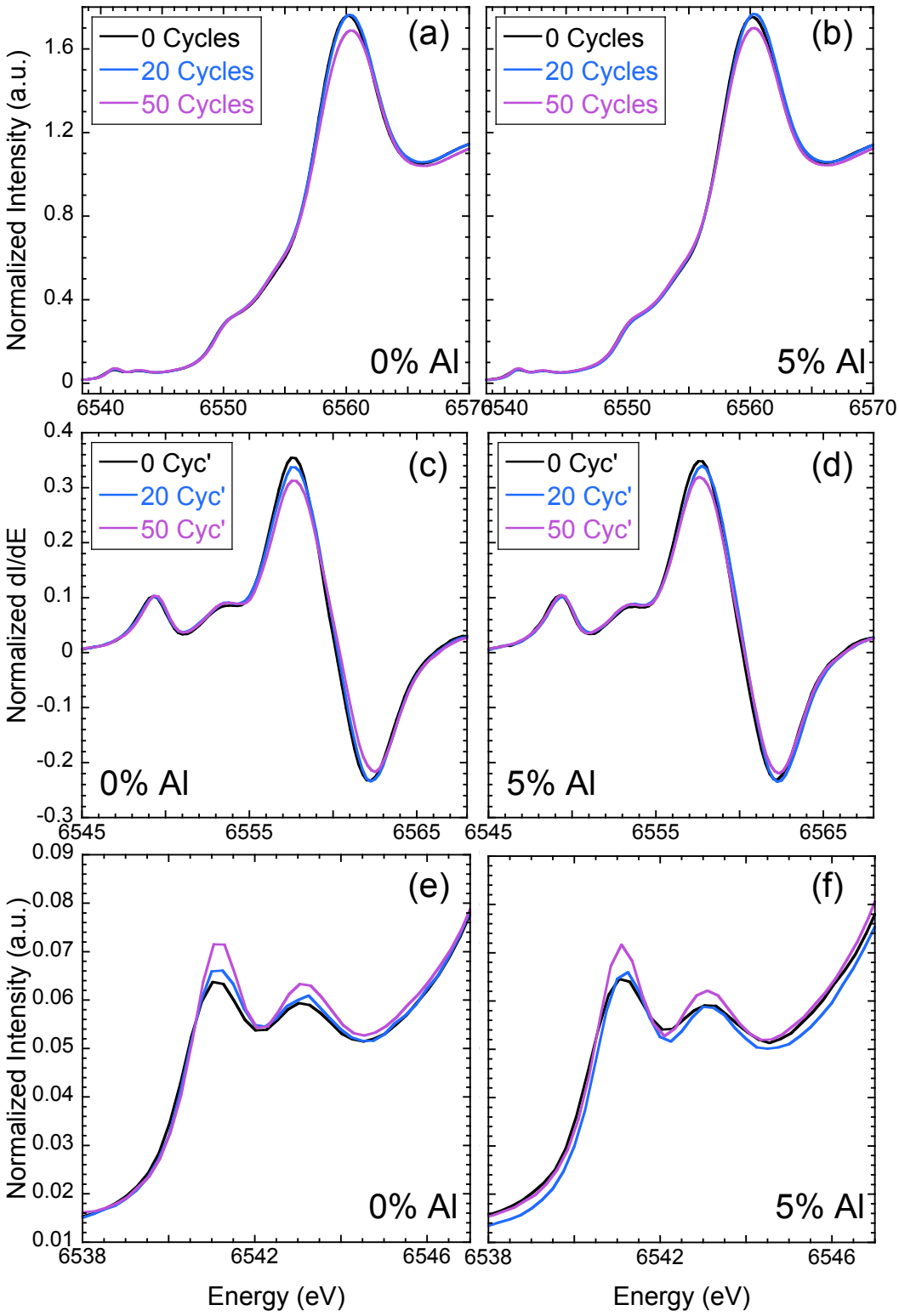

Figure 4-24: Normalized Mn K-edge XANES of fresh and cycled $Li_{1-x}Ni_{0.45}Mn_{0.45}Co_{0.1-y}Al_yO_2$ electrode materials with a) y=0 and b) y=0.05. c, d) Derivative spectra and e, f) pre-edge peaks for the y=0 (c, e) and y=0.05 (d, f) samples.

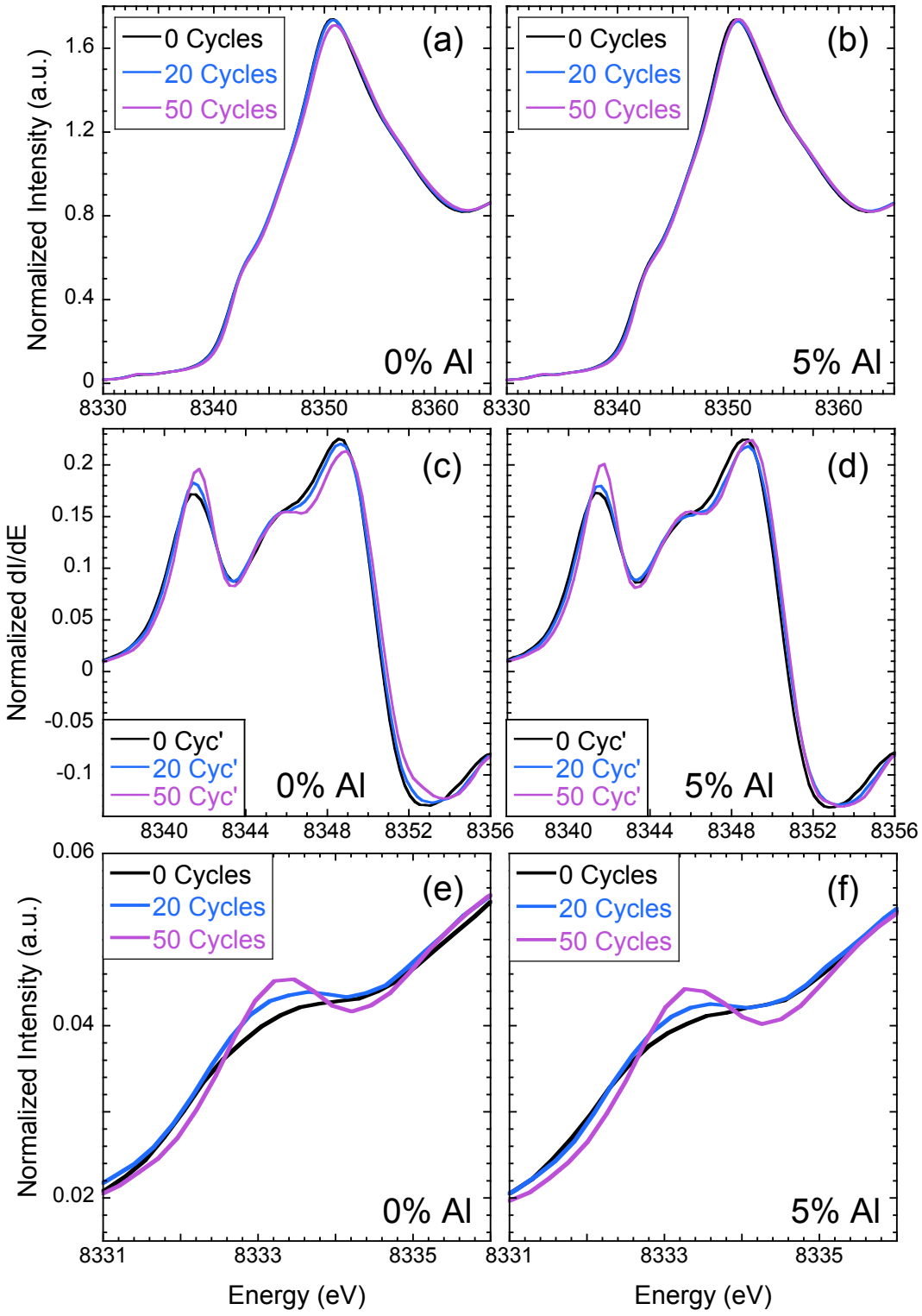

Figure 4-25: Normalized Ni K-edge XANES of fresh and cycled $Li_{1-x}Ni_{0.45}Mn_{0.45}Co_{0.1-y}Al_yO_2$ electrode materials with a) y=0 and b) y=0.05. c, d) Derivative spectra and e, f) pre-edge peaks for the y=0 (c, e) and y=0.05 (d, f) samples.

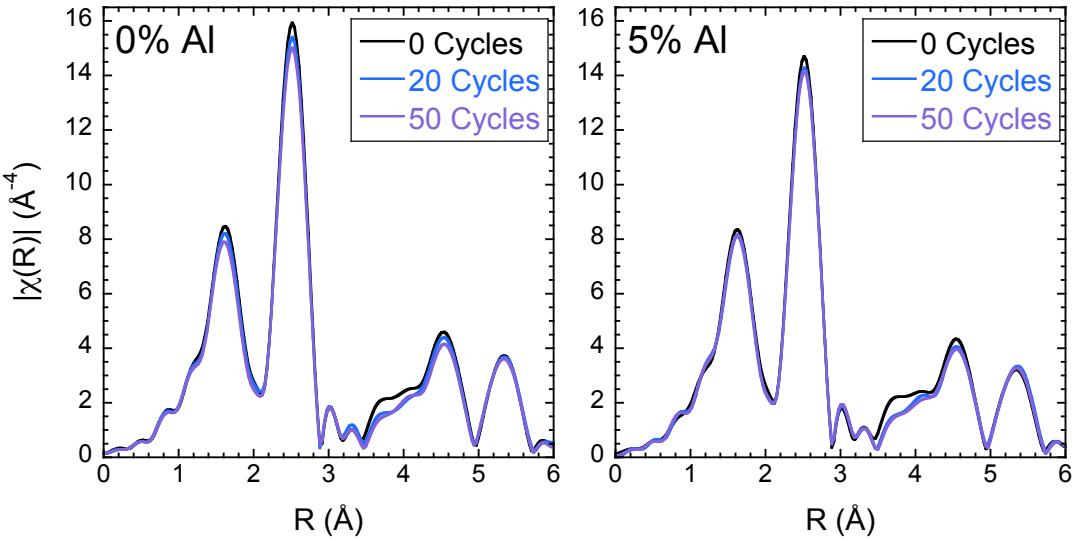

Figure 4-26: Magnitudes of the Fourier transformed k^3-weighted Ni K-edge EXAFS of fresh and cycled $LiNi_{0.45}Mn_{0.45}Co_{0.1-y}Al_yO_2$ electrode materials with a) y=0 (left) and b) y=0.05 (right).

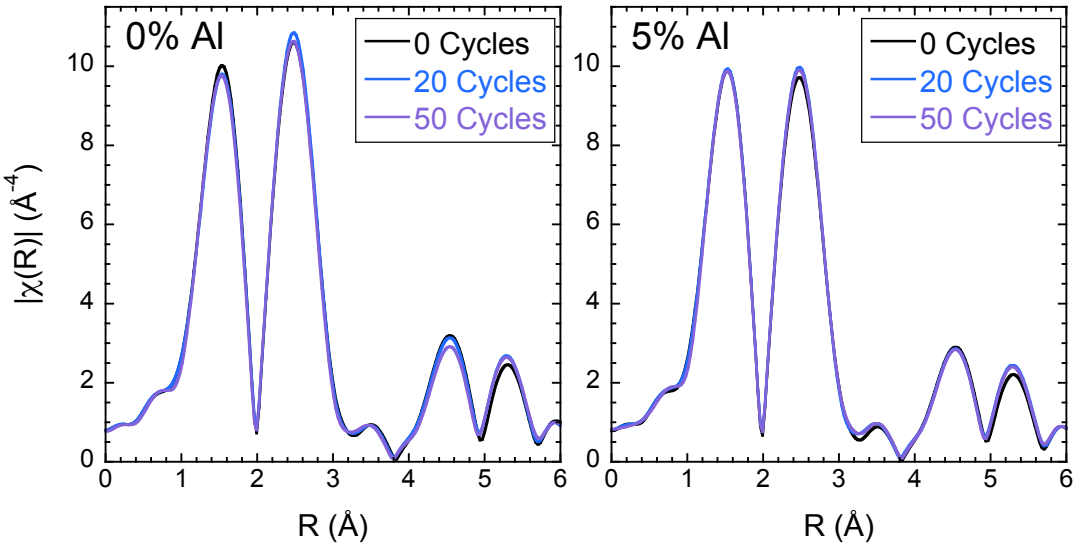

Figure 4-27: Magnitudes of the Fourier transformed k^3-weighted Mn K-edge EXAFS of fresh and cycled $LiNi_{0.45}Mn_{0.45}Co_{0.1-y}Al_yO_2$ electrode materials with a) y=0 (left) and b) y=0.05 (right).

The results of fitting the Fourier transformed spectra are presented in Figure 4-28. The calculated Mn-O bond distances do not vary significantly with cycling, and the differences are minimal between the y=0 and y=0.05 materials. The slight decrease observed for both $LiNi_{0.45}Mn_{0.45}Co_{0.1-y}Al_yO_2$ (y=0, 0.05) materials is not beyond the uncertainties of the fits. The Ni-O bond length of the parent material, however, decreases after 50 cycles, while that of the Al-substituted material does not. The difference is significant, and likely contributes to the improved electrochemical reversibility of the latter material – i.e. more complete reduction to Ni^{2+} is observed on discharge. The

calculated *M-M'* bond lengths are shown in Figure 4-28b. The y=0 and y=0.05 materials behave very similarly within the uncertainties of the data fits.

X-ray Absorption Spectroscopy is a powerful technique to probe the local geometric and electronic structures of the $LiNi_{0.45}Mn_{0.45}Co_{0.1-y}Al_yO_2$ materials. Analysis of the fresh materials ($0 \leq y \leq 0.1$) reveals a homogeneous distribution of Al in the substituted samples. A decrease in octahedral distortion of the transition metal environments is observed, providing further evidence of the strain-lowering effect. The charging mechanism is not obviously influenced by Al-substitution on the local scale probed here, but there is a structural consequence detected in the electrochemically cycled materials. The presence of Al enhances the cycling stability of the electrode materials, and can be seen to limit the deviation of the local structure of the substituted samples compared to the fresh layered oxides.

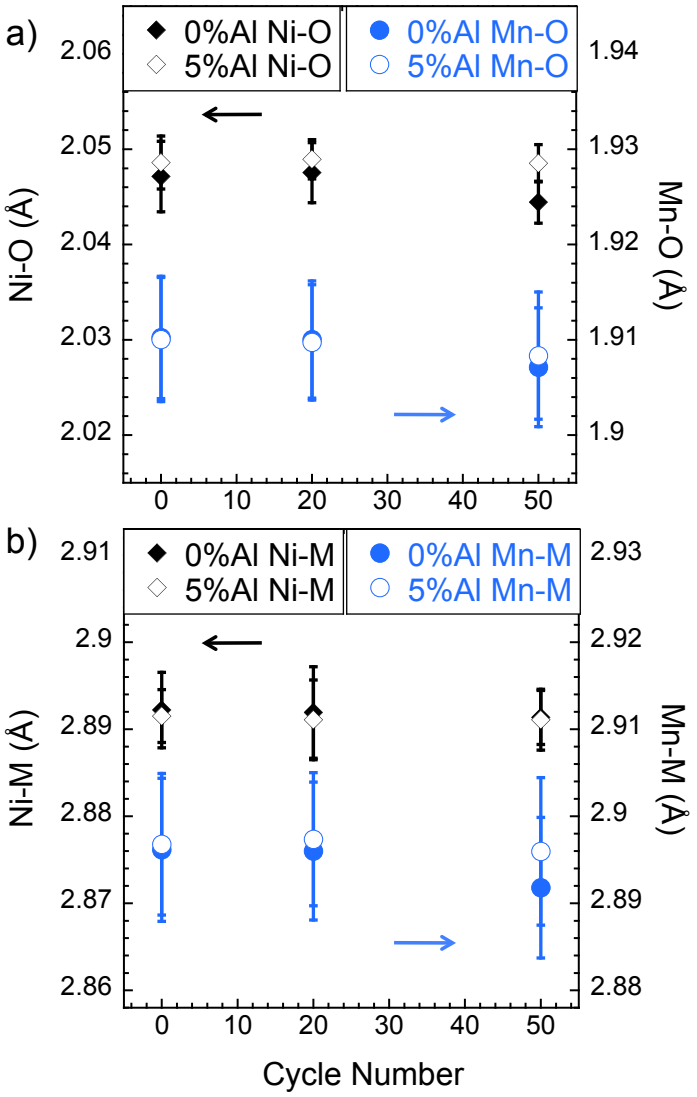

Figure 4-28: Fitted values of the a) first (*M*-O) and b) second (*M-M'*) coordination shells for the fresh and cycled $LiNi_{0.45}Mn_{0.45}Co_{0.1-y}Al_yO_2$ electrode materials (y=0, 0.05).

4.6 References

[1] G. Bunker, *Introduction to EXAFS*, Cambridge University Press, Cambridge, UK. **2010**

[2] F. De Groot. *Chem. Rev.* **2001,** *101,* 1779.

[3] S. Bare, "XANES Measurements and Interpretation." **2008.** Available at: http://xafs.org/Workshops/APS2008?action=AttachFile&do=get&target=Bare_XANES.pdf. Accessed 1/1/12.

[4] M. Newville, "Fundamentals of EXAFS." Revision 1.7, **2004.** Available at: http://xafs.org/Tutorials?action=AttachFile&do=get&target=Newville_xas_fundamentals.pdf. Accessed 1/1/12.

[5] S. D.Kelly, D. Hesterberg, B. Ravel. "Analysis of soils and minerals using X-ray absorption spectroscopy," in *Methods of Soil Analysis, Part 5 -Mineralogical Methods*; Ulery, A. L., Drees, L. R., Eds.; Soil Science Society of America: Madison, WI, USA, 2008; pp 367.

[6] E. Stern. *Phys. Rev. B,* **1974,** *10,* 3027.

[7] D. Sayers et al. *Phys. Rev. Lett.* **1971,** *27,* 1204.

[8] E. Stern et al. *Phys. Rev. B,* **1975,** *11,* 4836.

[9] F. Lytle et al. *Phys. Rev. B,* **1975,** *11,* 4825.

[10] G. Li, F. Bridges, C.H. Booth. *Phys. Rev. B,* **1995,** *52,* 6332.

[11] B. Ravel, M. Newville. *J. Synchrotron Rad.* **2005,** *12,* 537.

[12] M. Newville. *J. Synchrotron Rad.* **2001,** *8,* 322.

[13] S. I. Zabinsky, et al. *Phys. Rev. B,* **1995,** *52,* 2995.

[14] FEFF Project: http://leonardo.phys.washington.edu/feff/. Accessed 1/1/12.

[15] J. Rehr, R. Albers. *Rev. Mod. Phys.* **2000,** *72,* 621.

[16] S. DeBeer, et al. *J. Phys. Chem. B,* **2000,** *104,* 10814.

[17] DuBois et al. *J. Am. Chem. Soc.* **1997,** *119,* 8578.

[18] Kronig, R. de L. *Z. Phys.* **1931,** *70*, 317.

[19] Kronig, R. de L. *Z. Phys.* **1932,** *75*, 191.

[20] F. Lytle. *J. Synchrotron Rad.* **1999,** *6,* 123.

[21] J. D. Hanawalt. *Phys. Rev.* **1931,** *37,* 715.

[22] I. Kostarev. *Zh. Eksperim. Teor Fiz.* **1941,** *11*, 60.

[23] T. Shiraiwa, T. Ishimura, M. Sawada. *J. Phys. Soc. Jpn*. **1958,** *13,* 847.

[24] E. A. Stern. *J. Synchrotron Rad.* **2001,** *8,* 49.

[25] W. Yoon et al. *Electrochem. Solid State Lett.* **2002**, *5*, A263.

[26] W. Yoon et al. *Electrochem. Solid State Lett.* **2004,** *7,* A53.

[27] J. Reed, G. Ceder. *Electrochem. Solid State Lett.* **2002**, *7*, A145.

[28] M. S. Islam, R. Davies, J. Gale. *Chem. Mater*. **2003**, *15*, 4280.

[29] Y. Tsai et al. *Chem. Mater.* **2005,** *17,* 3191.

[30] W. Yoon et al. *Chem. Mater.* **2003,** *15,* 3161.

[31] P. Liao et al. *Electrochimica Acta,* **2007,** *53,* 1850.

[32] J. Kim, H. Chung. *Electrochimica Acta,* **2004,** *49,* 937.

[33] W. S. Yoon et al. *J. Am. Chem. Soc.* **2005,** *127,* 17479.

[34] C. Rumble, T. E. Conry, et al. *J. Electrochem. Soc.* **2010,** *157,* A1317.

[35] M. Kim et al. *J. Electrochem. Soc.* **2005,** *152,* A1320.

[36] H. Kobayashi et al. *J. Power Sources,* **2005,** *146,* 640.

[37] J. McBreen. *J. Solid State Electrochem.* **2009,** *13,* 1051.

[38] M. Newville, et al. *Phys. Rev. B*, **1993,** *47,* 14126.

[39] J. Rehr, S. Zabinsky, R. Albers. *Phys. Rev. Lett.* **1992,** *69,* 3397.

[40] D. Zeng et al. *Chem. Mater.* **2007,** *19,* 6277.

[41] J. Bréger et al. *Chem. Mater.* **2006,** *18,* 4768.

[42] R. Shannon. *Acta Cryst. Section A: Crystal Physics, Diffraction, Theoretical and General Crystallography*, **1976**, *32,* 751.

[43] P. Willmott. *An Introduction to Synchrotron Radiation: Techniques and Applications.* John Wiley & Sons, West Sussex, UK, **2011.**

[44] Product sheets for metal nitrate precursors: Nickel(II) nitrate hexahydrate: http://www.sigmaaldrich.com/catalog/DataSheetPage.do?brandKey=ALDRICH&symbol=203874; Cobalt(II) nitrate hexahydrate: http://www.sigmaaldrich.com/catalog/ProductDetail.do?lang=en&N4=239267|SIAL&N5=SEARCH_CONCAT_PNO|BRAND_KEY&F=SPEC

[45] M. Aydinol et al. *Phys. Rev. B,* **1997**, *56,* 1354.

[46] D. Abraham et al. *Electrochem. Commun.* **2002**, *4,* 620.

[47] D. Abraham et al. *J. Electrochem. Soc.* **2003**, *150,* A1450.

[48] N. Yabuuchi et al. *J. Electrochem. Soc.* **2007**, *154,* A566.

Chapter 5: Spray Pyrolysis of Olivine Materials

5.1 Spray Pyrolysis

Spray pyrolysis is a simple, scalable, and inexpensive material synthesis technique. The method has, rather unsurprisingly, become popular among Li-ion materials researchers, but is only recently being incorporated in industrial battery processes. Spray pyrolysis falls under the umbrella of aerosol processing techniques, which are versatile procedures that can be used to manufacture powders, thin films, coatings, or even larger solids. An aerosol is a suspension of solid or liquid particles in a gas, and is exploited during processing. For example, chemical vapor deposition (CVD) techniques utilize vaporized precursors to deposit thin films and coatings, while spray drying methods are used to produce particles from solutions or slurries containing thermally-sensitive materials, such as pharmaceutical compounds.[1]

Spray pyrolysis processes are a subset of these aerosol-based techniques. The method generally involves the mechanical formation of liquid droplets or dry particles ranging in size from sub-nanometer up to a hundred microns in a gas, which are subsequently passed into or through a hot furnace zone, flame, or some other thermal energy source. The precursor particles or droplets subsequently react – after evaporation of the solvent, if relevant – to generate the desired final powder, film, or coating. Spray pyrolysis itself has become a somewhat broad term. Technically, pyrolysis defines a process by which substances (usually organic) decompose at high temperatures, without the participation of oxygen.[2,3] Spray pyrolysis, however, has come to encompass most synthesis procedures involving thermally induced intraparticle reactions within the generated droplets; these include combustion, decomposition, or chemical reactions (including those in the gas phase).[1] These spray pyrolysis processes are sometimes equivalently referred to as particle-to-particle conversion or liquid/solid-to-solid conversion.

As the thermal or chemical reactions occur within each droplet or particle, spray pyrolysis processes have an inherent advantage over other synthesis techniques in producing chemically homogenous multicomponent materials such as complex oxides. Each droplet or particle in the precursor suspension already contains the correct stoichiometry for the final product, prior to aerosol generation. The pre-determined stoichiometry allows a versatile range of components to be processed. Gas-to-particle aerosol processes like CVD, by contrast, rely on nucleation and growth to generate particles, which can be quite difficult to control when many different species are involved. This is especially important in the production of Li-ion battery materials, which often contain many components – the $LiNi_{0.45}Mn_{0.45}Co_{0.1-y}Al_yO_2$ materials that were discussed in the previous chapters, for instance, have six elemental species. Due to the high temperatures at which the processes are carried out, high purity and excellent crystallinity are almost always achieved.[1]

Spray pyrolysis offers substantial command over not only the final product composition and crystallinity, but also particle size and morphology through the appropriate choice of processing conditions. Hollow, porous, or dense particles can be produced with very narrow size distributions, spanning the nano to micro scales. The

final product morphologies are strongly dependent on the details of the production schemes, such as the precursor chemistries, solvent volatility, initial droplet size, gas/particle flow rates, and reaction temperatures.[1]

This wide jurisdiction over the final product makes spray pyrolysis quite attractive when compared to solid state or solution precipitation synthesis techniques. It is very difficult to avoid agglomeration or particle coarsening during solid state synthesis, which requires the exposure of the precursor materials to high temperatures for long times. Spray pyrolysis, on the other hand, allows production of small, highly crystalline particles without the need for secondary processing. Stoichiometric control can be difficult during precipitation from liquid-phase precursors, and the liquid solutions can contain expensive components. As mentioned, stoichiometric control on a per-particle scale is achieved in spray pyrolysis, for which aqueous precursors are commonly used. Both solid state and liquid-precipitation methods tend to be batch processes, while spray pyrolysis can be a continuous process.

In addition to a number of other technologically important mixed-metal oxides and ceramics,[4,5,6] the production of many Li-ion battery materials by various spray pyrolysis methods has been demonstrated in the laboratory. The technique is attractive because homogeneous particles with complex stoichiometries, such as those used in electrode materials, can easily be produced. Layered oxides including $LiCoO_2$,[7] $LiNi_{1/3}Mn_{1/3}Co_{1/3}O_2$,[8,9,10] and spinel materials such as $LiMn_2O_4$,[10,11,12] $LiNi_{0.5}Mn_{1.5}O_4$,[10,13,14] and $Li_4Ti_5O_{12}$[10,15,16] have all been synthesized this way with high purity, and show good electrochemical properties. A significant advantage is, again, the simple, scalable, and comparatively fast manufacturing of spray pyrolysis processing. Olivine materials such as $LiFePO_4$,[17,18] $LiMnPO_4$,[19,20] and others[21] have also been produced quite successfully as well. The synthesis of various olivine materials by spray pyrolysis is the focus of this chapter, and will be further discussed in detail in the upcoming sections.

In our laboratory, a custom spray pyrolysis system was designed and built by the author. The basic necessities of a spray pyrolysis system are straightforward: a means of producing an aerosol of liquid droplets, a hot zone for thermally-induced reactions, a flowing gas or other means of transport of the aerosol though the hot zone, and a product collection scheme. The system designed and used in these studies, a schematic of which is shown in Figure 5-1a, was initially built and iteratively improved with simple and readily available laboratory equipment. Aerosol formation is achieved by steadily passing a precursor solution through an atomizer nozzle, delivered via a syringe pump. A modified end-cap allows aerosol delivery into an isolated reaction zone (Fig. 5-1b). A carrier gas is used to transport the droplets through the reaction zone, in this case a tube furnace using a standard quartz tube. Particles produced in the reaction are collected at the end of the tube, utilizing a Ni mesh filter used to catch passing particles. This spray pyrolysis system is arranged horizontally on a tabletop, with gas flow along the tube axis. Gravity allows some of the product to settle along the length of the tube before reaching the Ni mesh filter, thus particle collection proceeds piecewise along the tube, to ensure the collection of a homogeneous product.

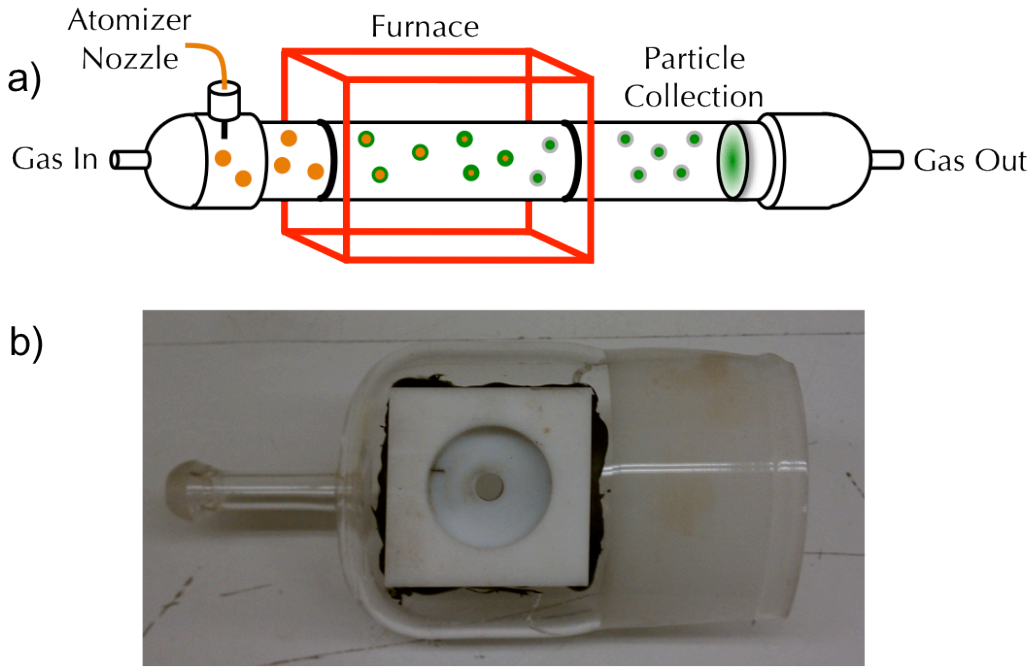

Figure 5-1: a) Schematic of the custom-built spray pyrolysis system. b) Picture of the modified furnace end cap showing the holder attachment for the atomizer nozzle.

5.2 Spray Pyrolysis of $LiFePO_4$

As discussed in Chapter 1, metal phosphate materials with the olivine structure have garnered intense focus from both the research and industrial communities. The most widely used and investigated is $LiFePO_4$, which is now produced commercially since the original paper regarding its use as a Li-ion cathode material appeared in 1997.[22] $LiFePO_4$ displays excellent cycling stability, and the material has very good electrochemical and thermal stability.[23] Additionally, the operating voltage (3.45 V vs. Li/Li^+) is well below the oxidation limit of the carbonate-based electrolytes commonly used today.

$LiFePO_4$ is also a relatively inexpensive material (based on raw materials costs), and coupled with spray pyrolysis production can allow for low cost manufacturing. Many investigations have produced $LiFePO_4$ via spray pyrolysis. Most studies have required a post-processing heat treatment to achieve the desired olivine phase or to remove impurities, and result in irregularly-shaped solid products with micron-scale dimensions and low specific surface areas <20 m^2/g.[24,25,26,27] Despite the incorporation of carbon-coatings, either during or after synthesis of the main phase, the materials cited display only moderately good electrochemical properties, with the best delivering low discharge capacities of about 140 mAh/g (theoretical is 170 mAh/g). Post-synthesis ball milling to produce nanoparticles has been shown to improve the electrochemical behavior, though post-processing somewhat negates the benefits of using the spray pyrolysis technique.[28]

As mentioned in Chapter 1, $LiFePO_4$ has very low values of electronic conductivity (10^{-10} S/cm) and ionic (Li^+) conductivity (10^{-13} S/cm). These intrinsic impediments have been mitigated by various engineering approaches. Reducing particle sizes to the nano-regime (by ball milling, like above) and encapsulating the $LiFePO_4$ powders with conductive agents, most commonly carbon, are established methods of improvement.[29,30] Nanostructuring the material limits the Li-ion diffusion distances from the particle bulk to the solid/electrolyte interface, at which the oxidation and reduction reactions occur. Carbon coating provides a complimentary electronically conductive network to facilitate charge transfer.

While the above approaches improve performance, nanostructuring and carbon coating complicate processing of composite electrode structures. In contrast to the nanoparticles ideal for material performance, battery manufacturers prefer spherical micron-sized particles for electrode production. Micron-sized particles not only remove some of the health and safety concerns that accompany the use of nanoparticle materials, but (spherical) microparticles also pack more densely than nanomaterials, improving the energy density (Wh/l) of the manufactured electrodes. Porous, micron-sized particles can help circumvent this paradox; increasing the surface area per particle limits the diffusion distances necessary for the redox reactions while maintaining the processing-friendly size characteristics.

There are several reports of porous micro-scale $LiFePO_4$ and $LiFePO_4$/C composite materials. Jamnik et al. pioneered the synthesis of three-dimensionally nanoporous $LiFePO_4$ using a sol–gel method.[31,32] More recently, Doherty et al. also obtained 3D nanoporous $LiFePO_4$ using templates.[33,34] These porous $LiFePO_4$ materials are not spherical, however, compromising their packing density and ease of electrode casting.[35] Oh et al.[36] and Qian et al.[37] have reported the preparation of nanoporous spherical micron-sized $LiFePO_4$ materials, but the pores in both cases are not well interconnected, resulting in some ‘‘dead” pores’ and thus ineffective access of the electrolyte into the bulk of the $LiFePO_4$ particles.

This previous work has been improved upon here through the production of porous, spherical micron-sized-diameter $LiFePO_4$/C composite particles by spray pyrolysis. The method has not previously been used to produce particles with a well-interconnected porosity. The particles, synthesized using the custom-built spray pyrolysis system described above, are composed of nanosized $LiFePO_4$ primary particles with a conformal carbon coating that provides an electronically conductive network. These composite particles contain a three-dimensional (3D) hierarchical pore structure that penetrates throughout the entire particle volume, while maintaining micron-scale secondary particle sizes for ease of handling and improved packing density.

Synthesis and Experimental Details

A schematic of the synthesis procedure is shown in Figure 5-2. Water-soluble precursors $Fe(NO_3)_3 \cdot 9H_2O$, $LiNO_3$, $NH_4H_2PO_4$, and citric acid ($HOC(COOH)(CH_2COOH)_2$) were dissolved in a minimum amount of de-ionized water in a molar ratio of 1:1:1:2, respectively, to form an aqueous precursor solution. The citric acid molecule contains functional groups able to complex with the metal ions, similar to glycine (Chapter 2), thus producing an intimately mixed precursor solution.

This solution was delivered via syringe pump to an atomizer nozzle (Sonozap Model 120K50ST, 120 kHz), at a rate of about 0.8 mL/min. An aerosol of microdroplets is generated at the tip of the nozzle, which was subsequently transported through a heated quartz tube (700°C) by a carrier gas (5% H_2 + 95% N_2). The forming gas was utilized to promote Fe-reduction from the Fe^{3+} used in the precursor solution to the desired Fe^{2+} in $LiFePO_4$ during the synthesis.

As the droplets travel through the heated tube, rapid evaporation of water concentrates the precursor until a self-sustaining combustion reaction occurs, resulting in the desired $LiFePO_4$ phase. Additionally, some residual carbon from the decomposition of excess organic components remains in the generated product, leaving, as will be shown, a thin, conformal carbon coating. Previous work has shown that citric acid, a comparatively bulky molecule, results in an optimized carbon coating,[38] though organic ingredients such as glycine ($C_2H_5NO_2$), urea (CH_4N_2O), or sucrose ($C_{12}H_{22}O_{11}$) can also be used.[39]

The evolution and escape of gaseous reaction by-products (mostly NO_X, CO_2, and H_2O)[39] during the synthesis step helps to create an interconnected pore structure throughout the generated particles. The $LiFePO_4$/C composite material was collected from the end of the tube. A further heat treatment at 700 °C in N_2 for 2h was used to improve the conductivity of the residual carbon coating.

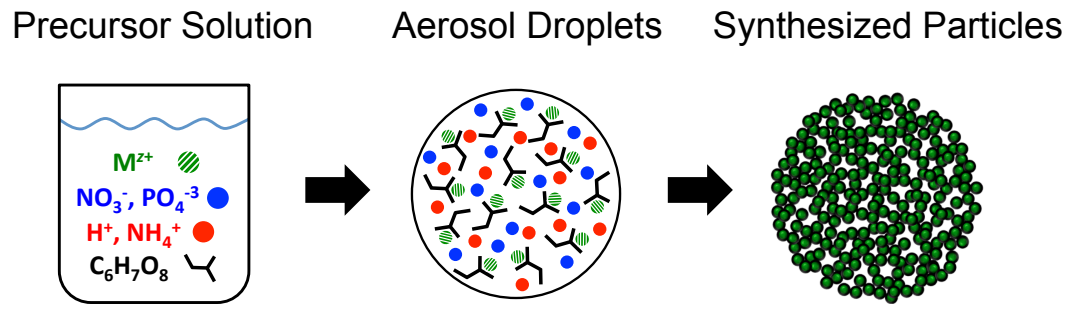

Figure 5-2: Schematic of the particle formation process.

Composite electrodes were prepared by mixing 85 wt % $LiFePO_4$/C composite material with 10 wt % carbon black and 5 wt % polytetrafluoroethylene (PTFE) binder. The slurry was rolled into thin sheets and dried in a vacuum oven at 120°C overnight. Circular electrodes (1.26 cm^2 area) were cut, each with a typical active material loading of 4-5 mg. Size 2032 coin cells were assembled with the composite cathodes, metallic lithium anodes, 1 M $LiPF_6$ in 1:1 diethyl carbonate/ethylene carbonate electrolyte, and two pieces of Celgard 2500 polypropylene separator. Cells were cycled between 2.0 and 4.3 V for electrochemical testing.

Material Characterization

The XRD pattern and Rietveld refinement of the nanoporous $LiFePO_4$/C composite material are shown in Figure 5-3, with the refinement results summarized in Table 5-1. All observed diffraction peaks could be indexed in the orthorhombic space group *Pnma* characteristic of the olivine materials, and the calculated parameters are in

agreement with other reported values.[40] The good fit between the observed and calculated patterns is consistent with the absence of substitutional defects, and refinement of the lithium site occupancy factor does not indicate the presence of iron on this site. The average primary $LiFePO_4$ particle size, determined from peak broadening, is about 72 nm.

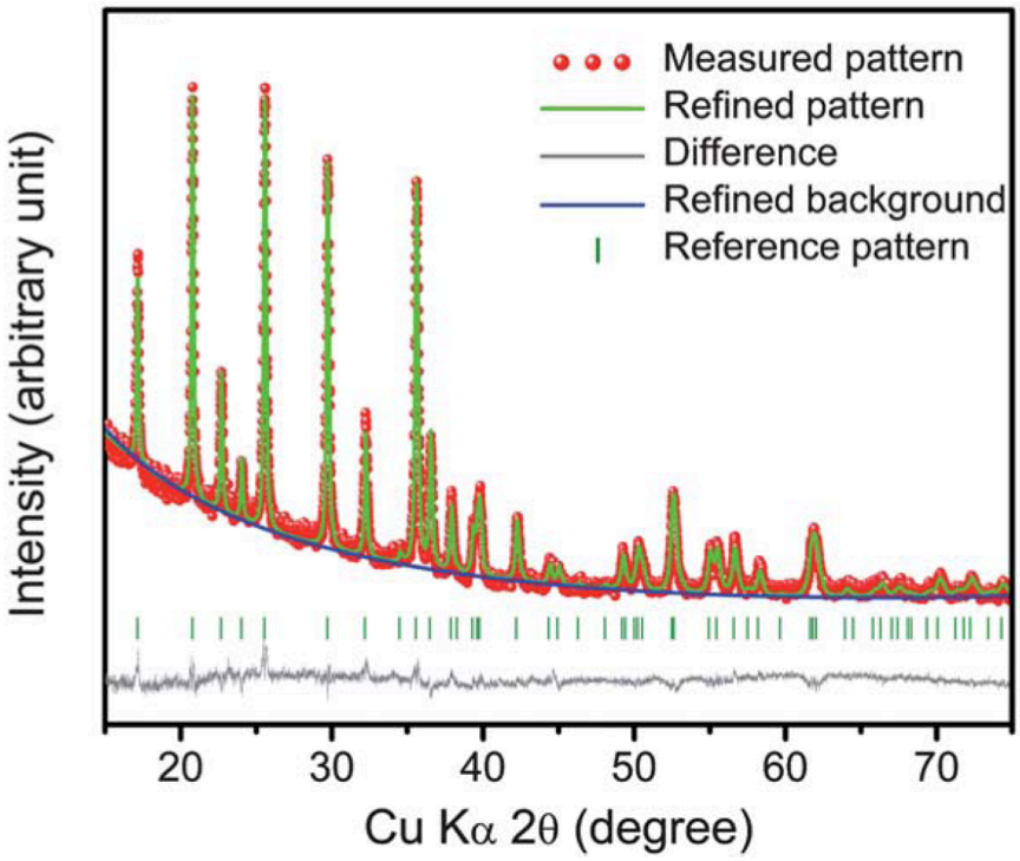

Figure 5-3: XRD pattern and Rietveld refinement of the $LiFePO_4$/C composite material.

Table 5-1: Rietveld refinement results for spray pyrolysis $LiFePO_4$/C

Parameter	Value	Uncertainty
a	10.3248 Å	0.0003 Å
b	6.0053 Å	0.0002 Å
c	4.6921 Å	0.0002 Å
V	290.90 Å^3	0.01 Å^3
R	5.63 %	
R_{wp}	6.88 %	

The scanning electron microscopy (SEM) images in Figure 5-4 show that all of the particles are spherical, with diameters ranging from about 2 to 10 μm. Figure 5-4b illuminates the porous surface of an individual particle in which the varying pore sizes can be observed, the largest having diameters <500 nm. Particles were purposely fractured to reveal the inner structure by mechanically grinding the material. The cross-sectional images shown in Figures 5-4c and d display the three-dimensionally interconnected porosity of the $LiFePO_4$/C composite particles, which clearly extends from the surface to the center of the spherical particles. This interconnected pore structure is important; it allows the liquid electrolyte to penetrate into the particles when assembled into batteries, limiting the necessary solid-state diffusion distance of Li-ions during charge and discharge.

Elemental mapping by energy dispersive X-ray spectroscopy (EDS) of a single $LiFePO_4$/C particle is shown in Figure 5-5. The distribution of Fe, P, and O are quite uniform. Carbon is additionally observed to be well distributed over the entire surface of the observed particle, as would be expected for a well-interconnected conducting network throughout the structure. Further evidence of the conformal coating is provided below.

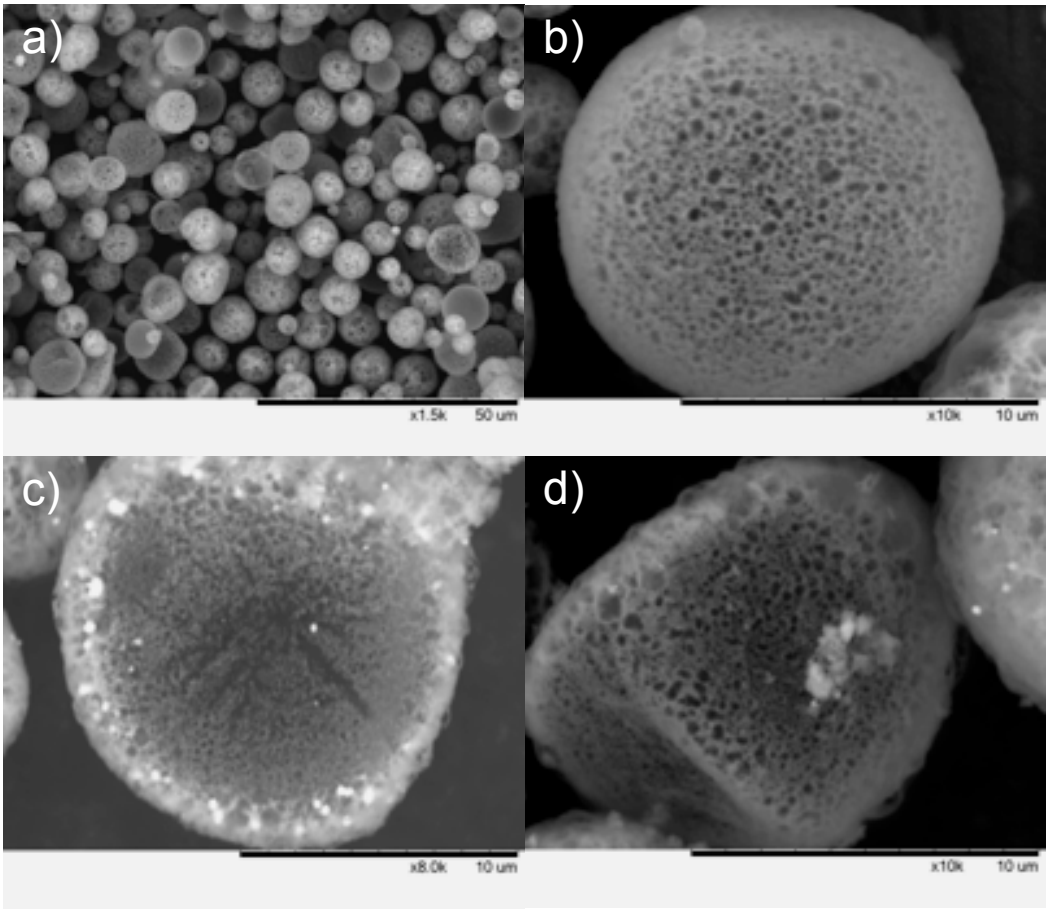

Figure 5-4: SEM images of the $LiFePO_4$/C particles. The porous structure can be seen in (b-d).

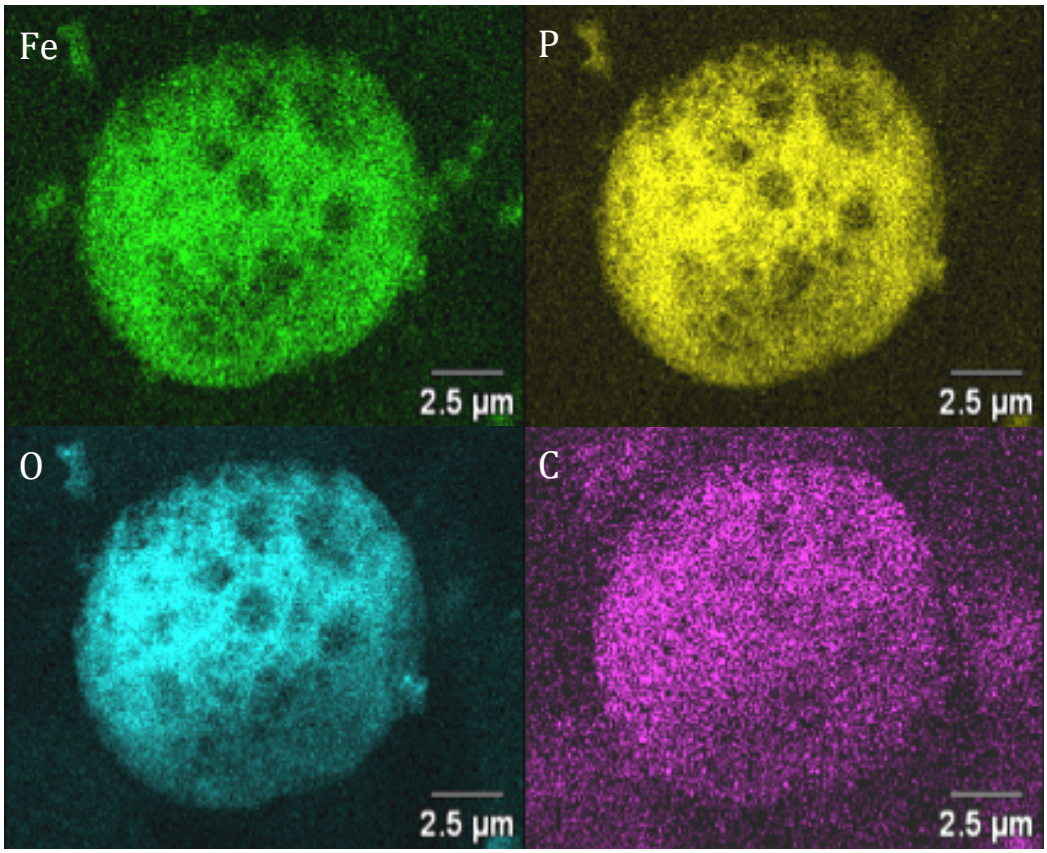

Figure 5-5: EDS images of a single $LiFePO_4$/C particle.

The detailed microstructure of the coated surfaces could be observed by high-resolution transmission electron microscopy (HRTEM). The $LiFePO_4$/C particles were previously fractured by mechanical grinding to allow observation of the particle interior. In Figure 5-6, an amorphous, conformal carbon layer with a thickness of 3–5 nm is clearly seen on the surfaces of the highly crystalline $LiFePO_4$ primary particles. This carbon coating provides a conductive network throughout the micron-diameter composite particles. This is important for electrochemical performance because it ameliorates the effects of the highly insulating (both electronically and ionically) nature of the $LiFePO_4$.

Accurate evaluation of the $LiFePO_4$/C composite material cannot be achieved, however, without knowledge of the specific carbon-content contained in the as-synthesized materials. The inherent weight distribution between carbon and $LiFePO_4$ was measured using thermogravimetric analysis (TGA). A TGA calibration curve is needed, though, because $LiFePO_4$ has an observed weight increase upon heating to 700°C in an oxygen environment, due to the formation of Fe_2O_3 and $Li_3Fe_2(PO_4)_3$ (Eqn. 5-1).[41] For calibration, the weight change of pure (carbon-free) $LiFePO_4$ is measured upon heating to 700°C. The carbon-free material was provided as a gift from Hydro-Quebec, a large government-owned corporation, which provides electricity in Quebec province. (Hydro-Quebec has a long history of synthesis and development of $LiFePO_4$).[42] This relative change is then compared to the weight changes of the same $LiFePO_4$ material

mechanically mixed with various amounts of added carbon – 2.5, 5, and 10 wt % (Fig. 5-7a). The TGA curve of the nanoporous $LiFePO_4$/C composite material is consistent with oxidation of iron and carbon, allowing the amount of carbon in the original sample to be calculated (Fig. 5-7b).

$$12LiFePO_4 + 3O_2 \rightarrow 4Li_3Fe_2(PO_4)_3 + 2Fe_2O_3 \qquad \text{(Eqn. 5-1)}$$

As an important check, the X-ray diffraction (XRD) patterns of all samples after heating to 700°C during the TGA tests were measured, and are identical (Figure 5-7c). Thus, it is assumed that all of the carbon decomposes during the experiment, and the $LiFePO_4$ component reacted completely. By normalizing the measurements against the weight increase of the carbon-free $LiFePO_4$, the relative weight loss of all samples was found to vary linearly with carbon content, thus resulting in a simple calibration curve. Comparison of the observed 8.1% relative weight loss of the as-synthesized novel material with the calibration curve shown in Figure 5-7d suggests a carbon content of approximately 7.2 wt% present in the nanoporous $LiFePO_4$/C particles.

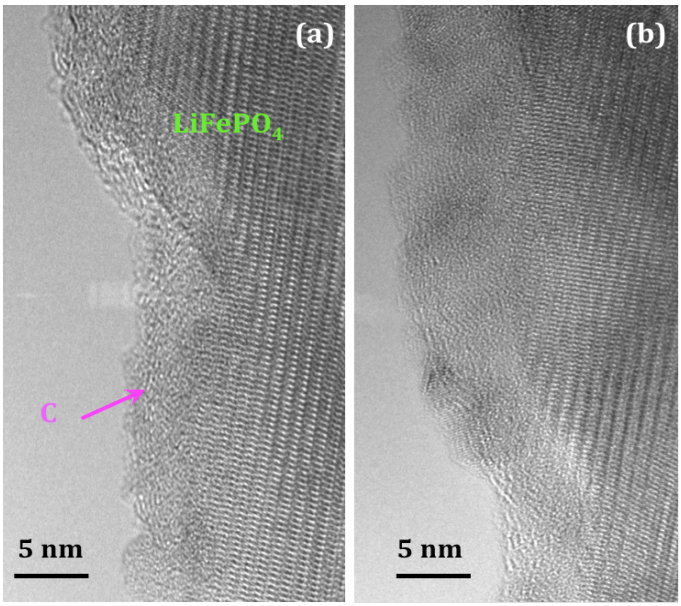

Figure 5-6: TEM images of a single $LiFePO_4$/C particle. The conformal carbon coating can be seen.

N_2 adsorption/desorption isotherms, shown in Figure 5-8, were used to determine a Brunauer–Emmett–Teller (BET) surface area of 102 m^2/g and an average pore size of 75 nm diameter for the nanoporous $LiFePO_4$/C particle material. The type IV curve with a large H3 hysteresis loop is consistent with N_2 adsorption in a nanoporous material.[43] The loop closes abruptly at P/P°=0.42, corresponding to the emptying of pores with small apertures into the intergranular void space. Based on the measured porosity and particle morphology, an estimated upper limit for the tap density of the $LiFePO_4$/C composite material is 0.82 g/cm^3.

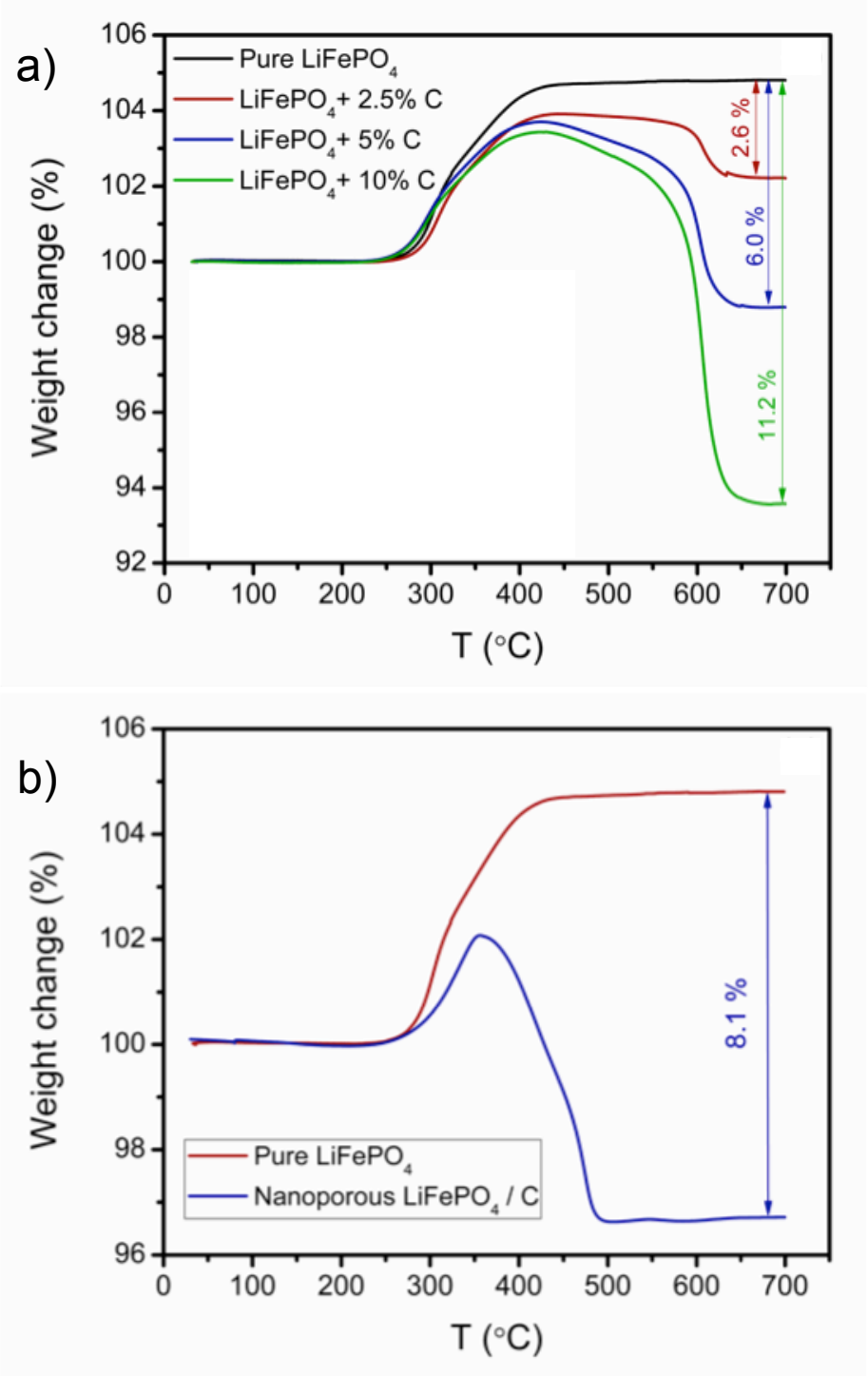

Figure 5-7: a) TGA curves of pure (C-free) $LiFePO_4$ and $LiFePO_4$ mixed with various amounts of carbon. b) TGA curves of the pure material and $LiFePO_4$/C composite particles. c) XRD patterns of the heated materials are all identical. d) Calibration curve used to determine the C-content of the $LiFePO_4$/C composite materials.

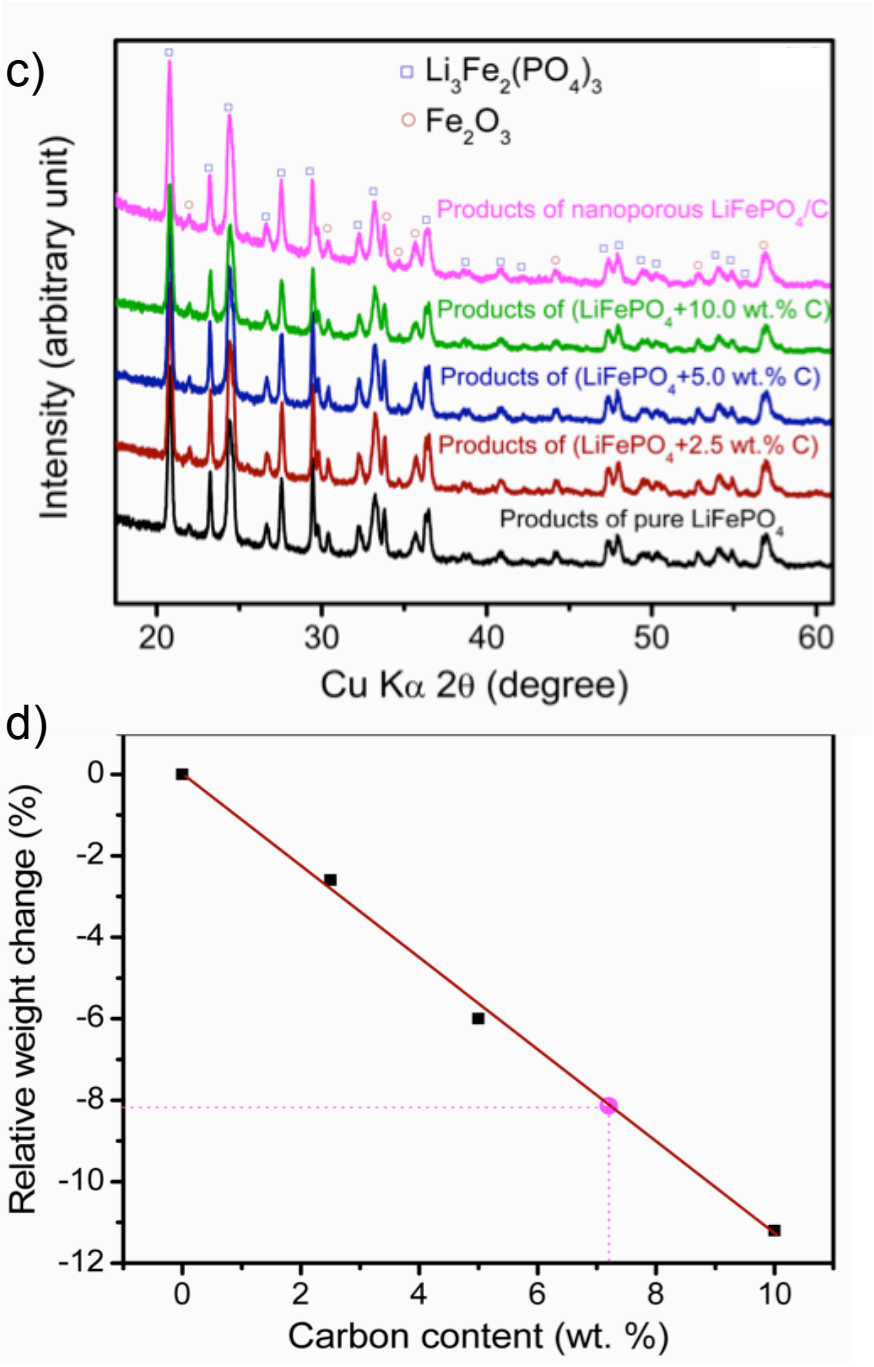

Figure 5-7 (cont'd): a) TGA curves of pure (C-free) $LiFePO_4$ and $LiFePO_4$ mixed with various amounts of carbon. b) TGA curves of the pure material and $LiFePO_4$/C composite particles. c) XRD patterns of the heated materials are all identical. d) Calibration curve used to determine the C-content of the $LiFePO_4$/C composite materials.

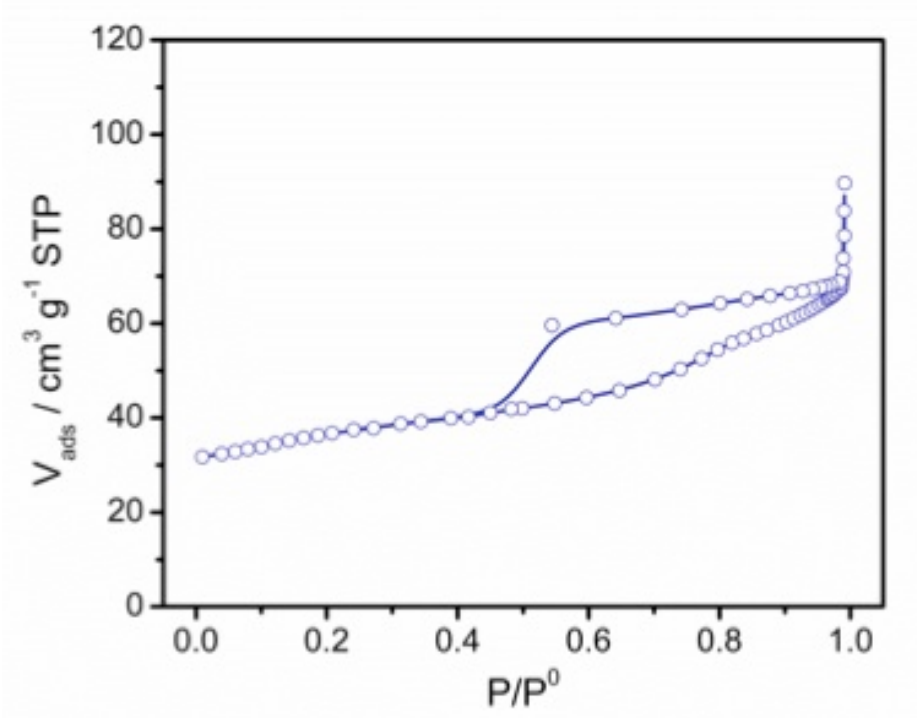

Figure 5-8: N_2 adsorption/desorption isotherms of the porous $LiFePO_4$/C composite particles.

Electrochemical Performance

The porous nature of the $LiFePO_4$/C composite material, with the nanosized primary particles and conformal carbon coating distributed throughout the material, leads to excellent electrochemical performance. Figure 5-9 shows the behavior of the nanoporous $LiFePO_4$/C composite material cycled at different C-rates. At low current density (20 mA/g = C/8), the composite electrode can deliver a capacity of 153 mAh/g. Taking into account the intrinsic carbon content (7.2 wt %), this corresponds to 165 $mAh/g_{LiFePO4}$, which is very close to the theoretical capacity of $LiFePO_4$ (170 mAh/g). The average coulombic efficiency (Fig. 5-9a, inset) is 99.8% during cycling, indicating highly reversible lithium insertion/extraction kinetics (and the lack of significant side reactions). Even at high current density (1700 mA/g = 10C), the material delivers over 120 mAh/g, with 98% capacity retention over 100 cycles (Fig. 5-9b). The average coulombic efficiency is 99.2%.

The rate capability of the nanoporous $LiFePO_4$/C composite material is presented in Figure 5-10. Capacities as high as 123 mAh/g and 106 mAh/g are achieved at 10C and 20C, respectively. This performance is among the best reported for $LiFePO_4$/C systems,[44,45] and is attributed to the porous structure of the particles that permits electrolyte access throughout the particle bulk. This structure realizes the advantages of nanosized primary particles, such as short diffusion distances, as well as the conformal carbon coating that forms an electronically conductive network throughout the particles. The impressive performance demonstrates the composite material's potential use for high power applications, such as HEV's and PHEV's, especially in light of the simple and scalable spray pyrolysis synthesis method that can potentially lower production costs of this material.

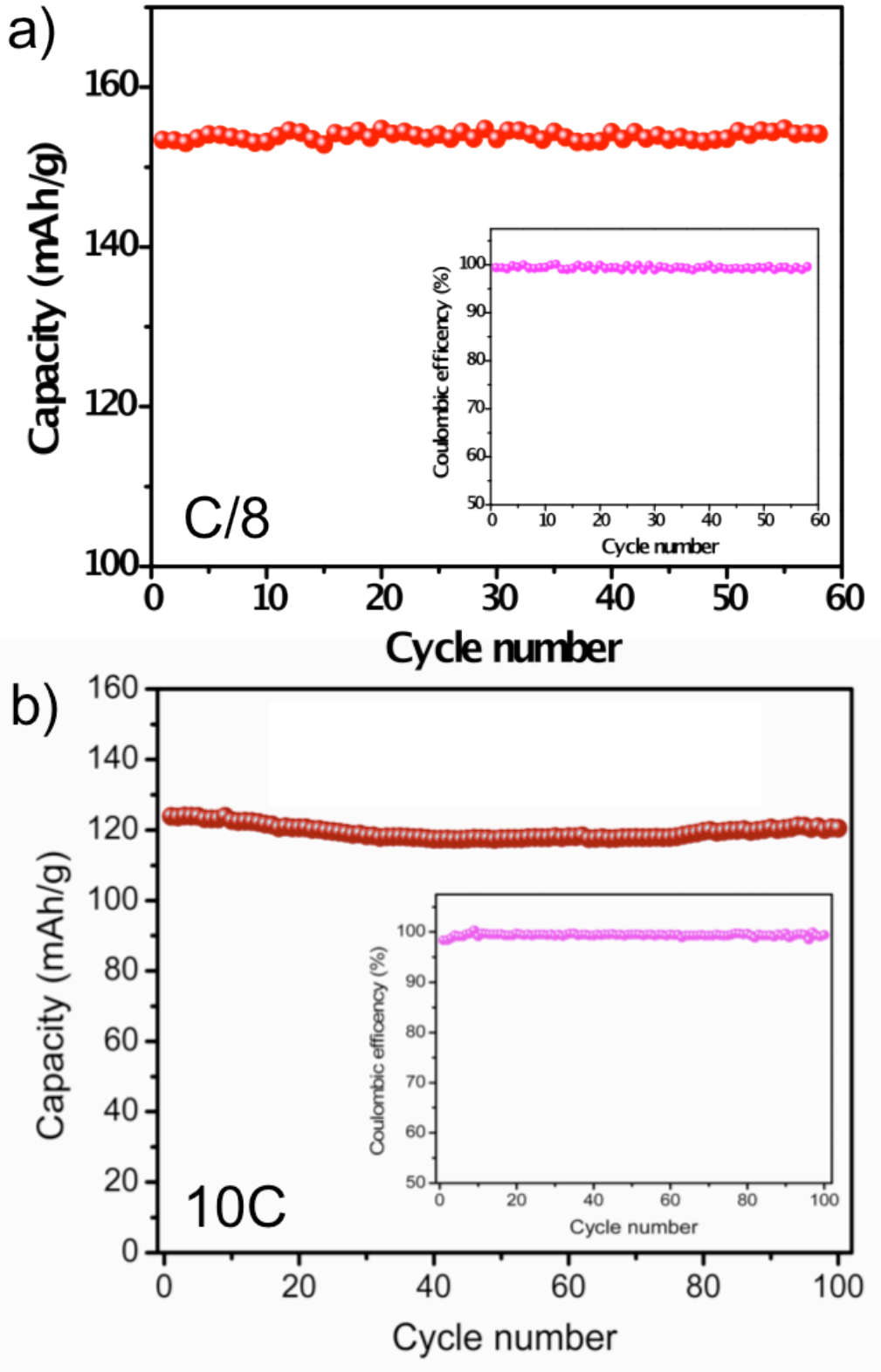

Figure 5-9: Discharge capacities as a function of cycle number for cells cycled at a) C/8 and b) 10C rates. The insets show the corresponding coulombic efficiencies.

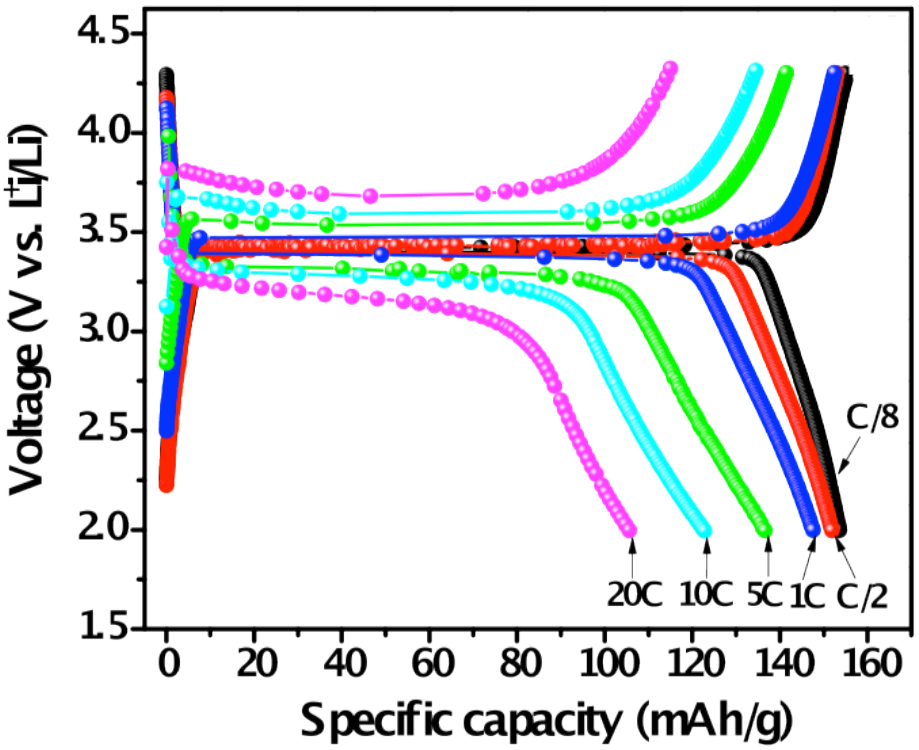

Figure 5-10: Charge and discharge profiles of the $LiFePO_4$/C electrode materials at various rates. The materials display excellent rate capability.

5.3 Spray Pyrolysis of $LiCoPO_4$

There has been substantially less work on $LiCoPO_4$ with the olivine structure. $LiCoPO_4$, as described in Chapter 1, is a high voltage cathode material that operates at a potential of ~4.8 V vs. Li/Li^+; this can enhance the energy density of the battery system and thus lower costs, especially those associated with packaging and other inert components. This is particularly significant for the large 300 V battery packs used in EV's, as fewer cells are therefore required for the vehicle power systems.[46,47] The first report on the electrochemical performance of $LiCoPO_4$ was in 2000 by Amine et. al.,[48] $LiCoPO_4$ suffers from the same intrinsic limitations of $LiFePO_4$, namely, very low values of the electronic and ionic conductivities.[49,50] Additionally, the high operating voltage of the material is well beyond the practical voltage stability region (~4.3 V vs. Li/Li^+) of the common non-aqueous electrolytes used in modern Li-ion batteries. Thus, early reports showed discharge capacities of only about 80 mAh/g (theoretical is 167 mAh/g), which quickly faded on subsequent cycles.

Interestingly, a fundamental difference in the Li extraction mechanism from $LiCoPO_4$ was found to exist as compared to other olivine materials like $LiFePO_4$ and $LiMnPO_4$. The latter two materials undergo a two-phase delithiation reaction, with end members of $Li_{1-\alpha}MPO_4$ and $Li_{\beta}MPO_4$ (M=Fe, Mn) close to the fully lithiated and delithiated stoichiometries.[51] This two-phase behavior results in a single, flat (dis)charge

potential curve. $LiCoPO_4$, in contrast, is found to undergo two separate two-phase reactions.[52,53] In this case, two first-order phase transitions corresponding to $LiCoPO_4 \leftrightarrow Li_{0.7}CoPO_4$ and $Li_{0.7}CoPO_4 \leftrightarrow CoPO_4$ result in the observation of two plateaus in the (dis)charge profiles. The different plateaus are only separated by about 100 mV, and thus do not present a major potential change during cell operation. It does, however, represent an underlying difference between otherwise similar olivine materials. The exact cause for the differing phase behavior is not currently understood.[52]

The safety aspects of $LiCoPO_4$ in the charged state are unfortunately not as good as $LiFePO_4$, which, as previously discussed, is one of the safest cathode materials in production.[54] The charged and discharged states of $LiFePO_4$ are both stable against oxygen gas-forming reactions with temperature; the delithiated $FePO_4$, for instance, is stable to at least 600°C, and at higher temperatures transforms to a quartz-like $FePO_4$ structure without evolving oxygen.[55,56] Upon heating Li_xCoPO_4 in a Li-deficient state, however, $Co_2P_2O_7$ is formed with accompanying oxygen evolution. This occurs at temperatures <200°C, which can severely limit possible applications for the material unless steps are taken to improve the safety.[54]

Regardless, there are few high voltage materials currently under investigation. Among these are $LiNi_{0.5}Mn_{1.5}O_4$ and $Li_2FeMn_3O_8$ spinels, though both have lower theoretical capacities in the high voltage region – 140 mAh/g or less – compared to $LiCoPO_4$ (167 mAh/g).[57,58] Thus, further studies on $LiCoPO_4$ are beneficial to the battery community, and a better understanding of the material's advantages and limitations will aid future electrode material design. Similar to the $LiFePO_4$ polymorph above, a high-performance $LiCoPO_4$/C composite material was achieved through spray pyrolysis synthesis using the custom-built system.

Synthesis and Experimental Details

In an analogous manner to the $LiFePO_4$ composite material synthesized above, porous, spherical micron-sized particles composed of nanosized $LiCoPO_4$ primary particles with a conformal carbon coating were produced by spray pyrolysis. For $LiCoPO_4$, water-soluble $Co(CH_3CO_2)_2 \cdot 4H_2O$, $LiNO_3$, $NH_4H_2PO_4$ and citric acid ($HOC(COOH)(CH_2COOH)_2$) were dissolved in a 1:1:1:0.5 molar ratio in distilled water to form an aqueous precursor solution in which the concentration of Co^{2+} was 0.5 mol/L.

This solution was delivered via syringe pump to an atomizer nozzle (Sonozap Model 120K50ST, 120 kHz) to generate an aerosol of microdroplets, which was subsequently transported through a 700°C quartz tube by a carrier gas (5% H_2 + 95% N_2). Although $LiCoPO_4$ is air stable and usually synthesized in air, the reducing atmosphere was used to promote residual carbon in the product. As the microdroplets travelled through the heated tube, rapid evaporation of water concentrated the precursor material until a self-sustaining combustion reaction occurred, resulting in the desired crystalline $LiCoPO_4$ phase along with a residual carbon coating on the particles from the decomposition of excess citric acid. The evolution of gaseous reaction by-products during the formation step facilitated the creation of an interconnected pore structure throughout the generated particles. The crystalline $LiCoPO_4$ product collected at the end of the tube was further heat-treated at 700°C in N_2 for 3 h to improve the conductivity of the carbon coating.

Composite electrodes were prepared by mixing 85 wt% $LiCoPO_4$/C material with 10 wt% carbon black and 5 wt% polytetrafluoroethylene (PTFE) binder, rolling the mixture into thin sheets, and drying overnight in a vacuum oven at 120°C. Circular electrodes of 1.26 cm^2 area with a typical active material loading of 4–5 mg were cut. Size 2032 coin cells were assembled with composite cathodes, metallic lithium anodes, 1M $LiPF_6$ in 1:1 (v/v) ethylene carbonate (EC)/diethyl carbonate (DEC) electrolyte with 1 wt% LiBOB (lithium bis(oxalato) borate) additive and Celgard 2500 polypropylene separators. The LiBOB additive was employed to stabilize the interface between the cathode material and electrolyte, as the operating voltage (~4.8 V vs. Li/Li^+) is above the stability range of the organic electrolyte. The cells were cycled between 3 and 5 V.

Material Characterization

The spray pyrolysis synthesis produced an impurity-free $LiCoPO_4$/C composite material, as revealed by the X-ray diffraction pattern shown in Figure 5-11. All peaks could be indexed in the *Pnma* space group, and Rietveld refinement of the XRD pattern gave lattice parameters (Table 5-2) that are in good agreement with previously reported values.[48] The results of site-occupancy refinement suggest the presence of few defects. The average primary particle size, determined from peak broadening, is about 70 nm.

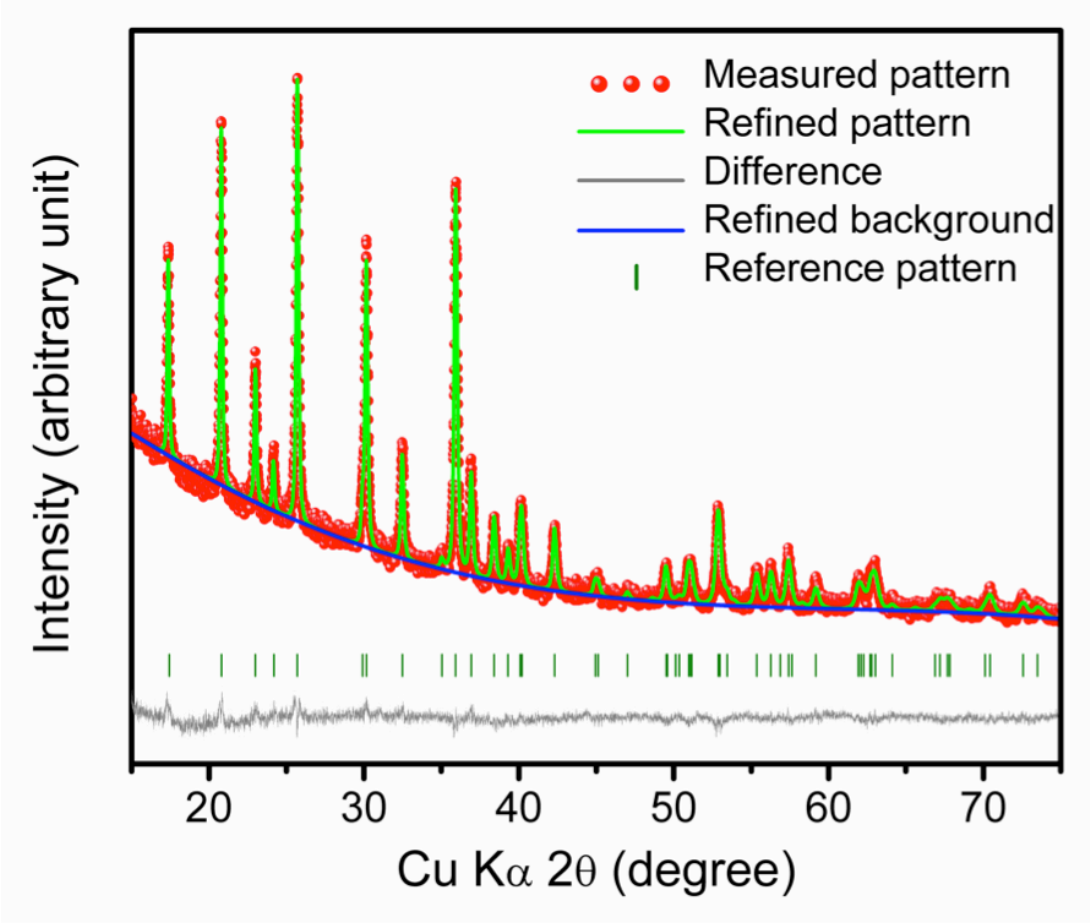

Figure 5-11: XRD pattern and Rietveld refinement of the $LiCoPO_4$/C composite material.

Table 5-2: Rietveld refinement results for spray pyrolysis $LiCoPO_4$/C

Parameter	Value	Uncertainty
a	10.1997 Å	0.0003 Å
b	5.9209 Å	0.0002 Å
c	4.7002 Å	0.0002 Å
V	283.85 Å^3	0.02 Å^3
R	4.34 %	
R_{wp}	4.82 %	

Similar to the $LiFePO_4$/C particles discussed above, the spherical $LiCoPO_4$/C composite particles have micron-scale diameters ranging from a few to 15 μm for most particles (Fig. 5-12). The surface of an individual particle with a very porous structure is shown in Figure 5-12b. Fracturing some of the particles reveals that, in contrast to the $LiFePO_4$ case, some of the $LiCoPO_4$ particles are hollow (Fig. 5-12c), while others are not (Fig. 5-12d). Either hollow or dense particles can be formed during the solvent evaporation step in the spray pyrolysis process.[1] As the aqueous solvent evaporates, a solid or crust precipitate forms on the surface, with the morphology being carried through to the final particle. Residence time in the heated tube (determined by tube length and flow rate) will affect the final morphology, with denser particles produced for increased residence times. Initial droplet size can also have a strong effect, but the employment of the same atomizer nozzle as in $LiFePO_4$ synthesis suggests the use of Co acetate rather than a nitrate salt has an effect on the formation mechanism. The gas flow rate was likely higher than that used for $LiFePO_4$ as well – the value was finely adjusted to improve aerosol transport, and the system was only equipped with a course flow meter. These processes are additionally complicated, though, by the combustion reactions occurring within the precursor particles. Regardless, hierarchically organized pores extend throughout the secondary particles in both morphologies, allowing the liquid electrolyte to penetrate throughout the thicknesses and into the particle interiors.

EDS elemental mapping (Fig. 5-13) indicates a uniform distribution of Co, P, O and C, consistent again with the $LiCoPO_4$ phase purity determined by XRD and the expectations from the previous $LiFePO_4$ study. TEM characterization of $LiCoPO_4$/C particles, purposely fractured by mechanical grinding, show the distribution of pore sizes throughout the secondary particles, ranging from a few nanometers to a few hundred nanometers (Fig. 5-14a). The HRTEM image of a single crystallite (Fig. 5-14b) reveals an amorphous carbon layer, 3–5 nm thick, on the surfaces. This carbon layer, again, provides a distributed electronically conductive network throughout the otherwise electronically insulating particles.

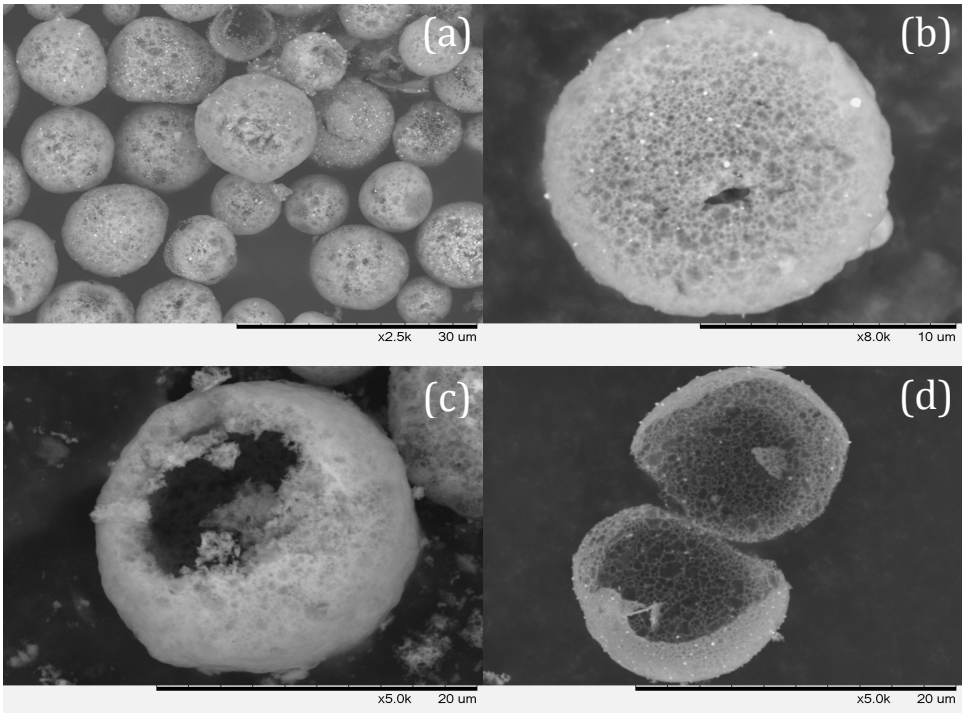

Figure 5-12: SEM images of the $LiCoPO_4$/C particles. The images show the porous structure of the materials. Some particles are hollow (c) while others are not (d).

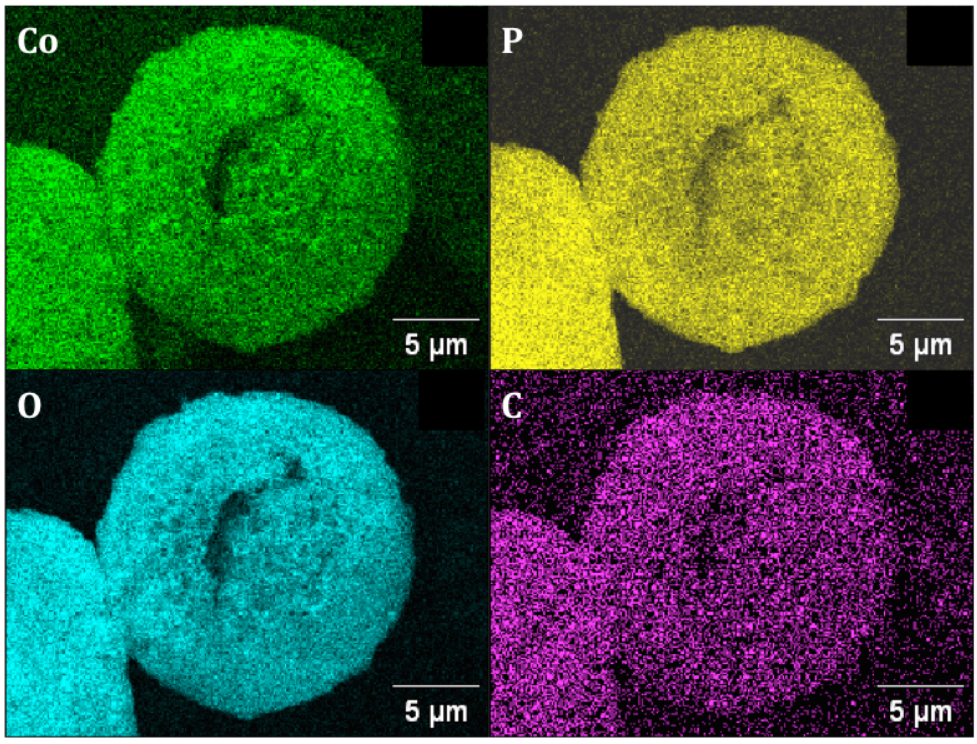

Figure 5-13: EDS of a single $LiCoPO_4$/C composite particle.

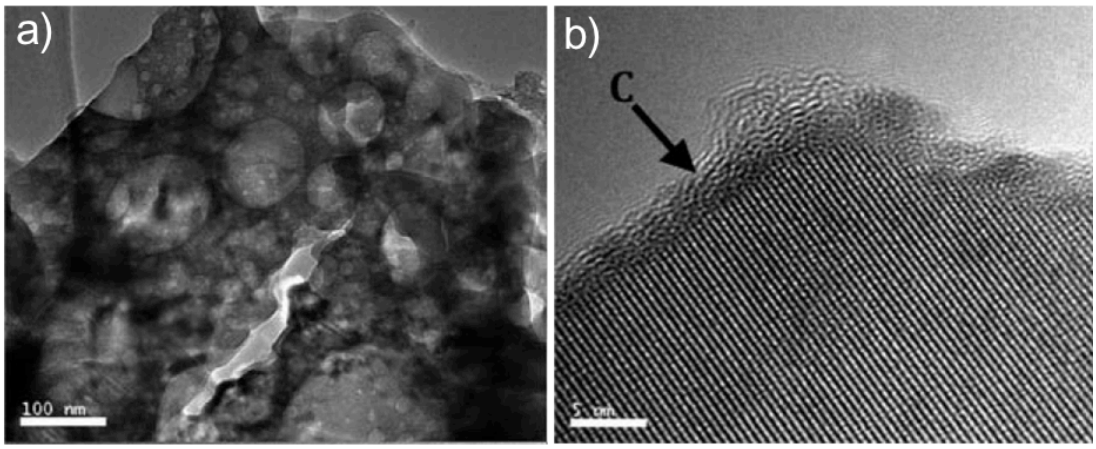

Figure 5-14: TEM images of the $LiCoPO_4$/C materials showing a) the nanoscale pore structure and b) the conformal carbon coating on the primary particles.

The carbon content contained in the $LiCoPO_4$/C composite material was also determined by TGA (Fig. 5-15). A weight loss of 2.4% was recorded for the composite, while that for uncoated, carbon-free $LiCoPO_4$ was negligible. $LiCoPO_4$, in the fully lithiated state, is stable against oxidation in air, unlike $LiFePO_4$ in these conditions. XRD patterns (Fig. 5-15b) measured before and after heating of the materials are identical, indicating that the change in weight is entirely due to combustion of carbon. Therefore, no calibration curve is necessary, and the $LiCoPO_4$/C composite material could be assumed to contain 2.4 wt% C. A smaller carbon content in $LiCoPO_4$ material compared to similarly produced $LiFePO_4$ was previously seen in another study as well.[59]

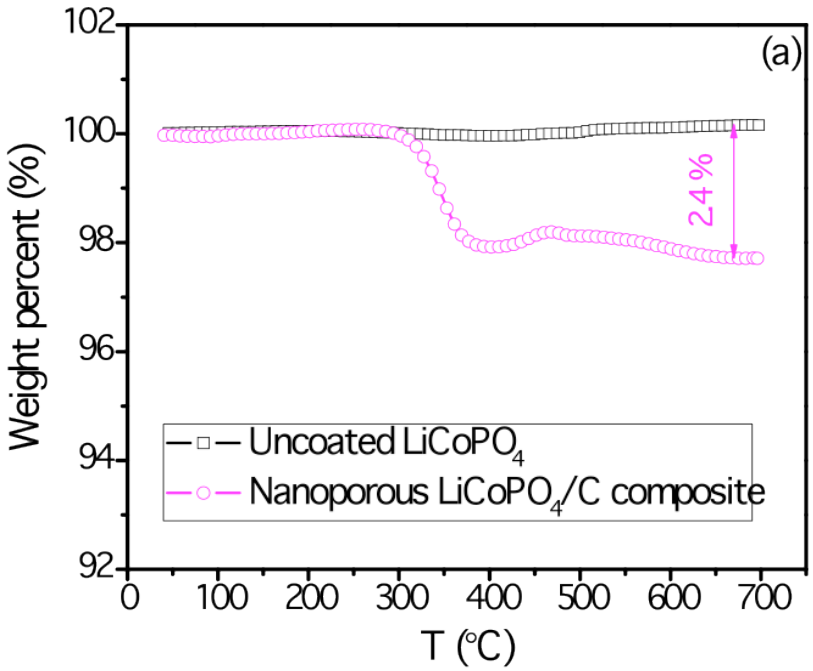

Figure 5-15: a) TGA curves of a carbon-free $LiCoPO_4$ and the $LiCoPO_4$/C composite materials. b) XRD patterns of the composite material before and after heating are identical.

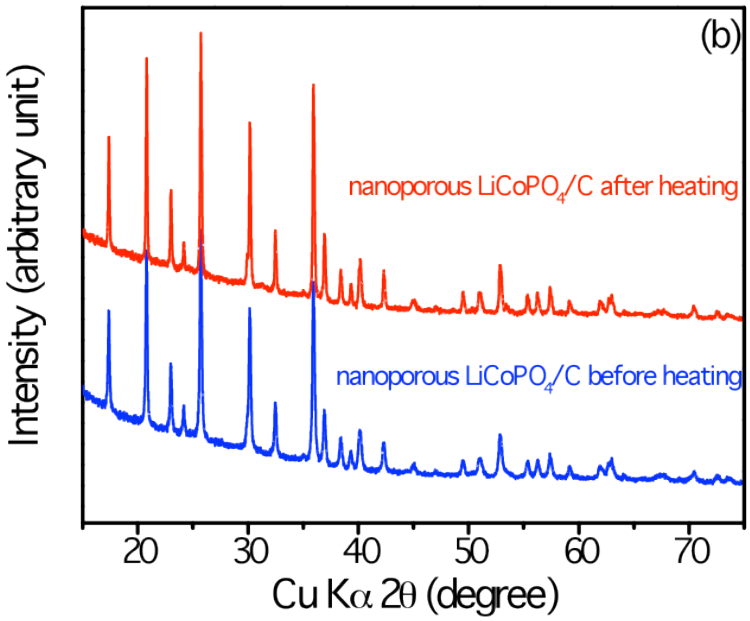

Figure 5-15 (cont'd): a) TGA curves of a carbon-free $LiCoPO_4$ and the $LiCoPO_4$/C composite materials. b) XRD patterns of the composite material before and after heating are identical.

N_2 adsorption/desorption isotherms, shown in Figure 5-16, were used to determine the Brunauer-Emmett-Teller (BET) surface area and the average pore size. The type IV curve with a large H3 hysteresis loop is consistent with N_2 adsorption in a nanoporous solid.[43] The BET surface area and average pore size were found to be 76 m^2/g and 68 nm, respectively. The smaller measured surface area compared to the $LiFePO_4$/C material is most likely due to the presence of some hollow particles.

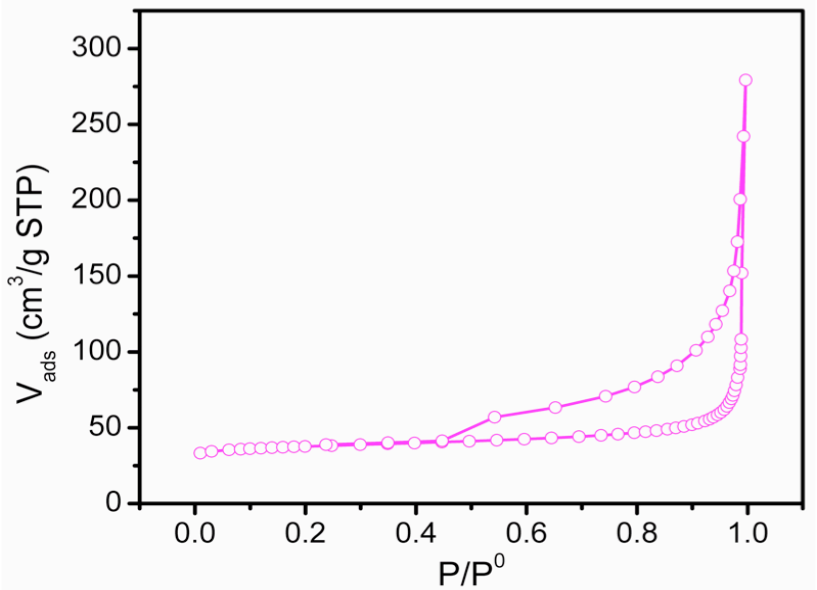

Figure 5-16: N_2 adsorption/desorption isotherms of the porous $LiCoPO_4$/C composite particles.

Electrochemical Performance

The electrochemical performance of the nanoporous $LiCoPO_4$/C in lithium half-cell configurations is summarized in Figure 5-17. As mentioned above, in contrast to the behavior of isostructural $LiFePO_4$ and $LiMnPO_4$, which both have a single, flat voltage plateau, two voltage plateaus are observed during both charge and discharge, as shown in Figure 5-17a for C/10 cycling. These two plateaus are associated with two first-order phase transitions: $LiCoPO_4 \leftrightarrow Li_{0.7}CoPO_4$ and $Li_{0.7}CoPO_4 \leftrightarrow CoPO_4$.

A discharge capacity of 123 mAh/g was obtained at C/10. The observed coulombic inefficiency on the first cycle is most likely due to side reactions involving the electrolyte. $LiCoPO_4$ cathodes have generally suffered from poor cycling stability due to the high voltage of the material.[53] In contrast, the nanoporous $LiCoPO_4$/C composite exhibits a capacity retention of 95% over 20 cycles (Fig. 5-17b). This may be attributable to the stabilization effect introduced by the LiBOB additive,[60] in addition to the presence of the conformal carbon coating and porous particle structure. The coulombic efficiency steadily increases from 86% for the 1st cycle to 97%, consistent with a protective effect developing from the products of an irreversible reaction of the LiBOB on cathode particle surfaces during early cycles, akin to the solid electrolyte interface (SEI) that forms on graphite anodes. Discharge profiles at various C-rates are shown in Figure 5-17c. Even when discharged at 5C, a capacity as high as 82 mAh/g is achieved, indicating that the nanostructuring strategy employed in this study results in very good rate capability for this $LiCoPO_4$/C composite material, among the best reported to date.

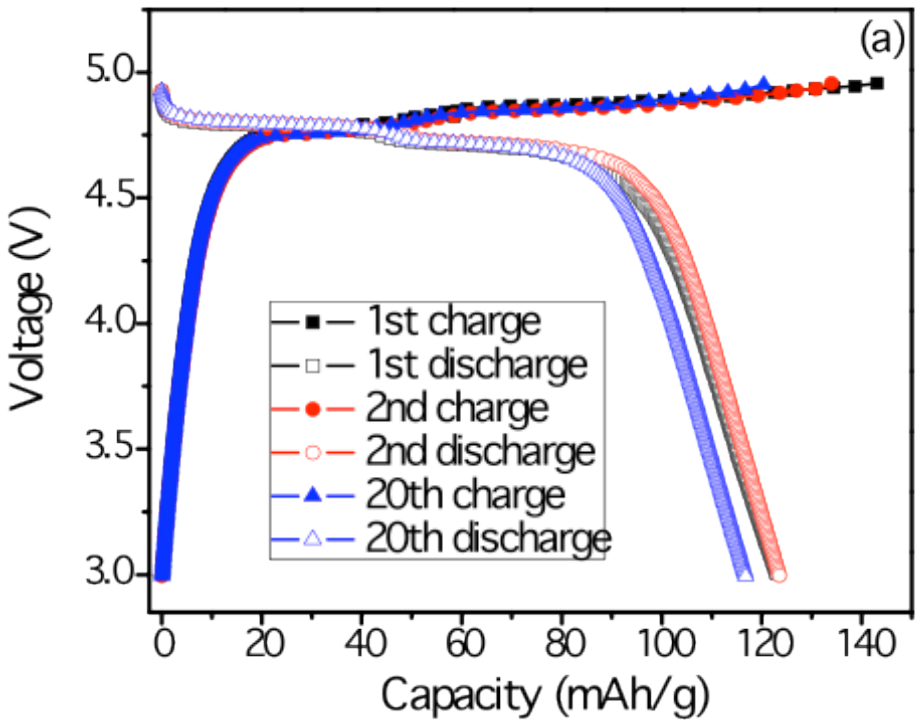

Figure 5-17: The $LiCoPO_4$/C composite materials display excellent electrochemical performance. a) the 1st, 2nd, and 20th charge and discharge profiles. b) Discharge capacity vs. cycle number showing the cycling stability of the electrodes (inset: corresponding coulombic efficiencies). c) Rate capability of the $LiCoPO_4$/C cathode materials.

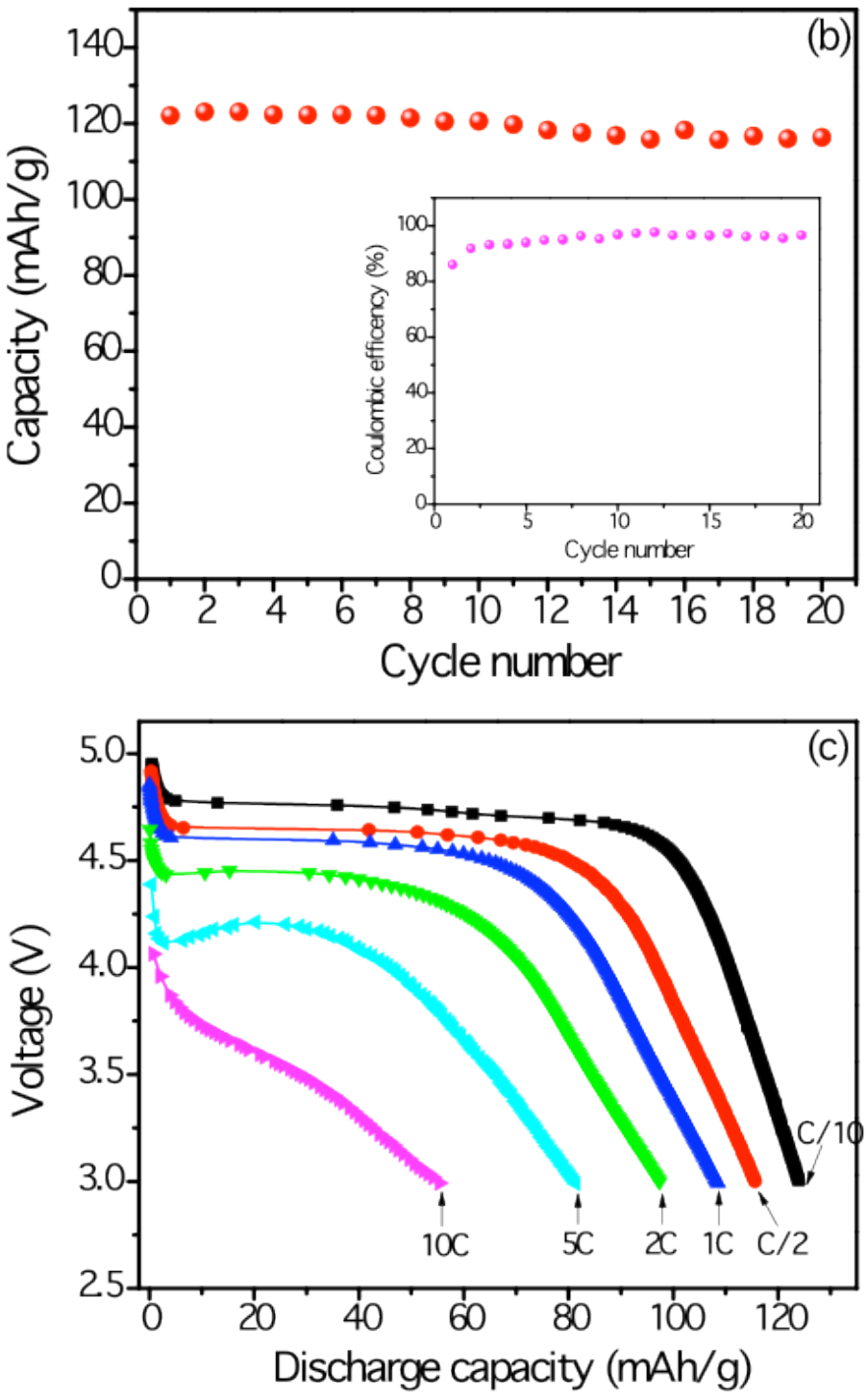

Figure 5-17 (cont'd): The $LiCoPO_4$/C composite materials display excellent electrochemical performance. a) the 1st, 2nd, and 20th charge and discharge profiles. b) Discharge capacity vs. cycle number showing the cycling stability of the electrodes (inset: corresponding coulombic efficiencies). c) Rate capability of the $LiCoPO_4$/C cathode materials.

5.4 Summary

In summary, two different olivine materials – $LiFePO_4$ and $LiCoPO_4$, both having excellent electrochemical performance – have been successfully produced using the custom-built, lab-scale spray pyrolysis system. The manufactured micron-sized particles were porous and spherical in shape, and were composed of nanoscale primary particles with a conformal carbon coating. The conductive carbon and pore structure each formed continuous networks throughout the bulk of the particles, allowing electrolyte access for full material utilization. Both the $LiFePO_4$ and $LiCoPO_4$ materials in this study showed superior cycling and rate performance. As they are produced using an inexpensive and scalable spray pyrolysis process, these studies demonstrate the high potential of battery materials produced in this manner for EV, PHEV, or other cost-conscious applications.

5.5 References

[1] T. T. Kodas, M. Hampden-Smith, *Aerosol Processing of Materials*. Wiley-VCH, New York, NY. **1999.**

[2] Definition. Pyrolysis: the application of heat to chemical compounds in order to cause decomposition. *Collins English Dictionary - Complete and Unabridged*, 10th ed. **2009**.

[3] "Pyrolysis." Wikipedia, http://en.wikipedia.org/wiki/Pyrolysis. Accessed 12/14/11.

[4] Bickmore et al. *J. European Ceramic Soc.* **1998**, *18*, 287.

[5] Kim et al. *Chem. Mater.* **2004**, *16*, 2336.

[6] Lorentzou et al. *Granular Matter*, **2008**, *10*, 113.

[7] Choi et al. *J. Mater. Proc. Tech.* **2006**, *171*, 118.

[8] Park et al. *Electrochimica Acta,* **2004**, *49*, 557.

[9] Oh et al. *Solid State Ionics,* **2004**, *171*, 167.

[10] Ogihara et al. *Materials Science and Engineering: B*, **2009**, *161*, 109.

[11] Doi et al. *Electrochimica Acta* **2008**, *53*, 8064.

[12] Hirose et al. *Journal of Alloys and Compounds,* **2010**, *506*, 883.

[13] Park et al. *Solid State Ionics,* **2005**, *176*, 481.

[14] S. Park, Y. Sun. *Electrochimica Acta*, **2004**, *50,* 431.

[15] S. Ju, Y. Kang. *J. Power Sources,* **2009**, *189*, 185.

[16] Doi et al. *Chem. Mater.* **2005**, *17*, 1580.

[17] J. Liu, T. E. Conry, et al. *Energy Environ. Sci.* **2011,** *4,* 885.

[18] Waser et al. *Journal of Aerosol Science* **2011**, *42*, 657.

[19] Z. Bakenov, I. Taniguchi. *Electrochem. Commun.* **2010**, *12*, 75.

[20] Z. Bakenov, I. Taniguchi. *J. Electrochem. Soc.* **2010**, *157*, A430.

[21] J. Liu, T. E. Conry, et al. *J. Mater. Chem.* **2011,** *21,* 9984

[22] A. K. Padhi, et. al. *J. Electrochem. Soc.* **1997,** *144*, 1188.

[23] J. Jiang, J.R. Dahn, *Electrochem Commun.* **2004**, *6,* 724.

[24] S. Ju, Y. Kang. *Materials Chemistry and Physics* **2008**, *107*, 328.

[25] Yang et al. *J. Power Sources,* **2006**, *159*, 307.

[26] M. Konarova, I. Taniguchi. *Mater. Res. Bull.* **2008**, *43*, 3305.

[27] K. Konstantinov et al. *Electrochimica Acta* **2004**, *50*, 421.

[28] M. Konarova, I. Taniguchi. *J. Power Sources,* **2009,** *194,* 1029.

[29] B. Kang, G. Ceder. *Nature,* **2009**, *458*, 190.

[30] A. V. Murugan, T. Muraliganth, A. Manthiram, *Electrochem. Commun.* **2008**, *10*, 903.

[31] Dominko et al. *J. Electrochem. Soc.* **2005**, *152*, A858.

[32] R. Dominko, M. Bele, J. M. Goupil, M. Gaberscek, M. Remskar, D. Hanzel, I. Arcon and J. Jamnik, *Chem. Mater.* **2007**, *19*, 2960.

[33] C. M. Doherty, R. A. Caruso, B. M. Smarsly and C. J. Drummond, *Chem. Mater.* **2009**, *21*, 2895.

[34] C. M. Doherty, R. A. Caruso, B. M. Smarsly, P. Adelhelm and C. J. Drummond, *Chem. Mater.* **2009**, *21*, 5300.

[35] F. Yu, J.-J. Zhang, Y.-F. Yang and G.-Z. Song, *J. Mater. Chem.* **2009**, *19*, 9121.

[36] S. W. Oh, S.-T. Myung, H. J. Bang, C. S. Yoon, K. Amine and Y. K. Sun, *Electrochem. Solid State Lett.* **2009**, *12*, A181.

[37] J. Qian, M. Zhou, Y. Cao, X. Ai and H. Yang, *J. Phys. Chem. C*, **2010**, *114*, 3477.

[38] M. M. Doeff, J. Chen, T. E. Conry, et al. *J. Mater. Res*. **2010**, *25*, 1460.

[39] K.C. Patil, M. S. Hegde, T. Rattan, S. T. Aruna, *Chemistry of Nanocrystalline Oxide Materials: Combustion Synthesis, Properties and Applications.* World Scientific, **2008**.

[40] A. Ait Salah, A. Mauger, K. Zaghib, J. B. Goodenough, N. Ravet, M. Gauthier, F. Gendron and C. M. Julien, *J. Electrochem. Soc.,* **2006**, *153*, A1692.

[41] I. Belharouak, C. Johnson and K. Amine, *Electrochem. Commun.* **2005**, *7*, 983.

[42] K. Zaghib, et. al. *Electrochimica Acta,* **2004,** *50,* 263.

[43] S. J. Gregg and K. S. W. Sing, *Adsorption, Surface Area, and Porosity*, Academic Press, New York, NY, 2nd edn, **1982**.

[44] Y.-S. Hu, Y.-G. Guo, R. Dominko, M. Gaberscek, J. Jamnik and J. Maier, *Adv. Mater.* **2007**, *19*, 1963.

[45] X.-L. Wu, L.-Y. Jiang, F.-F. Cao, Y.-G. Guo and L.-J. Wan, *Adv. Mater.* **2009**, *21*, 2170.

[46] M. Armand and J.-M. Tarascon, *Nature*, **2008**, *451*, 652.

[47] J. B. Goodenough and Y. Kim, *Chem. Mater.* **2010**, *22*, 587.

[48] K. Amine, H. Yasuda, M. Yamachi, *Electrochem. Solid State Lett.* **2000**, *3*, 178.

[49] Wolfenstine. *J. Power Sources,* **2006**, *158*, 1431.

[50] Wolfenstine et al. *J. Power Sources,* **2007**, *163*, 1070.

[51] Ellis et al. *Chem. Mater.* **2010**, *22*, 691.

[52] Bramnik et al. *J. Solid State Electrochem.* **2004**, *8*, 558.

[53] Bramnik et al. *Chem. Mater.* **2007**, *19*, 908.

[54] Bramnik et al. *Electrochem. Solid State Lett.* **2008**, *11*, A89.

[55] G. Rousse, J. Rodríguez-Carvajal, S. Patoux, C. Masquelier, *Chem. Mater.* **2003**, *15*, 4082.

[56] "Batteries: Overview of Battery Cathodes." Doeff, M. M., in *Springer Encyclopedia of Sustainability Science and Technology,* Springer Science + Business Media, LLC, New York, in press **2011**.

[57] Ma et al. *J. Electrochem. Soc.* **2010**, *157*, A925.

[58] Kawai et al. *Che. Mater.* **1998**, *10*, 3266.

[59] J. Yang, J. Xu, *J. Electrochem. Soc.* **2006**, *153*, A716.

[60] J. Liu, Z. Chen, S. Busking and K. Amine, *Electrochem. Commun.* **2007**, *9*, 475.

Chapter 6: Conclusions and Future Work

6.1 Al-Substitution in Layered Oxides

The bulk of the work described in this dissertation focused on understanding the structural and electrochemical consequences of Al-substitution in place of Co in layered oxide cathode materials, using the model system $LiNi_{0.45}Mn_{0.45}Co_{0.1-y}Al_yO_2$. The full substitution range ($0 \leq y \leq 0.1$) was investigated. Aluminum impacts the charge and discharge behavior of electrodes by increasing the (de)intercalation potential up to 50-75 mV. When cycled between voltage limits, an enhanced cycling stability is observed for charging potentials of 4.3-4.7 V. The delivered capacity of the unsubstituted material diminishes at a quicker rate than that of Al-substituted samples. The effect is observed with Al-contents as low as 5%.

The Al is homogeneously incorporated for all values of y, as seen in the EXAFS. High resolution XRD uncovered a slight symmetry-lowering structural distortion in the high-Al materials (y=0.1). We hypothesize that the distortion indicates increased cation ordering within the transition metal layer, relieving strain associated with the edge-sharing octahedra that compose the structure. This is supported by the XANES data of the fresh $LiNi_{0.45}Mn_{0.45}Co_{0.1-y}Al_yO_2$ materials. *In situ* observation of the material structure during battery operation shows a clear effect of Al-incorporation by limiting changes along the layer-stacking direction (*c*-parameter) during charge and discharge. The contraction of the structure along the axial direction during the second half of Li deintercalation (after the initial expansion) is pushed to a higher state-of-charge with the presence of Al. Although no significant local effect of Al-substitution on the charging mechanism of the layered oxides is observed, there is an influence seen in the electrochemically cycled materials. The presence of Al limits the induced distortion of the local structure of the substituted samples compared to the fresh $LiNi_{0.45}Mn_{0.45}Co_{0.1-y}Al_yO_2$ materials.

A number of experiments will provide further insight into the effect of Al-substitution in these layered oxide systems. First, a more detailed understanding of the cation ordering in the transition metal layers would be very informative. Nuclear Magnetic Resonance (NMR) is a non-destructive, element specific technique that can give complimentary information about the local chemical environment of the observed element. As mentioned throughout the text, Li NMR measurements have been instrumental in the experimental observation of the flower pattern-type ordering in NMC systems.[1,2] Here, it would be instructive to measure both Li and Al NMR for the as-synthesized powders to aid the determination of ordering schemes due to Al-substitution, especially whether Al is randomly distributed throughout the transition metal layers, as assumed.[3,4] Comparison of NMR measurements on fresh and cycled samples of varying Al-content would also be useful in determining the evolution of the cation configuration throughout the operation lifetime of the cathodes. Neutron diffraction, is another method to pursue for information about the long-range order of the metal constituents.[1,5,6] Unlike XRD, neutron diffraction is able to distinguish Ni, Mn, and Co due to different scattering lengths, and the technique is additionally sensitive to Li. It will be instructive to examine both fresh $LiNi_{0.45}Mn_{0.45}Co_{0.1-y}Al_yO_2$ materials with different Al-contents and those

charged to various SOCs. Any additional superstructure due to Al-substitution should be resolvable, and any differences in metal-migration (for instance, to tetrahedral sites in the layered oxide structure) between samples during Li deintercalation will be exposed.[7]

A transition electron microscopy (TEM) study will also be useful to characterize the structural effect of Al-substitution in as-synthesized powders, as well as the evolution of the electrode materials with cycling. Electron diffraction should provide improved resolution of the structural distortion uncovered by the high-resolution synchrotron XRD.[8] Owing to the nanoscale dimensions of the primary particles synthesized here, convergent beam electron diffraction will be necessary for single particle diffraction studies.[9,10] Powder patterns will be useful to further understand the microscopic evolution of the material structure during the operation lifetime. Additionally, imaging the electrode materials before and after electrochemical cycling will provide insight into the macroscopic behavior of the active material particles, such as particle fracturing.[11,12] To this end, a collaboration with microscopists at Lawrence Berkeley National Laboratory has already commenced.

There is much further XAS work that will also be beneficial. First, the metal K-edge XANES regions are rife with information about the absorbing atom environment. The current analysis was not able to extend much beyond a qualitative interpretation, as is common.[13] It was mentioned in Chapter 4 that a well-developed analysis package for the XANES data region does not yet exist on par with that available for EXAFS. The understanding does, however, continue to mature. The Multiple Scattering XANES (MXAN) package calculates many theoretical spectra using a full multiple scattering approach, changing various parameters from a starting structure, then performs a least-squares fit to the experimental data to accurately explain the structure.[14,15] Using this approach, a more precise description of the strain-lowering effect of Al can be obtained by quantitatively evaluating the XANES, including the pre-edge peaks and features in the rising edge. The cycling-induced distortions, and the limitation of such due to Al-substitution, can also be quantified. Furthermore, the evolution of the edges (especially the Mn and Co edges) during Li deintercalation can also be evaluated to more accurately describe the electronic structure reconfiguration during cell operation.

Additionally, the O K-edge and transition metal L-edges should be measured to determine the role of the oxygen anions in the charge compensation mechanism and the bonding nature between the metals and ligands. Both the transition metal $L_{II,III}$-edges (which directly probe dipole-allowed 2p→3d electronic transitions) and the O K-edge are very sensitive to the occupation of the metal d-states and overlap with the ligand orbitals.[16,17] The data can be measured using soft X-rays or electron energy loss spectroscopy (EELS). All of the further experiments mentioned should significantly enhance the understanding of the beneficial structural role of Al-substitution in NMC layered oxide battery materials.

6.2 Spray Pyrolysis of Olivine Materials

A spray pyrolysis system was designed, assembled, and used to produce two different olivine materials, $LiFePO_4$ and $LiCoPO_4$. The as-synthesized particles are porous and spherical in shape with micron-scale diameters, composed of nanoscale

primary particles with a conformal carbon coating. The hierarchical pore structure and conductive carbon network both extend throughout the particle volumes; almost full material utilization is possible due to the penetrating electrolyte and electronic access. The $LiFePO_4$ and $LiCoPO_4$ materials display excellent electrochemical properties, in terms of both cycling stability and rate performance. The use of the inexpensive and scalable spray pyrolysis technique to produce high-performance electrode materials is a practical step towards developing a low-cost cathode for EV's and PHEV's.

Further work must focus on developing control over the synthesis process such that particle sizes and pore distributions can be tailored and uniformly produced. Particle morphology is strongly dependent on the gas flow rates, temperature, and furnace length.[18] The precursor chemistry will also play a leading role, as the gaseous combustion products are believed to be an important part of the pore-forming mechanism. Secondary particle sizes are mostly determined by the initial droplet sizes, so a tunable atomizer[†] (frequency and amplitude) and solution additives should provide more control. The carbon content and quality should also be managed, also through the understanding of precursor chemistry and process specifics. Control of these variables will help to improve the tap densities of the processed materials, such that optimized electrodes can be manufactured with high energy densities while maintaining excellent electrochemical performance.

Additionally, the spray pyrolysis system is not limited to the production of olivine-type materials. The porous-particle approach should be extended to other materials systems with intrinsically slow kinetics, such as the Li_2MSiO_4 (M=transition metal) materials. Layered oxides and spinel materials should also be explored. The three-dimensional pore structure and carbon networks can allow for further improvements in the power capabilities for these systems, while lowering material production costs.

[†] The tunable atomizer will likely have to be custom-built, as no commercial products can be found at this time.

6.3 References

[1] J. Bréger et al. *J. Am. Chem. Soc.* **2005,** *127,* 7529.

[2] J. Bréger et al. *J. Solid State Chemistry,* **2005,** *178,* 2575.

[3] E. Gaudin et al. *J. Phys. Chem. B,* **2001,** *105,* 8081.

[4] Y. K. Lee et al. *Electrochimica Acta,* **2004,** *50,* 491.

[5] M. Ma et al. *J. Power Sources,* **2007,** *165,* 517.

[6] H. Kobayashi et al. *J. Power Sources,* **2005,** *146,* 640.

[7] J. Bréger et al. *Chem. Mater.* **2006,** *18,* 4768.

[8] H. Li et al. *Chem. Mater.* **2007,** *19,* 2551.

[9] D. Abraham et al. *J. Electrochem. Soc.* **2003,** *150,* A1450.

[10] D. Abraham et al. *Electrochem. Commun.* **2002,** *4,* 620.

[11] S. Muto et al. *J. Electrochem. Soc.* **2009,** *156,* A371.

[12] H. Gabrisch et al. *J. Power Sources,* **2003,** *119,* 674.

[13] C. Natoli, M. Benfatto, S. Della Longa, K. Hatada. *J. Synchrotron Rad.* **2003,** *10,* 26.

[14] M. Benfatto, S. Della Longa. *J. Synchrotron Rad.* **2001,** *8,* 1087.

[15] M. Benfatto, S. Della Longa, C. Natoli. *J. Synchrotron Rad.* **2003,** *10,* 51.

[16] S. Miao, et. al. *J. Phys. Chem. B,* **2005,** *109,* 23473.

[17] W. Yoon et. al. *J. Am. Chem. Soc.* **2005,** *127,* 17479.

[18] T. T. Kodas, M. Hampden-Smith, *Aerosol Processing of Materials*. Wiley-VCH, New York, NY. **1999.**